Vortices, Zonal Flows, and Transport in Gyrokinetic Plasma Turbulence

Motoki Nakata

DOCTOR OF PHILOSOPHY

Department of Fusion Science

School of Physical Science

The Graduate University for Advanced Studies

March, 2011

To Osaya

Acknowledgements

First of all, I would like to express sincere gratitude to my advisers Professor Tomo-Hiko Watanabe and Professor Hideo Sugama for their guidance, support, and encouragement over five years of my doctoral course. Especially, I really do appreciate their unlimited generosity to my interest in different fields of physics, and to my inefficiency and unskillfulness. It is my great pleasure to compile the doctoral dissertation as an accumulation of many discussions with them.

I would also like to extend my appreciation to Professor Wendell Horton of Institute for Fusion Studies, The University of Texas at Austin for his kind and fruitful suggestions. I am deeply honored to share the strong interest in complicated, but beautiful nature of vortices in plasma turbulence with the great plasma physicist.

Special thanks goes to Professor Yasuaki Kishimoto (Kyoto univ.), Dr. Jiquan Li (Kyoto univ.), Dr. Kenji Imadera (Kyoto univ.), Dr. Yasuhiro Idomura (JAEA), Dr. Nobuyuki Aiba (JAEA), Dr. Ken Uzawa (JAEA), Dr. Akihiro Ishizawa (NIFS), Dr. Shinsuke Satake (NIFS), Dr. Ryutaro Kanno (NIFS), Dr. Masanori Nunami (NIFS), Dr. Atsushi Ito (NIFS), Dr. Seiya Nishimura (NIFS), and Dr. Gakushi Kawamura (NIFS), who have provided me with useful comments on this study and also discussed various topics in physics, mathematics, politics, and history.

Furthermore, I thank Dr.(to be) Seikichi Matsuoka, Dr.(to be) Kunihiro Ogawa, and the other Ph.D students in NIFS for mutual encouragement, and for sharing hopes and concerns about the future. And I am sincerely grateful to my family and friends for their support and understanding.

Finally, I absolutely love day-to-day lives in Toki-city!

Abstract

Plasma turbulence driven by drift wave instabilities is a key issue for understanding anomalous transport of particle, momentum, and heat observed in magnetically confined plasmas. Ion temperature gradient (ITG) and electron temperature gradient (ETG) driven instabilities are considered as main causes of the micro-scale turbulence with the spatial scale of the ion and electron gyroradii, respectively. Various flow structures, i.e., fine-scale turbulent vortices, axisymmetric zonal flows, and radially elongated streamers, are generated through complicated nonlinear interactions in plasma turbulence. From the aspect of regulating the turbulent transport in future burning plasmas, it is worthwhile to understand fundamental physics behind the formation of vortex and zonal flow structures and their stability as well as the related transport properties. Since the high temperature plasmas with weak collisionality inherently involve a lot of kinetic processes, i.e., the Landau damping, the finite gyroradius effect, the particle drift, and the magnetic trapping, the gyrokinetic theory is a powerful method for the precise investigation of the physical mechanisms of plasma turbulent transport.

In this dissertation, the ITG and ETG turbulence are explored based on nonlinear gyrokinetic theory and direct numerical simulations. Then, the results concerning (i) formation of coherent vortex streets and the resultant transport reduction, (ii) effects of parallel dynamics on the zonal flow generation, and (iii) nonlinear entropy transfer among turbulent vortices and zonal flows, are presented.

First, vortex structures in the slab ETG turbulence are investigated, including comparisons with those in the slab ITG case. Depending on parameters which determine the growth rate of linear ETG modes, two different flow structures are observed, i.e., statistically steady turbulence with a weak zonal flow and coherent vortex streets along a strong zonal flow. The former involves many isolated vortices with complicated motion and their mergers, which leads to steady electron heat transport. When the latter is formed, the high wavenumber components of potential and temperature fluctuations are reduced, and the electron heat transport decreases significantly. It is found that the transport reduction is mainly associated with the phase matching between the potential and temperature fluctuations rather than the reduction of fluctuation amplitudes. A traveling wave solution of a Hasegawa-Mima type equation derived from the gyrokinetic equation with the electron temperature gradient agrees well with the coherent vortex streets found in the slab ETG turbulence.

Second, effects of parallel dynamics on transition of vortex structures and zonal flows, which are closely associated with transport reduction found in the slab ETG turbulence, are intensively

examined. Numerical results show three different types of vortex structures, i.e., coherent vortex streets accompanied with the transport reduction, turbulent vortices with steady transport, and a zonal-flow-dominated state, depending on the relative magnitude of the parallel compression to the diamagnetic drift. In particular, the formation of coherent vortex streets is correlated with strong generation of zonal flows for the cases with weak parallel compression, even though the maximum growth rate of linear ETG modes is relatively large. A physical mechanism of the secondary growth of zonal flows is discussed based on the modulational instability analysis with a truncated fluid model, where the parallel dynamics with acoustic modes is incorporated. The modulational instability for zonal flows is found to be stabilized by the effect of the finite parallel compression. The theoretical analysis qualitatively agrees with the secondary growth of zonal flows found in the slab ETG turbulence simulations, where the transition of vortex structures is observed.

Finally, the investigations of vortex structures and zonal flows are extended to toroidal ITG and ETG turbulence by means of five-dimensional nonlinear gyrokinetic simulations. In the steady state, the formation of the strong zonal flow is observed in the toroidal ITG turbulence, while the radially elongated streamers, which yield the significant enhancement of heat transport, develop in the toroidal ETG case. Gyrokinetic entropy balance relations for zonal and non-zonal modes, and the nonlinear entropy transfer function, which is regarded as a kinetic extension of the zonal-flow energy production due to the hydrodynamic Reynolds stress, are carefully examined. The different entropy transfer processes in saturation and steady phases are revealed for the ITG turbulence. The entropy transfer from non-zonal to zonal modes is substantial in the saturation phase of the instability growth, while the entropy transfer to zonal modes becomes quite weak in the steady phase. Instead, the entropy variable of the low radial-wavenumber modes driving the heat transport are successively transferred to the higher radial-wavenumber modes with less contribution to turbulent heat flux via the strong interaction with zonal flows. On the other hand, in both the saturation and steady phases of the ETG turbulence, the catalytic role of zonal flows in the entropy transfer to the higher radial-wavenumber modes is much weaker than that in the ITG case. Then, the entropy transfer processes among low-wavenumber non-zonal modes including radially elongated streamers are dominant and the higher heat transport level is sustained.

The formation of vortices and zonal flows, and the related entropy transfer processes in the ITG and ETG turbulence are comprehensively examined in this study, then the transport regulation due to the nonlinear interactions with zonal flows are clarified in the framework of kinetic theory. The results obtained by a novel method of the entropy transfer analysis provide one with not only deeper understandings of the physics of the turbulent transport and zonal flows, but fruitful suggestions for advanced turbulence diagnostics such as the bi-spectrum analysis.

The one who doesn't go forward goes backward.
The one who doesn't go backward goes forward.

Contents

5 Nonlinear entropy transfer via zonal flows in toroidal plasma turbulence   **79**

6 Summary   **117**

List of publications

Chapter 1

Introduction

Drift wave turbulence driven by micro-instabilities is a key issue for understanding and predicting anomalous (or turbulent) transport of particle, momentum, and heat in the core region of magnetically confined plasmas, where the experimentally observed transport level is much higher than that predicted from both the classical and neoclassical transport theory based on Coulomb collision processes of ions and electrons [1]. In particular, the turbulent heat transport determines the energy confinement time which is directly connected to the quality of future fusion reactors so that tremendous efforts have been devoted so far to theoretical prediction, numerical simulations and dedicated experiments. Since the dynamics of turbulent vortices and the related transport processes in high temperature plasmas with weak collisionality are inherently nonlinear, and involve a lot of kinetic processes, i.e., the Landau damping, the finite gyroradius effect, the particle drift, and the magnetic trapping, the direct numerical simulations by means of an appropriate kinetic model are indispensable for understandings of physical mechanisms of plasma turbulent transport and for quantitative estimation of the transport level. The gyrokinetic model (for example, see Ref. 2 – 4) is a reduced kinetic equation averaged over the fast gyromotion without losing important kinetic effects described above, and is the most reliable and useful kinetic description of the nonlinear dynamics of low-frequency turbulence in collisionless (or weakly collisional) magnetized plasmas.

In general, magnetically confined plasmas with high ion and electron temperature involve various fluctuations observed in a wide range of spatial scales, and the turbulent transport is considered to be driven by micro-instabilities originated from inhomogeneities of density, temperature, and magnetic fields, where the scale lengths related to ion and electron gyroradii are much shorter than the equilibrium scales. Drift waves are destabilized by the equilibrium density and temperature gradients above thresholds, even if the plasma equilibrium is stable to the macroscopic instabilities such as MHD modes. Then, the turbulent vortices with various spatial

scales develop through the complicated nonlinear interactions due to $\boldsymbol{E} \times \boldsymbol{B}$ convective flows.

The ion temperature gradient (ITG) driven mode, which is one of the micro-instabilities, is considered to be a main cause of the turbulent ion heat transport in the core region of tokamak and helical plasmas, and the ITG turbulence has been extensively investigated by means of numerical simulations based on gyrokinetic and gyrofluid models [5–13]. The spatial scales of the ITG turbulence perpendicular to the confinement magnetic field are of the order of ion gyroradii, and the phase velocity is basically associated with the ion diamagnetic drift motion. One of the remarkable results obtained by the ITG turbulence simulations is that the meso-scale zonal flows, which are spontaneously generated through the nonlinear interactions among turbulent fluctuations, effectively suppress the turbulent heat transport by the strong flow shear in the radial direction. Intensive simulation studies have confirmed that the transport reduction by zonal flows leads to the nonlinear up-shift of the critical temperature gradient which is larger than the linear stability threshold of the ITG modes (that is, so-called Dimits shift) [14]. The self-generated zonal flow in the plasma turbulence is now recognized as a key constituent of a "drift-wave – zonal-flow system". Existence of ion-scale zonal flows has been revealed by a direct measurement of spatial structures of electrostatic potential fluctuations in laboratory experiments [15].

Zonal flows are nonlinearly generated through the Reynolds stress in the drift-wave turbulence. The detailed physical mechanisms of the zonal flow generation have discussed from the view point of the nonlinear parametric instabilities through coupling of zonal flows and coherent drift waves [16, 17], or the Kelvin-Helmholtz (K-H) instability of radially elongated drift-wave vortices [18, 19]. The zonal flow generation is, thus, regarded as a "secondary" instability by contrast with the primary drift-wave instability. For the saturation of the zonal-flow growth in drift-wave turbulence, several mechanisms have been discussed (reviewed in Ref. 20). Generalized K-H instability, which is regarded as a "tertiary" instability, is one of the candidates for a saturation mechanism of zonal flows in the ITG turbulence [18, 19]. Furthermore, the importance of parallel flows and viscosity in the zonal flow dynamics has also been pointed out [21, 22].

The electron temperature gradient (ETG) driven mode is the counterpart of the ITG mode, and the ETG turbulence is considered as a possible cause of the electron heat transport. However, the gyro-Bohm scaling for the ETG turbulence with $T_e = T_i$ predicts the smaller electron heat transport by a factor of $\sqrt{m_e/m_i}$ than the ion heat transport driven by the ITG turbulence, where T_s and m_s mean the temperature and the mass of ions (s = i) and electrons (s = e), respectively. Many experimental observations, nevertheless, commonly indicate the strong anomaly of the electron heat transport, which is of the same order as the ion one. Even when the ion heat transport is reduced by the internal transport barrier [23, 24], the anomalous electron heat

transport is still observed. From the view point of theoretical model, the linear ETG modes with an adiabatic ion response are isomorphic to the linear ITG modes with an adiabatic electron response. However, the nonlinear evolution of the ETG instability is crucially different from that of the ITG one, because the intensity of nonlinearly generated zonal flows in the ETG turbulence is much lower than that in the ITG turbulence. In the ITG turbulence, since the electron gyroradius is negligibly smaller than the radial wavelengths of the zonal-flow potentials, the radial motion of the electrons can not shield the zonal-flow potentials which are constant on a flux surface. Thus, the ITG-driven zonal flows with high amplitude can develop. On the other hand, in the ETG turbulence, the radial motion of ions resulted from the large gyroradius shields the zonal-flow potentials. The different radial motion of the background species (electrons for the ITG case, or ions for the ETG case) is, thus, responsible for the different zonal-flow generations, and higher transport level in the gyro-Bohm unit is observed in the ETG turbulence [25]. Furthermore, the ETG turbulence involves various vortex structures, such as turbulent vortices, zonal flows, and radially elongated streamers, of which the appearance strongly depends on geometrical and plasma parameters [26]. Recently, a number of gyrokinetic simulations of the toroidal ETG turbulence have been performed and benchmarked with various simulation codes [25–31]. Especially, the nonlinear dynamics of streamers, which may lead to substantial enhancement of the heat transport in toroidal systems, has been actively pursued [25, 29]. Nevertheless, the saturation mechanism of the toroidal ETG instability under the strong magnetic shear and the estimation of resultant transport level are still open problems.

From the aspect of the turbulence-control with regulating the turbulent heat transport in the future fusion plasmas, it is worthwhile to understand fundamental physics behind the formation of vortex structures including zonal flows and their stability as well as the related transport properties. One of the objectives of this study is elucidating what kind of the vortex structures enhance or suppress the turbulent transport, and how the zonal flows play a role in the transport suppression in the ITG and ETG turbulence in the framework of gyrokinetic theory. We believe that detailed analyses of the vortex structures and the velocity-space structures of the distribution function are necessary for better understandings of the underlying turbulent transport processes in high temperature plasmas. To this end, vortex and zonal flow structures and velocity-space structures of the distribution function in the slab/toroidal ITG/ETG turbulence are extensively explored based on nonlinear gyrokinetic theory and the direct numerical simulations. The five-dimensional nonlinear gyrokinetic Vlasov simulations with high phase-space resolution enable us to examine in detail the gyrokinetic entropy balance relation and the associated entropy transfer processes which provide ones with deeper physical insight into the nonlinear interaction between drift-wave turbulence and zonal flows as well as the associated transport processes.

The outline of this dissertation is given as follows. First, gyrokinetic models and the entropy balance relation used in the present study are briefly described in Chap. 2. In Chap. 3, vortex structures in the slab ETG turbulence are investigated, including comparisons with those in the slab ITG case. Then, formation of the coherent vortex streets, which is closely associated with the transport reduction, in the slab ETG turbulence is discussed in detail. In Chap. 4, effects of parallel dynamics on the transition of vortex structures and zonal flows are intensively examined by the comprehensive parameter studies. Also, the physical mechanism of the secondary growth of zonal flows is discussed based on the modulational instability analysis with a truncated fluid model, where the parallel dynamics with acoustic modes is incorporated. In Chap. 5, the investigations of vortex structures and zonal flows are extended to toroidal ITG and ETG turbulence by means of five-dimensional nonlinear gyrokinetic simulations. Furthermore, the gyrokinetic entropy balance relations for zonal and non-zonal modes, and the nonlinear entropy transfer processes are carefully examined by means of the spectral analysis of the triad entropy transfer function, which is regarded as a kinetic extension of the zonal-flow energy production due to the hydrodynamic Reynolds stress. Finally, the results obtained in the present study are summarized in Chap. 6.

Bibliography for Chapter 1

[1] W. Horton, Rev. Mod. Phys. **71**, 735 (1999)

[2] D. H. E. Dubin, J. Krommes, C. Oberman, and W. W. Lee, Phys. Fluids **26**, 3524 (1983)

[3] T. M. Antonsen and B. Rane, Phys. Fluids **23**, 1205 (1980)

[4] H. Sugama, Phys. Plamsas **7**, 466 (2000)

[5] Z. Lin, T. S. Hahm, W. W. Lee, W. M. Tang, and R. B. White, Science **18**, 1835 (1998)

[6] X. Garbet, Y. Idomura, L. Villard, and T. -H. Watanabe, Nucl. Fusion **50**, 043002 (2010)

[7] T.-H. Watanabe, H. Sugama, and S. Ferrando-Margalet, Phys. Rev. Lett. **100**, 195002 (2008)

[8] T.-H. Watanabe and H. Sugama, Nucl. Fusion **46**, 24 (2006)

[9] R. E. Waltz and C. Holland, Phys. Plasmas **15**, 122503 (2008)

[10] Y. Idomura, S. Tokouda, N. Aiba, and H. Urano, Nucl. Fusion **49**, 65029 (2009)

[11] H. Sugama, T.-H. Watanabe, and W. Horton, Phys. plasmas **10**, 726 (2003)

[12] G. W. Hammett and F. W. Perkins, Phys. Rev. Lett. **64**, 3019 (1990)

[13] M. A. Beer, S. C. Cowley, and G. W. Hammett, Phys. plasmas **2**, 2687 (1995)

[14] A. M. Dimits, G. Bateman, M. A. Beer, B. I. Cohen, W. Dorland, G. W. Hammett, C. Kim, J. E. Kinsey, M. Kotschenreuther, A. H. Kritz, L. L. Lao, J. Mandrekas, W. M. Nevins, S. E. Parker, A. J. Redd, D. E. Shumaker, R. Sydora, and J. Weiland, Phys. Plasmas **7**, 969 (2000)

[15] A. Fujisawa, K. Itoh, H. Iguchi, K. Matsuoka, S. Okamura, A. Shimizu, T. Minami, Y. Yoshimura, K. Nagaoka, C. Takahashi, M. Kojima, H. Nakano, S. Oshima, S. Nishimura, M. Isobe, C. Suzuki, T. Akiyama, K. Ida, K. Toi, S. -I, Itoh, and P. H. Diamond, Phys. Rev. Lett. **93**, 165002 (2004)

[16] L. Chen, Z. Lin, and R. B. White, Phys. plasmas **7**, 3129 (2000)

[17] P. N. Guzdar, R. G. Kleva, and L. Chen, Phys. plasmas **8**, 459 (2001)

[18] E.-J. Kim and P. H. Diamond, Phys. plasmas **7**, 3551 (2000)

[19] B. N. Rogers, W. Dorland, and M. Kotschenreuther, Phys. Rev. Lett. **18**, 5336 (2000)

[20] P. H. Diamond and S. -I. Itoh, K. Itoh, and T. S. Hahm, Plasma. Phys. Control. Fusion **47**, R35 (2005)

[21] P. N. Guzdar, R. G. Kleva, A. Das, and P. K. Kaw, Phys. plasmas **8**, 3907 (2001)

[22] K. Hallatscheck, Phys. Rev. Lett. **93**, 065001 (2004)

[23] B. W. Stallard, C. M. Greenfield, G. M. Staebler, C. L. Rettig, M. S. Chu, M. E. Austin, D. R. Baker, L. R. Baylor, K. H. Burrell, J. C. DeBoo, J. S. deGrassie, E. J. Doyle, J. Lohr, G. R. McKee, R. L. Miller, W. A. Peebles, C. C. Petty, R. I. Pinsker, B. W. Rice, T. L. Rhodes, R. E. Waltz, L. Zeng, and The DIII-D Team, Phys. Plasmas. **6**, 1978 (1999)

[24] H. Shirai, M. Kikuchi, T. Takizuka, T. Fujita, Y. Koide, G. Rewoldt, D. Mikkelsen, R. Budny, W. M. Tang, Y. Kishimoto, Y. Kamada, T. Oikawa, O. Naito, T. Fukuda, N. Isei, Y. Kawano, M. Azumi, and JT-60 Team, Nucl. Fusion **39**, 1713 (1999)

[25] F. Jenko, W. Dorland, M. Kotschenreuther, and B. N. Rogers, Phys. Plasmas **7**, 1904 (2000)

[26] Y. Idomura, S. Tokuda, and Y. Kishimoto, Nucl. Fusion **45**, 1571 (2005)

[27] W. M. Nevins, J. Candy, S. Cowley, T. Dannert, A. Dimits, W. Dorland, C. Estrada-Mila, G. W. Hammett, F. Jenko, M. J. Pueschel, and D. E. Shumaker, Phys. Plasmas **13**, 122306 (2006)

[28] W. M. Nevins, S. E. Parker, Y. Chen, J. Candy, A. Dimits, W. Dorland, G. W. Hammett, and F. Jenko, Phys. Plasmas **14**, 084501 (2007)

[29] Z. Lin, I. Holod, L. Chen, P. H. Diamond, T. S. Hahm, and S. Ethier, Phys. Rev. Lett. **99**, 265003 (2007)

[30] J. Candy, R. E. Waltz, M. R. Fahey, and C. Holland, Plasma. Phys. Control. Fusion **49**, 1209 (2007)

[31] Y. Idomura, Phys. Plasmas **13**, 080701 (2006)

Chapter 2

Gyrokinetic description for plasma turbulence

2.1 Brief review of kinetic theory

Theoretical backgrounds for kinetic simulations of turbulent transport in high temperature magnetized plasmas are briefly presented in this section. The magnetized plasmas consist of the charged particles (ions and electrons) coupled with the electromagnetic fields so that the fundamental description of plasma dynamics is given by Newton-Maxwell or Klimontovich-Maxwell system [1] as follows,

$$\frac{D\mathcal{N}_s}{Dt} = \frac{\partial \mathcal{N}_s}{\partial t} + \{\mathcal{N}_s, \mathcal{H}_s\}_z = 0 \,, \tag{2.1}$$

$$\mathcal{H}_s(\boldsymbol{q}, \boldsymbol{p}, t) = \frac{1}{2m_s} \left| \boldsymbol{p} - \frac{e_s}{c} \boldsymbol{A}(\boldsymbol{q}, t) \right|^2 + e_s \phi(\boldsymbol{q}, t) \,, \tag{2.2}$$

and

$$\nabla \cdot \boldsymbol{E} = 4\pi \sum_s \rho_s^{(e)}(\boldsymbol{q}, t) \,, \tag{2.3}$$

$$\nabla \cdot \boldsymbol{B} = 0 \,, \tag{2.4}$$

$$\nabla \times \boldsymbol{B} = \frac{4\pi}{c} \sum_s \boldsymbol{j}_s(\boldsymbol{q}, t) + \frac{1}{c} \frac{\partial \boldsymbol{E}}{\partial t} \,, \tag{2.5}$$

$$\nabla \times \boldsymbol{E} = -\frac{1}{c} \frac{\partial \boldsymbol{B}}{\partial t} \,, \tag{2.6}$$

where $\mathcal{N}_s(\boldsymbol{q}, \boldsymbol{p}, t) \equiv \sum_i \delta[\boldsymbol{q} - \boldsymbol{q}_i(t)] \delta[\boldsymbol{p} - \boldsymbol{p}_i(t)]$ and $\mathcal{H}_s(\boldsymbol{q}, \boldsymbol{p}, t)$ denote the particle number density for the species "s" ($\delta[\cdot]$ is the Dirac delta-function) and the Hamiltonian of single particle motion in the six-dimensional phase-space represented by the canonical coordinates $\boldsymbol{q}$ and $\boldsymbol{p}$, respectively. (The particle mass, the electric charge, and the speed of lights are denoted by m_s, e_s, and c,

respectively.) The Poisson bracket in the canonical coordinates $z = (q, p)$ is represented by $\{F, G\}_z = (\partial F/\partial q) \cdot (\partial G/\partial p) - (\partial F/\partial p) \cdot (\partial G/\partial q)$. The electric and magnetic fields, which are, respectively, written as $E = -\nabla\phi - c^{-1}\partial A/\partial t$ and $B = \nabla \times A$ in terms of the electrostatic scalar potential $\phi(q, t)$ and the magnetic vector potential $A(q, t)$, are determined by the Maxwell equations (2.3) – (2.6), where the microscopic electric charge and current densities are given by

$$\rho_s^{(e)}(q, t) = e_s \int dp \mathcal{N}_s(q, p, t) \, , \tag{2.7}$$

$$j_s(q, t) = e_s \int dp \, v \mathcal{N}_s(q, p, t) \, , \tag{2.8}$$

respectively, where $v = [p - (e_s/c)A]/m_s$ is the particle-velocity vector.

Although the Newton-Maxwell or Klimontovich-Maxwell system provides ones with the rigorous description of the whole plasma behavior, it is unrealistic to trace all of $\sim 10^{20}$ particles in typical fusion plasmas, even with the most powerful computers in the present-day and the foreseeable future. Thus, a statistical approach is introduced to describe the plasma behavior by a particle distribution function, instead of solving all the particle motion for each species. Since, in high temperature plasmas with $\sim 10\text{keV}$, the kinetic energy of particles is much larger than the potential energy, the multiple particle correlations involving three particles or more are negligible, and two-particle correlation is reduced to the Coulomb collision operator $C_{ss'}(\mathcal{F}_s, \mathcal{F}_{s'})$ for an one-body distribution function $\mathcal{F}_s(q, p, t) \equiv \langle\!\langle \mathcal{N}_s(q, p, t) \rangle\!\rangle$, where $\langle\!\langle \cdots \rangle\!\rangle$ denotes an ensemble average. Consequently, the time evolution of $\mathcal{F}_s$ is described by the Boltzmann equation,

$$\frac{\partial \mathcal{F}_s}{\partial t} + \{\mathcal{F}_s, \mathcal{H}_s\}_z = \sum_{s'} C_{ss'}(\mathcal{F}_s, \mathcal{F}_{s'}) \equiv C_s(\mathcal{F}_s) \, . \tag{2.9}$$

In the collisionless limit, Eq. (2.9) is referred to as the Vlasov equation. The Landau expression is frequently used as the Coulomb collision operator for high temperature plasmas [2],

$$C_{ss'}(\mathcal{F}_s, \mathcal{F}_{s'}) = \frac{\gamma_{ss'}}{2} \frac{\partial}{\partial p} \cdot \int dp' \, U \cdot \left[\mathcal{F}_{s'}(p')\frac{\partial \mathcal{F}_s(p)}{\partial p} - \mathcal{F}_s(p)\frac{\partial \mathcal{F}_{s'}(p')}{\partial p'} \right] \, , \tag{2.10}$$

where $U \equiv |u|^{-3}(|u|^2 I - uu)$ with $u = v - v'$ and the unit tensor I, and $\gamma_{ss'} \equiv 4\pi e_s^2 e_{s'}^2 \ln \Lambda$ with the Coulomb logarithm $\ln \Lambda$.

The Vlasov-Maxwell (or Boltzmann-Maxwell) system is a reduced kinetic description in comparison to the Klimontovich-Maxwell system. However, it involves enormous ranges of spatio-temporal scales so that it is still difficult to carry out the numerical simulation of low-frequency phenomena such as drift-wave turbulence and MHD waves. Actually, the typical frequency of the drift-wave turbulence driven by micro-instabilities is much lower than the gyrofrequency so that it is useful for the direct numerical simulation of plasma turbulence if the

fast dependence on gyrophase is eliminated from the Vlasov equation. To this end, a gyrokinetic model has been developed [3–12] by eliminating high-frequency phenomena while keeping essential kinetic effects, i.e., the Landau damping, the finite gyroradius effect, the particle drifts, and the magnetic trapping.

The gyrokinetic model was first formulated by averaging the Vlasov equation over the gyrophase based on the recursive method for the study of the micro-instabilities, and its application to numerical simulations started in the early 1980s [3–6]. The modern gyrokinetic theory [7–12] has been developed based on the Hamiltonian or Lagrangian formalism with the Lie-transform method [13, 14]. The basis of the modern formulation widely used at present was constructed by the careful modeling of the guiding-center dynamics [15–18]. Indeed, the modern gyrokinetic theory consists of the guiding-center transform [15–17] and the gyrocenter transform [7, 9, 18]. The modern gyrokinetic theory provides ones with a rigorous treatment of collisionless turbulent dynamics while keeping important principles such as the symmetry and conservation properties, which are essential to describe underlying physics and are useful for nonlinear simulations. The nonlinear gyrokinetic simulation is now considered to be an powerful tool for the study of the turbulent transport driven by the micro-instabilities.

2.2 Gyrokinetic model

In this section, the gyrokinetic model is briefly presented. One can find easily the detailed review including the derivations in the papers listed in the bibliography.

The drift-wave turbulence observed experimentally in core plasmas is considered to obey the gyrokinetic orderings in ϵ_{g},

$$\frac{\omega}{\Omega_{\mathrm{s}}} \sim \frac{e_{\mathrm{s}}\delta\phi}{T_{\mathrm{s}}} \sim \frac{\delta B}{B_0} \sim \frac{k_{\parallel}}{k_{\perp}} \sim \frac{\rho_{\mathrm{ts}}}{L} \sim O(\epsilon_{\mathrm{g}}) \,, \tag{2.11}$$

where ω is a characteristic frequency of the turbulence, $\Omega_{\mathrm{s}} = e_{\mathrm{s}}B_0/m_{\mathrm{s}}c$ denotes the gyrofrequency evaluated with the representative strength of the equilibrium magnetic field $B_0 = |\boldsymbol{B}_0| = |\nabla \times \boldsymbol{A}_0|$, $e_{\mathrm{s}}\delta\phi/T_{\mathrm{s}}$ and δB are the potential fluctuation normalized by the equilibrium temperature T_{s} and the magnetic field perturbation, respectively. The parallel and perpendicular components of the wavenumber vector $\boldsymbol{k}$ to the unit vector of the equilibrium magnetic field $\boldsymbol{b} = \boldsymbol{B}_0/B_0$ are denoted by $k_{\parallel}$ and $k_{\perp}$, respectively. The ratio of thermal gyroradius to the equilibrium gradient scale-length is represented by ρ_{ts}/L, where $\rho_{\mathrm{ts}} = v_{\mathrm{ts}}/\Omega_{\mathrm{s}}$ with the thermal velocity v_{ts}. It should be noted that the drift-wave turbulence in the strongly magnetized plasmas considered here is inherently anisotropic, that is, the wavelength of fluctuations on the plane perpendicular to the magnetic field line is comparable to the thermal gyroradius, i.e., $k_{\perp}\rho_{\mathrm{ts}} \sim O(1)$, while the fluctuations are

elongated along the magnetic field lines, i.e., $k_\parallel L \sim O(1)$. For a fusion plasma with finite but small β (typically $\beta \sim 1\%$), the perturbed field is given as $\delta \boldsymbol{B} = \nabla \times \delta A_\parallel \boldsymbol{b}$, and the parallel component of $\delta \boldsymbol{B}$ is often neglected compared with B_0, where $\beta = (n_0 T_{\rm i} + n_0 T_{\rm e})/(B_0^2/8\pi)$ is the ratio of the plasma kinetic pressure to the magnetic pressure (the equilibrium density is denoted by n_0).

For the purpose of gyrokinetic simulations, it is convenient to transform the canonical variables $(\boldsymbol{q}, \boldsymbol{p})$ into the non-canonical guiding-center variables $\boldsymbol{Z} = (\boldsymbol{X}, U, \mu, \xi)$, where $\boldsymbol{X} = \boldsymbol{q} - \boldsymbol{\rho}_s$ is a guiding-center position, $\boldsymbol{\rho}_s = \boldsymbol{b} \times \boldsymbol{v}/\Omega_s$ is the gyroradius vector, $U = v_\parallel + (e_s/m_s c)\delta A_\parallel$ is a generalized parallel velocity, $\mu = m_s v_\perp^2/2B_0$ is the magnetic moment, $\xi = \tan^{-1}(\boldsymbol{v} \cdot \boldsymbol{e_1}/\boldsymbol{v} \cdot \boldsymbol{e_2})$ is the gyrophase angle, and $\boldsymbol{e}_1$ and $\boldsymbol{e}_2$ are orthogonal unit vectors defined as $\boldsymbol{e}_1 \times \boldsymbol{e}_2 = \boldsymbol{b}$. The preliminary non-canonical guiding-center transform for Hamiltonian shown in Eq. (2.2) leads to the following perturbed Hamiltonian,

$$
\begin{aligned}
\mathcal{H}_{\rm s} &= \frac{1}{2}m_{\rm s}\left|U - \frac{e_{\rm s}}{m_{\rm s}c}\delta A_\parallel\right|^2 + \mu B_0 + e_{\rm s}\phi \\
&= \frac{1}{2}m_{\rm s}U^2 + \mu B_0 + e_{\rm s}\Psi + O(\epsilon_{\rm g}^2),
\end{aligned}
\tag{2.12}
$$

where $\Psi(\boldsymbol{X}, U, \xi, t) = \phi - U\delta A_\parallel/c$ is the generalized potential fluctuation. Note that the magnetic moment μ in the guiding-center coordinates is not exact, but approximate adiabatic invariant because of the existence of the microscopic electromagnetic fluctuations in plasma turbulence so that μ is no longer conserved. By applying Lie-transform technique, the guiding-center coordinates $\boldsymbol{Z}$ are transformed to new coordinates $\bar{\boldsymbol{Z}} = T_{\rm G}\boldsymbol{Z} = (\bar{\boldsymbol{X}}, \bar{U}, \bar{\mu}, \bar{\xi})$ such that the new magnetic moment $\bar{\mu}$ becomes an exact invariant even in the presence of the low-frequency perturbations and the conjugate angle-variable $\bar{\xi}$ is regarded as an ignorable coordinate. The coordinates $\bar{\boldsymbol{Z}}$ and the map $T_{\rm G}$ are referred to as "gyrocenter coordinates" and as "gyrocenter transform", respectively. The gyrocenter transform is a near-identity transform, i.e., $T_{\rm G} = {\rm id}_{\boldsymbol{Z}} + O(\epsilon_{\rm g})$. It should be noted here that one can choose the gyrocenter transform to be canonical one, by the use of the generalized parallel velocity $U = v_\parallel + (e_{\rm s}/m_{\rm s}c)\delta A_\parallel$ as a guiding-center variable, rather than $U = v_\parallel$. Hence, the specific expression of the gyrocenter transform is given as

$$
\bar{\boldsymbol{Z}} = T_{\rm G}\boldsymbol{Z} = \boldsymbol{Z} + \{\tilde{S}, \boldsymbol{Z}\}_{\bar{\boldsymbol{Z}}} + O(\epsilon_{\rm g}^2),
\tag{2.13}
$$

where $\{F, G\}_{\bar{\boldsymbol{Z}}}$ is the Poisson bracket in the gyrocenter coordinates (Note that the form of the Poisson bracket is unchanged from that in the guiding-center coordinates because $T_{\rm G}$ is a canonical transform),

$$
\{F, G\}_{\bar{\boldsymbol{Z}}} \equiv \frac{\Omega_{\rm s}}{B_0}\left(\frac{\partial F}{\partial \xi}\frac{\partial G}{\partial \mu} - \frac{\partial F}{\partial \mu}\frac{\partial G}{\partial \xi}\right) - \frac{\boldsymbol{B}^*}{m_{\rm s}B_\parallel^*} \cdot \left(\frac{\partial F}{\partial U}\nabla G - \frac{\partial G}{\partial U}\nabla F\right) - \frac{c}{e_{\rm s}B_\parallel^*}\boldsymbol{b} \cdot \nabla F \times \nabla G.
\tag{2.14}
$$

Here, $B^*_\parallel = \boldsymbol{b} \cdot \boldsymbol{B}^*$ is a parallel component of $\boldsymbol{B}^* \equiv \boldsymbol{B}_0 + (B_0 \bar{U} / \Omega_s) \nabla \times \boldsymbol{b}$. The generating function $\tilde{S}$ is solved as

$$\tilde{S}(\boldsymbol{Z}, t) = \frac{e_s}{\Omega_s} \int^\xi d\xi' \left[\Psi - \langle \Psi \rangle_g \right] , \tag{2.15}$$

where $\langle F \rangle_g \equiv \oint d\xi F / 2\pi$ represents the gyrophase-average. This gyrocenter transform is formulated based on the canonical Lie-transform so that the phase-space volume is conserved up to arbitrary order in ϵ_g. After the transform, ξ-dependent perturbations are absorbed in the generating function $\tilde{S}$, and hence, the Hamiltonian represented by the gyrocenter coordinates, which is independent of $\bar{\xi}$, is given as

$$\mathcal{H}_s = \frac{1}{2} m_s \bar{U}^2 + \bar{\mu} B_0 + e_s \langle \Psi \rangle_g . \tag{2.16}$$

Several different choices of independent variables, especially in the electromagnetic case, are possible, and we have chosen here to use the generalized parallel velocity, which is transformed as $\bar{U} = U + \{\tilde{S}, U\} + O(\epsilon_g^2)$ [10]. In this choice, functional forms of the Poisson bracket in Eq. (2.14) become the same as those in the electrostatic limit, and one easily finds that the electromagnetic gyrocenter transform is replaced by the electrostatic one.

By using the gyrocenter variables, a gyrocenter distribution function is defined by $\mathcal{F}_s^{(g)}(\bar{\boldsymbol{Z}}, t) = \mathcal{F}_s(\boldsymbol{q}, \boldsymbol{p}, t)$, where the Jacobian is given by $\mathcal{D}(\bar{\boldsymbol{Z}}) = m_s^2 B^*_\parallel(\bar{\boldsymbol{Z}})$. The gyrokinetic equation which describes time evolution of the gyrocenter distribution function $\mathcal{F}_s^{(g)} = \mathcal{F}_s^{(g)}(\bar{X}, \bar{U}, \bar{\mu}, \bar{\xi}, t)$ is, then, written as

$$\frac{\partial \mathcal{F}_s^{(g)}}{\partial t} + \left\{ \mathcal{F}_s^{(g)}, \mathcal{H}_s \right\}_{\bar{Z}} = \frac{\partial \mathcal{F}_s^{(g)}}{\partial t} + \left\{ \bar{\boldsymbol{Z}}, \mathcal{H}_s \right\}_{\bar{Z}} \cdot \frac{\partial \mathcal{F}_s^{(g)}}{\partial \bar{\boldsymbol{Z}}}$$
$$= \left(\frac{\partial}{\partial t} + \frac{d\bar{X}}{dt} \cdot \frac{\partial}{\partial \bar{X}} + \frac{d\bar{U}}{dt} \cdot \frac{\partial}{\partial \bar{U}} + \frac{d\bar{\mu}}{dt} \cdot \frac{\partial}{\partial \bar{\mu}} + \frac{d\bar{\xi}}{dt} \cdot \frac{\partial}{\partial \bar{\xi}} \right) \mathcal{F}_s^{(g)} = 0, \tag{2.17}$$

where the expressions of gyrocenter equations of motion are obtained by means of the Hamiltonian [Eq. (2.16)] and the Poisson bracket [Eq. (2.14)] in the gyrocenter coordinates,

$$\frac{d\bar{X}}{dt} = \bar{U} \boldsymbol{b} - \frac{e_s}{m_s c} \langle \delta A_\parallel \rangle_g \frac{\boldsymbol{B}^*}{B^*_\parallel} + \frac{c}{e_s B^*_\parallel} \boldsymbol{b} \times \left(e_s \nabla \langle \Psi \rangle_g + m_s \bar{U}^2 \boldsymbol{b} \cdot \nabla \boldsymbol{b} + \bar{\mu} \nabla B_0 \right) , \tag{2.18}$$

$$\frac{d\bar{U}}{dt} = -\frac{\boldsymbol{B}^*}{m_s B^*_\parallel} \cdot \left(e_s \nabla \langle \Psi \rangle_g + \bar{\mu} \nabla B_0 \right) , \tag{2.19}$$

$$\frac{d\bar{\mu}}{dt} = 0 , \tag{2.20}$$

$$\frac{d\bar{\xi}}{dt} = \Omega_s + \frac{e_s^2}{m_s c} \frac{\partial \langle \Psi \rangle_g}{\partial \bar{\mu}} . \tag{2.21}$$

As seen from Eqs. (2.18) – (2.21), the gyrocenter equations of motion are independent of the gyrophase $\bar{\xi}$, and the magnetic moment $\bar{\mu}$ is exactly conserved. Hence, the $\bar{\xi}$-dependence no

longer appears in the gyrocenter distribution function $\mathcal{F}_s^{(g)} = \mathcal{F}_s^{(g)}(\bar{X}, \bar{U}, \bar{\mu}, t)$ at any time t if it is initially independent of $\bar{\xi}$, i.e., $\partial \mathcal{F}_s^{(g)}/\partial \bar{\xi}|_{t=0}$. As a result, the gyrokinetic equation for $\mathcal{F}_s^{(g)}$ in the five-dimensional phase-space is rearranged as

$$\left(\frac{\partial}{\partial t} + \frac{d\bar{X}}{dt} \cdot \frac{\partial}{\partial \bar{X}} + \frac{d\bar{U}}{dt} \cdot \frac{\partial}{\partial \bar{U}} \right) \mathcal{F}_s^{(g)}(\bar{X}, \bar{U}, \bar{\mu}, t) = 0 \ . \tag{2.22}$$

Since the gyrokinetic equation (2.22) is regarded as the Liouville equation in the five-dimensional phase-space, $\mathcal{F}_s^{(g)}$ is conserved along the characteristics. Also, another important property is the conservation of the phase-space volume,

$$\frac{\partial}{\partial \bar{Z}} \cdot \left(\mathcal{D} \frac{d\bar{Z}}{dt} \right) = \frac{\partial}{\partial \bar{X}} \cdot \left(\mathcal{D} \frac{d\bar{X}}{dt} \right) + \frac{\partial}{\partial \bar{U}} \left(\mathcal{D} \frac{d\bar{U}}{dt} \right) = 0 \ . \tag{2.23}$$

From this property, the gyrokinetic equation (2.22) is written also in a conservative form,

$$\frac{\partial}{\partial t} \mathcal{D} \mathcal{F}_s^{(g)} + \frac{\partial}{\partial \bar{X}} \cdot \left(\mathcal{D} \mathcal{F}_s^{(g)} \frac{d\bar{X}}{dt} \right) + \frac{\partial}{\partial \bar{U}} \left(\mathcal{D} \mathcal{F}_s^{(g)} \frac{d\bar{U}}{dt} \right) = 0 \ . \tag{2.24}$$

Since the collisional dissipation violates the Hamiltonian structure of the problem, we can not construct the Lagrangian-Hamiltonian formalisms including collisions. Thus, after applying the guiding-center transform to the collision operator, the gyrophase independent form is obtained by using a gyrophase-averaging procedures [19, 20],

$$C_s^{(g)}(\mathcal{F}_s^{(g)}) \equiv \sum_{\boldsymbol{k}_\perp} e^{i\boldsymbol{k}_\perp \cdot \bar{X}} \left\langle e^{i\boldsymbol{k}_\perp \cdot \rho_s} C_s \left(e^{-i\boldsymbol{k}_\perp \cdot \rho_s} \mathcal{F}_{s\boldsymbol{k}_\perp}^{(g)} \right) \right\rangle_g \ , \tag{2.25}$$

where the Fourier representation is used. Also, the contribution from the polarization term [the second term in the right hand side of Eq. (2.26) shown below] is neglected here.

Finally, the equation system is closed by the Poisson-Ampère equations. The pull-back transform from $\mathcal{F}_s^{(g)}$ to $\mathcal{F}_s$ is given as

$$\mathcal{F}_s = \mathcal{F}_s^{(g)} + \left\{ \tilde{S}, \mathcal{F}_s^{(g)} \right\} + O(\epsilon_g^2) = \mathcal{F}_s^{(g)} + \left\{ \tilde{S}, F_{Ms} \right\} + O(\epsilon_g^2) \ , \tag{2.26}$$

where F_{Ms} is a local Maxwellian distribution, and the second relation is obtained because $\delta f_s^{(g)} \equiv \mathcal{F}_s^{(g)} - F_{Ms}$ is small compared with F_{Ms}, i.e., $\delta f_s^{(g)}/F_{Ms} \sim O(\epsilon_g)$. The electric charge density $\rho_s^{(e)}$

and the parallel current density $j_{s\parallel}$ are, respectively, calculated as

$$
\begin{aligned}
\rho_s^{(e)} &= e_s \int \mathcal{D}d\mathbf{Z}\, \delta\left[(\mathbf{X}+\boldsymbol{\rho}_s) - \mathbf{q}\right] \mathcal{F}_s(\mathbf{Z}) \\
&= e_s \int \mathcal{D}d\mathbf{Z}\, \delta\left[(\mathbf{X}+\boldsymbol{\rho}_s) - \mathbf{q}\right]\left(\mathcal{F}_s^{(g)}(\mathbf{Z}) + \frac{\Omega_s}{B_0}\frac{\partial \tilde{S}}{\partial \xi}\frac{\partial F_{Ms}}{\partial \mu}\right) \\
&= e_s \int \mathcal{D}d\mathbf{Z}\, \delta\left[(\mathbf{X}+\boldsymbol{\rho}_s) - \mathbf{q}\right]\mathcal{F}_s^{(g)}(\mathbf{Z}) - \frac{e_s}{T_s}\left(\phi(\mathbf{q},t) - \langle\phi(\mathbf{X}+\boldsymbol{\rho}_s)\rangle_g\,|_{X=q-\rho_s}\right), \quad (2.27) \\
j_{s\parallel} &= e_s \int \mathcal{D}d\mathbf{Z}\, \delta\left[(\mathbf{X}+\boldsymbol{\rho}_s) - \mathbf{q}\right] v_\parallel \mathcal{F}_s(\mathbf{Z}) \\
&= e_s \int \mathcal{D}d\mathbf{Z}\, \delta\left[(\mathbf{X}+\boldsymbol{\rho}_s) - \mathbf{q}\right]\left(U\mathcal{F}_s^{(g)}(\mathbf{Z}) - \frac{e_s}{m_s c}\delta A_\parallel F_{Ms} + U\frac{\Omega_s}{B_0}\frac{\partial \tilde{S}}{\partial \xi}\frac{\partial F_{Ms}}{\partial \mu}\right) \\
&= e_s \int \mathcal{D}d\mathbf{Z}\, \delta\left[(\mathbf{X}+\boldsymbol{\rho}_s) - \mathbf{q}\right] U\mathcal{F}_s^{(g)}(\mathbf{Z}) - \frac{e_s n_0}{m_s c}\langle\delta A_\parallel(\mathbf{X}+\boldsymbol{\rho}_s)\rangle_g\,|_{X=q-\rho_s}. \quad (2.28)
\end{aligned}
$$

Here, the second term in the right hand side of Eq. (2.27) shows the polarization density due to the finite gyroradius effect. In Eq. (2.28), a part of the magnetization current (the third term in the second equation) is cancelled with the second term in the second equation, which appears due to the use of the generalized parallel velocity U. By using the above equations, the Maxwell equations yield the gyrokinetic Poisson-Ampère equations as follows,

$$
\begin{aligned}
-\nabla^2\phi &= \sum_s 4\pi e_s \int \mathcal{D}d\mathbf{Z}\, \delta\left[(\mathbf{X}+\boldsymbol{\rho}_s) - \mathbf{q}\right] \mathcal{F}_s^{(g)} \\
&\quad - \sum_s \frac{1}{\lambda_{Ds}^2}\left(\phi(\mathbf{q},t) - \langle\phi(\mathbf{X}+\boldsymbol{\rho}_s)\rangle_g\,|_{X=q-\rho_s}\right), \quad (2.29) \\
-\nabla_\perp^2 \delta A_\parallel &= \sum_s \frac{4\pi e_s}{c} \int \mathcal{D}d\mathbf{Z}\, \delta\left[(\mathbf{X}+\boldsymbol{\rho}_s) - \mathbf{q}\right] U\mathcal{F}_s^{(g)} \\
&\quad - \sum_s \frac{\omega_{ps}^2}{c^2}\langle\delta A_\parallel(\mathbf{X}+\boldsymbol{\rho}_s)\rangle_g\,|_{X=q-\rho_s}, \quad (2.30)
\end{aligned}
$$

where λ_{Ds} is the Debye-length, and ω_{ps} is the plasma oscillation frequency. The displacement current in Eq. (2.5) is neglected for low-frequency phenomena considered here. In deriving Eqs. (2.29) and (2.30), the nonlinear polarization and magnetization effects, which are higher order in ϵ_g, and other higher order terms are neglected. The gyrokinetic Vlasov-Maxwell system, Eqs. (2.22), (2.29) and (2.30), is a standard kinetic model to describe the drift-wave turbulence in the core region of low-β plasmas.

Another important approach in modelling an open plasma system is to introduce a multi-scale expansion with respect to a smallness parameter ϵ_g. In this approach, we consider a quasi-steady

plasma in a source free region, and separate the Hamiltonian into the static and perturbed parts,

$$\mathcal{H}_{s} = \mathcal{H}_{0s} + \delta\mathcal{H}_{s} , \tag{2.31}$$

$$\mathcal{H}_{0s} = m_{s}\bar{U}^2 + \bar{\mu}B_0 , \tag{2.32}$$

$$\delta\mathcal{H}_{s} = e_{s}\langle\delta\Psi\rangle_{g} , \tag{2.33}$$

where $\delta\Psi \equiv \Psi - \Psi_0$ denotes the perturbed part of the generalized potential, and the unperturbed part $\Psi_0 = \phi_0$ is not considered here. The gyrocenter distribution function $\mathcal{F}_{s}^{(g)}$ is also divided into the equilibrium part, which is assumed here to be the Maxwellian, and the perturbed part, i.e., $\mathcal{F}_{s}^{(g)} = F_{Ms} + \delta f_{s}^{(g)}$. By substituting the above relations into the gyrokinetic equation, one obtains

$$\frac{\partial\delta f_{s}^{(g)}}{\partial t} + \left\{\delta f_{s}^{(g)}, \mathcal{H}_{0s}\right\} + \{F_{Ms}, \delta\mathcal{H}_{s}\} + \left\{\delta f_{s}^{(g)}, \delta\mathcal{H}_{s}\right\} = C_{s}^{(g)}(\delta f_{s}^{(g)}) , \tag{2.34}$$

where the nonlinearity resulting from $\boldsymbol{E}\times\boldsymbol{B}$ convection appears in the fourth term in the left hand side of the above equation.

The nonlinear gyrokinetic simulations of the ITG and ETG turbulence presented here are based on Eqs. (2.34) and (2.29), where the electrostatic limit ($\delta A_{\parallel} \to 0$) is considered. Here, the perturbed part of the gyrocenter distribution function is written as $\delta f_{s}^{(g)}(X, U = v_{\parallel}, \mu, t) = \sum_{\boldsymbol{k}_\perp} \delta f_{s\boldsymbol{k}_\perp}^{(g)}(X, v_{\parallel}, \mu, t) \exp[i\mathcal{S}_{\boldsymbol{k}_\perp}(X)]$ in terms of the eikonal representation [2,21], where the overline for the gyrocenter variables is omitted, and the perpendicular wavenumber vector is defined by $\boldsymbol{k}_\perp \equiv \nabla\mathcal{S}_{\boldsymbol{k}_\perp}$. Then, the electrostatic gyrokinetic equation for perturbed distribution function $\delta f_{s\boldsymbol{k}_\perp}^{(g)}$ written in the $\boldsymbol{k}_\perp$-space is given by

$$\left[\frac{\partial}{\partial t} + v_{\parallel}\boldsymbol{b}\cdot\nabla + i\omega_{Ds} - \frac{\mu}{m_{s}}\boldsymbol{b}\cdot\nabla B\frac{\partial}{\partial v_{\parallel}}\right]\delta f_{s\boldsymbol{k}_\perp}^{(g)} - \frac{c}{B}\sum_{\Delta}\boldsymbol{b}\cdot(\boldsymbol{k}_\perp' \times \boldsymbol{k}_\perp'')\,\delta\psi_{\boldsymbol{k}_\perp'}\delta f_{s\boldsymbol{k}_\perp''}^{(g)}$$
$$= F_{Ms}(i\omega_{*Ts} - i\omega_{Ds} - v_{\parallel}\boldsymbol{b}\cdot\nabla)\frac{e_{s}\delta\psi_{\boldsymbol{k}_\perp}}{T_{s}} - C_{s}^{(g)}\left[\delta f_{s\boldsymbol{k}_\perp}^{(g)}\right] , \quad (2.35)$$

where $\omega_{Ds} \equiv (c/e_{s}B)\boldsymbol{k}_\perp\cdot\boldsymbol{b} \times (\mu\nabla B + m_{s}v_{\parallel}^2\boldsymbol{b}\cdot\nabla\boldsymbol{b})$ and $\omega_{*Ts} \equiv (cT_{s}/e_{s}B)\{1 + \eta_{s}[((m_{s}v_{\parallel}^2 + 2\mu B)/2T_{s}) - (3/2)]\}\boldsymbol{k}_\perp\cdot\boldsymbol{b}\times\nabla\ln n_{s}$ with $\eta_{s} = |\nabla\ln T_{s}|/|\nabla\ln n_{s}| = L_{n_{s}}/L_{T_{s}}$. Here, $\delta\psi_{\boldsymbol{k}_\perp}$ are the electrostatic potential fluctuation averaged over the gyrophase. The symbol $\sum_{\Delta}$ appearing in the nonlinear term of Eq. (2.1) stands for the summation over Fourier modes which satisfy the triad-interaction condition, i.e., $\boldsymbol{k}_\perp = \boldsymbol{k}_\perp' + \boldsymbol{k}_\perp''$. The gyrocenter position X, the parallel velocity $U = v_{\parallel}$ and the magnetic moment μ are used as the five-dimensional phase-space coordinates, where μ is defined by $\mu \equiv m_{s}v_{\perp}^2/2B$ with the perpendicular velocity $v_{\perp}$. The equilibrium part of the distribution function is given by the local Maxwellian distribution, i.e., $F_{Ms} = n_{s}(m_{s}/2\pi T_{s})^{3/2} \exp[-(m_{s}v_{\parallel}^2 + 2\mu B)/2T_{s}]$.

The potential fluctuation evaluated at the particle position, $\delta\phi_{\boldsymbol{k}_\perp}$, is related to the gyrophase-averaged one, i.e., $\delta\psi_{\boldsymbol{k}_\perp} = J_{0s}\delta\phi_{\boldsymbol{k}_\perp}$, and is determined by the Poisson equation written in the

wavenumber space as follows,

$$k_\perp^2 \lambda_{\mathrm{De}}^2 n_0 \frac{e\delta\phi_{k_\perp}}{T_\mathrm{e}} = \left[\int d\boldsymbol{v} J_{0\mathrm{i}} \delta f_{\mathrm{i}k_\perp}^{(\mathrm{g})} - n_0 \frac{e\delta\phi_{k_\perp}}{T_\mathrm{i}} (1 - \Gamma_{0\mathrm{i}})\right]$$
$$- \left[\int d\boldsymbol{v} J_{0\mathrm{e}} \delta f_{\mathrm{e}k_\perp}^{(\mathrm{g})} + n_0 \frac{e\delta\phi_{k_\perp}}{T_\mathrm{e}} (1 - \Gamma_{0\mathrm{e}})\right], \tag{2.36}$$

where $|e_\mathrm{i}| = |e_\mathrm{e}| = e$ and $n_\mathrm{i} = n_\mathrm{e} = n_0$ are assumed. The electron Debye-length is denoted by $\lambda_{\mathrm{De}} \equiv (T_\mathrm{e}/4\pi n_0 e^2)^{1/2}$. The first and the second groups of terms on the right hand side of Eq. (2.36) indicate the ion- and the electron-particle-density fluctuations represented with the gyrocenter distribution function and the electrostatic potential, respectively. The factors $J_{0\mathrm{s}}$ and $\Gamma_{0\mathrm{s}}$ are defined by $J_{0\mathrm{s}} \equiv J_0(k_\perp v_\perp/\Omega_\mathrm{s})$ and $\Gamma_{0\mathrm{s}} \equiv I_0(b)\exp(-b)$ with the zeroth-order Bessel and modified-Bessel functions, respectively, where $b \equiv k_\perp^2 v_{\mathrm{ts}}^2/\Omega_\mathrm{s}^2$. In the turbulence simulations, the closed set of equations (2.35) and (2.36) is solved numerically by means of the Fourier spectral method and the finite difference method.

2.3 Entropy balance relation

Since the dynamics of turbulent vortices in high temperature collisionless (or weakly collisional) magnetized plasmas involves a lot of kinetic processes such as the Landau damping, the finite gyroradius effect, the particle drift, the magnetic trapping, the kinetic approach is essential for understanding physical mechanisms of turbulent transport. It also should be emphasized that the kinetic turbulent transport processes is discussed more appropriately by the entropy balance relation [19, 22–24] given below, which describes the relation between the microscopic fluctuations of the distribution function and the turbulent heat flux, rather than the energy balance relation.

From the closed set of equations (2.35) and (2.36) described in Sec. 2.2, one can derive a balance equation with respect to the entropy variable $\delta S_\mathrm{s} \equiv S_{\mathrm{Ms}} - \langle\!\langle S_{\mathrm{ms}} \rangle\!\rangle$ defined as a functional of the perturbed gyrocenter distribution function $\delta f_\mathrm{s}^{(\mathrm{g})}$, where $\langle\!\langle \cdots \rangle\!\rangle$ means the ensemble average, where the macroscopic and the microscopic entropy per unit volume are defined by $S_{\mathrm{Ms}} \equiv -\int d\boldsymbol{v}\, F_{\mathrm{Ms}} \ln F_{\mathrm{Ms}}$ and $S_{\mathrm{ms}} \equiv -\int d\boldsymbol{v}\, \mathcal{F}_\mathrm{s}^{(\mathrm{g})} \ln \mathcal{F}_\mathrm{s}^{(\mathrm{g})}$, respectively. Then, one finds

$$\delta S_\mathrm{s} = S_{\mathrm{Ms}} - \langle\!\langle S_{\mathrm{ms}} \rangle\!\rangle \simeq \int d\boldsymbol{v} \left\langle\!\!\left\langle \frac{\delta f_\mathrm{s}^{(\mathrm{g})2}}{2F_{\mathrm{Ms}}} \right\rangle\!\!\right\rangle = \sum_{k_\perp} \int d\boldsymbol{v} \frac{\left|\delta f_{\mathrm{s}k_\perp}^{(\mathrm{g})}\right|^2}{2F_{\mathrm{Ms}}}, \tag{2.37}$$

which is correct to $O(\delta f_\mathrm{s}^{(\mathrm{g})2})$. Here, we assume the perpendicular components of turbulent fluctuations to be statistically homogeneous in space. Thus, the ensemble average is replaced by the spatial average in the last equality of Eq. (2.37). The velocity space integral and the field line

average of Eq. (2.35) multiplied by $\delta f_{sk_\perp}^{(g)*}/F_{Ms}$ lead to

$$\frac{\partial}{\partial t}(\delta S_{sk_\perp} + W_{sk_\perp}) = L_{T_s}^{-1}Q_{sk_\perp} + \mathcal{T}_{sk_\perp} + D_{sk_\perp} \,, \tag{2.38}$$

where

$$\delta S_{sk_\perp} \equiv \left\langle \int d\boldsymbol{v}\, \frac{|\delta f_{sk_\perp}^{(g)}|^2}{2F_{Ms}} \right\rangle \,, \tag{2.39}$$

$$L_{T_s}^{-1}Q_{sk_\perp} \equiv L_{T_s}^{-1}\mathrm{Re}\left\langle iv_{ts}\int d\boldsymbol{v}\, \delta f_{sk_\perp}^{(g)}\left(\frac{m_s v_\parallel^2 + 2\mu B}{2T_s}\right)k_y\rho_{ts}\frac{e\delta\psi_{k_\perp}^*}{T_s}\right\rangle \,, \tag{2.40}$$

$$D_{sk_\perp} \equiv \mathrm{Re}\left\langle \int d\boldsymbol{v}\, C_s\big[\delta f_{sk_\perp}^{(g)}\big]\frac{h_{sk_\perp}^*}{F_{Ms}}\right\rangle \,, \tag{2.41}$$

denote the entropy variable, the entropy production due to the conjugate pair of the turbulent heat flux and the temperature gradient (thermodynamic force), and the collisional dissipation, respectively. Note that, in the present study, the adiabatic response of background particles is assumed so that there is no particle flux. Also, $W_{sk_\perp}$ denotes the potential energy, where the specific form is given in Sec. 5.2 for the ITG and ETG turbulence with adiabatic background species. The non-adiabatic part of the perturbed gyrocenter distribution function, $h_{sk_\perp}$, is defined by

$$\delta f_{sk_\perp}^{(g)} = -\frac{e_s\delta\psi_{k_\perp}}{T_s}F_{Ms} + h_{sk_\perp} \,. \tag{2.42}$$

The second term in the right hand side of Eq. (2.38) represents the nonlinear transfer of the entropy variable. The definition of the entropy transfer function $\mathcal{T}_{sk_\perp}$ is given by

$$\mathcal{T}_{sk_\perp} = \sum_{\boldsymbol{p}_\perp}\sum_{\boldsymbol{q}_\perp}\delta_{\boldsymbol{k}_\perp+\boldsymbol{p}_\perp+\boldsymbol{q}_\perp,0}\,\mathcal{J}_s\big[\boldsymbol{k}_\perp|\boldsymbol{p}_\perp,\boldsymbol{q}_\perp\big] \,, \tag{2.43}$$

$$\mathcal{J}_s\big[\boldsymbol{k}_\perp|\boldsymbol{p}_\perp,\boldsymbol{q}_\perp\big] \equiv \left\langle \frac{c}{B}\boldsymbol{b}\cdot(\boldsymbol{p}_\perp\times\boldsymbol{q}_\perp)\int d\boldsymbol{v}\,\frac{1}{2F_{Ms}}\mathrm{Re}\left[\delta\psi_{\boldsymbol{p}_\perp}h_{s\boldsymbol{q}_\perp}h_{s\boldsymbol{k}_\perp} - \delta\psi_{\boldsymbol{q}_\perp}h_{s\boldsymbol{p}_\perp}h_{s\boldsymbol{k}_\perp}\right]\right\rangle \,, \quad (2.44)$$

where the notation with $\boldsymbol{k}_\perp'$ and $\boldsymbol{k}_\perp''$ shown in Eq. (2.35) is replaced here by $-\boldsymbol{p}_\perp$ and $-\boldsymbol{q}_\perp$, respectively, in order to represent symmetrically the triad-interaction condition for three wavenumber vectors, i.e., $\boldsymbol{k}_\perp + \boldsymbol{p}_\perp + \boldsymbol{q}_\perp = 0$. In Eq. (2.43), $\mathcal{J}_s[\boldsymbol{k}_\perp|\boldsymbol{p}_\perp,\boldsymbol{q}_\perp]$ is summed over $\boldsymbol{p}_\perp$ and $\boldsymbol{q}_\perp$. For convenience, we call the function $\mathcal{J}_s[\boldsymbol{k}_\perp|\boldsymbol{p}_\perp,\boldsymbol{q}_\perp]$ the "triad (entropy) transfer function", hereafter. It should be noted that the triad transfer function possesses the following symmetry properties,

$$\mathcal{J}_s\big[\boldsymbol{k}_\perp|\boldsymbol{p}_\perp,\boldsymbol{q}_\perp\big] = \mathcal{J}_s\big[\boldsymbol{k}_\perp|\boldsymbol{q}_\perp,\boldsymbol{p}_\perp\big] \,, \tag{2.45}$$

$$\mathcal{J}_s\big[\boldsymbol{k}_\perp|\boldsymbol{p}_\perp,\boldsymbol{q}_\perp\big] = \mathcal{J}_s\big[-\boldsymbol{k}_\perp|-\boldsymbol{p}_\perp,-\boldsymbol{q}_\perp\big] \,. \tag{2.46}$$

Furthermore, one obtains straightforwardly the "detailed balance relation" for the triad-interactions,

$$\mathcal{J}_s\big[\boldsymbol{k}_\perp|\boldsymbol{p}_\perp,\boldsymbol{q}_\perp\big] + \mathcal{J}_s\big[\boldsymbol{p}_\perp|\boldsymbol{q}_\perp,\boldsymbol{k}_\perp\big] + \mathcal{J}_s\big[\boldsymbol{q}_\perp|\boldsymbol{k}_\perp,\boldsymbol{p}_\perp\big] = 0 \,. \tag{2.47}$$

Positive values of the triad transfer function $\mathcal{J}_s[\boldsymbol{k}_\perp|\boldsymbol{p}_\perp, \boldsymbol{q}_\perp]$ mean that the entropy is transferred from two modes with $\boldsymbol{p}_\perp$ and $\boldsymbol{q}_\perp$ toward the mode with $\boldsymbol{k}_\perp(=-\boldsymbol{p}_\perp-\boldsymbol{q}_\perp)$ and that the possible combinations of the signs of $(\mathcal{J}_s[\boldsymbol{k}_\perp|\boldsymbol{p}_\perp, \boldsymbol{q}_\perp], \mathcal{J}_s[\boldsymbol{p}_\perp|\boldsymbol{q}_\perp, \boldsymbol{k}_\perp], \mathcal{J}_s[\boldsymbol{q}_\perp|\boldsymbol{k}_\perp, \boldsymbol{p}_\perp])$ satisfying the detailed balance relation should be $(+, -, -)$, $(+, +, -)$ and $(+, -, +)$. Negative values of $\mathcal{J}_s[\boldsymbol{k}_\perp|\boldsymbol{p}_\perp, \boldsymbol{q}_\perp]$ indicate the entropy transfer in the opposite direction, then $(-, +, +)$, $(-, -, +)$ and $(-, +, -)$ are the possible combinations of the triad transfer functions.

The explicit description of the entropy balance relation for the non-zonal ($k_y \neq 0$) and zonal ($k_y = 0$) modes is useful for the following discussions concerning the entropy transfer processes among zonal flows and turbulence. By taking the integration of Eq. (2.38) over the non-zonal and zonal modes, one obtains

$$\frac{d}{dt}\left(\delta S_s^{\text{(trb)}} + W_s^{\text{(trb)}}\right) = L_{T_s}^{-1}Q_s - \mathcal{T}_s^{\text{(zf)}} + D_s^{\text{(trb)}} , \tag{2.48}$$

$$\frac{d}{dt}\left(\delta S_s^{\text{(zf)}} + W_s^{\text{(zf)}}\right) = \mathcal{T}_s^{\text{(zf)}} + D_s^{\text{(zf)}} , \tag{2.49}$$

where the superscripts "(trb)" and "(zf)" represent the turbulence (or non-zonal) and zonal-flow components, respectively. The above entropy balance relations for non-zonal and zonal modes have been derived and discussed in detail by Sugama *et al* [19]. Note here that zonal flows never contribute to the radial heat flux $Q_{sk_\perp}$ as seen from Eq. (2.49). The entropy transfer function integrated over the zonal modes, $\mathcal{T}_s^{\text{(zf)}}$, represents the entropy transfer from turbulence to zonal flows so that the negative sign of $\mathcal{T}_s^{\text{(zf)}}$ appears in Eq. (2.48). As shown in Ref. 19, by using the simplest approximation for the non-adiabatic part of the ion gyrocenter distribution function, i.e., $h_{ik_\perp} \simeq n_0 F_{\text{Mi}}(1 + k_\perp^2\rho_{ti}^2/2)e\delta\phi_{k_\perp}/T_i$, the entropy transfer function $\mathcal{T}_i^{\text{(zf)}}$ is simplified to the energy production term, which is described by the product of the Reynolds stress due to the non-zonal turbulent flows and the zonal-flow shear. Thus, $\mathcal{T}_s^{\text{(zf)}}$ is regarded as an appropriate kinetic extension of the zonal-flow energy production due to the hydrodynamic Reynolds stress. As seen from Eq. (2.48), the turbulent heat flux $L_{T_s}^{-1}Q_s$ works as the entropy source so that the turbulence part of the entropy variable and the potential energy $(\delta S_s^{\text{(trb)}} + W_s^{\text{(trb)}})$ is generated. At the same time, the entropy variable is partly dissipated by collisions and is partly transferred to the zonal flow components via the transfer term $\mathcal{T}_s^{\text{(zf)}}$. When the turbulence reaches a statistically steady state, the balance relations of $\overline{\mathcal{T}}_s^{\text{(zf)}} = -\overline{D}_s^{\text{(zf)}} \geqslant 0$ and $L_{T_s}^{-1}\overline{Q}_s - \overline{\mathcal{T}}_s^{\text{(zf)}} = -\overline{D}_s^{\text{(trb)}}$ are realized separately, where the overline denotes the time-average in a saturated phase. The entropy balance relations of Eqs. (2.48) and (2.49) provide us with not only the physical insight into the entropy transfer processes among zonal flows and turbulence, but also a good measure for the accuracy of turbulence simulations.

Bibliography for Chapter 2

[1] D. R. Nicholson, "Introduction to plasma theory", John Wiley & Sons, Inc. Scientific, (1983)

[2] R. D. Hazeltine and J. D. Meiss, "Plasma confinement", Addison-Wesley Publishing Company, (1992)

[3] P. H. Rutherford and E. A. Frieman, Phys. Fluids **11**, 569 (1968)

[4] T. M. Antonsen and B. Lane, Phys. Fluids **23**, 1205 (1980)

[5] E. A. Frieman and L. Chen, Phys. Fluids **25**, 502 (1982)

[6] W. W. Lee, Phys. Fluid **26**, 556 (1983)

[7] D. H. E. Dubin, J. Krommes, C. Oberman, and W. W. Lee, Phys. Fluids **26**, 3524 (1983)

[8] R. G. Littlejohn, J. Plasma Phys. **29**, 111 (1983)

[9] A. J. Brizard, J. Plasma Phys. **41**, 541 (1989)

[10] H. Sugama, Phys. Plasmas **7**, 466 (2000)

[11] A. J. Brizard and T. S. Hahm, Rev. Mod. Phys. **79**, 421 (2007)

[12] J. A. Krommes, Phys. Scr. **T142**, 014035 (2010)

[13] J. R. Cary, Phys. Rep. **79**, 129 (1981)

[14] J. R. Cary and R. G. Littlejohn, Ann. Phys. **151**, 1 (1983)

[15] Robert G. Littlejohn, J. Math. Phys. **20**, 2445 (1979)

[16] Robert G. Littlejohn, Phys. Fluids **24**, 1730 (1981)

[17] Robert G. Littlejohn, J. Math. Phys. **23**, 742 (1982)

[18] T. S. Hahm, Phys. Plasmas **3**, 4658 (1996)

[19] H. Sugama, T.-H. Watanabe, and M. Nunami, Phys. Plasmas **16**, 112502 (2009)

[20] X. Xu and M. N. Rosenbluth, Phys. Fluids B **3**, 627 (1991)

[21] R. L. Dewer and A. H. Glasser, Phys. Fluids **26**, 3038 (1983)

[22] J. A. Krommes and G. Hu, Phys. Plasmas **1**, 3211 (1994)

[23] H. Sugama, M. Okamoto, W. Horton, and M. Wakatani, Phys. Plasmas **3**, 2379 (1996)

[24] T.-H. Watanabe and H. Sugama, Phys. plasmas **11**, 1476 (2004)

Chapter 3

Vortex structures and transport properties in slab ITG and ETG turbulence

3.1   Introduction

Turbulent transport driven by micro-instabilities such as ion temperature gradient (ITG) modes, electron temperature gradient (ETG) modes has been extensively investigated so far by means of numerical simulations based on gyrokinetic and gyrofluid models in order to elucidate physical mechanisms of anomalous heat transport in the core region of magnetically confined plasmas [1, 2]. One of the remarkable results obtained by the ITG turbulence simulations is spontaneous generation of zonal flows which regulate the turbulent transport [3].

Many experimental observations commonly indicate the strong anomaly of the electron heat transport, which could be of the same order as the ion one, even when the ion heat transport is reduced by the internal transport barrier [4, 5]. The ETG turbulence is considered as a possible cause of such electron hear transport. Although the linear ETG modes with an adiabatic ion response are isomorphic to the linear ITG modes with an adiabatic electron response, the nonlinear evolution of the ETG turbulence is quite different from that of the ITG one, because the intensity of nonlinearly generated zonal flows in the ETG turbulence is much lower than that in the ITG turbulence due to the different adiabatic response of the background species to the zonal-flow potential [6, 7]. Thus, ETG turbulence involves various vortex structures, e.g., turbulent vortices, zonal flows and radially elongated streamers, where the intensities depend on the magnetic shear and other plasma parameters [8]. A number of gyrokinetic simulations of the toroidal ETG turbulence have been performed and benchmarked with various simulation codes [9–12]. Nevertheless, the saturation mechanism of the toroidal ETG instability under the strong magnetic shear and the estimation of resultant transport level are still open problems.

Zonal flow dynamics and the properties of large-scale coherent vortex structures in the slab ETG turbulence have also been discussed by means of gyrokinetic and gyrofluid simulations [13–18]. It has been pointed out that the weak magnetic shear is important for the zonal flow generation while the positive magnetic shear leads to the streamer formation [6, 13, 14]. The scale length of zonal flow is characterized by the Rhines scaling which is proportional to the density gradient scale length L_n, where the electron heat transport decreases with increasing of L_n [15]. The statistical analyses for the ETG turbulence dominated by zonal flows reveal the phase matching between potential and pressure fluctuations which is related to the reduction of the radial heat flux and the fractal dimension of the turbulent fluctuations [16, 17]. It has also been pointed out that, in addition to the zonal flows, the dynamics of nonlinearly excited long-wavelength modes is important for the saturation of the ETG instability and for the regulation of the electron heat transport [18].

In the present study, by means of the gyrokinetic Vlasov simulations, we investigate vortex structures of the slab ETG turbulence and velocity-space structures of the distribution function in detail. The nonlinear gyrokinetic simulations with high phase-space resolution shown below enable us to examine the entropy balance relation in the slab ETG turbulence with zonal flow generation, while it has been investigated for the collisionless and weakly collisional slab ITG turbulence [19–22]. Then, we discuss the role of zonal flows in the statistically steady turbulence and the transition of vortex structure from turbulent vortices to coherent vortex streets accompanied with the significant reduction of the electron heat transport. The transport reduction in the coherent state is also studied from the viewpoint of structural change of the perturbed distribution function in the velocity-space. In the latter part of this chapter, the coherent vortex streets found in the nonlinear simulation is compared with a traveling wave solution of a Hasegawa-Mima type equation.

The remainder of this chapter is organized as follows. Gyrokinetic models used in the present study are described in Sec. 3.2. Simulation results are presented in Sec. 3.3, where the statistically steady state with weak zonal flows in the slab ETG turbulence is compared with that in the slab ITG turbulence in Sec. 3.3.1. The spontaneous formation of the coherent vortex streets and resultant transport reduction, which are found in parameters different from those in Sec. 3.3.1, are discussed in Sec. 3.3.2. Derivation of a fluid model describing the coherent vortex streets and the application to the nonlinear simulation results are given in Secs. 3.4.1 and 3.4.2, respectively. Finally, the concluding remarks are given in Sec. 3.5.

3.2   Simulation model for slab plasmas

Governing equations for the slab ITG and ETG turbulence simulations are presented in this section. Here, a slab plasma system with an uniform magnetic field $\boldsymbol{B} = B\boldsymbol{b}$ is considered. The electrostatic gyrokinetic equation describing the time evolution of the electron gyrocenter distribution function $\mathcal{F}_e^{(g)} = \mathcal{F}_e^{(g)}(\boldsymbol{X}, v_\perp, v_\parallel, t)$ for the slab plasmas is written as [cf. Eq. (2.22)],

$$\frac{\partial \mathcal{F}_e^{(g)}}{\partial t} + v_\parallel \boldsymbol{b} \cdot \nabla \mathcal{F}_e^{(g)} + \frac{c}{B}\boldsymbol{b} \times \nabla \langle \phi(\boldsymbol{X} + \boldsymbol{\rho}_e)\rangle_g \cdot \nabla \mathcal{F}_e^{(g)} + \frac{e}{m_e}\boldsymbol{b} \cdot \nabla \langle \phi(\boldsymbol{X} + \boldsymbol{\rho}_e)\rangle_g \frac{\partial \mathcal{F}_e^{(g)}}{\partial v_\parallel} = 0 , \quad (3.1)$$

where $\boldsymbol{X}$, $\boldsymbol{\rho}_e$, c, e and m_e are the gyrocenter position, the electron gyroradius vector, the speed of light, the elementary charge and the electron mass, respectively. The gyro-averaged electrostatic potential is denoted by $\langle \phi(\boldsymbol{X} + \boldsymbol{\rho}_e)\rangle_g$, where $\langle \cdots \rangle_g$ means the gyrophase average for a fixed gyrocenter position. The total gyrocenter distribution function $\mathcal{F}_e^{(g)}$ is divided into equilibrium and perturbation parts: $\mathcal{F}_e^{(g)} = F + \delta f^{(g)}$. We assume that the former is given by the local Maxwellian distribution,

$$F = F_M(\boldsymbol{X}, v_\perp, v_\parallel) = n_0 \left(\frac{m_e}{2\pi T_e}\right)^{\frac{3}{2}} \exp\left(-\frac{m_e(v_\perp^2 + v_\parallel^2)}{2T_e}\right) , \quad (3.2)$$

where n_0 and T_e denote the equilibrium density and the electron temperature. The perturbed distribution function and the potential fluctuation are written in terms of the Fourier expansions,

$$\delta f^{(g)}(\boldsymbol{X}, v_\perp, v_\parallel, t) = \sum_{\boldsymbol{k}} \delta f_{\boldsymbol{k}}^{(g)}(v_\perp, v_\parallel, t)e^{i\boldsymbol{k}\cdot\boldsymbol{X}}, \quad (3.3)$$

$$\phi(\boldsymbol{X} + \boldsymbol{\rho}_e, t) = \sum_{\boldsymbol{k}} \delta\phi_{\boldsymbol{k}}(t)e^{i\boldsymbol{k}\cdot(\boldsymbol{X}+\boldsymbol{\rho}_e)}, \quad (3.4)$$

where the equilibrium part of the potential is not considered here. In order to keep high resolution in the real space and the $v_\parallel$-space, we assume that $v_\perp$-dependence of $\delta f_{\boldsymbol{k}}^{(g)}$ is also given by the local Maxwellian, i.e., $\delta f_{\boldsymbol{k}}^{(g)}(v_\perp, v_\parallel, t) = F_{M\perp}(v_\perp)\delta f_{\boldsymbol{k}}(v_\parallel, t)$, where $F_{M\perp} \equiv (m_e/2\pi T_e)\exp(-m_e v_\perp^2/2T_e)$. The gradient scale lengths of the equilibrium density $L_n \equiv -(d\ln n_0/dx)^{-1}$ and the equilibrium temperature $L_T \equiv -(d\ln T_e/dx)^{-1}$, which are much longer than fluctuation wavelengths in the direction perpendicular to the magnetic field $\lambda = 2\pi/|\boldsymbol{k}_\perp|$, are set to be constant.

We consider a periodic two-dimensional slab configuration where the plasma is assumed to be homogeneous in the z-direction. The magnetic field $\boldsymbol{B}$ is set in the y-z plane such that $\boldsymbol{B} = B(\boldsymbol{e}_z\cos\theta + \boldsymbol{e}_y\sin\theta) \simeq B(\boldsymbol{e}_z + \theta\boldsymbol{e}_y)$ for $\theta \ll 1$, where $\boldsymbol{e}_y$, $\boldsymbol{e}_z$ and θ denote the basis vectors in the y- and z-directions and the tilt angle of the field line, respectively. Substituting Eqs. (3.2) – (3.4) into Eq. (3.1) and integrating over the $v_\perp$-space, one can obtain the gyrokinetic equation for the

perturbed distribution function $\delta f_{\boldsymbol{k}_\perp}(v_\parallel, t)$ written in the wavenumber space as

$$\left(\frac{\partial}{\partial t} + ik_\parallel v_\parallel\right)\delta f_{\boldsymbol{k}_\perp} - \frac{c}{B}\sum_\Delta \boldsymbol{b}\cdot(\boldsymbol{k}'_\perp \times \boldsymbol{k}''_\perp)\,\delta\psi_{\boldsymbol{k}'_\perp}\delta f_{\boldsymbol{k}''_\perp} - C_\parallel(\delta f_{\boldsymbol{k}_\perp})$$

$$= -i\left\{\omega_{*e}\left[1 + \eta_e\left(\frac{m_e v_\parallel^2}{2T_e} - \frac{1}{2} - \frac{k_\perp^2\rho_{te}^2}{2}\right)\right] - k_\parallel v_\parallel\right\}F_{M\parallel}\frac{e\delta\psi_{\boldsymbol{k}_\perp}}{T_e}\,. \qquad (3.5)$$

Here, $k_\parallel \equiv \boldsymbol{k}\cdot\boldsymbol{b} \simeq \theta k_y$ is the parallel wavenumber (k_z vanishes because of the translational symmetry in the z-direction), $k_\perp^2\rho_{te}^2$ is the square of the perpendicular wavenumber normalized by the electron thermal gyroradius $\rho_{te} \equiv v_{te}/\Omega_e$, where $v_{te} \equiv (T_e/m_e)^{1/2}$ and $\Omega_e \equiv eB/m_e c$ are the electron thermal speed and the electron gyrofrequency, respectively. The symbol $\sum_\Delta$ appearing in the nonlinear term of Eq. (3.5) stands for the summation over Fourier modes which satisfy the triad-interaction condition, i.e., $\boldsymbol{k}_\perp = \boldsymbol{k}'_\perp + \boldsymbol{k}''_\perp$. Inhomogeneities of n_0 and T_e in the x-direction are taken into account through the electron drift frequency $\omega_{*e} \equiv -(cT_e/eB)\boldsymbol{k}_\perp \cdot \boldsymbol{b}\times\nabla\ln n_0$ and the parameter $\eta_e \equiv L_n/L_T$. The gyro-averaged potential integrated over the $v_\perp$-space is denoted by $\delta\psi_{\boldsymbol{k}_\perp} \equiv \delta\phi_{\boldsymbol{k}_\perp}\exp(-k_\perp^2\rho_{te}^2)$, where the factor $\exp(-k_\perp^2\rho_{te}^2/2)$ reflects the finite-Larmor-radius (FLR) effect. The Maxwellian distribution of $v_\parallel$ is denoted by $F_{M\parallel} \equiv n_0(m_e/2\pi T_e)^{1/2}\exp(-m_e v_\parallel^2/2T_e)$. In the derivation of the above equation, the parallel nonlinearity $(e/m_e)\boldsymbol{b}\cdot\nabla\langle\phi(\boldsymbol{X}+\boldsymbol{\rho}_e)\rangle_g\,\partial\delta f^{(g)}/\partial v_\parallel$ included in Eq. (3.1) is neglected because of the the gyrokinetic ordering $k_\parallel/k_\perp \sim \rho_{te}/L_T \ll 1$. In order to maintain this ordering, the value of the tilt angle θ is expressed by the dimensionless parameter $\Theta \equiv k_\parallel L_T/k_y\rho_{te} \simeq \theta L_T/\rho_{te}$.

In the present model, a weak but finite collisionality effect is introduced in terms of a model collision operator $C_\parallel(\delta f_{\boldsymbol{k}_\perp})$ as follows,

$$C_\parallel(\delta f_{\boldsymbol{k}_\perp}) = \nu_e\frac{\partial}{\partial v_\parallel}\left(v_{te}^2\frac{\partial}{\partial v_\parallel} + v_\parallel\right)\delta f_{\boldsymbol{k}_\perp}\,. \qquad (3.6)$$

Here, ν_e denotes the electron collision frequency. The collision operator acting on $\delta f_{\boldsymbol{k}_\perp}$ smooths out the fine-scale fluctuations in the $v_\parallel$-space. Although the above collision operator does not conserve the momentum and the energy, its influence on the main results shown below, such as the transport level, are not crucial as long as $\nu_e L_T/v_{te} \ll 1$ [20].

The electrostatic potential is determined by the quasi-neutrality condition $\delta n_e = \delta n_i$, where the Laplacian term $\nabla^2\delta\phi$ in the Poisson equation is neglected. Since the potential should be evaluated at the particle position, not at the gyrocenter position, the distribution function should be transformed from the gyrocenter coordinates to the particle ones. The relation between the particle distribution function $\delta f_{\boldsymbol{k}_\perp}^{(p)}$ and the gyrocenter distribution function $\delta f_{\boldsymbol{k}_\perp}^{(g)}$ is given by

$$\delta f_{s\boldsymbol{k}_\perp}^{(p)} = \delta f_{s\boldsymbol{k}_\perp}^{(g)}e^{-i\boldsymbol{k}_\perp\cdot\boldsymbol{\rho}_s} - \frac{e_s\delta\phi_{\boldsymbol{k}_\perp}}{T_s}\left[1 - J_0(k_\perp v_\perp/\Omega_s)e^{-i\boldsymbol{k}_\perp\cdot\boldsymbol{\rho}_s}\right]F_{Ms}\,, \qquad (3.7)$$

where the subscript "s" represents particle species [s = {i, e} for ions and electrons], so that e_s has a sign of the electric charge for each species, and $J_0(z)$ is the zeroth-order Bessel function. The last group of terms on the right-hand side represents the polarization due to the potential fluctuations. By taking the velocity-space integral of Eq. (3.7) for electrons, one can obtain the electron density fluctuation in the particle coordinates

$$
\begin{aligned}
\delta n_{e\boldsymbol{k}_\perp} &= \int d\boldsymbol{v} \left\{ \delta f_{e\boldsymbol{k}_\perp}^{(g)} e^{-i\boldsymbol{k}_\perp \cdot \rho_e} + \frac{e\delta\phi_{\boldsymbol{k}_\perp}}{T_e} \left[1 - J_0(k_\perp v_\perp / \Omega_e) e^{-i\boldsymbol{k}_\perp \cdot \rho_e} \right] F_{Me} \right\} \\
&= e^{-\frac{1}{2}k_\perp^2 \rho_{te}^2} \int dv_\parallel \, \delta f_{e\boldsymbol{k}_\perp} + n_0 \frac{e\delta\phi_{\boldsymbol{k}_\perp}}{T_e} \left[1 - \Gamma_0(k_\perp^2 \rho_{te}^2) \right] ,
\end{aligned}
\tag{3.8}
$$

where Γ_0 is defined by $\Gamma_0(z) \equiv I_0(z) \exp(-z)$ with the zeroth-order modified Bessel function $I_0(z)$. Similarly, the ion particle density fluctuation is given as

$$
\delta n_{i\boldsymbol{k}_\perp} = e^{-\frac{1}{2}k_\perp^2 \rho_{ti}^2} \int dv_\parallel \, \delta f_{i\boldsymbol{k}_\perp} - n_0 \frac{e\delta\phi_{\boldsymbol{k}_\perp}}{T_i} \left[1 - \Gamma_0(k_\perp^2 \rho_{ti}^2) \right] \simeq -n_0 \frac{e\delta\phi_{\boldsymbol{k}_\perp}}{T_i} \quad (k_\perp \rho_{ti} \gg 1) .
\tag{3.9}
$$

Since the characteristic wave length in the ETG turbulence, which is comparable to the electron gyroradius, is much shorter than the ion gyroradius, i.e., $k_\perp \rho_{ti} \gg 1$, the ion response to the potential fluctuation is reduced to the adiabatic one as shown in the last equality of Eq. (3.9). Combining Eq. (3.8) and Eq. (3.9), the quasi-neutrality condition $\delta n_e = \delta n_i$ with the adiabatic ion response is rewritten as

$$
\int dv_\parallel \, \delta f_{e\boldsymbol{k}_\perp} = -e^{\frac{1}{2}k_\perp^2 \rho_{te}^2} \left[1 + \frac{T_e}{T_i} - \Gamma(k_\perp^2 \rho_{te}^2) \right] n_0 \frac{e\delta\phi_{\boldsymbol{k}_\perp}}{T_e} .
\tag{3.10}
$$

In ITG turbulence simulations, the electron response is often assumed to be adiabatic except for the zonal-flow component of $k_\parallel = k_y = 0$. The electron response in ITG turbulence is denoted by $\delta n_e = n_0 e(\delta\phi - \langle \delta\phi \rangle)/T_e$ while the ion response in the ETG turbulence is given by Eq. (3.9), where $\langle \cdots \rangle$ means a flux surface average. The physical pictures of the responses to the zonal-flow potential in ITG and ETG turbulence are quite different. In the ITG turbulence, electrons do not respond to the zonal-flow potential, i.e., $\delta n_{ek_\parallel = 0} = 0$, because the parallel electric field $E_\parallel$ vanishes for the mode of $k_\parallel = 0$. On the other hand, ions in the ETG turbulence can move in the perpendicular direction because of the large ion gyroradius, i.e., $k_\perp \rho_{ti} \gg 1$ even if $E_\parallel = 0$. As a result of the different responses of ions and electrons to the zonal-flow potential, the relative intensity of the zonal flow in the ETG turbulence is lower than that in the ITG turbulence [3].

From the closed set of equations described in Eqs. (3.5) and (3.10), one can derive a balance equation with respect to the entropy variable $\delta S \equiv S_M - \langle\langle S_m \rangle\rangle$, where $\langle\langle \cdots \rangle\rangle$ means the ensemble average [23, 24]. (Remember that the macroscopic and the microscopic entropy per unit volume are defined by $S_M \equiv -\int d\boldsymbol{v} \, F_M \ln F_M$ and $S_m \equiv -\int d\boldsymbol{v} \, \mathcal{F}_e^{(g)} \ln \mathcal{F}_e^{(g)}$, respectively, as described in Sec.

2.3.) Then, one finds

$$\delta S = S_{\mathrm{M}} - \langle\!\langle S_{\mathrm{m}} \rangle\!\rangle \simeq \int d\boldsymbol{v} \left\langle\!\left\langle \frac{\delta f^{(\mathrm{g})2}}{2F_{\mathrm{M}}} \right\rangle\!\right\rangle = \sum_{\boldsymbol{k}_{\perp}} \int dv_{\|} \frac{|\delta f_{\boldsymbol{k}_{\perp}}|^2}{2F_{\mathrm{M}\|}} , \tag{3.11}$$

which is correct to $O(\delta f^{(\mathrm{g})2})$. Here, we assume the turbulent fluctuations to be statistically homogeneous in space. Thus, the ensemble average is replaced by the spatial average in the last equality of Eq. (3.11). Taking the $v_{\|}$-space integral and the summation over $\boldsymbol{k}_{\perp}$ of Eq. (3.5) multiplied by $\delta f_{\boldsymbol{k}_{\perp}}^* / F_{\mathrm{M}\|}$ (where the asterisk denotes the complex conjugate), one can obtain the entropy balance equation,

$$\frac{d}{dt}(\delta S + W) = L_T^{-1} Q_{\mathrm{e}} + D , \tag{3.12}$$

by use of Eq. (3.10). The quantities W, $L_T^{-1} Q_{\mathrm{e}}$ and D denote the potential energy, the entropy production by the turbulent electron heat flux and the collisional dissipation, respectively. The definitions are as follows:

$$W = \sum_{\boldsymbol{k}_{\perp}} W_{\boldsymbol{k}_{\perp}} = \sum_{\boldsymbol{k}_{\perp}} \frac{n_0}{2} \left(1 + \frac{T_{\mathrm{e}}}{T_{\mathrm{i}}} - \Gamma_0(k_{\perp}^2 \rho_{\mathrm{te}}^2) \right) \left| \frac{e\delta\phi_{\boldsymbol{k}_{\perp}}}{T_{\mathrm{e}}} \right|^2 , \tag{3.13}$$

$$L_T^{-1} Q_{\mathrm{e}} = \frac{\boldsymbol{q}_{\perp \mathrm{e}}}{T_{\mathrm{e}}} \cdot (-\nabla \ln T_{\mathrm{e}})$$

$$= \sum_{\boldsymbol{k}_{\perp}} \frac{c}{B} \frac{d\ln T_{\mathrm{e}}}{dx} \, \mathrm{Re} \left[ik_y \delta\psi_{\boldsymbol{k}_{\perp}} \int dv_{\|} \left(\frac{m_{\mathrm{e}} v_{\|}^2}{2T_{\mathrm{e}}} - \frac{1}{2} \right) \delta f_{\boldsymbol{k}_{\perp}}^* \right] ,$$

$$= n_0 \left(\frac{d\ln T_{\mathrm{e}}}{dx} \right)^2 \sum_{\boldsymbol{k}_{\perp}} \chi_{\mathrm{e}\boldsymbol{k}_{\perp}} \tag{3.14}$$

$$D = \sum_{\boldsymbol{k}_{\perp}} \mathrm{Re} \int dv_{\|} \, C_{\|}(\delta f_{\boldsymbol{k}_{\perp}}) \frac{\delta f_{\boldsymbol{k}_{\perp}}^*}{F_{\mathrm{M}\|}} , \tag{3.15}$$

where $\boldsymbol{q}_{\perp \mathrm{e}}$ denotes the electron perpendicular heat flux due to the $\boldsymbol{E} \times \boldsymbol{B}$ convection. The electron heat transport coefficient is defined by $\chi_{\mathrm{e}} = \sum_{\boldsymbol{k}_{\perp}} \chi_{\mathrm{e}\boldsymbol{k}_{\perp}} = \boldsymbol{q}_{\perp \mathrm{e}} \cdot \boldsymbol{e}_x / (n_0 T_{\mathrm{e}} / L_T)$, where $\boldsymbol{e}_x$ denotes the basis vector in the x-direction. The production, transfer and dissipation processes of δS have been thoroughly investigated for the slab ITG turbulence [20]. The entropy variable δS is generated by the turbulent heat transport $L_T^{-1} Q_{\mathrm{e}}$ in macro-velocity scale, then it cascades to micro-velocity scale through the phase mixing process caused by the parallel advection term $ik_{\|} v_{\|} \delta f_{\boldsymbol{k}_{\perp}}$ in Eq. (3.5). Finally, the entropy variable is dissipated by the collision in the micro-velocity scale. The entropy balance relation also provides us a good measure for the accuracy of the nonlinear simulation.

In the followings, physical quantities are normalized as $x = x'/\rho_{\mathrm{te}}$, $y = y'/\rho_{\mathrm{te}}$, $v_{\|} = v_{\|}'/v_{\mathrm{te}}$, $t = t' v_{\mathrm{te}}/L_T$, $v_{\mathrm{e}} = v_{\mathrm{e}}' L_T / v_{\mathrm{te}}$, $F_{\mathrm{M}\|} = F_{\mathrm{M}\|}' v_{\mathrm{te}}/n_0$, $\delta f_{\boldsymbol{k}_{\perp}} = \delta f_{\boldsymbol{k}_{\perp}}' L_T v_{\mathrm{te}}/\rho_{\mathrm{te}} n_0$ and $\delta\phi_{\boldsymbol{k}_{\perp}} = e\delta\phi_{\boldsymbol{k}_{\perp}}' L_T / T_{\mathrm{e}} \rho_{\mathrm{te}}$, where

the prime means a dimensional quantity. In the numerical simulations, time integrations are carried out by the fourth-order Runge-Kutta-Gill method with appropriate time step. The nonlinear advection term is calculated by means of the spectral method with 3/2-rule for the de-aliasing in the wavenumber space. In order to keep high phase-space resolution, our code is parallelized with respect to the $v_{\parallel}$-coordinates, and the fourth-order central finite difference methods are used for evaluating the velocity-space derivatives in the collision operator. The nonlinear simulations have been carried out for two cases which have different dimensionless parameters η_e and Θ. The detailed simulation conditions for each parameter are given in the Sec. 3.3.1.

3.3 Nonlinear simulations

3.3.1 Physical and numerical parameters

Physical and numerical parameters for nonlinear simulations of the slab ETG turbulence are summarized below. We consider two sets of the physical parameters $\{\eta_e = 6,\ \Theta = 1/6\}$ (Case 1) and $\{\eta_e = 10,\ \Theta = 1/20\}$ (Case 2). The linear growth rate γ_L and real frequency ω_L for the two cases are plotted for k_y in Fig. 3.1. Here, we set $k_x = 0$ because the finite k_x has a stabilizing effect. It is found that Case 2 has relatively lower real frequencies, larger growth rates, and a wider range
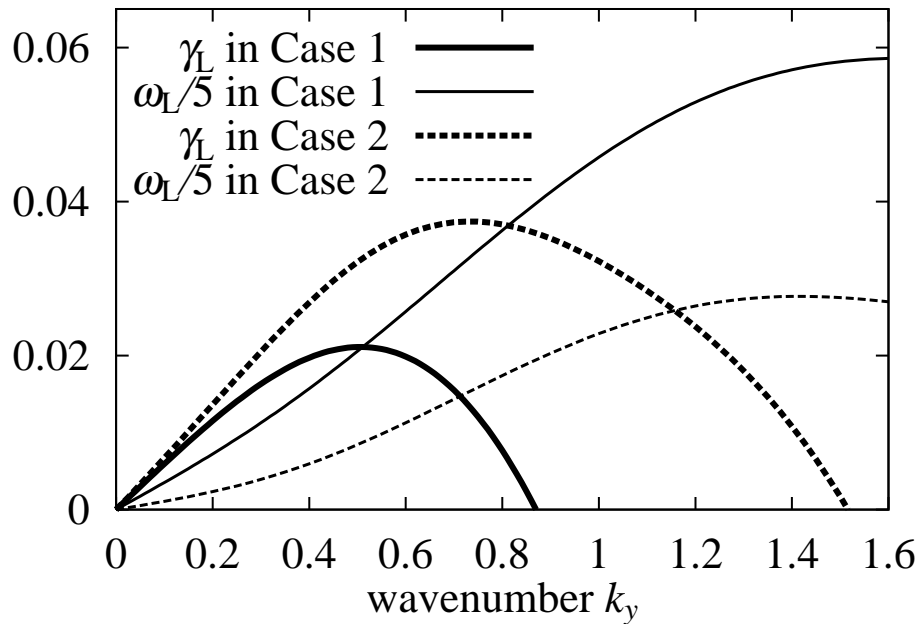

FIG. 3.1: Growth rates γ_L and real frequencies ω_L of the linear ETG modes for $k_x = 0$ in Case 1 ($\eta_e = 6,\ \Theta = 1/6$) and Case 2 ($\eta_e = 10,\ \Theta = 1/20$).

TABLE 3.1: Physical parameters used for nonlinear simulations.

	η_e	Θ	$v_{\parallel}$-grids	γ_{Lmax}	ν_e
Case 1	6	1/6	1025	0.021	2.08×10^{-4}
Case 2	10	1/20	2049	0.037	1.25×10^{-4}

of the unstable modes than those in Case 1. The parameters used for nonlinear simulations are summarized in Table 3.1. Here, sufficiently small collision frequency ν_e, which does not affect the linear growth rates and the real frequencies, is introduced in the both cases. Also, we set $\tau \equiv T_e/T_i = 1$. The number of modes in the wavenumber space, the minimum and maximum wavenumbers are set to be $(N_{k_x}, N_{k_y})=(129, 257)$, $k_{min} = 0.05$ and $k_{max} = 6.4$, respectively. The range of $v_{\parallel}$-coordinates is $|v_{\parallel}| \leqslant v_{max} = 10$. Furthermore, the simulation domain is set to be a square with $L_x = L_y = 40\pi\rho_{te}$. In the ITG turbulence, as will be discussed in Sec. 3.3.2, the parameters are the same as those in the slab ETG turbulence of Case 1 except for the use of the ion thermal gyroradius ρ_{ti} on the normalizations.

3.3.2   Steady turbulence and zonal flows

Simulation results for Case 1 as well as the comparison between slab ETG and ITG turbulence are shown and discussed below. Time evolution of each term in Eq. (3.12), i.e., $d(\delta S)/dt$, dW/dt, Q_e and D is plotted in Fig. 3.2. (Note that $L_T^{-1}Q_e'$ is reduced to Q_e in terms of the normalization with L_T, where the prime means the dimensional quantity.) It is confirmed that the entropy balance relation described in Eq. (3.12) is accurately satisfied within an error less than 1% with respect to the amplitude of the collisional dissipation. In the nonlinear phase $(t \geqslant 700)$, one can find a statistically steady state in the entropy balance, where the mean heat transport balances with the mean collisional dissipation, namely, $\overline{Q_e} \simeq -\overline{D}$ while $\overline{d(\delta S)/dt} \simeq \overline{dW/dt} \simeq 0$ (the overline denotes the time average for $t \geqslant 1000$). The statistically steady state of slab ITG turbulence was confirmed by Watanabe and Sugama [20], where the zonal flow components of the distribution function were not included for studying the entropy balance with strong ion heat transport. The present turbulence simulation results demonstrate that the similar steady state with finite electron heat transport exists in the slab ETG turbulence including zonal flows self-consistently.

The time evolutions of the heat transport coefficients χ_s are shown in Fig. 3.3, where "s" denotes the particle species. Here, $\chi_{e,nz}$ and χ_e represent the results without and with the zonal flow generation, respectively. In the former case, the zonal flow components of the perturbed

distribution function $\delta f_{k_x,k_y=0}$ are artificially neglected. In addition, a slab ITG case with the zonal flow generation is also plotted as χ_i in the figure. The saturation levels of the transport coefficients are $\overline{\chi_{e,nz}} = 1.34 \times 10^{-1}$ $[\rho_{te}^2 v_{te}/L_T]$, $\overline{\chi_e} = 4.65 \times 10^{-2}$ $[\rho_{te}^2 v_{te}/L_T]$ and $\overline{\chi_i} = 4.36 \times 10^{-5}$ $[\rho_{ti}^2 v_{ti}/L_T]$, respectively, where the time average is taken over $6000 \leqslant t \leqslant 8000$. We find a quite small ratio of saturation levels $\overline{\chi_i}/\overline{\chi_e} \simeq 9.38 \sqrt{m_i/m_e} \times 10^{-4} \simeq 0.04$. This is because the zonal flow driven by the slab ITG turbulence is much stronger than that driven by the slab ETG turbulence due to the difference of the adiabatic response to the zonal-flow potential $\delta\phi_{k_x,k_y=0}$ as described in Sec. 3.2. Also, in the present slab configuration with the constant magnetic field, the zonal flow damping due to the neoclassical polarization is not included. Therefore, the strong zonal flow is driven by the slab ITG turbulence and sustained for a long time. The time evolution of $\chi_{e,nz}$ indicates the higher level and the slow time-variation while the value of χ_e reaches to the steady state. The averaged value $\overline{\chi_{e,nz}}$ is about 2.9 times larger than $\overline{\chi_e}$. These results suggest that the weak but finite zonal flows driven by the slab ETG turbulence play a major role in regulating the slow time-variation and in realizing the steady transport.

Comparisons of the cases with and without zonal flows provide us clear understandings of the role of the zonal flow in regulating the turbulent transport. Figures 3.4(a) – (c) show the wavenumber spectra of the potential energy $W_{k_x,k_y=0}$, $W_{k_x=0,k_y}$ [see Eq. (3.13)] and the transport coefficient $|\chi_{ek_x=0,k_y}|$ [see Eq. (3.14)], respectively, where the amplitudes are averaged over $3000 \leqslant$
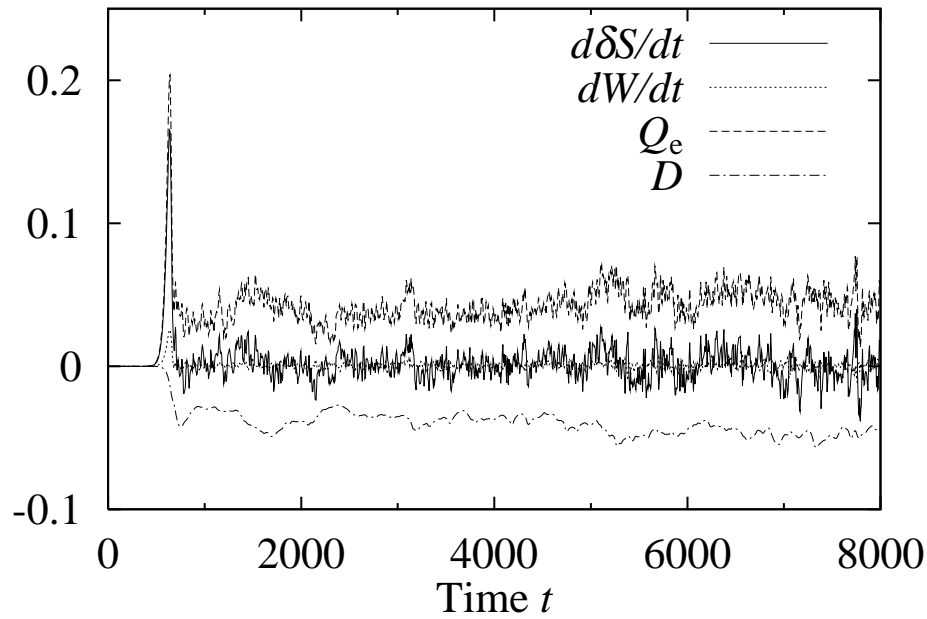

FIG. 3.2: Time evolution of each term in Eq. (3.12), $d(\delta S)/dt$, dW/dt, Q_e and D in Case 1.
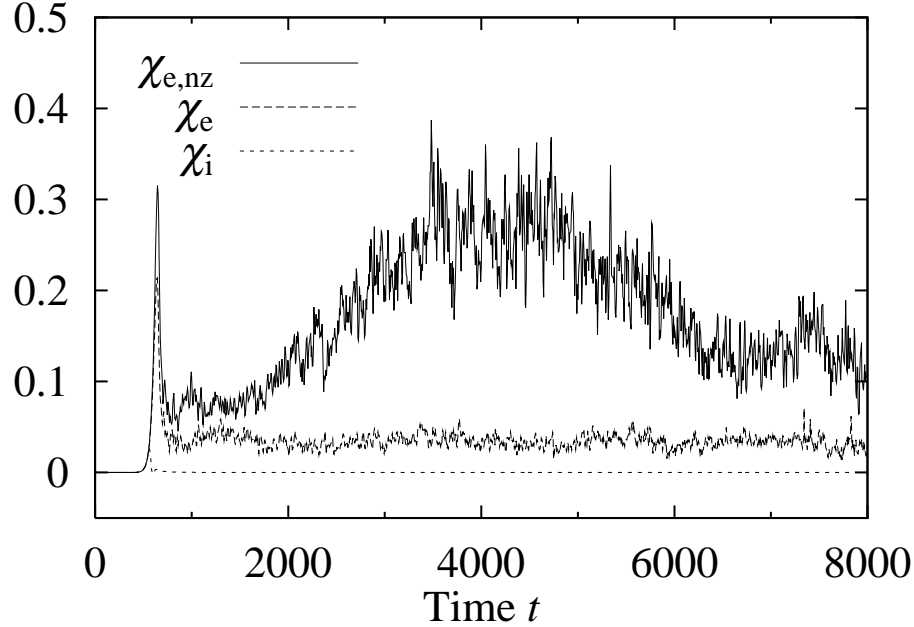
FIG. 3.3: Time evolutions of the transport coefficients $\chi_{e,nz}$ (ETG without zonal flows), χ_e (ETG with zonal flows) and χ_i (ITG with zonal flows), where the gyro-Bohm units $\rho_{ts}^2 v_{ts}/L_T$ (s = e, i) are used.

$t \leqslant 5000$. In Fig. 3.4(b), one can see a much larger amplitude of the $(k_x = 0, \, k_y = k_{min} = 0.05)$-mode compared to the other modes in the case without zonal flows, while its amplitude significantly decreases by a factor of about 30 in the case with zonal flows. A similar reduction is also found for $|\chi_{ek_x=0,k_y=k_{min}}|$ in Fig. 3.4(c). The correlation between $W_{k_\perp}$ and $|\chi_{ek_\perp}|$ indicates that the high level of $\chi_{e,nz}$ with the slow time-variation shown in Fig. 3.3 is mainly caused by low-$k_\perp$ modes, where the $(k_x = 0, \, k_y = k_{min})$-mode makes the largest contribution to the heat transport. The zonal flows with finite amplitudes shown in Fig. 3.4(a) suppress the low-$k_\perp$ modes and reduce the transport level. Also, the contribution of $|\chi_{ek_x=0,k_y=k_{min}}|$ to the total χ_e, that is 27% in the case without zonal flows, decreases to 7% in the case with zonal flows. The reduction of the amplitudes of low-$k_\perp$ modes by zonal flows leads to the steady χ_e.

The different evolutions of turbulent transport and the role of the zonal flow discussed above are also understood from the comparison of vortex structures. Color contours of the electrostatic potential fluctuations on the (x,y)-plane at $t = 4980$ are shown in Figs. 3.5(a) – (c) for the above three cases [(a)ETG without zonal flows, (b)ETG with zonal flows, (c)ITG with zonal flows], respectively. In Fig. 3.5(a), one can see formation of isolated vortices with the positive and the negative signs of the potential values. The size and amplitude of each vortex are typically $\Delta_{vortex} \simeq 8 \, [\rho_{te}]$ and $|\delta\phi|_{vortex} \simeq 18 \, [\rho_{te}T_e/L_T e]$, respectively. In addition, the $(k_x = 0, \, k_y = k_{min})$-
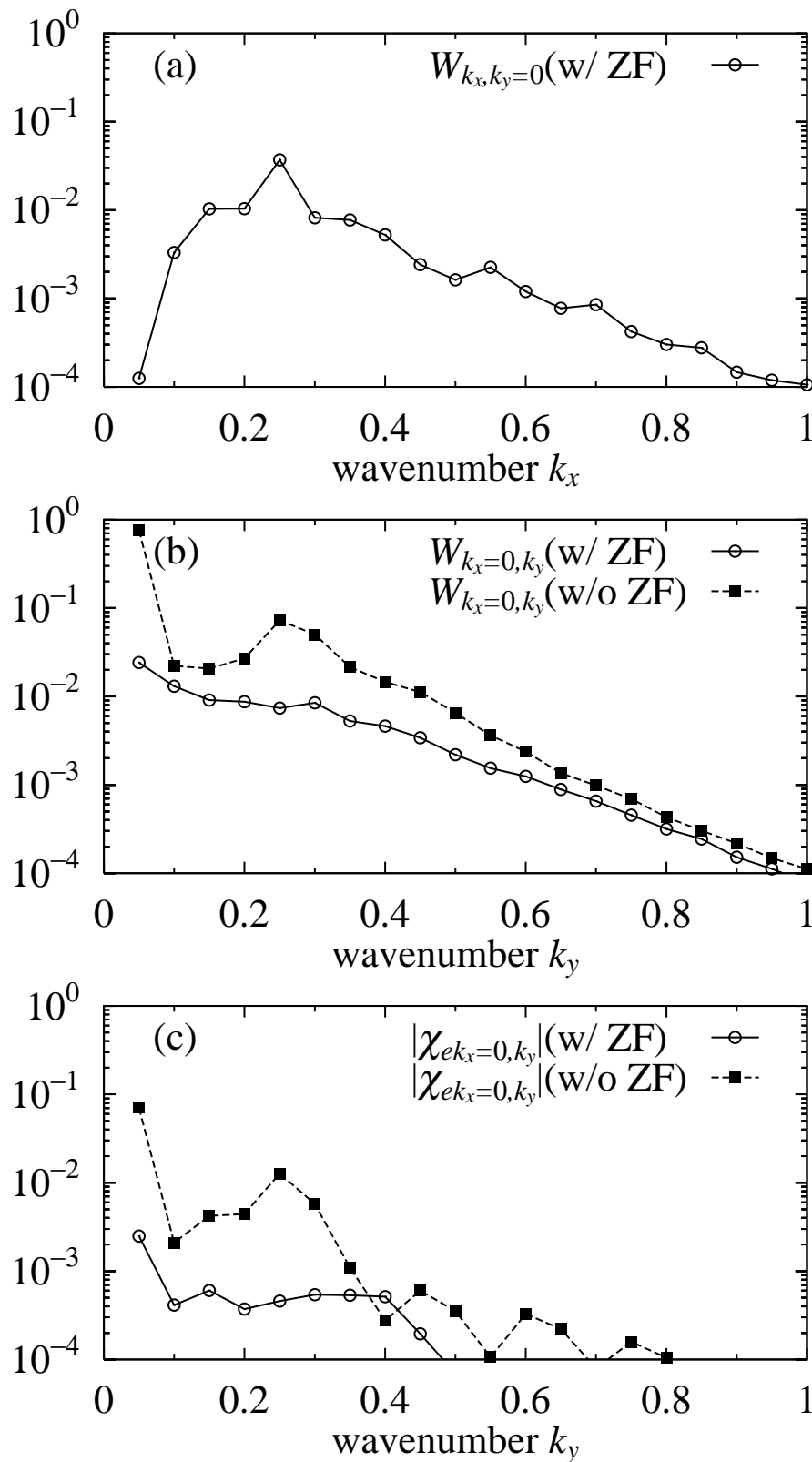
FIG. 3.4: The wavenumber spectra of (a)$W_{k_x,k_y=0}$, (b)$W_{k_x=0,k_y}$ and (c)$|\chi_{ek_x=0,k_y}|$ in the cases with and without zonal flows, where the amplitudes are averaged over $3000 \leqslant t \leqslant 5000$. The units $(\rho_{te}/L_T)^2(T_e/e)^2$ and $\rho_{te}^2 v_{te}/L_T$ are used for $W_{k_\perp}$ and $\chi_{ek_\perp}$, respectively.
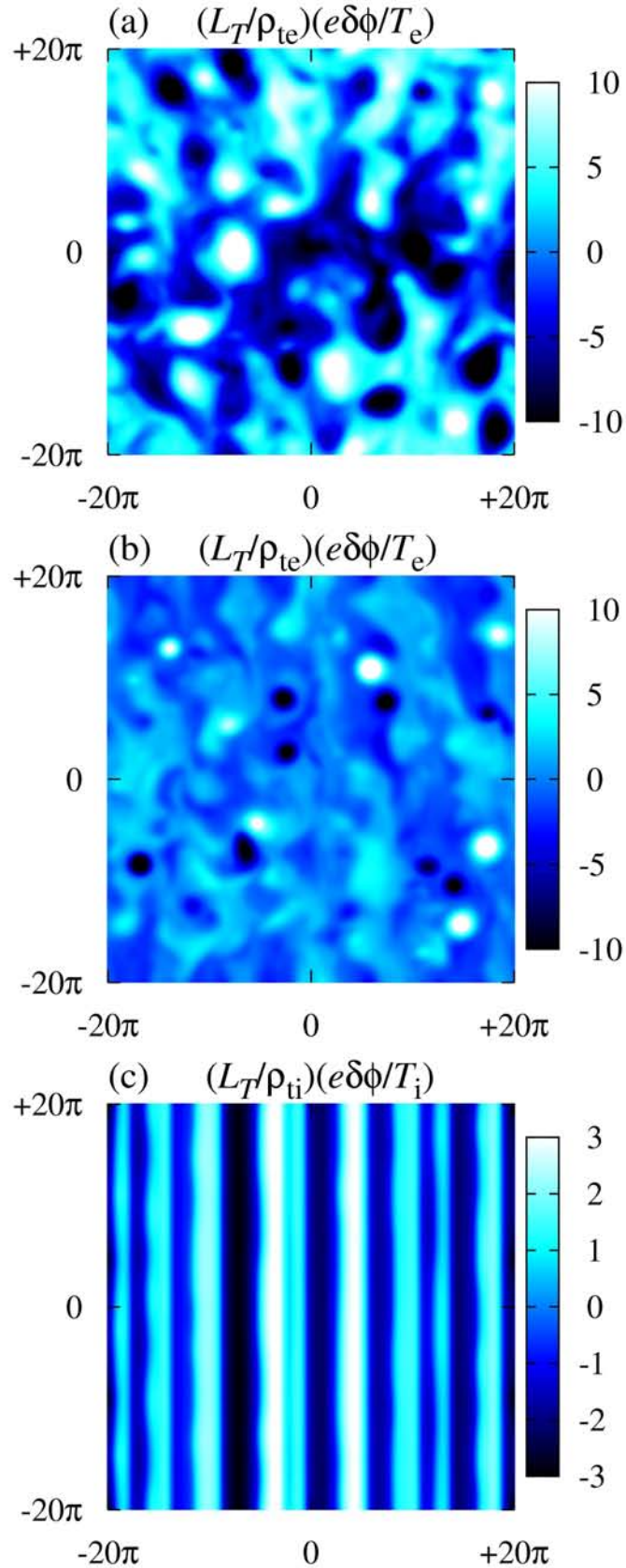
FIG. 3.5: Contours of the normalized potential fluctuations at $t = 4980$ in (a)ETG without zonal flows, (b)ETG with zonal flows and (c)ITG with zonal flows.

mode, which makes a dominant contribution to the heat transport, is clearly observed behind the isolated vortices. The isolated vortices are also observed in Fig. 3.5(b), where the typical size and amplitude of each vortex are slightly smaller than those found in the case without zonal flows. However, the ($k_x = 0$, $k_y = k_{\min}$)-mode no longer appears in the present case because it is suppressed by the zonal flows with finite amplitudes. Also, the isolated vortices exhibit the complicated motion and their mergers. Mergers of like-signed vortices have also been observed in the two-dimensional decaying plasma turbulence with Hasegawa-Mima model (see, for example, Ref. 15 and 25). In the present case, the zeroth velocity moment of the gyrokinetic equation used here includes the similar nonlinearity to that in the Hasegawa-Mima equation which is derived from Eqs. (3.5) and (3.10) in the limits of $k_\parallel = 0$ and $k_\perp \rho_{\mathrm{te}} \ll 1$. Thus, it is considered that the formation of the isolated vortices and their mergers found in the slab ETG turbulence reflect the similarities between the gyrokinetic and the Hasegawa-Mima equations. In the ITG case with the zonal flow generation [Fig. 3.5(c)], an anisotropic flow structure dominated by the strong zonal flow ($k_x \simeq 0.4$, $k_y = 0$) is observed, where the amplitude of the zonal flow potential is $|\delta\phi|_{\mathrm{zonal}} \simeq 2$ [$\rho_{\mathrm{ti}} T_{\mathrm{i}}/L_T e$]. The slab ITG driven zonal flows with the large amplitude and its strong flow shear completely suppress the turbulent transport.

3.3.3   Formation of coherent vortex streets and transport reduction

Here, we discuss the results of the slab ETG turbulence simulation in Case 2 which is linearly more unstable in comparison with Case 1. The entropy balance relation is also satisfied in the present case. However, we find quite different behavior of the electron heat flux and the vortex structures as shown below.

Figure 3.6 shows the time evolutions of electron heat transport coefficients for Case 1 and Case 2. As the linear dispersion relation for Case 2 shows the larger growth rate and the wider range of unstable modes than those in Case 1, one finds earlier saturation and higher transport level at $t \leqslant 3000$. In Case 2, however, a transition of vortex structure, which will be shown in Figs. 3.8, occurs from a turbulent to a coherent states accompanied with the significant reduction of transport level at $t \sim 3500$. In contrast, Case 1 keeps the steady transport level of $\overline{\chi_{\mathrm{e}}} = 4.65 \times 10^{-2}$ [$\rho_{\mathrm{te}}^2 v_{\mathrm{te}}/L_T$] for $t \geqslant 6000$. The time averaged heat transport coefficients for Case 2 in the turbulent and coherent states are summarized in Table 3.2. Surprisingly, the transport level in the coherent state of Case 2 is about 2.6 times less than the steady transport level in Case 1 with a relatively moderate growth rates of the linear ETG modes. The reversal of transport level between Case 1 and Case 2 is expected from neither quasilinear theory nor mixing-length estimates. Since zonal flows play a major role in realizing the steady χ_{e} as shown in Fig. 3.3,

TABLE 3.2: Time averaged heat transport coefficients in Case 2.

	$\overline{\chi_e}$ $[\rho_{te}^2 v_{te}/L_T]$	averaging time
turbulent state	3.37×10^{-1}	$1000 \leqslant t \leqslant 3000$
coherent state	1.77×10^{-2}	$6000 \leqslant t \leqslant 8000$

we consider that the onset of the transition of the transport level also depends on the zonal flow amplitude.

Comparisons of the time evolutions of the potential energy for Case 1 and Case 2 are shown in Figs. 3.7(a) and 3.7(b), where the total potential energy W in Eq. (3.13) is divided into zonal flow and turbulence components defined by $W_{zf} \equiv \sum_{k_x} W_{k_x,k_y=0}$ and $W_{trb} \equiv \sum_{k_x} \sum_{k_y \neq 0} W_{k_x,k_y}$, respectively. In Fig. 3.7(a), we see that the turbulence energy W_{trb} in the both cases gradually increases after the initial saturation of the ETG instability, then they reach to steady states at $t \geqslant 5200$. The time averaged values are $\overline{W_{trb}} = 8.99$ $[(\rho_{te}/L_T)^2(T_e/e)^2]$ for Case 1 and $\overline{W_{trb}} = 12.6$ $[(\rho_{te}/L_T)^2(T_e/e)^2]$ for Case 2, respectively, where the time averages are taken over $5200 \leqslant t \leqslant 8000$. Evolutions of the zonal flow energy W_{zf} are quite different between Case 1 and Case 2
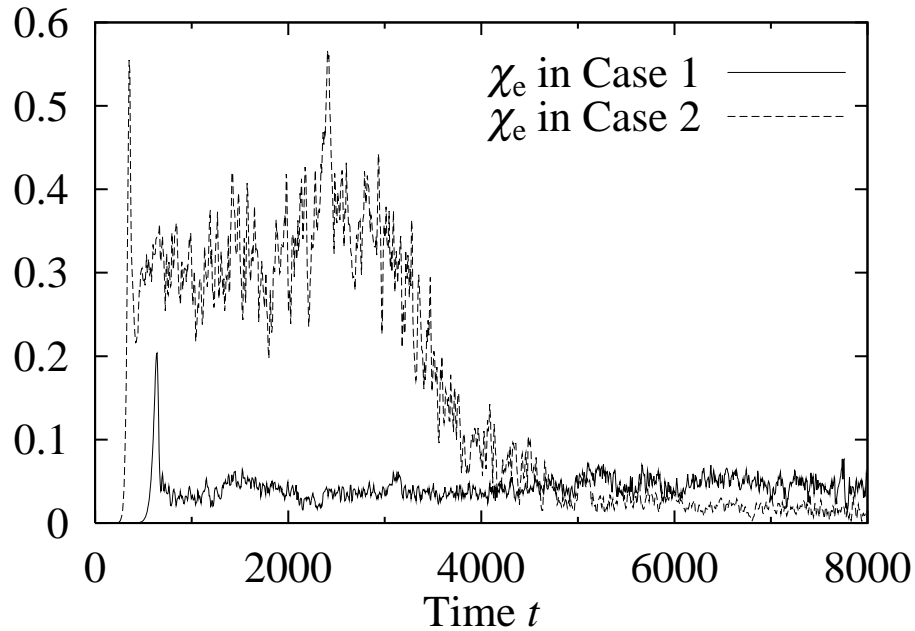

FIG. 3.6: Comparison of the time evolutions of the transport coefficients χ_e in Case 1 and Case 2, where the gyro-Bohm units $\rho_{te}^2 v_{te}/L_T$ are used.
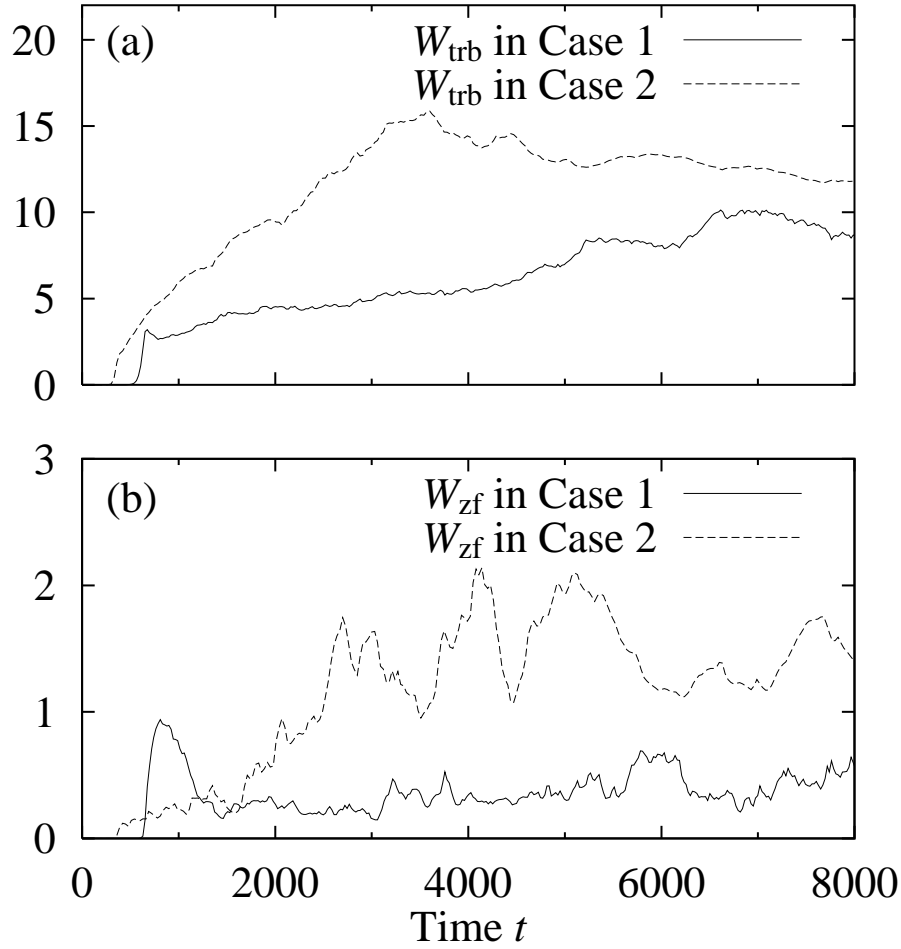
FIG. 3.7: Time evolutions of (a)turbulence energy W_{trb} and (b)zonal flow energy W_{zf} in Case 1 and Case 2, where the units $(\rho_{\text{te}}/L_T)^2(T_{\text{e}}/e)^2$ are used.

as shown in Fig. 3.7(b). In Case 1, the nonlinearly generated zonal flows increase exponentially at $t \leqslant 810$. After that, the zonal flow energy, however, decays quickly and keeps a steady level of $\overline{W_{\text{zf}}} = 0.428$ $[(\rho_{\text{te}}/L_T)^2(T_{\text{e}}/e)^2]$, where the time averages are taken over $6000 \leqslant t \leqslant 8000$. In contrast to Case 1, the zonal flow energy for Case 2 continue to increase gradually until $t \sim 2700$. Finally, it sustains about 3.2 times higher level of $\overline{W_{\text{zf}}} = 1.36$ $[(\rho_{\text{te}}/L_T)^2(T_{\text{e}}/e)^2]$ than that in Case 1. The higher level of the zonal flow energy found in Case 2 is associated with the stronger linear ETG instability causing the higher level of turbulence energy that is a source of zonal flows. Furthermore, the smaller value of the parameter Θ $(=k_{\parallel}/k_y)$, which denotes the normalized parallel wavenumber, may also be related to the stronger zonal-flow generation. The different behavior of the zonal flow energy between Case 1 and Case 2 lead to the different evolutions of χ_{e} with the steady level or the transport reduction, as shown in Fig. 3.6.
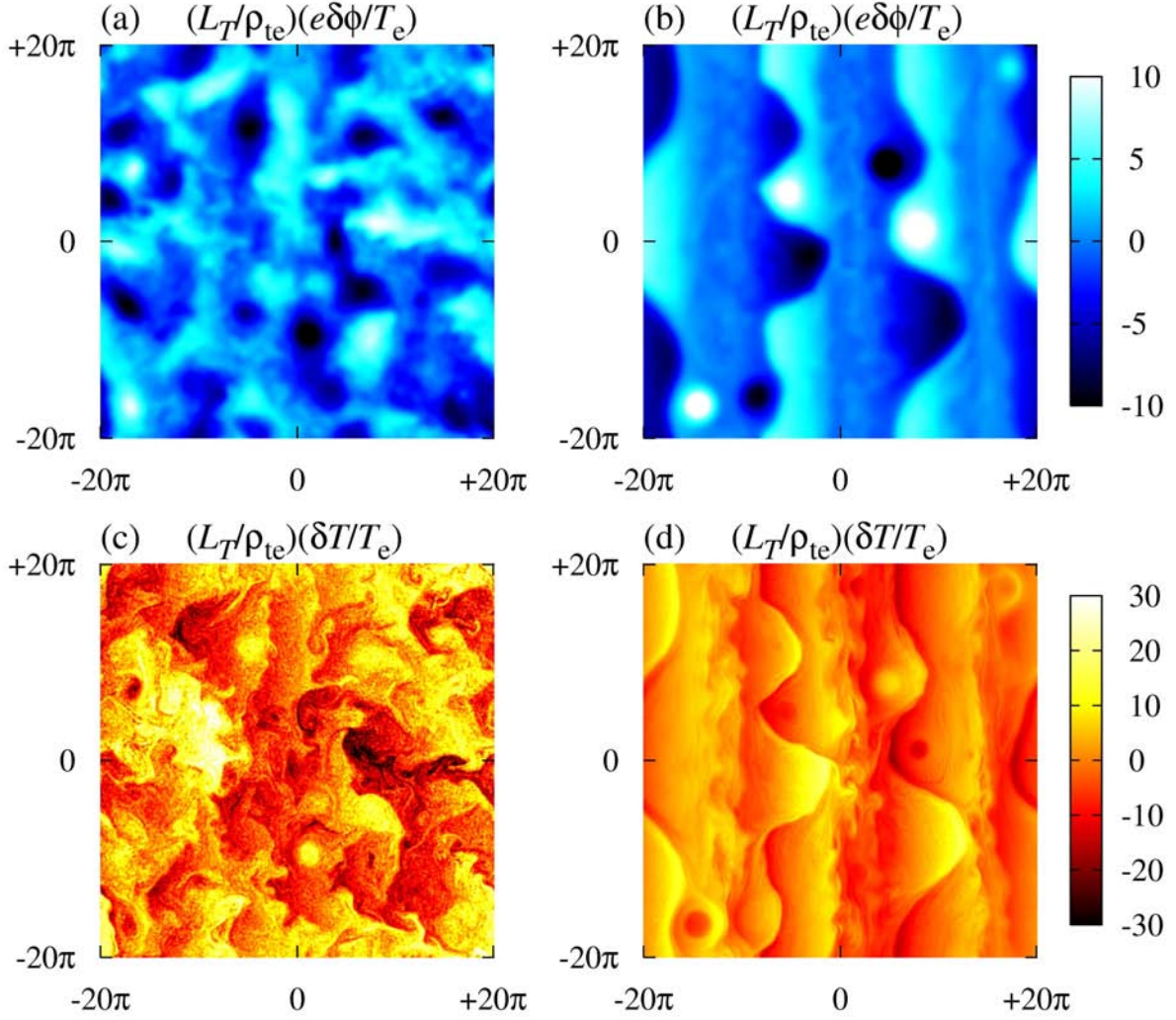
FIG. 3.8: Contours of normalized potential fluctuations at (a)$t = 2400$ (turbulent state), (b)$t = 7800$ (coherent state) and normalized temperature fluctuations at (c)$t = 2400$ (turbulent state), (d)$t = 7800$ (coherent state) for Case 2.

Figures 3.8(a) – (d) show color contours of potential and temperature fluctuations found in Case 2 in the turbulent state at $t = 2400$ and the coherent state at $t = 7800$, respectively, where the temperature fluctuations are defined by $\delta T_{k_\perp} = \int dv_\parallel (v_\parallel^2 - 1)\delta f_{k_\perp}$. In the turbulent state, the spatial structures of the both fluctuations are nearly isotropic on the x-y plane [Figs. 3.8(a) and 3.8(c)]. Moreover, the temperature fluctuations contain finer spatial-scale components than those in the potential fluctuations. The generation of the fine-scale fluctuations reflects development of the fine-scale structures of the distribution function in the phase-space. On the other hand, in the coherent state, vortex streets along the strong zonal flow are observed in the potential and temperature fluctuations [Figs. 3.8(b) and 3.8(d)] which are almost in-phase. A low wavenumber

mode with $k_x = 0.05$ and $k_y = 0.15$, and the zonal flow component with $k_x = 0.15$ and $k_y = 0$ mainly contribute to the formation of coherent vortex streets, where they have the comparable amplitude of $|\delta\phi_{k_x=0.05,k_y=0.15}| = 0.664\ [(\rho_{te}/L_T)(T_e/e)]$ and $|\delta\phi_{k_x=0.15,k_y=0}| = 0.598\ [(\rho_{te}/L_T)(T_e/e)]$. The coherent vortex streets slowly propagate in the ion diamagnetic direction (the negative y-direction) which is opposite to the propagation direction of the linear ETG modes. Moreover, the fine-scale structures of temperature fluctuations disappear in the coherent state while the amplitude are as large as that in the turbulent state.

In order to find a relation between the transition of vortex structure and transport level, the power spectra of $\delta\phi_{k_\perp}$, $\delta T_{k_\perp}$ and $\chi_{ek_\perp}$ are shown in Figs. 3.9(a) – (c), respectively, where the quantities are summed over k_x components and the time averages are taken for $1000 \leqslant t \leqslant 3000$ in the turbulent state and for $6000 \leqslant t \leqslant 8000$ in the coherent state. The low wavenumber components of $|\delta\phi_{k_y}|$ for $k_y \leqslant 0.2$ in the coherent state are slightly larger than those in the turbulent state while the higher wavenumber components for $k_y \geqslant 0.25$ significantly decrease by a factor of 3–10. On the other hand, the amplitude of $|\delta T_{k_y}|$ for all k_y in the coherent state is less than that in the turbulent state, where the reduction of high wavenumber components for $k_y \geqslant 1.0$ is significant. These features are consistent with the coherent structures shown in Figs. 3.8(b) and 3.8(d), where the fine-scale fluctuations of $\delta\phi$ and δT are smoothed out. It is noteworthy that the low wavenumber components of $|\chi_{ek_y}|$ around $k_y = 0.1$, which make dominant contributions to the total heat transport, decrease by a factor of 15.9 in the coherent state, while the changes in amplitudes of low wavenumber components of $|\delta\phi_{k_y}|$ and $|\delta T_{k_y}|$ are within a factor of 3. The above results for Case 2 suggest that the transport reduction in the coherent state is mainly associated with a decrease of phase difference between $\delta\phi_{k_\perp}$ and $\delta T_{k_\perp}$ rather than the reduction of fluctuation amplitudes. Indeed, the transport coefficient $\chi_{ek_\perp}$ can be expressed as [see Eq. (3.14)],

$$
\begin{aligned}
\chi_{ek_\perp} &= -e^{-\frac{1}{2}k_\perp^2} k_y |\delta\phi_{k_\perp}|^2 \int dv_\parallel \left(v_\parallel^2 - 1\right) \mathrm{Im}\left[\frac{\delta f_{k_\perp}}{\delta\phi_{k_\perp}}\right] \\
&= -e^{-\frac{1}{2}k_\perp^2} k_y |\delta\phi_{k_\perp}|^2 \mathrm{Im}\left[\frac{\delta T_{k_\perp}}{\delta\phi_{k_\perp}}\right],
\end{aligned}
\tag{3.16}
$$

where normalized quantities are used here. The above equation shows that the transport coefficient is proportional to the squared amplitude $|\delta\phi_{k_\perp}|^2$ and the imaginary part of the distribution function (or temperature fluctuation) divided by the potential fluctuation $\mathrm{Im}[\delta f_{k_\perp}/\delta\phi_{k_\perp}]$ (or $\mathrm{Im}[\delta T_{k_\perp}/\delta\phi_{k_\perp}]$). In general, the phase difference $\Delta\theta_{k_\perp}$ between two Fourier modes $X_{k_\perp}$ and $Y_{k_\perp}$ is given by $\Delta\theta_{k_\perp} = \sin^{-1}(\mathrm{Im}[Y_{k_\perp}/X_{k_\perp}])$. Thus, velocity moments of the quantity $\mathrm{Im}[\delta f_{k_\perp}/\delta\phi_{k_\perp}]$ are related to the phase difference between potential fluctuations and other fluid variables. The reduction of the phase difference between potential and pressure fluctuations in the coherent vortex structures dominated by zonal flows has also been observed in gyrofluid simulations of
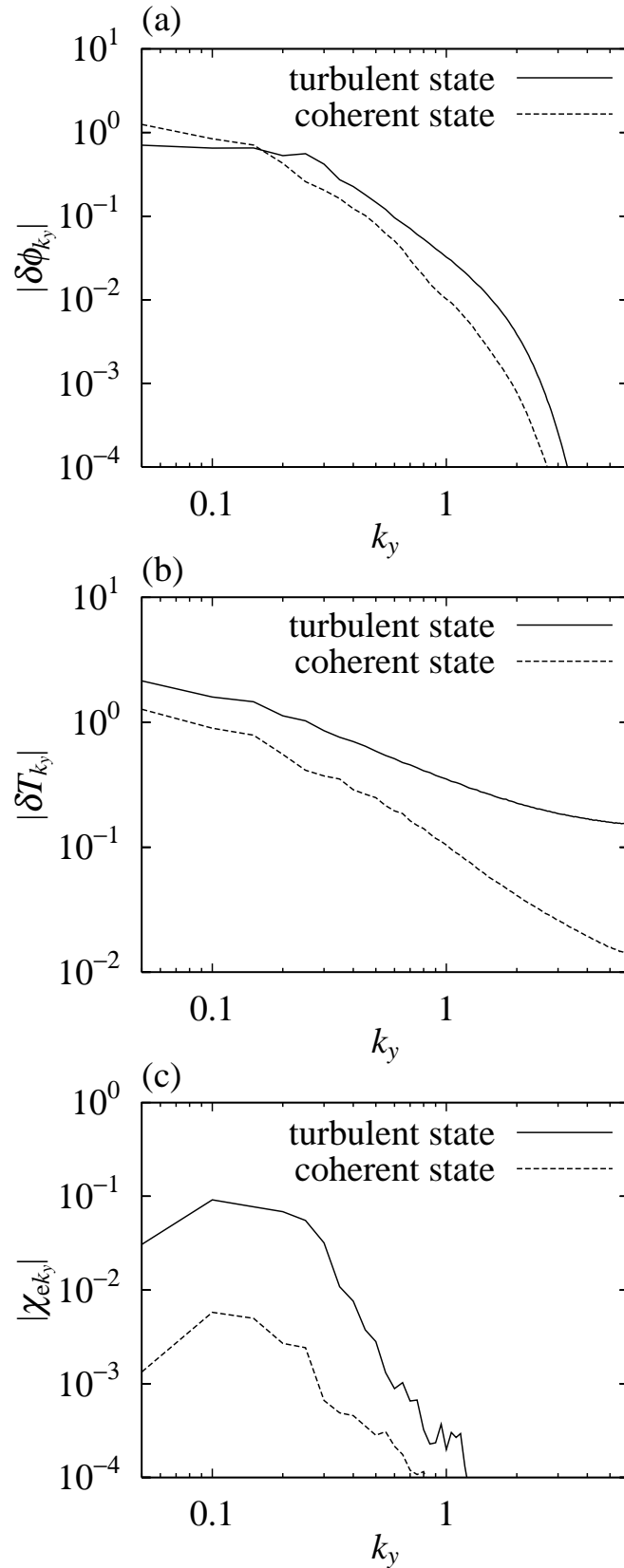
FIG. 3.9: Power spectra of (a)$|\delta\phi_{\boldsymbol{k}_\perp}|$, (b)$|\delta T_{\boldsymbol{k}_\perp}|$ and (c)$|\chi_{\mathrm{e}\boldsymbol{k}_\perp}|$ in the turbulent ($1000 \leqslant t \leqslant 3000$) and coherent ($6000 \leqslant t \leqslant 8000$) states, where the quantities are summed over k_x components and taken time averages.

sheared-slab ETG turbulence with small magnetic shear parameter $\hat{s} = 0.1$ [16, 17].

In the present gyrokinetic simulation study, the transition of vortex structure from a turbulent to a coherent state, which is accompanied with the reduction of the phase difference between $\delta\phi$ and δT, is related to velocity-space structures of the perturbed distribution function, or, especially, to its imaginary part. Figure 3.10 shows velocity-space profiles of the quantity $-\mathrm{Im}[\delta f_{k_\perp}/\delta\phi_{k_\perp}]$ in Eq. (3.16). Here, the solid and dashed lines correspond to the results in turbulent and coherent states, respectively, where the mode giving the dominant contribution to the heat transport ($k_x = 0, k_y = 0.1$) are plotted. The linear eigenfunction is also shown by the dotted line in the figure, where a scale factor of 1/2 is multiplied. One can see that the profile in turbulent state is qualitatively similar to the linear eigenfunction, which can drive large heat transport. In contrast, the significant decrease of $-\mathrm{Im}[\delta f_{k_\perp}/\delta\phi_{k_\perp}]$ is found in the coherent state, which is related to the transport reduction. The decrease of $-\mathrm{Im}[\delta f_{k_\perp}/\delta\phi_{k_\perp}]$ corresponds to the phase matching of $\delta\phi$ and δT, and it is consistent with the spatial structures shown in Figs. 3.8(b) and 3.8(d). Furthermore, the smaller value of $-\mathrm{Im}[\delta f_{k_\perp}/\delta\phi_{k_\perp}]$ in the coherent state suggests that the reduction of phase difference to potential fluctuations $\delta\phi_{k_\perp}$ is found not only for temperature fluctuations $\delta T_{k_\perp}$, but also for any n-th velocity moments of the perturbed distribution function $\delta M_{k_\perp}^{(n)} \equiv \int dv_\parallel\, v_\parallel^n\, \delta f_{k_\perp}$. This fact is utilized for a derivation of a model equation describing the
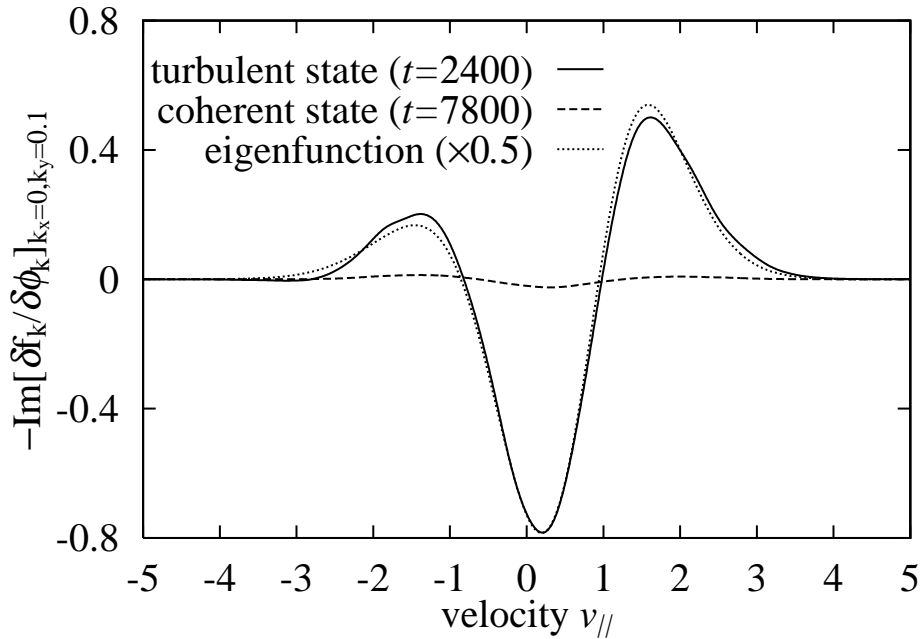

FIG. 3.10: Velocity-space profiles of the quantity $-\mathrm{Im}[\delta f_{k_\perp}/\delta\phi_{k_\perp}]$ for the mode giving the dominant contribution to the heat transport ($k_x = 0, k_y = 0.1$).

coherent vortex streets.

The results of nonlinear simulations suggest that the onset of the transition to the coherent state and the formation of vortex streets, which is accompanied with the phase matching phenomena, are closely related to the behavior of zonal flows. It depends on the parameters $\eta_e \equiv L_n/L_T$ and $\Theta \equiv k_\parallel/k_y$, which determine the linear ETG instability in the present model with the fixed ν_e and $\tau \equiv T_i/T_e$. In particular, the parameter Θ, which is relevant to the magnitude of the parallel compression, is considered to be influential on the growth of zonal flows through nonlinear mode couplings with $k_\parallel \neq 0$ modes. It has also been pointed out that the parallel electron flows are essential to the stabilization of the Kelvin-Helmholtz modes for zonal flows [14]. A comprehensive parameter-scan is given in the next chapter in order to clarify which parameters are crucial for the strong zonal-flow generation and the formation of the coherent vortex structures. These analyses are expected to contribute to finding a critical condition for the transition of vortex structures from turbulent to coherent states with transport reduction, and may provide ones a useful insight in relation to the chaos- or turbulence-control. In fact, by means of the Hasegawa-Wakatani model, Klinger *et al*. [26] pointed out that an externally applied perturbation of the parallel flow leads to the transition from the drift wave turbulence to a coherent state.

The simple shear-less slab configuration with constant Θ used in the present study is associated with a local model for the neighborhood of the minimum-q surface (q denotes the safety factor), which has a weak magnetic shear $\hat{s} \ll 1$, in the toroidal system with a reversed magnetic shear profile [4, 5]. In the case with a weak magnetic shear, each position of the rational surface becomes more distant and the toroidal-mode couplings weaken so that the slab ETG modes can also be destabilized. Actually, the global gyrokinetic PIC simulations of the slab ETG turbulence for the reversed magnetic shear profile have found out the strong zonal-flow generation and the significant reduction of the electron heat transport around the minimum-q surface where the $\hat{s}$ vanishes [14].

3.4   Identification of coherent vortex streets

3.4.1   Hasegawa-Mima type model for coherent vortex streets

Here, we derive a model equation by which the coherent vortex streets shown in the previous section can be described. It can also be utilized for the detailed comparison with nonlinear simulation results.

Main features of the coherent vortex streets with significantly low transport level found in the previous section are summarized as follows. First, the spatial profile of $\delta\phi$ mainly consists of

large-scale vortices and zonal flows with comparable amplitudes [see Fig. 3.8(b)]. Second, the propagating direction of these vortices are opposite to that of the linear ETG modes. Third, the phase matching occurs between the potential fluctuation $\delta\phi_{k_\perp}$ and the fluctuations $\delta M_{k_\perp}^{(n)}$ defined by the n-th velocity moments of the perturbed distribution function. These features allow us to derive a fluid equation for the coherent vortex streets. By taking the $v_\parallel$-space integral of gyrokinetic equation in Eq. (3.5) and by use of the quasi-neutrality condition in Eq. (3.10), one can obtain the following equation,

$$\frac{\partial}{\partial t}\Lambda_{k_\perp}\delta\psi_{k_\perp} - ik_y\left(1 - \frac{\eta_e}{2}k_\perp^2\right)\delta\psi_{k_\perp} - \sum_{k=k'_\perp+k''_\perp}\boldsymbol{b}\cdot(\boldsymbol{k}'\times\boldsymbol{k}'')\,\delta\psi_{k'_\perp}\Lambda_{k''_\perp}\delta\psi_{k''_\perp} = 0\,, \qquad (3.17)$$

which is formally similar to the Hasegawa-Mima equation written in the wavenumber space. Here, the moment of parallel advection term $\int dv_\parallel ik_\parallel v_\parallel\delta f_{k_\perp}$ ($= ik_\parallel u_\parallel$), which causes the linear ETG instability through a coupling with higher order moments, is neglected for simplicity because it is relatively smaller than the other terms in the coherent state. The validity for neglecting the parallel advection term will be discussed in Sec. 3.4.2. The FLR-factor is denoted by $\Lambda_{k_\perp} \equiv e^{k_\perp^2}[1 + \tau - \Gamma_0(k_\perp^2)]$. Normalizations are the same as shown in Sec. 3.2 except that the macroscopic gradient scale length is changed from L_T into L_n for comparison with the original Hasegawa-Mima equation. The original Hasegawa-Mima model (HM model) is derived from fluid equations for cold ions ($T_i \to 0$) with the adiabatic electron response, then the model describes the density gradient driven drift waves. In contrast to the original HM model, Eq. (3.17) is derived from the gyrokinetic equation for electrons with the adiabatic ion response and includes the electron temperature gradient η_e described by $ik_y(\eta_e k_\perp^2/2)\delta\psi_{k_\perp}$, which does not appeared in the cold-electron limit ($T_e \to 0$). Hereafter, an abbreviation for our model in Eq. (3.17) is denoted by "HM-η_e model" for convenience. Similar to the original HM model, the HM-η_e model also has no source driving linear instabilities.

Figure 3.11 shows the comparison of real frequencies for $k_x = 0$ between the linear ETG mode described by the gyrokinetic model and linear drift waves described by the HM-η_e model. The real frequency for the HM-η_e model is given by

$$\omega_L = \frac{-e^{-k_\perp^2}k_y}{1 + \tau - \Gamma_0(k_\perp^2)}\left(1 - \frac{\eta_e}{2}k_\perp^2\right)\,. \qquad (3.18)$$

We see that the real frequencies in HM-η_e model have negative values for the low wavenumber modes of $k_y \leqslant \sqrt{2/\eta_e} \simeq 0.447$ while the ETG modes have positive real frequencies for all modes. The negative frequency means that the direction of the mode propagation is opposite to that of the linear ETG modes. Indeed, as described in the previous section, the coherent vortex streets propagate in the negative y-direction.
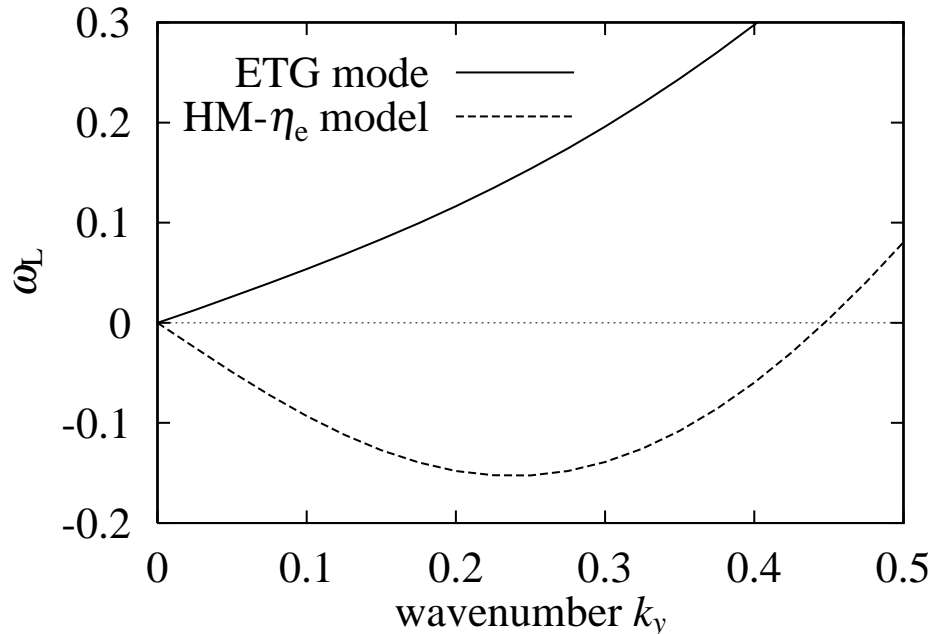
FIG. 3.11: Comparison of the real frequencies $\omega_L(k_x=0, k_y)$ between the linear ETG modes and HM-η_e model, where ω_L is normalized by v_{te}/L_n.

In the long wavelength limit of $k_\perp \rho_{te} \ll 1$, Eq. (3.17) is represented in the real space as follows:

$$\frac{\partial}{\partial t}\left\{\tau - (1+\tau)\nabla_\perp^2\right\}\delta\psi - \frac{\partial}{\partial y}\left(1 + \frac{\eta_e}{2}\nabla_\perp^2\right)\delta\psi - \left[\delta\psi,\, (1+\tau)\nabla_\perp^2\delta\psi\right] = 0\,, \qquad (3.19)$$

where the square brackets denote the Poisson brackets $[A, B] = (\partial_x A)(\partial_y B) - (\partial_x B)(\partial_y A)$. An isomorphic form to the original Hasegawa-Mima equation, which has an opposite sign of the drift frequency, is derived by taking a cold-electron limit $T_e \to 0$ and $\eta_e \to 0$. In analogy with the HM model having a traveling wave solution [27], e.g., isolated dipole vortices, one can derive a condition for the traveling wave solution of the HM-η_e equation in the long wavelength limit. Suppose the potential fluctuation of $\delta\psi = \delta\psi(x, y - ut)$ in Eq. (3.19) with constant traveling velocity parameter u, then the time derivative is replaced with the y-derivative, $\partial_t \delta\psi = -u\partial_y \delta\psi = [-ux, \delta\psi]$. After some simple algebra, one finds the following equation,

$$[S_1,\, S_2] \equiv \left[\nabla_\perp^2\delta\psi - \left(\frac{1+\tau u}{1+\tau}\right)x\,,\ \delta\psi - \left\{u - \frac{\eta_e}{2(1+\tau)}\right\}x\right] = 0\,. \qquad (3.20)$$

This condition shows that $\delta\psi$ is a traveling wave solution of the HM-η_e equation if there is a functional relation between S_1 and S_2, i.e., $S_1 = F(S_2)$ with an arbitrary function F. The analysis of the functional dependence on S_1 and S_2 is similar to that demonstrated in two-dimensional rotating fluid turbulence by Jung and Morrison $et\ al.$ [28]. They introduced a method of averaging
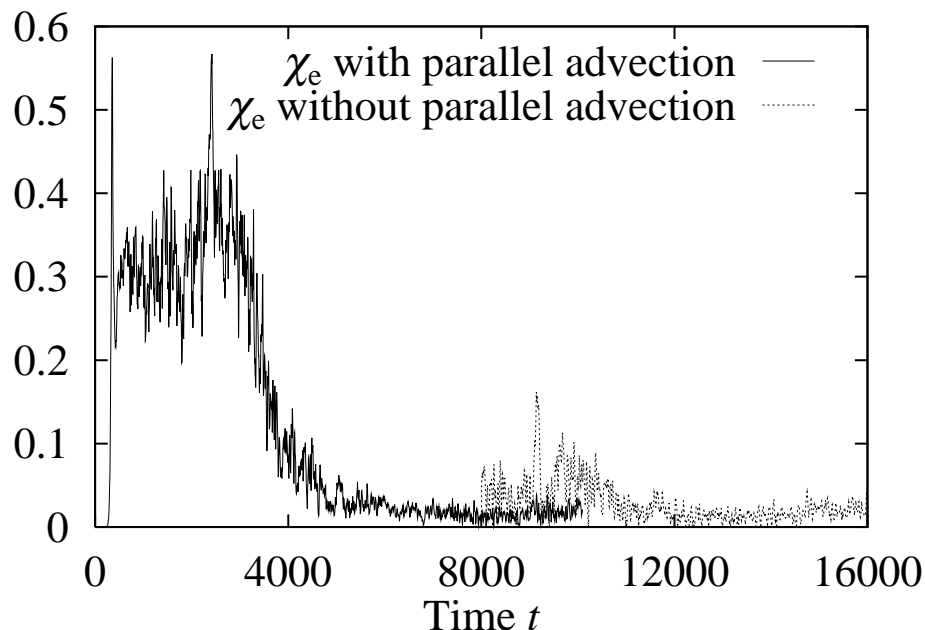
FIG. 3.12: Comparison of the time evolutions of χ_e with and without the parallel advection term.

the stream function that allows them to find the linear functional relation between the generalized vorticity and the stream function. In the present study, we investigate the functional relation between S_1 and S_2 as a measure for characterizing the coherent vortex streets to be a traveling wave solution of the HM-η_e equation.

3.4.2 Comparison between HM-η_e model and simulation results

In this section, the coherent vortex streets found in the gyrokinetic simulation for Case 2 is compared with the traveling wave solution of HM-η_e equation.

In order to confirm the validity for neglecting the parallel advection term in the derivation of HM-η_e model in Eq. (3.17) [or Eq. (3.19)] for the coherent vortex streets, we compare gyrokinetic simulation results for cases with and without the parallel advection term $ikv_\parallel \delta f_{k_\perp}$. Figure 3.12 shows the time evolution of χ_e, where the solid line is the same as that shown in Fig. 3.6 for Case 2. The dotted line corresponds to the result where the parallel advection term is artificially eliminated in the coherent state at $t = 8000$ and later. Although the initial increase of χ_e arisen from the discontinuity of the parallel advection term are observed for $8000 \leqslant t \leqslant 10000$, the long-time behavior of χ_e for $t \geqslant 10000$ shows the quite low transport level, which is the same level as that in the coherent state at around $t = 8000$ shown by the solid line.

Snapshots of vortex structures for the cases with and without the parallel advection term are

compared in Figs. 3.13(a) and 3.13(b), respectively, where the gyro-averaged potentials $\delta\psi$ are plotted by color contours. In Fig. 3.13(b), one finds that the vortex streets found in the coherent state at $t = 7800$ [Fig. 3.13(a)] sustain its spatial structure for a long time after eliminating the parallel advection term. Also, the vortices propagate in the negative y-direction, which is consistent with the negative real frequency for low wavenumber modes of the HM-η_e model. These results justify the neglect of the parallel advection term in the derivation of HM-η_e model for the coherent vortex streets. In addition, the propagation of the vortices keeping the spatial structure suggests that the coherent vortex streets are described by a traveling wave solution of Eq. (3.19).

Direct evaluations of the functional relation of S_1 and S_2 in Eq. (3.20) are shown in Figs. 3.14(a) and 3.14(b) for the nonlinear simulation results in Case 2, where the traveling velocity parameter $u \simeq -\pi/4$ is estimated from the simulation results. Here, we used simulation data taken from $+3\pi \leqslant x \leqslant +15\pi$ [see Fig. 3.13(a)] for the single vortex street on the right side of simulation domain, because the vortices on the left side propagate with slightly different speed. The puncture plots of S_1 versus S_2 in the turbulent ($t = 2400$) and coherent ($t = 7800$) states are shown in Fig. 3.14(a). A nonlinear functional relation between S_1 and S_2 are clearly found in the coherent state while the dot pattern broadens and looks disturbed in the turbulent state. The same plots are made for the simulation without the parallel advection term, which corresponds to a simulation of HM-η_e model [Fig. 3.14(b)]. One can see that the nonlinear functional relation, which is similar to that in the coherent state shown in Fig. 3.14(a), is apparently sustained for a long time. The puncture plot for the coherent state in Fig. 3.14(a) clearly shows the qualitative agreement with that in Fig. 3.14(b) even with a stronger curvature in the functional relation between S_1 and S_2. Therefore, it is concluded that the coherent vortex streets found in the slab ETG turbulence for Case 2, which leads to the transport reduction, is described by a traveling wave solution of the HM-η_e equation.

3.5 Concluding remarks

We have investigated the vortex structure and related transport reduction in the slab ETG turbulence by means of the gyrokinetic Vlasov simulation. The nonlinear simulations with high phase-space resolution enable us to examine the entropy balance relation, detailed structures of distribution function in the velocity-space and coherent vortex structures of fluid variables, e.g., potential and temperature fluctuations, which have rarely been discussed in earlier studies on ETG turbulence.

The evaluation of entropy balance relation in the slab ETG turbulence with a moderate linear
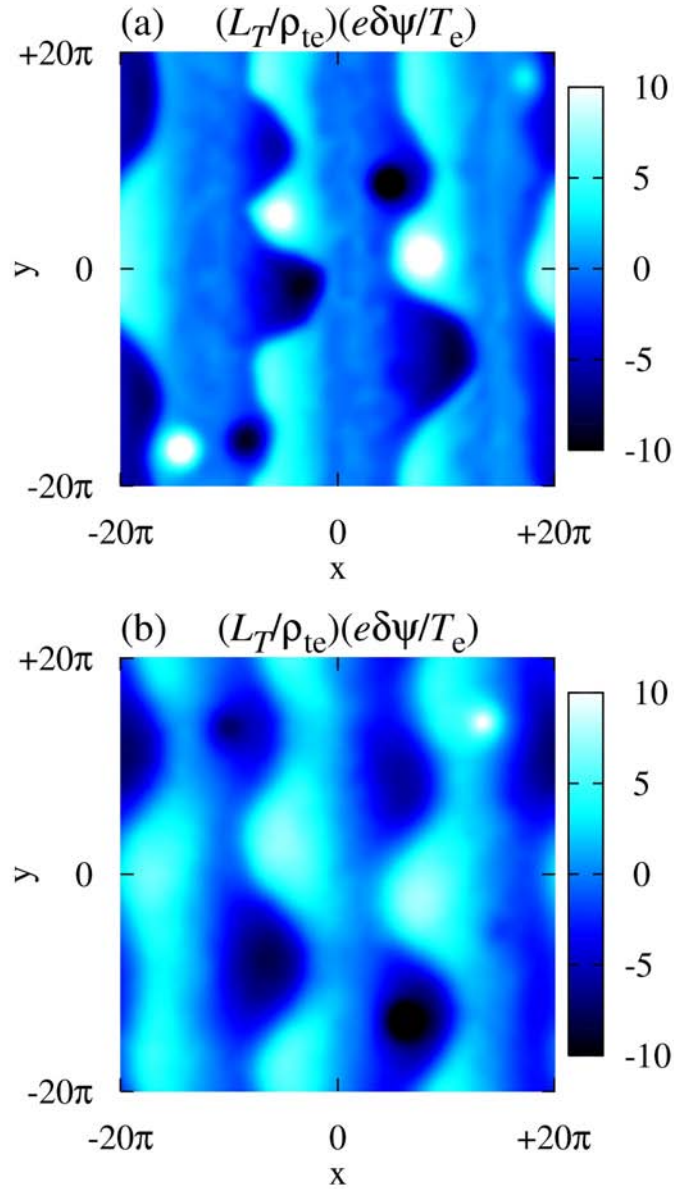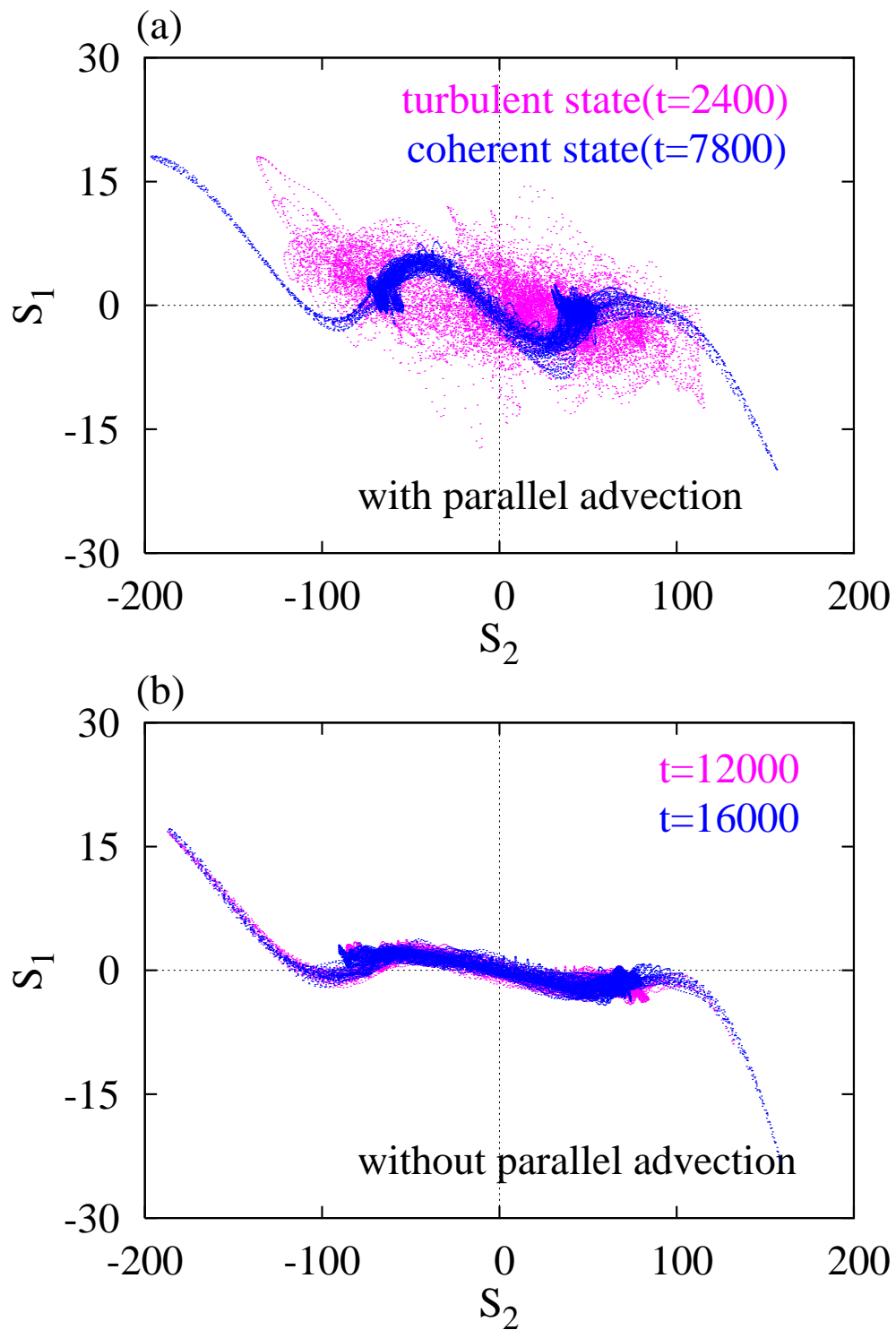
FIG. 3.13: Contours of the gyro-averaged potential with the parallel advection term at (a)$t = 7800$ and without one at (c)$t = 16000$.

growth rate (Case 1) shows that the turbulence reaches to the statistically steady state accompanied with weak zonal flow generations. Through the comparison of the slab ETG (with and without zonal flows) and the slab ITG turbulence simulations, it is found that the zonal flows driven by the slab ETG turbulence play a crucial role in suppressing the ($k_x = 0$, $k_y = k_{min}$)-mode and in realizing the steady transport. Formation of isolated vortices and their mergers with complicated motion are observed in the slab ETG turbulence while the slab ITG turbulence is dominated by strong zonal flows which completely suppress the turbulent transport.

In the slab ETG turbulence with larger growth rates (Case 2), we observed a transition of the vortex structure from a turbulent state with finer-scale fluctuations to a coherent state dominated by coherent vortex streets, which are composed of large-scale vortices and strong zonal flows. At the same time, the turbulent transport reduces to a quite low level which is less than the time-averaged χ_e in Case 1. The spectral analysis of $|\delta\phi_{k_\perp}|$, $|\delta T_{k_\perp}|$ and $|\chi_{ek_\perp}|$ in the wavenumber space shows that the transport reduction in the coherent state is mainly associated with a decrease of phase difference between $\delta\phi_{k_\perp}$ and $\delta T_{k_\perp}$, not with the reduction of the amplitudes. The transport reduction through the phase matching is confirmed more clearly by the velocity-space plots of $-\mathrm{Im}[\delta f_{k_\perp}/\delta\phi_{k_\perp}]$. The amplitude of $-\mathrm{Im}[\delta f_{k_\perp}/\delta\phi_{k_\perp}]$ is quite small in the coherent state while its profile in the turbulent state is qualitatively similar to the linear eigenfunction which drives large heat transport. Furthermore, the smallness of $-\mathrm{Im}[\delta f_{k_\perp}/\delta\phi_{k_\perp}]$ in the coherent state shows that the phase matching with $\delta\phi_{k_\perp}$ occurs not only for $\delta T_{k_\perp}$, but also for any n-th velocity moments of the perturbed distribution function, i.e., $\delta M_{k_\perp}^{(n)} \equiv \int dv_\parallel\, v_\parallel^n\, \delta f_{k_\perp}$.

In order to describe the coherent vortex streets, we have derived a fluid model from the gyrokinetic equation, where the velocity moment of the parallel advection term $\int dv_\parallel\, ik_\parallel v_\parallel \delta f_{k_\perp}$ is ignored. The validity of neglecting the parallel advection term in the derivation has been confirmed by comparisons of the nonlinear simulations. In addition to a formal similarity to the original Hasegawa-Mima equation, the HM-η_e model derived in Eq. (3.19) involves the electron temperature gradient term. By evaluating the functional relation of S_1 and S_2 [see Eq. (3.20)] from the nonlinear simulation results, it is concluded that the coherent vortex streets found in the slab ETG turbulence, which are related to the transport reduction, are explained by a traveling wave solution of HM-η_e equation.

FIG. 3.14: Puncture plots for S_1 versus S_2 given in Eq. (3.20), where the plots corresponds to the case (a)with and (b)without the parallel advection term, respectively.

Bibliography for Chapter 3

[1] W. Horton, Rev. Mod. Phys. **71**, 735 (1999)

[2] A. M. Dimits, G. Bateman, M. A. Beer, B. I. Cohen, W. Dorland, G. W. Hammett, C. Kim, J. E. Kinsey, M. Kotschenreuther, A. H. Kritz, L. L. Lao, J. Mandrekas, W. M. Nevins, S. E. Parker, A. J. Redd, D. E. Shumaker, R. Sydora, and J. Weiland, Phys. Plasmas **7**, 969 (2000)

[3] P. H. Diamond and S. -I. Itoh, K. Itoh, and T. S. Hahm, Plasma. Phys. Control. Fusion **47**, R35 (2005)

[4] B. W. Stallard, C. M. Greenfield, G. M. Staebler, C. L. Rettig, M. S. Chu, M. E. Austin, D. R. Baker, L. R. Baylor, K. H. Burrell, J. C. DeBoo, J. S. deGrassie, E. J. Doyle, J. Lohr, G. R. McKee, R. L. Miller, W. A. Peebles, C. C. Petty, R. I. Pinsker, B. W. Rice, T. L. Rhodes, R. E. Waltz, L. Zeng, and The DIII-D Team, Phys. Plasmas. **6**, 1978 (1999)

[5] H. Shirai, M. Kikuchi, T. Takizuka, T. Fujita, Y. Koide, G. Rewoldt, D. Mikkelsen, R. Budny, W. M. Tang, Y. Kishimoto, Y. Kamada, T. Oikawa, O. Naito, T. Fukuda, N. Isei, Y. Kawano, M. Azumi, and JT-60 Team, Nucl. Fusion **39**, 1713 (1999)

[6] F. Jenko, W. Dorland, M. Kotschenreuther, and B. N. Rogers, Phys. Plasmas **7**, 1904 (2000)

[7] W. Dorland and G. W. Hammett, Phys. Fluids B **5**, 812 (1993)

[8] Y. Idomura, S. Tokuda, and Y. Kishimoto, Nucl. Fusion **45**, 1571 (2005)

[9] J. Candy, R. E. Waltz, M. R. Fahey, and C. Holland, Plasma. Phys. Control. Fusion **49**, 1209 (2007)

[10] W. M. Nevins, S. E. Parker, Y. Chen, J. Candy, A. Dimits, W. Dorland, G. W. Hammett, and F. Jenko, Phys. Plasmas **14**, 084501 (2007)

[11] W. M. Nevins, J. Candy, S. Cowley, T. Dannert, A. Dimits, W. Dorland, C. Estrada-Mila, G. W. Hammett, F. Jenko, M. J. Pueschel, and D. E. Shumaker, Phys. Plasmas **13**, 122306 (2006)

[12] Z. Lin, I. Holod, L. Chen, P. H. Diamond, T. S. Hahm, and S. Ethier, Phys. Rev. Lett. **99**, 265003 (2007)

[13] J. Li, Y. Kishimoto, N. Miyato, T. Matsumoto, and J. Q. Dong, Nucl. Fusion **45**, 1293 (2005)

[14] Y. Idomura, M. Wakatani, and S. Tokuda, Phys. Plasmas **7**, 3551 (2000)

[15] Y. Idomura, Phys. Plasmas **13**, 080701 (2006)

[16] T. Matsumoto, J. Li, and Y. Kishimoto, Nucl. Fusion **47**, 880 (2007)

[17] T. Matsumoto, Y. Kishimoto, N. Miyato, and J. Q. Li, J. Plasma Phys. **72**, 1183 (2006)

[18] J. Li and Y. Kishimoto, Phys. Plasmas **15**, 112504 (2008)

[19] T.-H. Watanabe and H. Sugama, Nucl. Fusion **46**, 24 (2006)

[20] T.-H. Watanabe and H. Sugama, Phys. plasmas **11**, 1476 (2004)

[21] T.-H. Watanabe and H. Sugama, Phys. plasmas **9**, 3659 (2002)

[22] H. Sugama, T.-H. Watanabe, and W. Horton, Phys. plasmas **10**, 726 (2003)

[23] H. Sugama, M. Okamoto, W. Horton, and M. Wakatani, Phys. Plasmas **3**, 2379 (1996)

[24] J. A. Krommes and G. Hu, Phys. Plasmas **1**, 3211 (1994)

[25] A. Hasegawa and K. Mima, Phys. Fluids **21**, 87 (1978)

[26] T. Klinger, C. Schröder, D. Block, F. Greiner, A. Piel, G. Bonhomme, and V. Naulin, Phys. Plasmas **8**, 1961 (2001)

[27] W. Horton and Y.-H. Ichikawa, "Chaos and Structures in Nonlinear plasmas", World Scientific, Singapore, (1996)

[28] S. Jung, P. J. Morrison, and H. L. Swinney, J. Fluid Mech. **554**, 433 (2006)

Chapter 4

Effects of parallel dynamics on transition of vortex structures

4.1 Introduction

Electron temperature gradient (ETG) modes are more recently investigated theoretically and numerically as a main cause of the anomalous electron heat transport [1–9]. The ETG turbulence inherently involves various vortex structures, such as turbulent vortices, zonal flows, and radially elongated streamers, which strongly depend on geometrical and plasma parameters, due to the weakness of the zonal flow generation. Especially, the nonlinear dynamics of streamers, which may lead to substantial enhancement of the heat transport in toroidal systems, has been actively pursued [1, 3, 6, 9]. Nevertheless, the detailed physical mechanism of the saturation of the toroidal ETG instability growth and the dependence on the magnetic shear are still open problem, as well as the precise estimation of resultant transport level. From the aspect of the turbulence-control with regulating the electron heat transport in the future burning plasmas, of which the electrons are preferentially heated by the collision with high-energy α-particles, it is worthwhile to understand fundamental physics behind the formation of vortex structures including zonal flows and its stability as well as the related transport properties.

In Chap. 2, we have investigated vortex structures in the slab ETG turbulence as well as velocity-space structures of the distribution function by means of the gyrokinetic Vlasov simulations with high phase-space resolution, and have found the formation of coherent vortex streets accompanied with the significant transport reduction in the nonlinear phase. Detailed analysis of the distribution function clarified that the transport reduction is associated with the phase matching between the potential and temperature fluctuations rather than the reduction of the fluctuation amplitude. Furthermore, we have revealed that a traveling wave solution of a Hasegawa-Mima

51

type equation derived from the gyrokinetic equation for electrons describes well the coherent vortex streets found in the turbulence simulation.

In this chapter, a comprehensive parameter study of the slab ETG turbulence is carried out by means of the nonlinear gyrokinetic Vlasov simulations, with the aim of elucidating underlying physical mechanisms of the transition of vortex structures from turbulent to coherent ones, which is closely associated with the zonal-flow generation, and the related transport reduction. Especially, the dependence on the magnitude of the parallel compression, which causes couplings with the higher-order fluid moments, and the electron temperature gradient is intensively examined. The detailed analyses reveal a critical condition of the transition of vortex structures associated with the parallel dynamics, and may provide ones an useful insight into the turbulence-control. Although the present study is limited to the two-dimensional slab system, it also contributes to deeper understanding of the toroidal ETG turbulence. Actually, in the neighborhood of the minimum-q surface (q denotes the safety factor) of the toroidal system with a reversed magnetic shear profile, the effect of the parallel compression becomes more important in a weak magnetic shear region where the magnetic drift frequency decreases. and then the slab ETG modes may be destabilised as well as the toroidal ones [5–8].

In the latter part of this chapter, we discuss the dependence of zonal flow generation on the magnitude of the parallel compression based on the modulational instability analysis with a truncated fluid model, where the parallel dynamics such as acoustic modes is taken into account. This is an extension of the conventional modulational instability analysis by means of the Hasegawa-Mima type model [9–13].

The remainder of this chapter is organized as follows. A physical parameters and linear properties of the present ETG turbulence simulations are described in Sec. 4.2. Nonlinear simulation results of the slab ETG turbulence are presented in Sec. 4.3. Then, we discuss in detail the transition of vortex structures, which is closely associated with the zonal flow generation, as well as the related transport properties. In order to find qualitative understanding of the transition of vortex structures, the modulational instability analysis is carried out in Sec. 4.4, where the dependence of the zonal flow growth rate on the magnitude of the parallel compression is compared with the turbulence simulation results. Finally, concluding remarks are given in Sec. 4.5.

4.2   Physical parameters and linear properties

Gyrokinetic model considered here is the same as that used in the previous section. For convenience, governing equations for the slab ETG turbulence simulations are again given here [cf. Sec. 3.2]. The electrostatic gyrokinetic equation for the perturbed distribution function $\delta f_{k_\perp}(v_\parallel, t)$

written in the wavenumber space is given as

$$\left(\frac{\partial}{\partial t} + ik_\parallel v_\parallel\right)\delta f_{k_\perp} - \frac{c}{B}\sum_\Lambda \boldsymbol{b}\cdot(\boldsymbol{k}'_\perp \times \boldsymbol{k}''_\perp)\,\delta\psi_{k'_\perp}\delta f_{k''_\perp} - C_\parallel(\delta f_{k_\perp})$$

$$= -i\left\{\omega_{*e}\left[1 + \eta_e\left(\frac{m_e v_\parallel^2}{2T_e} - \frac{1}{2} - \frac{k_\perp^2\rho_{te}^2}{2}\right)\right] - k_\parallel v_\parallel\right\}F_{M\parallel}\frac{e\delta\psi_{k_\perp}}{T_e}. \quad (4.1)$$

We introduce a dimensionless parameter Θ associated with the tilt angle of magnetic field lines, $\Theta \equiv k_\parallel L_T/k_y\rho_{te} = \theta L_T/\rho_{te}$. The tilt angle parameter Θ reflects the magnitude of the parallel advection (or the parallel compression) term in proportion to $k_\parallel$, and turns out to be an important parameter for the transition of the vortex structures in the slab ETG turbulence as discussed in Sec. 4.3.

The electrostatic potential fluctuation is determined by the quasineutrality condition with the adiabatic ion response given as follows,

$$\int dv_\parallel\,\delta f_{ek_\perp} = -n_0\Lambda_{k_\perp}\frac{e\delta\psi_{k_\perp}}{T_e}, \quad (4.2)$$

where $\Lambda_{k_\perp} \equiv \exp(k_\perp^2\rho_{te}^2)[1 + \tau - \Gamma_0(k_\perp^2\rho_{te}^2)]$ with $\tau \equiv T_e/T_i$.

Using the closed set of equations described above, the entropy balance equation is derived as follows,

$$\frac{d}{dt}(\delta S + W) = L_T^{-1}Q_e + D, \quad (4.3)$$

where $\delta S \equiv \sum_{k_\perp}\int dv_\parallel|\delta f_{k_\perp}|^2/2F_{M\parallel}$, $W \equiv \sum_{k_\perp}(n_0/2)[1+\tau-\Gamma_0^e]|e\delta\phi_{k_\perp}/T_e|^2 = \sum_{k_\perp}(n_0/2)\Lambda_{k_\perp}|e\delta\psi_{k_\perp}/T_e|^2$, $L_T^{-1}Q_e \equiv L_T^{-1}\sum_{k_\perp}(c/B)\,\mathrm{Re}[ik_y\delta\psi_{k_\perp}\int dv_\parallel(m_e v_\parallel^2/T_e - 1)\delta f_{k_\perp}^*/2]$, and $D \equiv \sum_{k_\perp}\mathrm{Re}\int dv_\parallel C_\parallel(\delta f_{k_\perp})\delta f_{k_\perp}^*/F_{M\parallel}$ denote the entropy variable, the potential energy, the entropy production due to the turbulent heat flux driven by the electron temperature gradient (thermodynamic force), and the collisional dissipation, respectively. It is confirmed that, for all the turbulence simulation results discussed below, the entropy balance relation is accurately satisfied within an error less than 0.5% of the mean collisional dissipation level.

The linear growth rate and the real frequency of the ETG modes depends on the collision frequency ν_e, the temperature ratio τ, the electron temperature gradient parameter η_e, and the tilt angle parameter Θ. Using Eqs. (4.1) and (4.2), the dispersion relation of the linear ETG mode is given by

$$1 + \Lambda_{k_\perp} - \frac{\zeta}{\sqrt{2}\Theta} - \left[\frac{\zeta^2}{\sqrt{2}\Theta} - \zeta + \frac{1}{\sqrt{2}\Theta}\left\{1 - \frac{\eta_e}{2}\left(1+k_\perp^2\rho_{te}^2\right)\right\}\right]Z(\zeta) = 0, \quad (4.4)$$

where ζ is defined as $\zeta \equiv \omega/\sqrt{2}k_\parallel v_{te}$ with a complex frequency ω. The plasma dispersion function is denoted by $Z(\zeta) \equiv i\sqrt{\pi}\exp(-\zeta^2)(1 + \mathrm{Erf}(i\zeta))$ in terms of the error function $\mathrm{Erf}(z)$. Since the collision frequency is set to be sufficiently small here ($\nu_e L_T/v_{te} = 2.0\times10^{-4}$), the effect of the

collisionality is neglected in the above dispersion relation. Also, the temperature ratio τ is fixed to unity so that the independent physical parameters are η_e and Θ in the present study discussed in detail below.

Figure 4.1 shows the contour of the maximum growth rate of the linear ETG modes $\gamma_{L(max)}$ on the two-dimensional (η_e, Θ)-space. Here, the parameter sets used in the turbulence simulations are also plotted with solid circular symbols. One finds that, in the normalization with L_T, the maximum growth rate $\gamma_{L(max)}$ has weak dependence on η_e, whereas it has stronger dependence on Θ. From this point of view, we have carried out the parameter scan of the ETG turbulence for $\eta_e \geqslant 6$ with focusing on the dependence on Θ. In the present parameter study, 45 nonlinear gyrokinetic simulations have been carried out in total [12 runs for $\eta_e = 6$ and 11 runs for $\eta_e = \{7, 8, 9\}$].

The k_y-spectra of the linear growth rate γ_L for $\eta_e = 6$ are shown in Fig. 4.2, where $\Theta = \{0.033, 0.050, 0.133, 0.150, 0.200\}$ are chosen as five representative cases. Here, we set $k_x = 0$ because the finite k_x has a stabilizing effect. From this figure, one can see that the parameter Θ is related to not only the magnitude of the growth rate, but also the width of unstable region in the k_y-space.
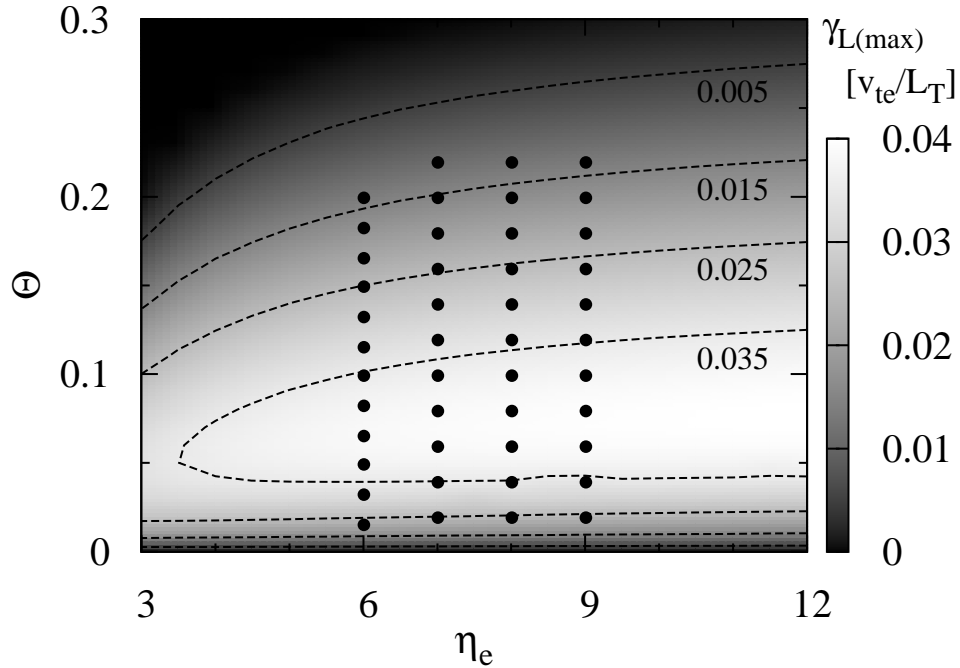

FIG. 4.1: Contour of the maximum linear growth rate $\gamma_{L(max)}$ of linear ETG modes with respect to η_e and Θ. Circular symbols represent the parameter sets used in turbulence simulations shown in Sec. 4.3.

In the nonlinear gyrokinetic simulations, physical quantities are normalized as $x = x'/\rho_{\text{te}}$, $y = y'/\rho_{\text{te}}$, $v_\| = v_\|'/v_{\text{te}}$, $t = t'v_{\text{te}}/L_T$, $\nu_e = \nu_e' L_T/v_{\text{te}}$, $F_{\text{M}\|} = F_{\text{M}\|}' v_{\text{te}}/n_0$, $\delta f_{\boldsymbol{k}_\perp} = \delta f_{\boldsymbol{k}_\perp}' L_T v_{\text{te}}/\rho_{\text{te}} n_0$ and $\delta\phi_{\boldsymbol{k}_\perp} = e\delta\phi_{\boldsymbol{k}_\perp}' L_T/T_e \rho_{\text{te}}$, where the prime means a dimensional quantity. The number of Fourier modes in the two-dimensional wavenumber space and the grids on the $v_\|$-space are set to be $(N_{k_x}, N_{k_y}, N_{v_\|}) = (129, 257, 2049)$. The range of the wavenumbers k_x, k_y and the $v_\|$-coordinate are $0 \leqslant k_x \leqslant k_{\max}$, $-k_{\max} \leqslant k_y \leqslant k_{\max}$ and $-v_{\max} \leqslant v_\| \leqslant v_{\max}$ with $k_{\max} = 12.8$ and $v_{\max} = 10$, respectively. The size of the simulation domain is set to be a square with $L_x = L_y = 20\pi\rho_{\text{te}}$, then the non-zero minimum absolute value of the wavenumber is $k_{\min} = 0.1$. The initial condition for the distribution function is given by the Maxwellian distribution with a small amplitude of 10^{-6} and random phases.

4.3 Nonlinear simulations

4.3.1 Dependence of vortex structures on parallel compression

Results of the parameter study with respect to η_e and Θ on the nonlinear gyrokinetic simulations are shown and discussed here. The results for $\Theta = \{0.033, 0.050, 0.133, 0.150, 0.200\}$ with $\eta_e = 6$ are selected as representative cases, where the growth rates of linear ETG modes are shown in
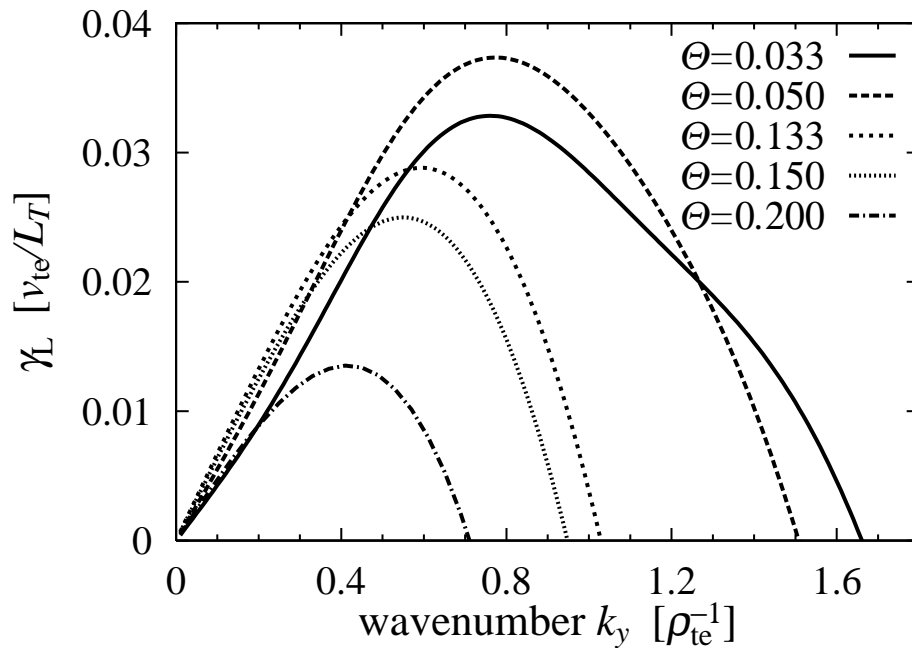

FIG. 4.2: Growth rates γ_L of linear ETG modes for $\Theta = \{0.033, \ 0.050, \ 0.133, \ 0.150, \ 0.200\}$, where $\eta_e = 6$ and $k_x = 0$.

TABLE 4.1: Time averaged heat diffusivity in the early and late nonlinear phases.

Θ	$\overline{\chi_e^<}$ $[\rho_{te}^2 v_{te}/L_T]$	$\overline{\chi_e^>}$ $[\rho_{te}^2 v_{te}/L_T]$	types of evolution
0.033	1.99×10^{-1}	1.01×10^{-2}	transitional
0.050	1.38×10^{-1}	3.55×10^{-3}	transitional
0.133	6.37×10^{-2}	1.23×10^{-2}	steady
0.150	6.84×10^{-2}	2.47×10^{-2}	steady
0.200	1.17×10^{-2}	2.29×10^{-3}	suppressed

Fig. 4.2. The other cases including the results for $\eta_e = \{7, 8, 9\}$ are also summarized in Sec. 4.3.2.

Figures 4.3(a) and 4.3(b) show time evolution of the heat diffusivity χ_e $(= Q_e)$ for the representative cases. (Note that $\chi_e' \equiv Q_e'/(n_0 L_T^{-1})$ is reduced to $\chi_e = Q_e$ in terms of the normalization with L_T, where the prime means dimensional quantities.) The initial perturbation linearly grows due to the ETG instability until the nonlinear saturation takes place. Then, one clearly finds the different behavior of χ_e depending on the value of Θ in nonlinear phases. Transition of the turbulence accompanied with the transport reduction for $t \gtrsim 1000$ is observed in the cases of $\Theta = \{0.033, 0.050\}$ [Fig. 4.3(a)] while the steady transport is sustained in the cases of $\Theta = \{0.0133, 0.150\}$ [Fig. 4.3(b)]. For the case of $\Theta = 0.200$ [Fig. 4.3(b)], we find that the turbulent transport is almost completely suppressed in the nonlinear phase. The significant suppression of the transport for $\Theta = 0.200$ is similar to that observed in the ITG turbulence simulations with L_T^{-1} below the nonlinearly upshifted critical gradient (Dimits-shift) [14, 15]. The heat diffusivity for the above cases are summarized in Table 4.1, where $\overline{\chi_e^<}$ and $\overline{\chi_e^>}$ denote the time-averaged values taken for an early (immediately after the saturation of linear ETG modes, e.g., $500 \leqslant t \leqslant 1300$ for $\Theta = 0.033$) and a late (e.g., $t \leqslant 2500$) nonlinear phases, respectively. Here, the fixed time-interval $\Delta t_{ave} = 750$ is used for the time-averages.

It is expected that the different behavior of the heat diffusivity discussed above is closely related to the zonal flow generation. The time evolution of the zonal flow potential energy normalized by the total one W, i.e., W_{zf}/W, is shown in Fig. 4.4(a) and 4.4(b), where W_{zf} represents the zonal flow component of W. It should be emphasized that after the initial saturation of the zonal flow growth ($t \gtrsim 1000$), the subsequent generation of the zonal flow to a higher level is found in the cases of $\Theta = \{0.033, 0.050\}$ [Fig. 4.4(a)], while the zonal-flow amplitude remains almost constant for the other cases [Fig. 4.4(b)]. The secondary growth of the zonal flow shows the clear correlation with the transport reduction found in the late nonlinear phase, as shown in
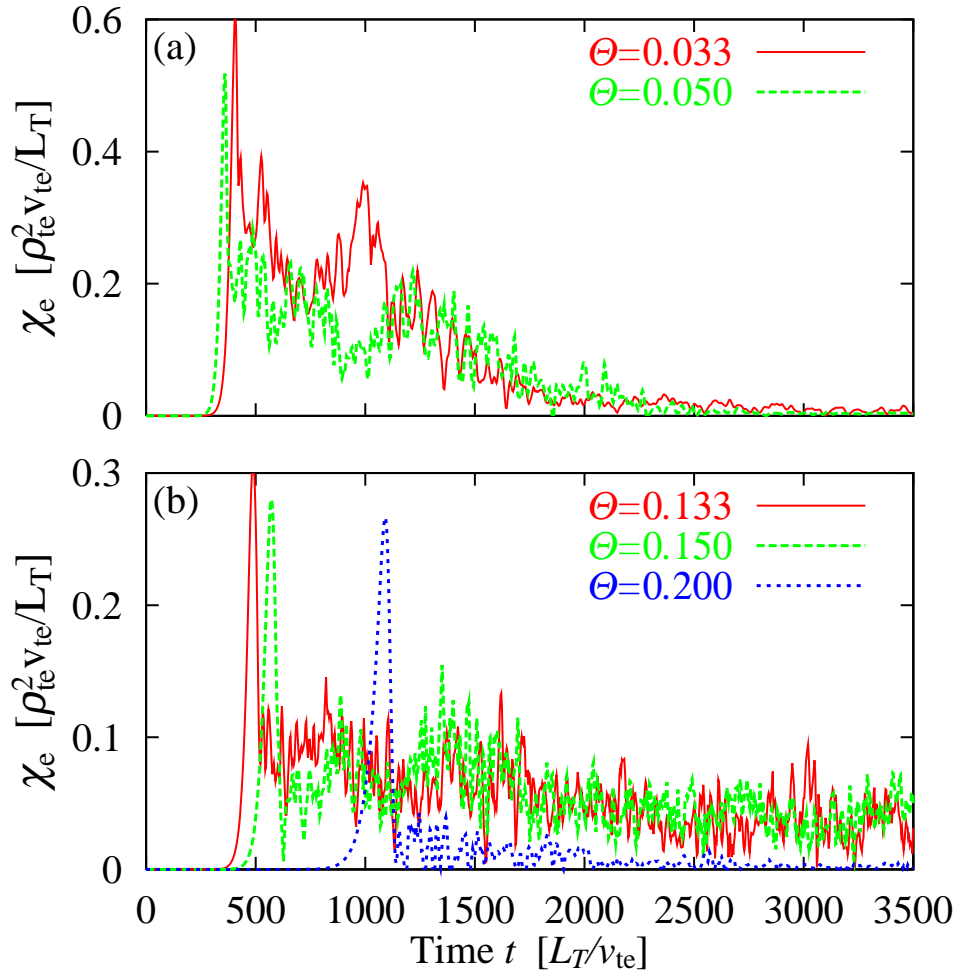
FIG. 4.3: Time evolution of the heat diffusivity χ_e for (a)$\Theta = \{0.033, 0.050\}$ and (b)$\Theta = \{0.133, 0.150, 0.200\}$, where $\eta_e = 6$.

Fig. 4.3(a). The other cases plotted in Fig. 4.4(b) are also correlated to the steady behavior of χ_e shown in Fig. 4.3(b). In addition, in the case of $\Theta = 0.2000$, we see the strong generation of the zonal flow which is responsible for the significant transport reduction at the saturation of the instability growth. The secondary growth of the zonal flow depending on Θ will be discussed in detail in Sec. 4.4 by means of the modulational instability analysis with a truncated fluid model.

The power spectra of potential and temperature fluctuations in the cases of $\Theta = \{0.050, 0.150, 0.200\}$ are shown in Figs. 4.5(a) – (c), respectively, where the quantities are summed over k_x-components and are time-averaged in the early and the late nonlinear phases. Here, the temperature fluctuation is defined by $\delta T_{k_\perp} \equiv \int dv_\parallel (v_\parallel^2 - 1) \delta f_{k_\perp}$. The case of $\Theta = 0.050$ [Fig. 4.5(a)] shows the significant reduction of higher wavenumber components of $|\delta \psi_{k_y}|$ and $|\delta T_{k_y}|$ in the late nonlinear
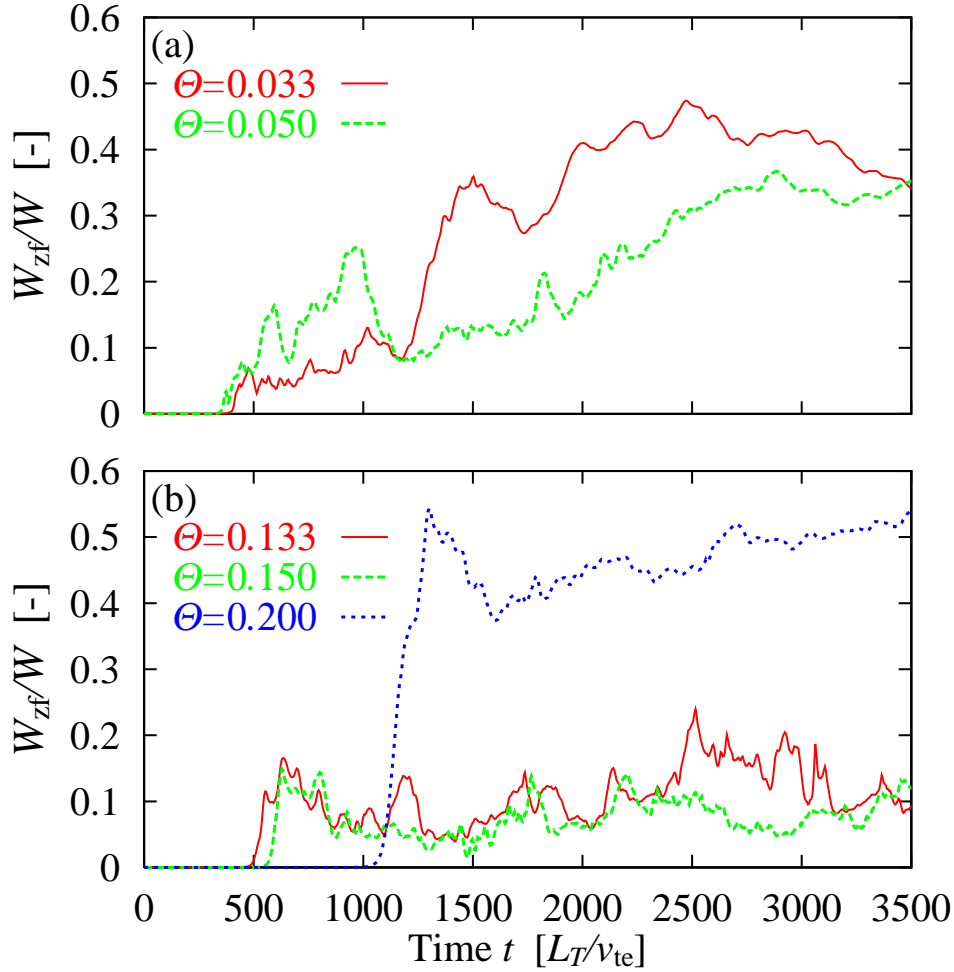
FIG. 4.4: Time evolution of normalized energy of zonal flows W_{zf}/W for (a)$\Theta = \{0.033,\ 0.050\}$ and (b)$\Theta = \{0.133,\ 0.150\ , 0.200\}$, where $\eta_{\mathrm{e}} = 6$.

phase in comparison with those in the early phase. Thus, the transitional behavior is expected to appear not only for the heat diffusivity, but also for potential and temperature fluctuation profiles in the real space in similar to Figs. 3.8. On the other hand, no significant change in the spectrum is observed for the two phases in the case of $\Theta = 0.150$ [Fig. 4.5(b)]. This is consistent with the steady behavior of the heat diffusivity as shown in Fig. 4.3(b). The case of $\Theta = 0.200$ [Fig. 4.5(c)] also shows similar spectrum, while, the amplitudes of $|\delta T_{k_y}|$ and $|\delta \psi_{k_y}|$ are smaller than those in the case of $\Theta = 0.150$. This implies that the strong zonal flow generation in the case of $\Theta = 0.200$ [see Fig. 4.4(b)] suppress the development of turbulent fluctuations.

Color contours of potential and temperature fluctuations in the real space at $t = 3480$ are shown in Figs. 4.6(a) – (e), and Figs. 4.6(f) – (j), respectively. Depending on Θ, three different types of vortex structures are clearly observed in the late nonlinear phase, i.e., coherent vortex
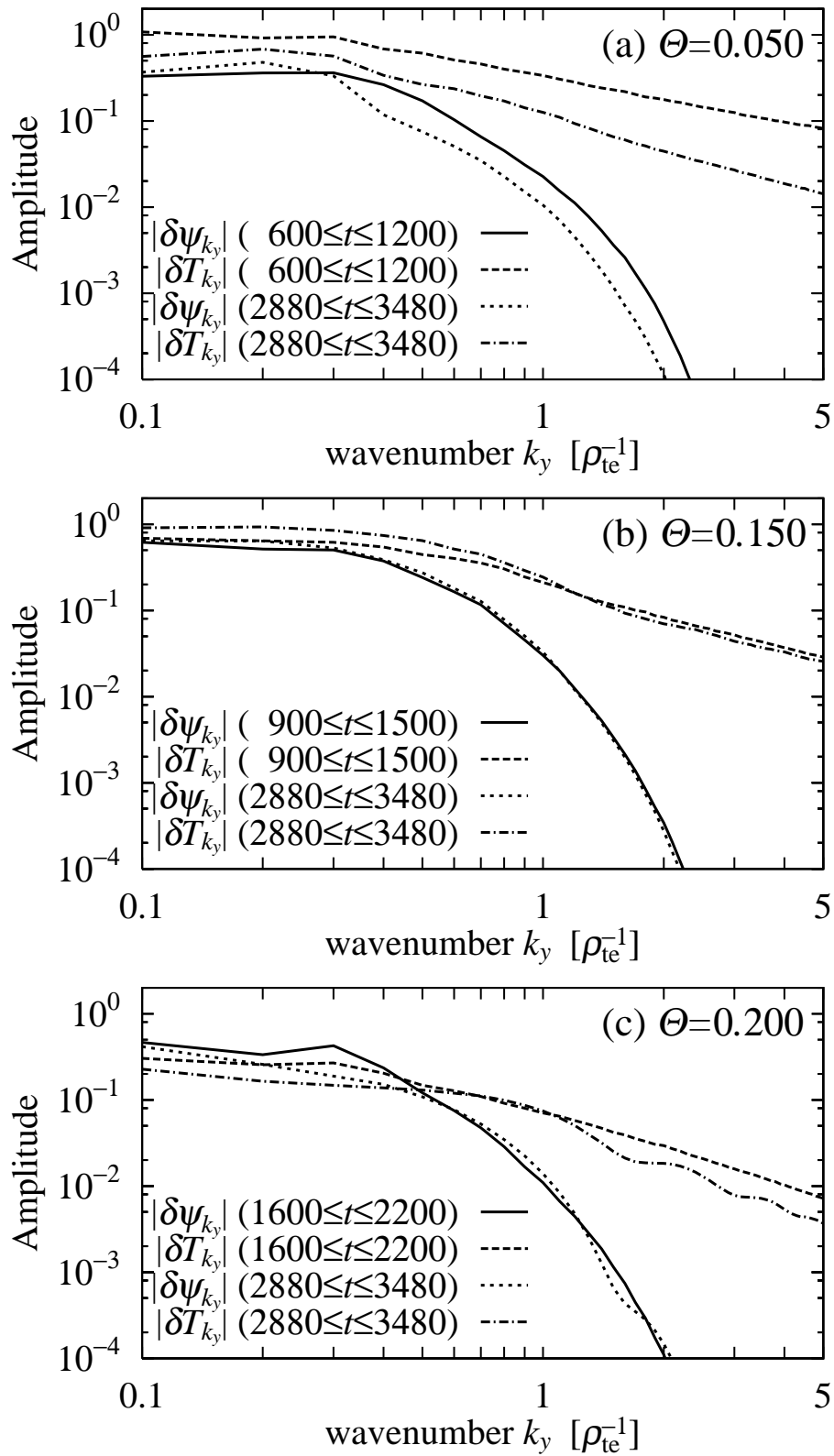
FIG. 4.5: Power-spectra of $|\delta\psi_{\mathbf{k}_\perp}|$ and $|\delta T_{\mathbf{k}}|$ for (a)$\Theta = 0.050$, (b)$\Theta = 0.150$ and (c)$\Theta = 0.200$, where the quantities are summed over k_x. Each line in the figures shows the results with different time-intervals. The units of $|\delta\psi_{k_y}|$ and $|\delta T_{k_y}|$ are $T_e\rho_{te}/eL_T$ and $T_e\rho_{te}/L_T$, respectively.

streets [(a), (b), (f) and (g)], turbulent vortices [(c), (d), (h) and (i)], and zonal-flow-dominated states [(e) and (j)]. It should be noted here that the coherent vortex streets, which appear in the cases of smaller value of $\Theta \lesssim 0.1$, are formed by the transition from turbulent vortices found in the early nonlinear phase, while no transition is observed for the other cases. The formation of the coherent vortex streets is associated with the phase matching of $\delta\phi$ and δT, where the heat transport is significantly reduced. On the other hand, for the cases of the turbulent vortices with $\Theta = \{0.133, \ 0.150\}$, the temperature fluctuations involve much finer scale structures than those in the potential fluctuations. We have verified that the transition of vortex structures, which depends on Θ, is commonly observed for the other cases with $\eta_e = \{7, \ 8, \ 9\}$.

Let us consider a quantity that represents the effect of the parallel compression on the formation of coherent vortex structures. From the Eqs. (4.1) and (4.2), one can derive the fluid equation for the potential fluctuations $\delta\psi_{k_\perp}$ as follows,

$$\frac{\partial}{\partial t}\Lambda_{k_\perp}\delta\psi_{k_\perp} - i\Theta k_y \delta u_{k_\perp} - ik_y\left(\frac{1}{\eta_e} - \frac{k_\perp^2}{2}\right)\delta\psi_{k_\perp} - \sum_{\Lambda} \boldsymbol{b}\cdot(\boldsymbol{k}_\perp' \times \boldsymbol{k}_\perp'')\,\delta\psi_{k_\perp'}\Lambda_{k_\perp''}\delta\psi_{k_\perp''} = 0, \qquad (4.5)$$

where the normalized quantities are used. The parallel flow is defined by $\delta u_{k_\perp} \equiv \int dv_\parallel v_\parallel \delta f_{k_\perp}$. Equation (4.5) is reduced to the Hasegawa-Mima like equation (designated as HM-η_e equation in Sec. 3.4) in the limit of $\Theta \to 0$ and the long-wavelength approximation, where the terms up to $O(k_\perp^2)$ are kept. Here, we define a quantity representing a relative magnitude of the parallel compression term (the second term) to the diamagnetic drift term (the third term) in Eq. (4.5), i.e., $\mathcal{R} \equiv \eta_e\Theta\sum_{k_\perp}\mathrm{Re}[\delta u_{k_\perp}\delta\psi_{k_\perp}^*]/\sum_{k_\perp}|\delta\psi_{k_\perp}|^2$. From the turbulence simulation results, it is found that $\overline{\mathcal{R}} \simeq 0.33$ for $\Theta = 0.050$, $\overline{\mathcal{R}} \simeq 0.87$ for $\Theta = 0.150$, and $\overline{\mathcal{R}} \simeq 1.41$ for $\Theta = 0.200$, where the time-average is taken for $2500 \leqslant t \leqslant 3500$. The small value of $\overline{\mathcal{R}}$ for $\Theta = 0.050$ suggests that the coherent vortex streets are approximately described by a traveling wave solution of the HM-η_e equation derived from Eq. (4.5) in the limit of $\Theta \to 0$, as discussed in Sec. 3.4.2. In contrast, for the cases with relatively larger Θ or $\overline{\mathcal{R}}$, the Hasegawa-Mima model is no longer valid. Thus, the effect of the finite parallel compression, which causes couplings with the higher-order fluid moments through electrostatic acoustic modes, becomes more important.

Comparisons of the power spectrum of the distribution function $\delta f_{k_\perp}$ in the velocity-space for the different Θ give us another physical insight into the different turbulence structures. Following the works of Watanabe and Sugama [see Ref. 20 and 21], we introduce the Hermite expansion of the distribution function, i.e., $\delta f_{k_\perp}(v_\parallel) = \sum_n \varphi_{k_\perp,n}H_n(v_\parallel)F_{M\parallel}(v_\parallel)$, where H_n denotes the Hermite polynomial of the order n. Note that the nth order coefficient of the Hermite expansion $\varphi_{k_\perp,n} = \int dv_\parallel H_n(v_\parallel)\delta f_{k_\perp}/n!$ represents not only the amplitude of the nth-order fluid moment, but also the structure of $\delta f_{k_\perp}$ in the $v_\parallel$-space (n is related to the usual Fourier wavenumber l in the $v_\parallel$-space with $n \sim l^2$ for $n \gg 1$), The Hermite expansion applied to the entropy balance equation in Eq.
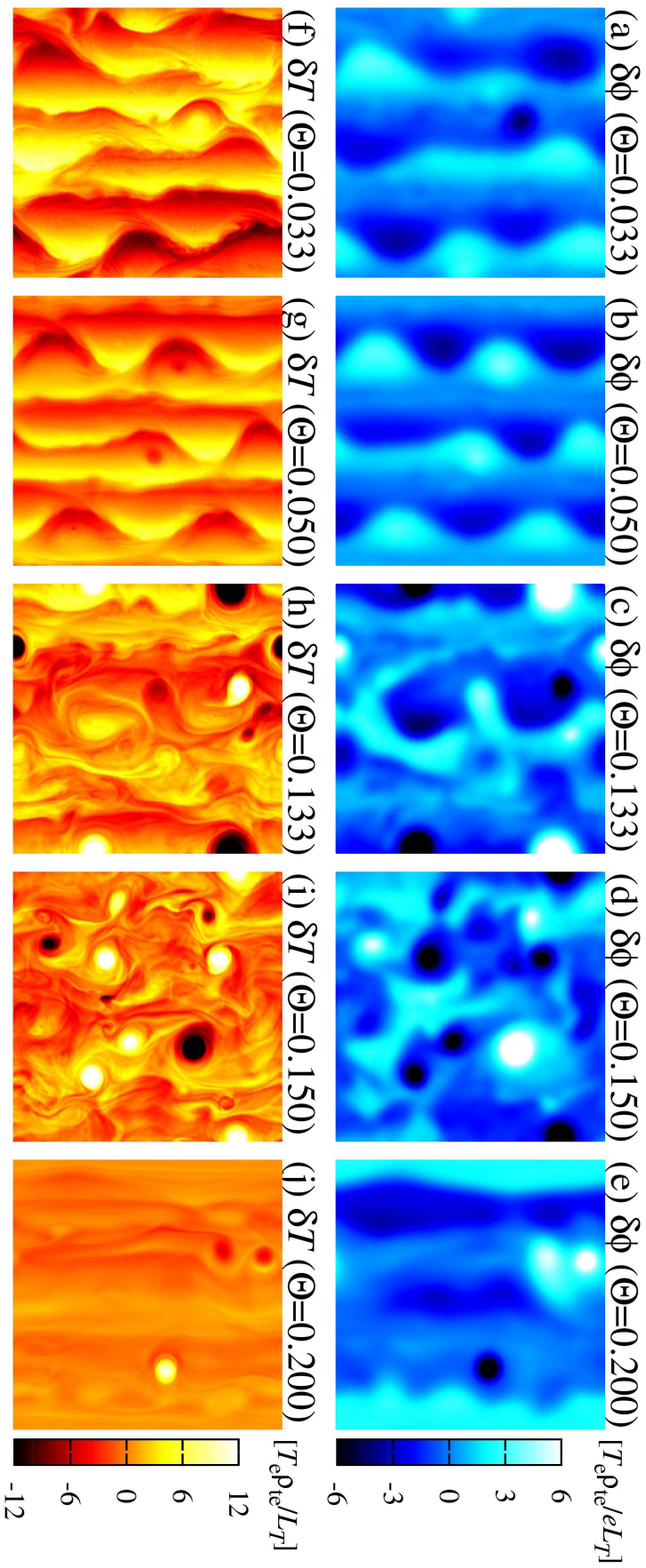
FIG. 4.6: Contours of [(a) − (e)]potential and [(f) − (j)]temperature fluctuations for $\Theta = \{0.033, 0.050, 0.133, 0.150, 0.200\}$ at $t = 3480$, where the box size is $20\pi\rho_{te} \times 20\pi\rho_{te}$.

(4.3) leads to

$$\frac{\partial}{\partial t}(\delta S_n + \delta_{n,1}W) = J_{n-\frac{1}{2}} - J_{n+\frac{1}{2}} + \delta_{n,2}Q_e + D_n , \tag{4.6}$$

where the quantities are defined as $\delta S_n \equiv \sum_{k_\perp}(n!/2)|\varphi_{k_\perp,n}|^2$, $J_{n-\frac{1}{2}} \equiv \sum_{k_\perp}\Theta k_y n!\,\mathrm{Im}[\varphi_{k_\perp,n-1}\varphi^*_{k_\perp,n}]$, $J_{n+\frac{1}{2}} \equiv \sum_{k_\perp}\Theta k_y(n+1)!\,\mathrm{Im}[\varphi_{k_\perp,n}\varphi^*_{k_\perp,n+1}]$, and $D_n \equiv -2\nu_e n\delta S_n$ (the normalized quantities are used). The symbol $\delta_{n,m}$ denotes the Kronecker delta. The term $J_{n-1/2}$ ($J_{n+1/2}$) stands for the entropy transfer from the $(n-1)$th (nth) to the nth [$(n+1)$th] components through the phase mixing process caused by the parallel advection term $ik_\parallel v_\parallel \delta f_{k_\perp}$ in Eq. (4.1). By treating the variable n as a continuous one, the entropy transfer terms are rewritten as $J_{n-1/2} - J_{n+1/2} \simeq -\partial J_n/\partial n$, where J_n is regarded as the entropy flux in analogy with the energy flux $\Pi(k) \equiv -\int_0^k dk'\,T(k')$ ($T(k)$ is the energy transfer function) in a theory of the neutral-fluid turbulence [16]. The positive entropy flux means the normal-cascade process of the entropy variable, namely, the entropy produced by the turbulent heat flux at the lower-n region is transferred to the higher-n region in accordance to the generation of the fine-scale fluctuations on the distribution function. In the statistically steady state, one obtains the following balance relation for $n \geqslant 3$,

$$J_{n-\frac{1}{2}} - J_{n+\frac{1}{2}} \simeq -\frac{\partial J_n}{\partial n} = -D_n . \tag{4.7}$$

It is expected that the inertial subrange, which is affected neither by the entropy production for $n \leqslant 2$ nor by the collisional dissipation, can be observed if these scales are well separated. Watanabe and Sugama had derived the analytical model of δS_n for the slab ITG turbulence, where the zonal flow generation are artificially suppressed, as follows,

$$\delta S_n = \left\{\frac{Q_i}{2\gamma n}\exp\left(-\frac{\nu_i n}{\gamma}\right) , \; \frac{Q_i}{2\gamma_M\sqrt{n}}\exp\left(-\frac{2}{3}\frac{\nu_i n^{\frac{3}{2}}}{\gamma_M}\right)\right\} , \tag{4.8}$$

where the former and the latter equations represent the solutions for the inertial and the dissipation ranges, respectively. Also, γ and γ_M are factors related to the growth of the averaged wavenumber $\langle|k_y|\rangle_n \equiv \sum_{k_\perp}|k_y|\,|\varphi_{k_\perp,n}|^2/\sum_{k_\perp}|\varphi_{k_\perp,n}|^2$ due to the strain produced by $\boldsymbol{E} \times \boldsymbol{B}$ flows (The detail descriptions are given in Ref. 20). The results of the present slab ETG turbulence simulations are compared with these theoretical predictions.

The power spectra of the entropy variable δS_n, the entropy flux J_n normalized by $-\overline{D}\,(\simeq \overline{Q}_e) \geqslant 0$ and the spectrum-averaged wavenumber $\langle|k_y|\rangle_n$ for the cases of $\Theta = \{0.050,\ 0.150,\ 0.200\}$ are shown in Figs. 4.7(a) – (c), respectively, where the time-average is taken for the late nonlinear phase. One can see that the n-spectra of $\overline{\delta S_n}$ and $-\overline{J_n}/\overline{D}$ depend on Θ, where the amplitude of $\overline{\delta S_n}$ for the case of $\Theta = 0.150$ is much higher than those of the other cases. Indeed, it reflects the development of the fine scale fluctuations of δT with large amplitude for $\Theta = 0.150$, as seen in Figs. 4.6. It is also recognized that the formation of the inertial subrange with $\overline{J_n} = -\overline{D}$ is not so
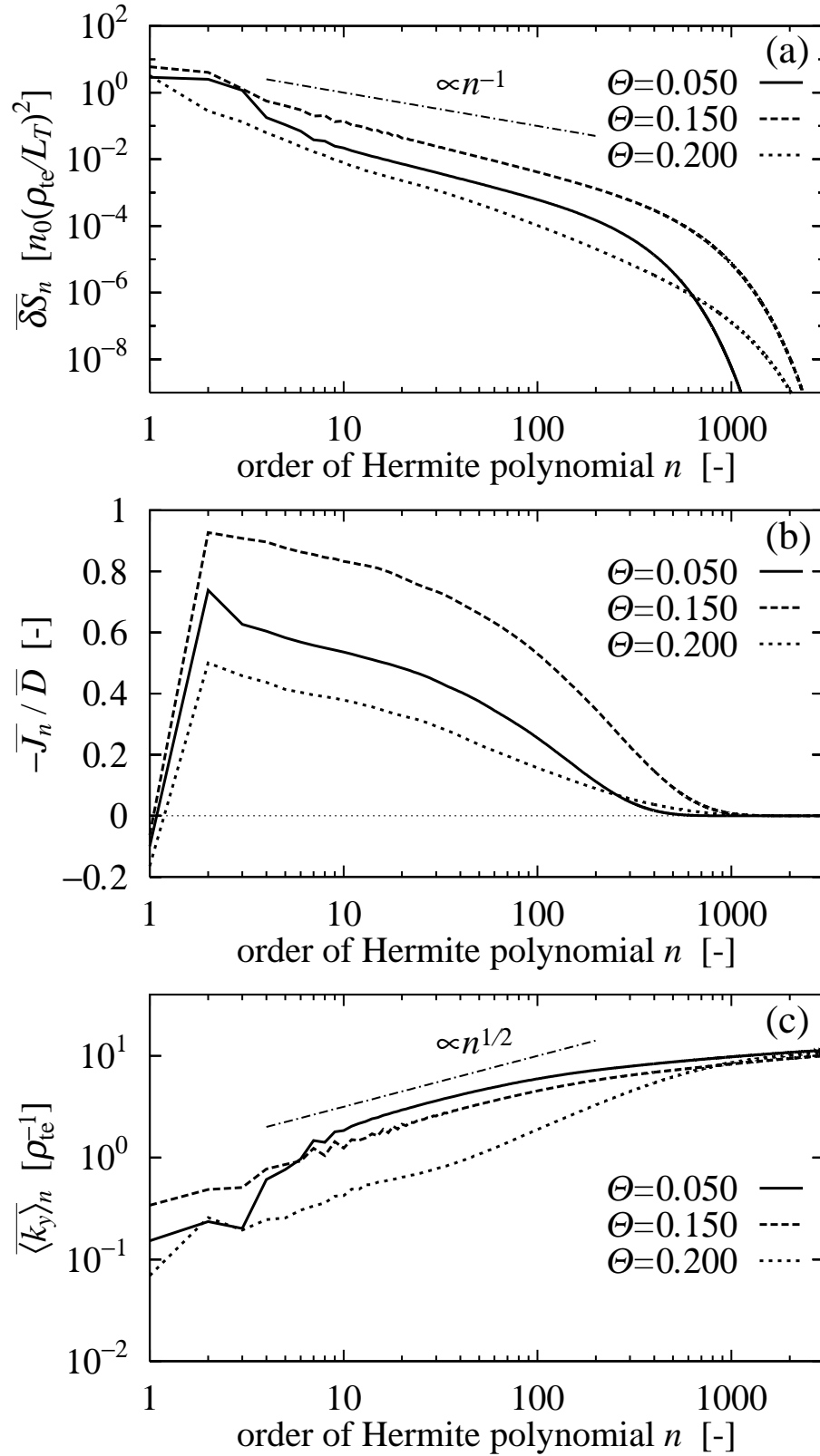
FIG. 4.7: Power-spectra of (a)δS_n, (b)$-J_n/\overline{D}$ and (c)$\langle|k_y|\rangle_n$ for $\Theta = \{0.050, \ 0.150, \ 0.200\}$, where the time average is taken for the late nonlinear phase.

clearly observed in the Fig. 4.7(b), even though the power-law profiles of $\overline{\delta S}_n$ in proportion to $n^{-\alpha}$ with $\alpha \simeq 1.3$ are commonly observed in the region of $5 \lesssim n \lesssim 100$ for all cases [Fig. 4.7(a)]. This is because the collision frequency $\nu_e = 2.0 \times 10^{-4}$ used here is not sufficiently small to separate the dissipation region from the entropy production one so that a slight deviation from the power-low profile of $\delta S_n \propto n^{-1}$, which is predicted theoretically, appears even in the turbulence-dominated case of $\Theta = 0.150$. (Actually, in Ref. 20, the power-law with n^{-1} has been clearly observed for the case with $\nu_i \leqslant 1.25 \times 10^{-5}$ in the unit of ν_{ti}/L_T.) It is, however, emphasized that the Θ-dependence of δS_n and J_n obviously tells us the importance of the parallel-compression effect also in the velocity-space spectrum.

It is also noteworthy that the different exponential decay of δS_n depending on Θ is observed in the dissipation range of $n \gtrsim 500$ even though the collision frequency is fixed in the present study. This is explained with the n-spectra of $\langle |k_y| \rangle_n$ as shown in Fig. 4.7(c). While the complicated behavior, which is owing to the strain produced by the different vortex structures depending on Θ, appears at the lower-n region, the almost same saturation level of $\langle |k_y| \rangle_n (\simeq \gamma_M/\Theta)$ is found at the higher-n region of $n \geqslant 500$, irrespective of Θ. Thus, by using Eq. (4.8), we obtain the scaling of the typical value of n for the dissipation range as $n_d \propto \nu_e^{-2/3} \gamma_M^{2/3} \propto \Theta^{2/3}$ (for fixed-ν_e),
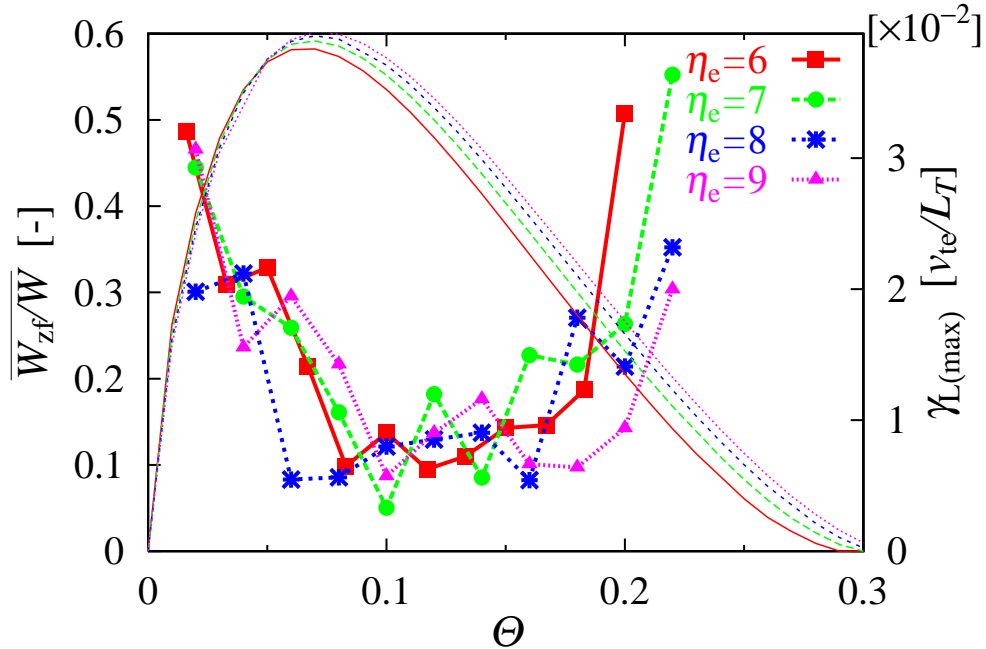

FIG. 4.8: Time-averaged value of W_{zf}/W as a function of Θ for $\eta_e = \{6, 7, 8, 9\}$, where the time-average is taken for the late nonlinear phase ($2500 \lesssim t \lesssim 3500$). Maximum linear growth rates are also shown by solid lines with the same colors.

which is consistent with the results shown in Fig. 4.7(a), where the relation of the dissipation ranges, $n_d(\Theta=0.050) < n_d(\Theta=0.150) < n_d(\Theta=0.200)$, are observed. These results indicate that the formation of coherent vortex structures (e.g., vortex streets or strong zonal flows) in the real space affects the n-spectra for the entropy production region on the lower-n side, but not for the dissipation region on the higher-n side except for the difference of the value of Θ.

4.3.2 Summary of parameter studies

Let us briefly summarize the vortex structures associated with zonal flows and the related transport properties found in the present parameter study of the slab ETG turbulence. The results
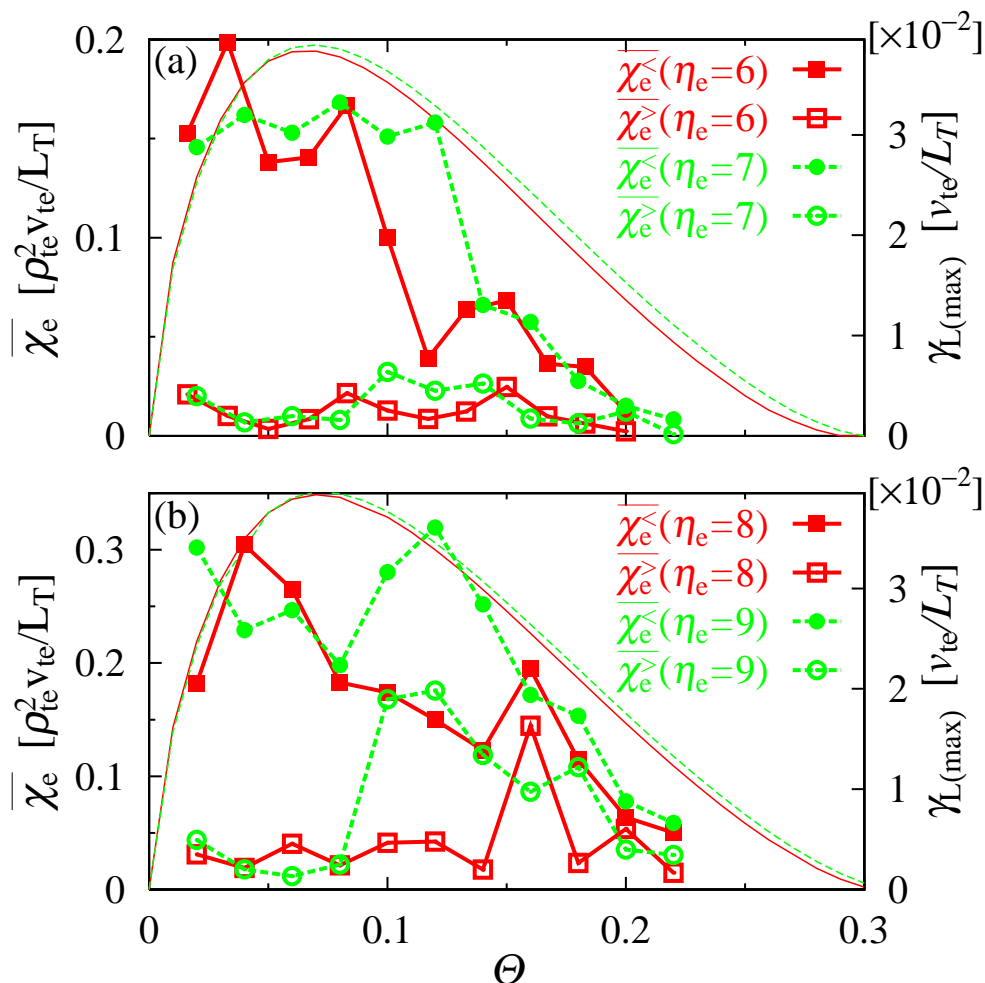

FIG. 4.9: Time-averaged value of χ_e as a function of Θ for (a)$\eta_e = \{6, 7\}$ and (b)$\eta_e = \{8, 9\}$, where $\overline{\chi_e^<}$ and $\overline{\chi_e^>}$ represent the values averaged over the early and late nonlinear phases, respectively. Maximum linear growth rates are also shown by solid lines with the same colors.

of the Θ-dependence of time-averaged values of the normalized zonal flow energy W_{zf}/W are shown in Fig. 4.8, where all cases of η_e are plotted. For reference, we also plotted the corresponding maximum growth rates of the linear ETG modes $\gamma_{L(max)}$ in the figure. One clearly finds that the strong zonal flow is generated in the regions of $\Theta \lesssim 0.1$ and $\Theta \gtrsim 1.8$, corresponding to the formation of coherent vortex streets and the zonal-flow-dominated structure, respectively. The zonal flow generation is weaker in the region of $0.1 \lesssim \Theta \lesssim 1.8$, where the turbulent vortices are observed. It is also remarkable that the similar Θ-dependence of W_{zf}/W is found in all cases of $\eta_e = \{6, 7, 8, 9\}$. This implies that the transition of the vortex structures in the slab ETG turbulence is mainly controlled by Θ rather than η_e if the value of η_e is large enough. Actually, in all cases of η_e, the completely different vortex structures have been realized depending on Θ, even for the cases with the same maximum growth rate $\gamma_{L(max)}$. It is confirmed by the fact that, for $\eta_e = 6$, the cases of $\Theta = \{0.033, 0.133\}$ with the same $\gamma_{L(max)}$ show quite different levels of W_{zf}/W.

In order to discuss the relation between the transition of vortex structures and the transport reduction, we plotted in Figs. 4.9(a) and 4.9(b) the Θ-dependence of χ_e averaged over the early and late nonlinear phases for $\eta_e = \{6, 7\}$ and $\eta_e = \{8, 9\}$, respectively. One finds that the distinct difference between $\overline{\chi_e^<}$ and $\overline{\chi_e^>}$ indicating the transport reduction is commonly found in the region of $\Theta \lesssim 0.1$ for all values of η_e. Also, we see the qualitatively similar dependence of χ_e on Θ such that the reduction of χ_e becomes smaller for the larger Θ. It is remarkable that, for small Θ, the transport reduction associated with the formation of coherent vortex streets is realized in the nonlinear phase, even if the maximum growth rate of linear ETG modes is relatively large.

4.4 Modulational instability analysis for zonal flow generation

4.4.1 Truncated fluid model

In the previous section, it is found that the formation of coherent vortex structures is closely related to the secondary growth of zonal flows in the nonlinear phase as shown in Figs. 4.4. Here, we discuss the dependence of zonal flow generation on Θ $(= k_\parallel L_T/k_y \rho_{te})$ based on the modulational instability analysis with a truncated fluid model, where the parallel dynamics such as acoustic modes due to the parallel compression is taken into account. These analyses give us qualitative understanding for mechanisms of the secondary growth of zonal flows found in the ETG turbulence simulations.

Here, we consider truncated fluid equations for the modulational instability analysis. In the derivation of the fluid model below, we employ the description with dimensional quantities again. By taking the fluid moments of the gyrokinetic equation [see Eq. (4.1)] up to the second order,

one obtains the following equations,

$$\frac{\partial}{\partial t}\delta n_{\boldsymbol{k}_\perp} + ik_\parallel n_0 \delta u_{\boldsymbol{k}_\perp} + i\omega_{*\mathrm{e}}n_0\left(1 - \frac{\eta_\mathrm{e}}{2}k_\perp^2\rho_\mathrm{te}^2\right)\frac{e\delta\psi_{\boldsymbol{k}_\perp}}{T_\mathrm{e}}$$
$$- \frac{c}{B}\sum_\Lambda \boldsymbol{b}\cdot(\boldsymbol{k}'_\perp \times \boldsymbol{k}''_\perp)\,\delta\psi_{\boldsymbol{k}'_\perp}\delta n_{\boldsymbol{k}''_\perp} = 0\,, \tag{4.9}$$

$$n_0 m_\mathrm{e}\frac{\partial}{\partial t}\delta u_{\boldsymbol{k}_\perp} + ik_\parallel\left(T_\mathrm{e}\delta n_{\boldsymbol{k}_\perp} + n_0\delta T_{\boldsymbol{k}_\perp} - n_0 e\delta\psi_{\boldsymbol{k}_\perp}\right)$$
$$- \frac{n_0 m_\mathrm{e} c}{B}\sum_\Lambda \boldsymbol{b}\cdot(\boldsymbol{k}'_\perp \times \boldsymbol{k}''_\perp)\,\delta\psi_{\boldsymbol{k}'_\perp}\delta u_{\boldsymbol{k}''_\perp} = 0\,, \tag{4.10}$$

$$n_0\frac{\partial}{\partial t}\delta T_{\boldsymbol{k}_\perp} + ik_\parallel\left(2n_0 T_\mathrm{e}\delta u_{\boldsymbol{k}_\perp} + \delta q_{\boldsymbol{k}_\perp}\right) + i\omega_{*\mathrm{e}}\eta_\mathrm{e}n_0 e\delta\psi_{\boldsymbol{k}_\perp}$$
$$- \frac{n_0 c}{B}\sum_\Lambda \boldsymbol{b}\cdot(\boldsymbol{k}'_\perp \times \boldsymbol{k}''_\perp)\,\delta\psi_{\boldsymbol{k}'_\perp}\delta T_{\boldsymbol{k}''_\perp} = 0\,, \tag{4.11}$$

where the fluid quantities are defined by $\delta n_{\boldsymbol{k}_\perp} \equiv \int dv_\parallel \delta f_{\boldsymbol{k}_\perp}$, $n_0\delta u_{\boldsymbol{k}_\perp} \equiv \int dv_\parallel v_\parallel \delta f_{\boldsymbol{k}_\perp}$, $n_0\delta T_{\boldsymbol{k}_\perp} \equiv \int dv_\parallel (m_\mathrm{e}v_\parallel^2 - T_\mathrm{e})\delta f_{\boldsymbol{k}_\perp}$ and $\delta q_{\boldsymbol{k}_\perp} \equiv \int dv_\parallel (m_\mathrm{e}v_\parallel^3 - 3T_\mathrm{e}v_\parallel)\delta f_{\boldsymbol{k}_\perp}$, which denote the fluctuations of the density, the parallel flow, the temperature and the parallel heat flux, respectively. Here, the collisional dissipation is neglected because of $\nu_\mathrm{e}L_T/v_\mathrm{te} \ll 1$.

In order to derive a reduced model describing the evolution of zonal flows, we postulate here that (i) the fluid equations are truncated by ignoring the parallel heat flux $\delta q_{\boldsymbol{k}_\perp}$ in Eq. (4.11), and that (ii) the third term $i\omega_{*\mathrm{e}}\eta_\mathrm{e}n_0 e\delta\psi_{\boldsymbol{k}_\perp}$, which drives the linear ETG instability, is also neglected in Eq. (4.11). The first assumption (i) is necessary for the truncation of the couplings of fluid equations. The second one (ii) is useful for the analysis of modulational instabilities driven by the "stable" pump wave, because we focus on the secondary growth of zonal flows after the initial saturation, where the ETG mode no longer grows linearly. Furthermore, (iii) we neglect the nonlinear terms in Eqs. (4.10) and (4.11) for simplicity, because they cause higher-order interactions which are not of interest here. Under these assumptions, the reduced fluid equations used here are derived by means of the quasineutrality condition Eq. (4.2),

$$\left(\frac{\partial}{\partial t} - i\mathcal{L}_{\boldsymbol{k}_\perp}\right)\psi_{\boldsymbol{k}_\perp} - ik_\parallel v_\mathrm{te}\Lambda_{\boldsymbol{k}_\perp}^{-1}u_{\boldsymbol{k}_\perp} - \sum_\Lambda \Gamma_{\boldsymbol{k}_\perp}^{\boldsymbol{k}'_\perp,\boldsymbol{k}''_\perp}\psi_{\boldsymbol{k}'_\perp}\psi_{\boldsymbol{k}''_\perp} = 0\,, \tag{4.12}$$

$$\frac{\partial}{\partial t}u_{\boldsymbol{k}_\perp} + ik_\parallel v_\mathrm{te}\left[T_{\boldsymbol{k}_\perp} - (1+\Lambda_{\boldsymbol{k}_\perp})\psi_{\boldsymbol{k}_\perp}\right] = 0\,, \tag{4.13}$$

$$\frac{\partial}{\partial t}T_{\boldsymbol{k}_\perp} + 2ik_\parallel v_\mathrm{te}u_{\boldsymbol{k}_\perp} = 0\,, \tag{4.14}$$

where

$$\mathcal{L}_{\boldsymbol{k}_\perp} \equiv \omega_{*\mathrm{e}}\left(1 - \frac{\eta_\mathrm{e}}{2}k_\perp^2\rho_\mathrm{te}^2\right)\Lambda_{\boldsymbol{k}_\perp}^{-1}\,, \tag{4.15}$$

$$\Gamma_{\boldsymbol{k}_\perp}^{\boldsymbol{k}'_\perp,\boldsymbol{k}''_\perp} \equiv \frac{1}{2}\frac{cT_\mathrm{e}}{eB}\boldsymbol{b}\cdot(\boldsymbol{k}'_\perp \times \boldsymbol{k}''_\perp)\left(\Lambda_{\boldsymbol{k}''_\perp} - \Lambda_{\boldsymbol{k}'_\perp}\right)\Lambda_{\boldsymbol{k}_\perp}^{-1}\,. \tag{4.16}$$

Here, abbreviations for $\psi_{k_\perp} \equiv e\delta\psi_{k_\perp}/T_e$, $u_{k_\perp} \equiv \delta u_{k_\perp}/v_{te}$ and $T_{k_\perp} \equiv \delta T_{k_\perp}/T_e$ are used. The symbol $\sum'_\Delta$ means the summation over the Fourier modes which consist of the triad-interaction, i.e., $k_\perp = k'_\perp + k''_\perp$. The above reduced fluid equations involve the effect of acoustic modes due to the parallel compression which has rarely been incorporated into the conventional modulational instability analysis for the zonal flow generation [9–13].

4.4.2   Dispersion relation of zonal flows

In order to derive the dispersion equation for zonal flows driven by the modulational instability, we consider the low-dimensional model (sometimes called the four-wave model) based on Eqs. (4.12) – (4.16). The field quantities $\xi = \{\psi, u, T\}$ are then assumed to be composed of a monochromatic pump mode, a zonal mode and two sideband modes, such that,

$$
\begin{aligned}
\xi(x,t) = \quad & \xi_{k_p}\exp(ik_p \cdot x - i\omega_{k_p}t) + \xi_{k_{zf}}\exp(ik_{zf} \cdot x - i\Omega_{k_{zf}}t) \\
+ \quad & \xi_{k^+}\exp(ik^+ \cdot x - i\omega_{k^+}t) + \xi_{k^-}\exp(ik^- \cdot x - i\omega_{k^-}t) \\
+ \quad & (\text{complex conjugate}) ,
\end{aligned}
\tag{4.17}
$$

where the complex frequency and the wavenumber vector of these four modes satisfy the frequency matching and the triad-interaction conditions, respectively, as follows,

$$
\omega_{k^\pm} = \omega_{k_p} \pm \Omega_{k_{zf}} , \quad k^\pm = k_p \pm k_{zf} .
\tag{4.18}
$$

Also, $k_{\|p} = k_\|^\pm$ ($\equiv k_\|$) and $\xi_k = \xi^*_{-k}$. The reduction to four resonant modes from Eqs. (4.12) – (4.16) leads to a nonlinear dynamical system of four ordinary differential equations. Here, we suppose that the complex amplitude of the zonal and the sideband modes are much smaller than that of the pump mode, i.e.,

$$
|\xi_{k_{zf}}| \sim |\xi_{k^\pm}| \sim \epsilon|\xi_{k_p}| ,
\tag{4.19}
$$

where $\epsilon \ll 1$. This subsidiary ordering enables us to linearize the nonlinear system so that one obtains the dispersion relation which determines the linear growth rate of zonal flows.

For the pump mode, one obtains the following equations,

$$
i\left(\omega_{k_p} + \mathcal{L}_{k_p}\right)\psi_{k_p} + ik_\| v_{te}\Lambda_{k_p}^{-1}u_{k_p} + \Gamma_{k_p}^{k^-,k_{zf}}\psi_{k^-}\psi_{k_{zf}} + \Gamma_{k_p}^{k^+,-k_{zf}}\psi_{k^+}\psi^*_{k_{zf}} = 0 ,
\tag{4.20}
$$

$$
i\omega_{k_p}u_{k_p} - ik_\| v_{te}\left[T_{k_p} - \left(1+\Lambda_{k_p}\right)\psi_{k_p}\right] = 0 ,
\tag{4.21}
$$

$$
i\omega_{k_p}T_{k_p} - 2ik_\| v_{te}u_{k_p} = 0 .
\tag{4.22}
$$

Considering the ordering of Eq. (4.19), one can neglect the last two terms on the left hand side of Eq. (4.20), which are of order $\epsilon^2|\psi_{k_p}|^2$, so that Eqs. (4.20) – (4.22) are reduced to the dispersion
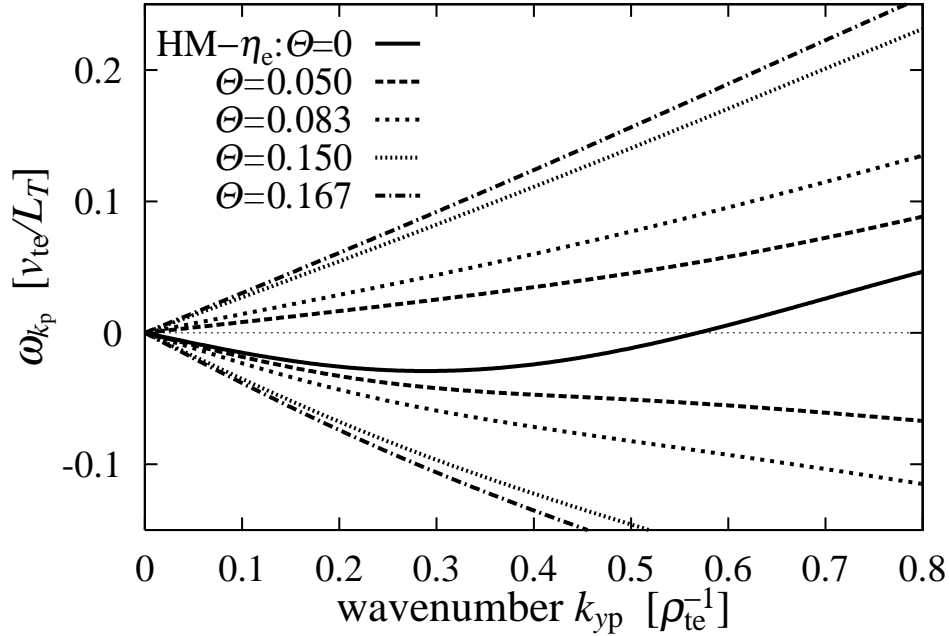
FIG. 4.10: Real frequency of the pump mode ω_{k_p} for $\Theta = \{0,\ 0.050,\ 0.083,\ 0.150,\ 0.167\}$, where $\eta_e = 6$ and $k_{xp} = 0.1$.

equation for the pump mode as follows,

$$1 + \frac{\mathcal{L}_{k_p}}{\omega_{k_p}} - \left(\frac{1 + \Lambda_{k_p}}{\Lambda_{k_p}}\right)\left(\frac{k_\parallel v_{te}}{\omega_{k_p}}\right)^2\left[1 - 2\left(\frac{k_\parallel v_{te}}{\omega_{k_p}}\right)^2\right]^{-1} = 0 . \tag{4.23}$$

This can be rewritten as a cubic equation of ω_{k_p}, then the root determines the frequency of the pump mode for given k_p and $k_\parallel$. By evaluating the sign of the discriminant of Eq. (4.23), it is easily shown that any root must be real-valued. Thus, there is neither instability nor damping. The dispersion relation of ω_{k_p} for $\Theta = \{0,\ 0.050,\ 0.083,\ 0.150,\ 0.167\}$ are shown in Fig. 4.10, where $\eta_e = 6$ and $k_{xp} = 0.1$. For the case of $\Theta \neq 0$, we plotted two of the three branches (the branches with positive- and negative-ω_{k_p}), which approach the solution of HM-η_e equation in the limit of $\Theta \to 0$ ($k_\parallel \to 0$). Another branch, which is not plotted here, approaches to the trivial solution of $\omega_{k_p} = 0$. As expected, we see that the deviation of the frequency from that for $\Theta = 0$ becomes larger as Θ increases.

From Eqs. (4.12) – (4.19), one obtains the equations for zonal and sideband modes as follows,

$$i\Omega_{k_{zf}}\psi_{k_{zf}} + \Gamma_{k_{zf}}^{k^+, -k_p}\psi_{k^+}\psi_{k_p}^* + \Gamma_{k_{zf}}^{-k^-, k_p}\psi_{k^-}^*\psi_{k_p} = 0 , \tag{4.24}$$

$$i\mathcal{P}_\pm\psi_{k^\pm} + \Gamma_{k^\pm}^{k_p, \pm k_{zf}}\psi_{k_p}\psi_{\pm k_{zf}} = 0 , \tag{4.25}$$

where

$$\mathcal{P}_\pm \equiv \omega_{k^\pm}\left[1 + \mathcal{K}_{k^\pm}(\omega_{k^\pm}, k_\parallel)\right] + \mathcal{L}_{k^\pm} . \tag{4.26}$$

Here, the effect of the coupling among $\psi_{k^\pm}$, $u_{k^\pm}$ and $T_{k^\pm}$ for sideband modes due to the parallel compression appears in $\mathcal{K}_{k^\pm}(\omega_{k^\pm}, k_\parallel)$ defined as,

$$\mathcal{K}_{k^\pm}(\omega_{k^\pm}, k_\parallel) \equiv -\left(\frac{1+\Lambda_{k^\pm}}{\Lambda_{k^\pm}}\right)\left(\frac{k_\parallel v_{\text{te}}}{\omega_{k^\pm}}\right)^2\left[1-2\left(\frac{k_\parallel v_{\text{te}}}{\omega_{k^\pm}}\right)^2\right]^{-1}. \tag{4.27}$$

These terms, which are ignored in the conventional analysis with the Hasegawa-Mima equation, play a crucial role in considering the effect of the finite parallel compression on the zonal flow generation. Indeed, one can obtain the conventional dispersion relation in the limit of $k_\parallel \to 0$ which annihilates $\mathcal{K}_{k^\pm}$ in Eq. (4.26), as well as in the long-wavelength limit ($k_\perp \rho_{\text{te}} \ll 1$). Finally, combining Eqs. (4.23) – (4.27), one obtains the dispersion relation of zonal flows as follows,

$$\Omega_{k_{\text{zf}}} + \left[\frac{\Gamma_{k_{\text{zf}}}^{k^+,-k_\text{p}}\Gamma_{k^+}^{k_{\text{zf}},k_\text{p}}}{\mathcal{P}_+} - \frac{\Gamma_{k_{\text{zf}}}^{k^-,-k_\text{p}}\Gamma_{k^-}^{-k_{\text{zf}},k_\text{p}}}{\mathcal{P}_-}\right]|\psi_{k_\text{p}}|^2 = 0. \tag{4.28}$$

The linear growth rate of zonal flows γ_{zf} is then given by the positive imaginary part of a complex solution $\Omega_{k_{\text{zf}}}$ of the above equation. Straightforward but somewhat tedious algebraic calculation shows that the left hand side of Eq. (4.28) is rearranged into a seventh-order polynomial of $\Omega_{k_{\text{zf}}}$ with real-valued coefficients, which has to be solved numerically. In the numerical calculations, we have found only two cases: namely, solutions with a pair of complex conjugate and five real-valued roots, or with seven real-valued roots.

Figure 4.11 shows the spectrum of the zonal flow growth rate γ_{zf} for $\Theta = \{0, 0.050, 0.083, 0.150, 0.167\}$, where the wavenumber and the amplitude of the pump mode are chosen as $k_{x\text{p}} = 0.1$, $k_{y\text{p}} = 0.35$ and $(L_T/\rho_{\text{te}})^2|\psi_{k\text{p}}|^2 = 2$, respectively. Here, the branch of the negative-ω_{k_p} [see Fig. 4.10] are chosen, because, for $k_{y\text{p}} = 0.35$, it converges to the non-trivial dispersion relation ($\omega_{k_\text{p}} \neq 0$) in the limit of $\Theta \to 0$. One clearly finds that growth rate of the modulational instability for zonal flows is decreased by increasing Θ, and no unstable solution exists for $\Theta \gtrsim 0.167$.

In order to discuss Θ-dependence of the critical pump-amplitude for the instability onset, we plotted in Fig. 4.12 the maximum growth rate of the zonal flow $\gamma_{\text{zf(max)}}$ as a function of the squared amplitude of the pump mode $(L_T/\rho_{\text{te}})^2|\psi_{k_\text{p}}|^2$. From this figure, we find that the critical amplitude for the instability becomes larger as Θ increases. In the region where the pump-amplitude is sufficiently large (e.g., $(L_T/\rho_{\text{te}})^2|\psi_{k_\text{p}}|^2 \gtrsim 3$), the instabilities are observed for all cases of Θ. However, in the region of $(L_T/\rho_{\text{te}})^2|\psi_{k_\text{p}}|^2 \lesssim 2$, one can see the existence of a critical value of Θ, beyond which the instability no longer occurs. In the present ETG turbulence simulations, we find $(L_T/\rho_{\text{te}})^2|\psi_{k_\text{p}}|^2 \sim 1$. Hence, the critical Θ is estimated as $\Theta \sim 0.1$, which qualitatively agrees with that for the secondary growth of zonal flows found in the cases of small Θ [see Figs. 4.4(a) and 4.4(b)].
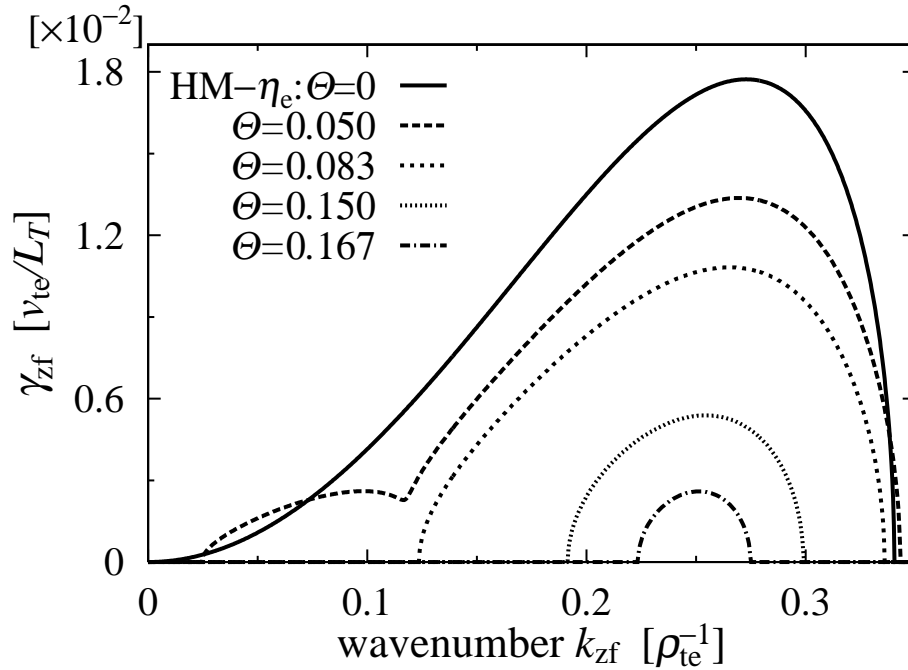
FIG. 4.11: Growth rate of zonal flows γ_{zf} for $\Theta = \{0,\ 0.050,\ 0.083,\ 0.150,\ 0.167\}$, where $k_{xp} = 0.1$, $k_{yp} = 0.35$ and $(L_T/\rho_{te})^2|\psi_{kp}|^2 = 2$.

We also plot in Figs. 4.13 the maximum growth rate $\gamma_{zf(max)}$ and the real frequency ω_{zf} for $\eta_e = \{6, 7, 8, 9\}$ as a function of Θ, where ω_{zf} is evaluated at the wavenumber giving the maximum growth rate. One finds that the maximum growth rate $\gamma_{zf(max)}$ shows the similar dependence on Θ for all values of η_e considered, except that the profiles are shifted downward. The stable region of Θ with $\gamma_{zf(max)} = 0$ then becomes wider for larger η_e. Also, we see that the value of ω_{zf} is larger than that of $\gamma_{zf(max)}$ in the region of $\Theta \gtrsim 0.1$, which means the oscillatory zonal flow. Since the steady zonal flow suppresses the turbulent transport more effectively compared to the oscillatory one, these results suggest that the relatively steady zonal flow with larger growth rate can be driven for smaller η_e if the pump amplitude is fixed. However, the pump amplitude is, in practice, associated with the turbulence intensity which should depend on η_e. Nevertheless, it is important that the critical value of Θ, which define the instability onset, commonly appears for all cases of η_e, and then these results well explain the turbulence simulation results.

Here, we have derived the dispersion relation of zonal flows based on the modulational instability analysis, where the coupling of fluid moments (density, parallel flow, and temperature) through the parallel compression term is incorporated. The results then show the stabilizing effect due to the parallel compression which is proportional to Θ.

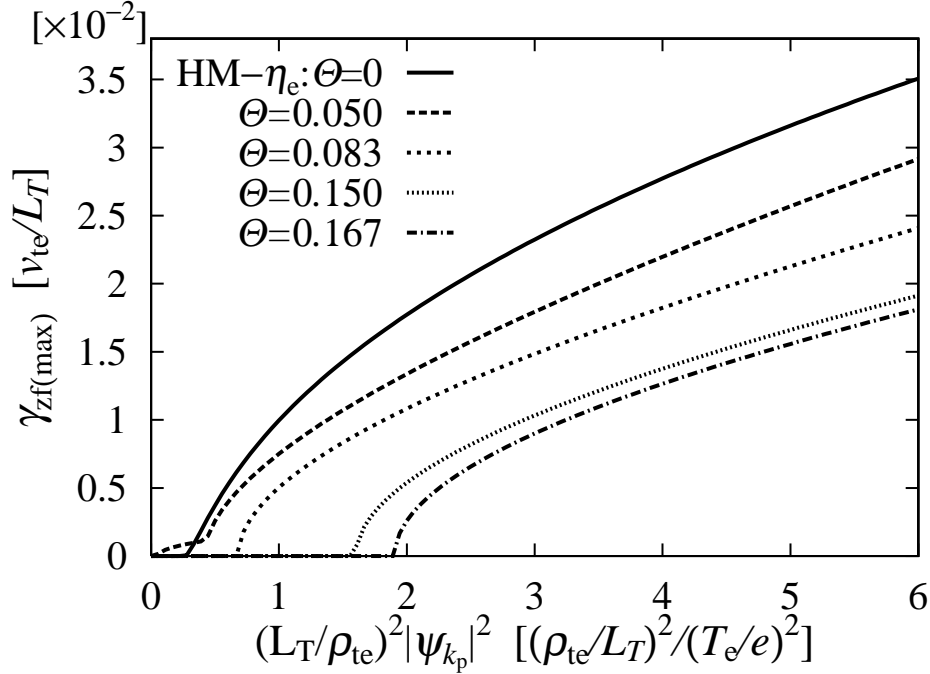The present theoretical analysis with a "stable" pump mode provides us with the qualitative

FIG. 4.12: Maximum growth rate of zonal flows $\gamma_{\text{zf(max)}}$ as a function of $(L_T/\rho_{\text{te}})^2|\psi_{k_{\text{p}}}|^2$ for $\Theta = \{0, 0.050, 0.083, 0.150, 0.167\}$. The wavenumbers of the pump mode are the same as those in Fig. 4.11.

explanations of the turbulence simulation results for $0 \lesssim \Theta \lesssim 0.15$. However, the analysis is limited to the case where the non-zonal fluctuations are dominant in the saturated ETG turbulence, because the subsidiary ordering Eq. (4.19) for the modulational instability analysis assumes the quite low amplitude of the zonal mode in comparison with the pump amplitude. It is, thus, not directly applicable to the case with the generation of the strong zonal flow accompanied with the transport suppression observed in the turbulence simulation for $\Theta \geqslant 0.200$ [see Figs. 4.4(b) and 4.7], where the strong zonal flow is predominantly generated by the nonlinear coupling of linear ETG modes in the initial saturation phase of the instability growth [e.g., $t \simeq 1200$ for $\Theta = 0.200$ in Fig. 4.4(b)]. In order to reveal the detailed mechanisms of the initial generation of strong zonal flows with the effect of parallel compression, one needs more refinement of the present model to incorporate the unstable evolution of the pump mode precisely which remains as a future work.

The coupling among the fluid moments of $\{\psi, u, T\}$ considered here suggests the importance of the parallel dynamics on the stability of zonal flows. It has also been verified that the similar stabilization of zonal flows due to the parallel compression is observed in a model with only a coupling of $\{\psi, u\}$. Anderson *et al.* had previously derived the dispersion relation of zonal flows for ITG turbulence by the similar approach with the fluid equations [17], then they showed fifth-order polynomial of $\Omega_{k_{\text{zf}}}$ which differs from our dispersion equation of seventh-order polynomial

as shown in Eq. (4.28). Consequently, the different dependence of γ_{zf} on $k_\parallel$ (or Θ) appears, e.g., the stabilization of zonal flows found in the present analysis for larger $k_\parallel$ is not observed in Ref. 17. This is because the coupling with the parallel flow, which corresponds to the second term of Eq. (4.14), had been ignored from the temperature equation shown in Ref. 17. Neglecting this term reduces the order of polynomial for the dispersion relation, but leads to an incomplete description of acoustic modes at the same time. The similar modulational instability analysis for zonal-flows/fields involving the parallel dynamics of shear-Alfvén waves had also been examined by Guzdar *et al.*, and by Chen *et al.* for the drift-Alfvén turbulence [18, 19].
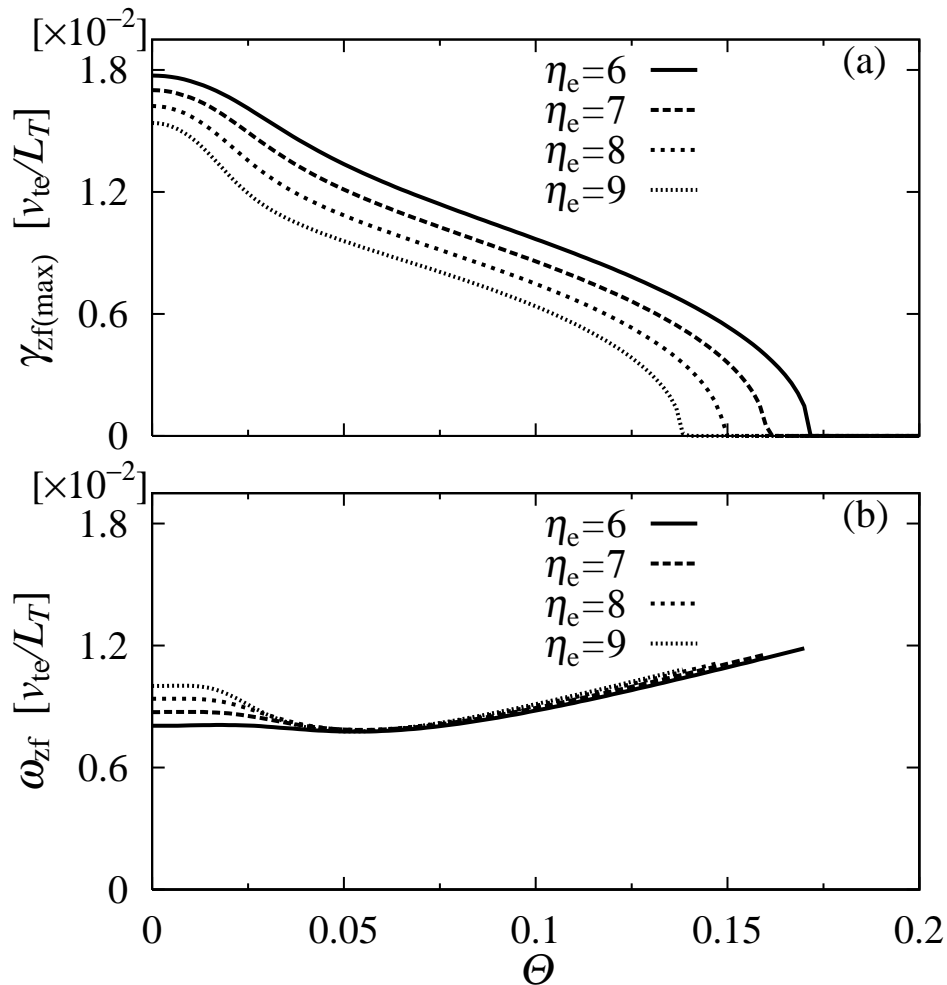

FIG. 4.13: (a)Maximum growth rate $\gamma_{zf(max)}$ and (b)real frequency ω_{zf} for zonal flows as a function of Θ for $\eta_e = \{6, 7, 8, 9\}$. The wavenumbers and the amplitude of the pump mode are the same as those in Fig. 4.11.

4.5 Concluding remarks

We have investigated the transition of vortex structures including zonal flows and the related transport properties in the slab ETG turbulence through the comprehensive parameter studies by means of the nonlinear gyrokinetic Vlasov simulations. Then, the dependence on the magnitude of the parallel compression, which is characterized by the parameter $\Theta \equiv k_\parallel L_T / k_y \rho_{\mathrm{te}} = \theta L_T / \rho_{\mathrm{te}}$, and the electron temperature gradient has been intensively examined.

Numerical results show three different types of the time evolution of the heat diffusivity depending on Θ, i.e., transitional evolution accompanied with transport reduction, steady turbulent behavior, and significant suppression of transport. Then, the zonal flow evolutions with or without secondary growth in the nonlinear phase are well correlated to the evolution of the heat diffusivity. Correspondingly, the detailed analyses of the spectral and the spatial structures of the potential and temperature fluctuations reveal the different types of vortex structures such as coherent vortex streets, turbulent vortices, and zonal-flow dominated state. The vortex structures depend on the value of Θ through the parallel compression.

Power spectra of the entropy variable $\overline{\delta S}_n$ and the entropy flux $\overline{J}_n$ in the $v_\parallel$-space for the different Θ have been examined by means of the Hermite polynomial expansion. The spectral structures strongly depend on Θ, then it is observed that the amplitude for the case with steady turbulent vortices much exceeds those of the other cases. While the power-law profiles of $\overline{\delta S}_n$ show a slight deviation from the theoretical prediction, the similar profiles, which are proportional to $n^{-\alpha}$ with $\alpha \simeq 1.3$, are commonly observed in the region of $5 \lesssim n \lesssim 100$. Spectral analysis of $\langle |k_y| \rangle_n$ indicates that the different vortex structures in the real space affects the n-spectra for the entropy production region in the lower-n side, but not for the dissipation region in the higher-n side, except for the difference of the value of Θ.

By examining the dependence of the heat diffusivity and the intensity of zonal flows on Θ, we found clear correlation between the formation of coherent vortex streets associated with the strong generation of the zonal flow and transport reduction for the cases with small values of $\Theta \lesssim 0.1$. These results indicate weak dependence on the value of η_e, which implies that the transition of vortex structures in the slab ETG turbulence is mainly controlled by Θ rather than η_e if η_e is large enough. The transport reduction associated with the formation of coherent vortex streets is realized for small Θ even if the maximum growth rate of linear ETG modes is relatively large.

We have discussed the dependence of zonal flow generation on Θ based on the modulational instability analysis with a truncated fluid model, where the parallel dynamics associated with acoustic modes is taken into account. The dispersion relation of zonal flows derived here shows

that the linear growth rate of the modulational instability is reduced as Θ increases, and that there is a critical value of Θ, beyond which the instability does not occur. The modulational instability analysis shows a qualitative agreement with the turbulence simulation results, where the secondary growth of zonal flows, the transition of vortex structures, and the related transport reduction are found in the cases of small Θ.

In the present study, the quasi two-dimensional shear-less slab configuration has been employed, where Θ and η_e are the main control parameters. Although the various values of Θ should be treated simultaneously in cylindrical or toroidal plasmas, the two-dimensional slab configuration with constant Θ used here is still meaningful as a reduced model for them. In these practical systems, $k_\parallel/k_y$ depends on the aspect ratio L_z/a (= "the length of plasma column"/ "the plasma radius") for cylindrical plasmas, or depends on the radial position through the magnetic shear for toroidal ones. Particularly, in the toroidal plasmas, it has been pointed out that the compression due to the geodesic curvature and the toroidal mode coupling become more important for the saturation of the toroidal ETG instability with strong magnetic shear, where the toroidal modes overlap each other significantly [4,5]. However, in the case with weak magnetic shear, the unstable-mode rational surfaces become more distant from each other so that the toroidal mode coupling weakens. The present study on the slab ETG turbulence may contribute to fundamental understandings of the effects of the parallel compression on the long-timescale evolution of zonal flows and the related transport reduction on the neighborhood of the minimum-q surface (q denotes the safety factor) in the reversed-shear tokamaks.

In Ref. 4 and 5, it has also been pointed out that the three-wave resonant interaction is crucial for the saturation of the toroidal ETG instability, rather than the zonal flow generation due to the modulational instability. Here, we have not quantitatively examined which of the three-wave interaction and the zonal flow generation driven by the modulational instability is dominant in the initial saturation of the slab ETG instability. Nevertheless, it is expected that the initial saturation is attributed to not only the three-wave interaction, but also to the zonal-flow generation, because the zonal flow generation in the slab ETG turbulence is stronger than that in the toroidal ETG case where the zonal flow is weakened by the neoclassical polarization effect. It should be emphasized here that the present study reveals the importance of the long-timescale evolution of zonal flows, which is closely related to the transition of vortex structures and transport level in the nonlinear phase long after the initial saturation of the slab ETG instability. Then, the long-timescale evolution of zonal flows generated by the modulational instability may also be important in the nonlinear phase of the toroidal ETG turbulence.

Bibliography for Chapter 4

[1] F. Jenko, W. Dorland, M. Kotschenreuther, and B. N. Rogers, Phys. Plasmas **7**, 1904 (2000)

[2] W. M. Nevins, J. Candy, S. Cowley, T. Dannert, A. Dimits, W. Dorland, C. Estrada-Mila, G. W. Hammett, F. Jenko, M. J. Pueschel, and D. E. Shumaker, Phys. Plasmas **13**, 122306 (2006)

[3] Z. Lin, I. Holod, L. Chen, P. H. Diamond, T. S. Hahm, and S. Ethier, Phys. Rev. Lett. **99**, 265003 (2007)

[4] Z. Lin, L. Chen, and F. Zonca, Phys. Plasmas **12**, 056125 (2005)

[5] L. Chen, F. Zonca, and Z. Lin, Plasma Phys. Controlled Fusion **47**, B71 (2005)

[6] Y. Idomura, S. Tokuda, and Y. Kishimoto, Nucl. Fusion **45**, 1571 (2005)

[7] Y. Idomura, M. Wakatani, and S. Tokuda, Phys. Plasmas **7**, 3551 (2000)

[8] J. Li, Y. Kishimoto, N. Miyato, T. Matsumoto, and J. Q. Dong, Nucl. Fusion **45**, 1293 (2005)

[9] J. Li and Y. Kishimoto, Phys. Plasmas **12**, 054505 (2005)

[10] F. Jenko, Phys. Lett. A **351**, 417 (2006)

[11] P. N. Guzdar, R. G. Kleva, and L. Chen, Phys. plasmas **8**, 459 (2001)

[12] L. Chen, Z. Lin, and R. B. White, Phys. plasmas **7**, 3129 (2000)

[13] G. Manfredi, C. M. Roach, and R. O. Dendy, Plasma Phys. Controlled Fusion **43**, 825 (2001)

[14] A. M. Dimits, G. Bateman, M. A. Beer, B. I. Cohen, W. Dorland, G. W. Hammett, C. Kim, J. E. Kinsey, M. Kotschenreuther, A. H. Kritz, L. L. Lao, J. Mandrekas, W. M. Nevins, S. E. Parker, A. J. Redd, D. E. Shumaker, R. Sydora, and J. Weiland, Phys. Plasmas **7**, 969 (2000)

[15] B. N. Rogers, W. Dorland, and M. Kotschenreuther, Phys. Rev. Lett. **18**, 5336 (2000)

[16] M. Lesieur, "Turbulence in Fluids", Kluwer academic publishers, (1990)

[17] J. Anderson, J. Li, and Y. Kishimoto, Phys. plasmas **14**, 082313 (2007)

[18] P. N. Guzdar, R. G. Kleva, A. Das, and P. K. Kaw, Phys. plasmas **8**, 3907 (2001)

[19] L. Chen, Z. Lin, R. B. White, and F. Zonca, Nucl. Fusion **41**, 747 (2001)

[20] T.-H. Watanabe and H. Sugama, Phys. plasmas **11**, 1476 (2004)

[21] H. Sugama, T.-H. Watanabe, and W. Horton, Phys. plasmas **10**, 726 (2003)

Chapter 5

Nonlinear entropy transfer via zonal flows in toroidal plasma turbulence

5.1 Introduction

One of the most important findings obtained from the gyrokinetic theory and the numerical simulations for drift-wave turbulence, especially the ITG driven turbulence, is effective regulation of the turbulent transport by self-generated zonal flows [1–3]. Zonal flows are nonlinearly generated through the Reynolds stress resulting from turbulent flows in the drift-wave turbulence, where the radial scale-length of the zonal-flow shear is associated with a typical wavenumber range of the turbulence. Existence of ion-scale zonal flows has been experimentally revealed by a direct measurement of electrostatic potential in laboratory experiments [4]. Tremendous efforts have been devoted so far to the study of the zonal-flow dynamics, with the aim of elucidating the physical mechanisms of the zonal-flow generation, the nonlinear saturation of the linear instability growth, and the transport suppression through the nonlinear interactions between the zonal flow and the drift-wave turbulence. A comprehensive review of earlier works on the physics of the zonal-flow generation is given in Ref. 5. In contrast with the primary drift-wave instability, the zonal-flow generation is considered as resulting from a "secondary" instability, e.g., the nonlinear parametric [6,7] or the Kelvin-Helmholtz [8,9] instabilities. For the saturation of the zonal-flow growth in the drift-wave turbulence, several mechanisms have been discussed. The generalized Kelvin-Helmholtz instability, which is considered as a "tertiary" instability, is one of the candidates for the saturation mechanism of the zonal flow generation in ITG turbulence [8,9].

In the ETG turbulence, potential fluctuations with scale lengths of electron thermal gyroradii are shielded by the adiabatic responses of ions resulting from the perpendicular gyromotion with

larger thermal gyroradii. Thus, the zonal-flow generation in the ETG turbulence is relatively weaker than that in the ITG turbulence so that the ETG turbulence involves not only zonal flows, but also various vortex structures, of which the appearance strongly depends on geometrical and plasma parameters [10–14]. Particularly, the ETG turbulence simulation for a tokamak with a reversed magnetic-shear profile has revealed that the electron heat transport is significantly reduced by the strong zonal-flow generation in the negative magnetic-shear region near the q-minimum surface (q denotes the safety factor) [11, 12].

Dynamics of turbulent vortices and zonal flows, and the related transport processes in high temperature collisionless (or weakly collisional) magnetized plasmas involves a lot of kinetic processes, i.e., the Landau damping, the finite gyroradius effect, the particle drift, and the magnetic trapping. In the kinetic turbulent transport processes, the microscopic fluctuations of the distribution function, the turbulent transport flux, and the collisional dissipation are closely related to each other through the entropy balance equation [15–19]. Particularly, the nonlinear entropy transfer between non-zonal and zonal modes is described by the entropy transfer function, which is regarded as a kinetic extension of zonal-flow energy production due to the Reynolds stress. The entropy balance relations for zonal and non-zonal modes provide ones with a systematic method to quantify the nonlinear interaction between drift-wave turbulence and zonal flows in turbulent transport processes based on the kinetic theory. Some earlier works have discussed the nonlinear energy (not entropy) transfer between zonal flows and the drift-wave turbulence based on the theoretical analysis with a fluid model [20, 21] and on the bi-spectrum analysis for the density (or potential) fluctuation data obtained from experiments [22–24].

In order to evaluate quantitatively the transport level resulted from the interactions between the zonal flow and drift-wave turbulence, the nonlinear gyrokinetic simulations are indispensable. Waltz *et al.* have extensively examined mechanisms of the transport suppression by zonal flows (including the geodesic acoustic modes) in terms of the nonlinear gyrokinetic simulations of the ITG-TEM turbulence and the ETG turbulence with adiabatic ions [25]. They have also discussed the spectral structures of the entropy transfer function in the steady state of the ITG-TEM turbulence. In addition, several works on the entropy transfer (or cascade) processes based on the gyrokinetic entropy balance have been reported recently [26–28]. However, the role of zonal flows in the nonlinear entropy transfer processes in the steady turbulence state, which is crucial for determining the resultant transport level, has not been fully clarified. Moreover, it has not been revealed whether the entropy transfer processes among turbulent vortices and zonal flows are different between the saturation phase of the instability growth and the steady phase of turbulence.

In this chapter, the nonlinear entropy transfer processes among non-zonal and zonal modes

in toroidal ITG and ETG turbulence are investigated by means of five-dimensional nonlinear gyrokinetic Vlasov simulations. The detailed spectral analysis of the entropy transfer function reveals the role of zonal flows in the nonlinear entropy transfer process, which leads to the saturation of instability growth and transport suppression in the steady state.

The remainder of this chapter is organized as follows. A theoretical model used in the present study is described in Sec. 5.2. Nonlinear gyrokinetic simulation results of the toroidal ITG and ETG turbulence are presented in Sec. 5.3. Then, in addition to the entropy balance relations for non-zonal and zonal modes, wavenumber spectra of turbulent fluctuations and the heat flux are compared. In Sec. 5.4, differences between entropy transfer processes in the ITG and ETG turbulence are discussed through the comparisons of the wavenumber spectra of the triad entropy transfer function. Also, comparisons of the entropy transfer processes between slab and toroidal systems are presented. Finally, concluding remarks are given in Sec. 5.5.

5.2 Theoretical model and linear stability analysis

Numerical simulations of the toroidal ITG and ETG turbulence presented here are carried out by using the GKV code [3] based on the electrostatic gyrokinetic model. The electrostatic gyrokinetic equation for the perturbed distribution function $\delta f_{s\boldsymbol{k}_\perp}^{(g)}$ written in the $\boldsymbol{k}_\perp$-space is given by

$$\left[\frac{\partial}{\partial t} + v_\parallel \boldsymbol{b}\cdot\nabla + i\omega_{\mathrm{Ds}} - \frac{\mu}{m_s}\boldsymbol{b}\cdot\nabla B\frac{\partial}{\partial v_\parallel}\right]\delta f_{s\boldsymbol{k}_\perp}^{(g)} - \frac{c}{B}\sum_\Delta \boldsymbol{b}\cdot(\boldsymbol{k}_\perp'\times\boldsymbol{k}_\perp'')\,\delta\psi_{\boldsymbol{k}_\perp'}\delta f_{s\boldsymbol{k}_\perp''}^{(g)}$$

$$= F_{\mathrm{Ms}}\left(i\omega_{*Ts} - i\omega_{\mathrm{Ds}} - v_\parallel\boldsymbol{b}\cdot\nabla\right)\frac{e_s\delta\psi_{\boldsymbol{k}_\perp}}{T_s} - C_s^{(g)}\left[\delta f_{s\boldsymbol{k}_\perp}^{(g)}\right], \quad (5.1)$$

where $\omega_{\mathrm{Ds}} \equiv (c/e_s B)\boldsymbol{k}_\perp\cdot\boldsymbol{b}\times(\mu\nabla B + m_s v_\parallel^2\boldsymbol{b}\cdot\nabla\boldsymbol{b})$ and $\omega_{*Ts} \equiv (cT_s/e_s B)\{1+\eta_s[(m_s v_\parallel^2 + 2\mu B)/2T_s - 3/2]\}\boldsymbol{k}_\perp\cdot\boldsymbol{b}\times\nabla\ln n_s$ with $\eta_s = |\nabla\ln T_s|/|\nabla\ln n_s|$ [the subscript "s" denotes the particle species for ions (s=i) or electrons (s=e)]. Here, $\boldsymbol{b}$, B, c, m_s, n_s, e_s, T_s and $\delta\psi_{\boldsymbol{k}_\perp}$ are the unit vector parallel to the magnetic field, the magnetic field strength, the speed of right, the particle mass, the particle number density, the electric charge, the equilibrium temperature and the electrostatic potential fluctuation averaged over the gyrophase, respectively. The symbol $\sum_\Delta$ appearing in the nonlinear term of Eq. (5.1) stands for the summation over Fourier modes which satisfy the triad-interaction condition, i.e., $\boldsymbol{k}_\perp = \boldsymbol{k}_\perp' + \boldsymbol{k}_\perp''$. The parallel velocity $v_\parallel$ and the magnetic moment μ are used as the velocity-space coordinates, where μ is defined by $\mu \equiv m_s v_\perp^2/2B$ with the perpendicular velocity $v_\perp$. The equilibrium part of the distribution function is given by the local Maxwellian distribution, i.e., $F_{\mathrm{Ms}} = n_s(m_s/2\pi T_s)^{3/2}\exp[-(m_s v_\parallel^2 + 2\mu B)/2T_s]$. A weak collisional effect is introduced in

terms of a model collision operator given by

$$C_s^{(g)} = \nu_s \left[\frac{1}{v_\perp} \frac{\partial}{\partial v_\perp} \left(v_\perp \frac{\partial}{\partial v_\perp} + \frac{v_\perp^2}{v_{ts}^2} \right) + \frac{\partial}{\partial v_\parallel} \left(\frac{\partial}{\partial v_\parallel} + \frac{v_\parallel}{v_{ts}^2} \right) \right] , \tag{5.2}$$

where ν_s and $v_{ts} \equiv (T_s/m_s)^{1/2}$ are the collision frequency and the thermal speed, respectively. The collision operator acting on $\delta f_{s\boldsymbol{k}_\perp}^{(g)}$ smooths out the fine-scale fluctuations in the velocity-space. Although the above collision operator does not conserve the momentum and the energy, its influence on the main results shown below, such as the transport level and the entropy transfer processes, are not crucial as long as $\nu_s L_{n_0}/v_{ts} \ll 1$.

A local toroidal flux-tube system in a large-aspect-ratio tokamak with the concentric circular flux surfaces is considered here [29]. The magnetic field is given by $\boldsymbol{B} = B[\mathbf{e}_\zeta + (r/R_0)\mathbf{e}_\theta]$ with neglecting $O[(r/R_0)^2]$ terms, where r, R_0, q, $\mathbf{e}_\zeta$ and $\mathbf{e}_\theta$ denote the minor and the major radii, the safety factor, the unit vectors in the toroidal(ζ) and poloidal(θ) directions, respectively. The field-aligned coordinates (x, y, z) are, then, introduced by $x = r - r_0$, $y = (r_0/q_0)[q\theta - \zeta]$, $z = \theta$ with $q = q_0[1 + \hat{s}(r - r_0)/r_0]$, where r_0 and $\hat{s}$ represent the radial position of the flux-tube center and the magnetic shear parameter assumed to be constant, respectively. Use of the field-aligned coordinates enables us to impose the periodic boundary condition in the x- and y-directions so that the nonlinear $\boldsymbol{E} \times \boldsymbol{B}$ convection term [the last term in the left-hand side of Eq. (5.1)] is calculated numerically by means of the Fourier spectral method, where the perpendicular wavenumber vector $\boldsymbol{k}_\perp$ and the squared norm $k_\perp^2$ are written as $\boldsymbol{k}_\perp = k_x \nabla x + k_y \nabla y$ and $k_\perp^2 = (k_x + \hat{s}zk_y)^2 + k_y^2$, respectively. (Note here that $\boldsymbol{b} \cdot \nabla x = 0$ and $\boldsymbol{b} \cdot \nabla y = 0$, but $\nabla x \cdot \nabla y \neq 0$.) In this coordinate system, the magnetic field strength B is reduced to $B = B_0(1 - \epsilon \cos z)$ with $\epsilon \equiv r_0/R_0$, and then the operators $\boldsymbol{b} \cdot \nabla$, ω_{Ds} and ω_{*Ts} in Eq. (5.1) are written as

$$\boldsymbol{b} \cdot \nabla = \frac{1}{q_0 R_0} \frac{\partial}{\partial z} , \tag{5.3}$$

$$\omega_{Ds} = -\sigma_s \frac{v_\parallel^2 + \mu B}{v_{ts} R_0} \left[k_x \rho_{ts} \sin z + k_y \rho_{ts} (\cos z + \hat{s}z \sin z) \right], \tag{5.4}$$

$$\omega_{*Ts} = -\sigma_s \frac{v_{ts}}{L_{n_s}} \left[1 + \eta_s \left(\frac{m_s v_\parallel^2 + 2\mu B}{2T_s} - \frac{3}{2} \right) \right] k_y \rho_{ts} , \tag{5.5}$$

in the low-β limit, respectively, where $\sigma_s = \{1$ (for s = i), -1 (for s = e)$\}$ and the thermal gyroradius is denoted by $\rho_{ts} = (v_{ts}/\Omega_s)|_{B=B_0}$ with the gyrofrequency $\Omega_s = m_s c/|e_s|B$. The gradient scale-length of the density profile is represented by $L_{n_s} \equiv |\nabla \ln n_s|^{-1}$.

The potential fluctuation evaluated at the particle position, $\delta\phi_{\boldsymbol{k}_\perp}$, is related to the gyrophase-averaged one, i.e., $\delta\psi_{\boldsymbol{k}_\perp} = J_{0s}\delta\phi_{\boldsymbol{k}_\perp}$, and is determined by the Poisson equation written in the

wavenumber-space as follows,

$$
\begin{aligned}
k_\perp^2 \lambda_{\mathrm{De}}^2 n_0 \frac{e\delta\phi_{k_\perp}}{T_{\mathrm{e}}} &= \left[\int d\boldsymbol{v} J_{0\mathrm{i}} \delta f_{\mathrm{i}k_\perp}^{(\mathrm{g})} - n_0 \frac{e\delta\phi_{k_\perp}}{T_{\mathrm{i}}} (1 - \Gamma_{0\mathrm{i}}) \right] \\
&\quad - \left[\int d\boldsymbol{v} J_{0\mathrm{e}} \delta f_{\mathrm{e}k_\perp}^{(\mathrm{g})} + n_0 \frac{e\delta\phi_{k_\perp}}{T_{\mathrm{e}}} (1 - \Gamma_{0\mathrm{e}}) \right],
\end{aligned}
\tag{5.6}
$$

where $|e_{\mathrm{i}}| = |e_{\mathrm{e}}| = e$ and $n_{\mathrm{i}} = n_{\mathrm{e}} = n_0$ are assumed. The electron Debye-length is denoted by $\lambda_{\mathrm{De}} \equiv (T_{\mathrm{e}}/4\pi n_0 e^2)^{1/2}$. The first and the second groups of terms on the right hand side of Eq. (5.6) indicate the ion and electron density fluctuations represented with the gyrocenter distribution function and the electrostatic potential, respectively. Here, $J_{0\mathrm{s}}$ and $\Gamma_{0\mathrm{s}}$ are defined by $J_{0\mathrm{s}} \equiv J_0(k_\perp v_\perp/\Omega_{\mathrm{s}})$ and $\Gamma_{0\mathrm{s}} \equiv I_0(b_{\mathrm{s}}) \exp(-b_{\mathrm{s}})$ with the zeroth-order Bessel and modified Bessel functions for $b_{\mathrm{s}} \equiv k_\perp^2 v_{\mathrm{ts}}^2/\Omega_{\mathrm{s}}^2$, respectively. For the ITG turbulence with $k_\perp \rho_{\mathrm{te}} \ll 1$, the adiabatic electron response is assumed (except for zonal modes) so that Eq. (5.6) is reduced to

$$
\int d\boldsymbol{v} J_{0\mathrm{i}} \delta f_{\mathrm{i}k_\perp}^{(\mathrm{g})} = n_0 \Lambda_{\mathrm{i}k_\perp} \frac{e\delta\phi_{k_\perp}}{T_{\mathrm{i}}} - n_0 \left\langle \frac{e\delta\phi_{k_\perp}}{T_{\mathrm{e}}} \right\rangle \delta_{k_y,0} \quad (\text{ for ITG }),
\tag{5.7}
$$

where $\Lambda_{\mathrm{i}k_\perp} \equiv 1 + T_{\mathrm{i}}/T_{\mathrm{e}} - \Gamma_{0\mathrm{i}}$ and $\delta_{m,n}$ is the Kronecker delta. The angular brackets $\langle \cdots \rangle$ stand for the field line average, i.e., $\langle A_{k_\perp} \rangle \equiv \int dz A_{k_\perp} B^{-1}/\int dz B^{-1}$. Thus, $\langle A_{k_\perp} \rangle \delta_{k_y,0}$ is equivalent to the flux surface average of A. For the ETG turbulence with $k_\perp \rho_{\mathrm{ti}} \gg 1$, the ion response to the potential fluctuation is reduced to the adiabatic one because of $J_{0\mathrm{i}} \ll 1$ and $\Gamma_{0\mathrm{i}} \ll 1$. Then, Eq. (5.6) is rewritten as

$$
\int d\boldsymbol{v} J_{0\mathrm{e}} \delta f_{\mathrm{e}k_\perp}^{(\mathrm{g})} = -n_0 \Lambda_{\mathrm{e}k_\perp} \frac{e\delta\phi_{k_\perp}}{T_{\mathrm{e}}} \quad (\text{ for ETG }).
\tag{5.8}
$$

Here, $\Lambda_{\mathrm{e}k_\perp} \equiv 1 + T_{\mathrm{e}}/T_{\mathrm{i}} - \Gamma_{0\mathrm{e}}$, and the finite Debye length effect $k_\perp^2 \lambda_{\mathrm{De}}^2$ is ignored.

Using the closed set of equations described above, one obtains a balance equation with respect to the entropy variable $\delta S_{sk_\perp}$ defined as a functional of the perturbed gyrocenter distribution function $\delta f_{sk_\perp}^{(\mathrm{g})}$. The velocity space integral and the field line average of Eq. (5.1) multiplied by $\delta f_{sk_\perp}^{(\mathrm{g})*}/F_{\mathrm{Ms}}$ lead to

$$
\frac{\partial}{\partial t} \left(\delta S_{sk_\perp} + W_{sk_\perp} \right) = L_{T_{\mathrm{s}}}^{-1} Q_{sk_\perp} + \mathcal{T}_{sk_\perp} + D_{sk_\perp} ,
\tag{5.9}
$$

where

$$
\delta S_{sk_\perp} \equiv \left\langle \int d\boldsymbol{v} \frac{|\delta f_{sk_\perp}^{(\mathrm{g})}|^2}{2F_{\mathrm{Ms}}} \right\rangle ,
\tag{5.10}
$$

$$
Q_{sk_\perp} \equiv \mathrm{Re} \left\langle i v_{\mathrm{ts}} \int d\boldsymbol{v}\, \delta f_{sk_\perp}^{(\mathrm{g})} \left(\frac{m_{\mathrm{s}} v_\parallel^2 + 2\mu B}{2T_{\mathrm{s}}} \right) k_y \rho_{\mathrm{ts}} \frac{e\delta\psi_{k_\perp}^*}{T_{\mathrm{s}}} \right\rangle ,
\tag{5.11}
$$

$$
D_{sk_\perp} \equiv \mathrm{Re} \left\langle \int d\boldsymbol{v}\, C_{\mathrm{s}}^{(\mathrm{g})} \left[\delta f_{sk_\perp}^{(\mathrm{g})} \right] \frac{h_{sk_\perp}^*}{F_{\mathrm{Ms}}} \right\rangle ,
\tag{5.12}
$$

denote the entropy variable, the turbulent heat flux, and the collisional dissipation, respectively. (Note that no particle flux is driven by the turbulence with the adiabatic response of background particles.) The gradient scale-length of the temperature profile is represented by $L_{T_s} \equiv |\nabla \ln T_s|^{-1}$. The non-adiabatic part of the perturbed gyrocenter distribution function, $h_{sk_\perp}$, is defined by

$$\delta f_{sk_\perp}^{(g)} = -\frac{e_s \delta \psi_{k_\perp}}{T_s} F_{Ms} + h_{sk_\perp} . \tag{5.13}$$

By using Eqs. (5.7) and (5.8), the potential energy $W_{sk_\perp}$ is given by

$$W_{ik_\perp} = \frac{n_0}{2} \left\langle \left(\Lambda_{ik_\perp} - \frac{T_i}{T_e} \delta_{k_y,0} \right) \left| \frac{e \delta \phi_{k_\perp}}{T_i} \right|^2 \right\rangle , \tag{5.14}$$

$$W_{ek_\perp} = \frac{n_0}{2} \left\langle \Lambda_{ek_\perp} \left| \frac{e \delta \phi_{k_\perp}}{T_e} \right|^2 \right\rangle , \tag{5.15}$$

for ions and electrons, respectively. The second term in the right hand side of Eq. (5.9) represents the nonlinear entropy transfer in the wavenumber space. The definition of the entropy transfer function $\mathcal{T}_{sk_\perp}$ is given by

$$\mathcal{T}_{sk_\perp} = \sum_{p_\perp} \sum_{q_\perp} \delta_{k_\perp + p_\perp + q_\perp, 0} \mathcal{J}_s [k_\perp | p_\perp, q_\perp] , \tag{5.16}$$

$$\mathcal{J}_s [k_\perp | p_\perp, q_\perp] \equiv \left\langle \frac{c}{B} b \cdot (p_\perp \times q_\perp) \int dv \frac{1}{2F_{Ms}} \mathrm{Re} \left[\delta \psi_{p_\perp} h_{sq_\perp} h_{sk_\perp} - \delta \psi_{q_\perp} h_{sp_\perp} h_{sk_\perp} \right] \right\rangle , \tag{5.17}$$

where the notation with $k_\perp'$ and $k_\perp''$ shown in Eq. (5.1) is replaced here by $-p_\perp$ and $-q_\perp$, respectively, in order to represent symmetrically the triad-interaction condition for three wavenumber vectors, i.e., $k_\perp + p_\perp + q_\perp = 0$. In Eq. (5.16), $\mathcal{J}_s[k_\perp | p_\perp, q_\perp]$ is summed over $p_\perp$ and $q_\perp$. For convenience, we call the function $\mathcal{J}_s[k_\perp | p_\perp, q_\perp]$ the "triad (entropy) transfer function", hereafter. It should be noted that the triad transfer function possesses the following symmetry properties,

$$\mathcal{J}_s [k_\perp | p_\perp, q_\perp] = \mathcal{J}_s [k_\perp | q_\perp, p_\perp] , \tag{5.18}$$

$$\mathcal{J}_s [k_\perp | p_\perp, q_\perp] = \mathcal{J}_s [-k_\perp | -p_\perp, -q_\perp] . \tag{5.19}$$

Furthermore, one obtains straightforwardly the "detailed balance relation" for the triad-interactions,

$$\mathcal{J}_s [k_\perp | p_\perp, q_\perp] + \mathcal{J}_s [p_\perp | q_\perp, k_\perp] + \mathcal{J}_s [q_\perp | k_\perp, p_\perp] = 0 . \tag{5.20}$$

Positive values of the triad transfer function $\mathcal{J}_s[k_\perp | p_\perp, q_\perp]$ mean that the entropy is transferred from two modes with $p_\perp$ and $q_\perp$ toward the mode with $k_\perp (= -p_\perp - q_\perp)$ and that the possible combinations of the signs of $(\mathcal{J}_s[k_\perp | p_\perp, q_\perp], \mathcal{J}_s[p_\perp | q_\perp, k_\perp], \mathcal{J}_s[q_\perp | k_\perp, p_\perp])$ satisfying the detailed balance relation should be $(+, -, -)$, $(+, +, -)$ and $(+, -, +)$. Negative values of $\mathcal{J}_s[k_\perp | p_\perp, q_\perp]$ indicate the entropy transfer in the opposite direction, then $(-, +, +)$, $(-, -, +)$ and $(-, +, -)$ are

the possible combinations of the triad transfer functions. The detailed balance relation Eq. (5.20) with the symmetric properties of Eqs. (5.18) and (5.19) is useful for the entropy transfer analysis of the toroidal ITG and ETG turbulence simulation results shown in Sec. 5.4, where the nonlinear interactions among turbulent fluctuations and zonal flows are quantified.

Similar discussions on the "energy transfer function" are often found in the study of the isotropic fluid turbulence governed by the Navier-Stokes equation [30]. The isotropic nature enables us to simplify the energy transfer function as a function of the only wavenumber magnitude so that the several analytic expressions are derived by means of closure models such as the quasi-normal Markovian (QNM) model [30] and the direct interaction approximation (DIA) [31, 32]. Then, the spectral analysis of the transfer function describes the local energy cascade processes, e.g., the normal and the inverse energy cascade processes for the three- and two-dimensional isotropic turbulence, respectively. On the other hand, since the (quasi) two-dimensional magnetized plasma turbulence considered here is inherently anisotropic due to the existence of meso-scale coherent flow structures such as zonal flows and streamers, the direct numerical simulation is a powerful tool for examining the entropy transfer function.

The explicit description of the entropy balance relation for the non-zonal ($k_y \neq 0$) and zonal ($k_y = 0$) modes is useful for the following discussions concerning the entropy transfer processes among zonal flows and turbulence. By taking the integration of Eq. (5.9) over the non-zonal and zonal modes and by using the detailed balance relation of Eq. (5.20), one obtains

$$\frac{d}{dt}\left(\delta S_{\rm s}^{\rm (trb)} + W_{\rm s}^{\rm (trb)}\right) = L_{T_{\rm s}}^{-1} Q_{\rm s} - \mathcal{T}_{\rm s}^{\rm (zf)} + D_{\rm s}^{\rm (trb)} , \qquad (5.21)$$

$$\frac{d}{dt}\left(\delta S_{\rm s}^{\rm (zf)} + W_{\rm s}^{\rm (zf)}\right) = \mathcal{T}_{\rm s}^{\rm (zf)} + D_{\rm s}^{\rm (zf)} , \qquad (5.22)$$

where the superscripts "(trb)" and "(zf)" represent the turbulence (or non-zonal) and zonal-flow components, respectively. The above entropy balance relations for non-zonal and zonal modes have been derived and discussed in detail by Sugama *et al.* [17]. Note here that zonal flows never contribute to the radial heat flux $Q_{{\rm s}k_\perp}$ as seen from Eq. (5.22). The entropy transfer function integrated over the zonal modes, $\mathcal{T}_{\rm s}^{\rm (zf)}$, represents the entropy transfer from turbulence to zonal flows so that the negative sign of $\mathcal{T}_{\rm s}^{\rm (zf)}$ appears in Eq. (5.21). As shown in Ref. 17, by using the simplest approximation for the non-adiabatic part of the ion gyrocenter distribution function, i.e., $h_{{\rm i}k_\perp} \simeq n_0 F_{\rm Mi}(1 + k_\perp^2 \rho_{\rm ti}^2/2)e\delta\phi_{k_\perp}/T_{\rm i}$, the entropy transfer function $\mathcal{T}_{\rm i}^{\rm (zf)}$ reduces to the energy production term, which is described by the product of the Reynolds stress due to the non-zonal turbulent flows and the zonal-flow shear. Thus, $\mathcal{T}_{\rm s}^{\rm (zf)}$ is regarded as a kinetic extension of the zonal-flow energy production due to the Reynolds stress.

As seen from Eq. (5.21), the turbulence part of the entropy $\delta S_{\rm s}^{\rm (trb)}$ is produced by the turbulent heat flux $L_{T_{\rm s}}^{-1} Q_{\rm s}$, partly dissipated by collisions $D_{\rm s}^{\rm (trb)}$, and partly transferred to the zonal
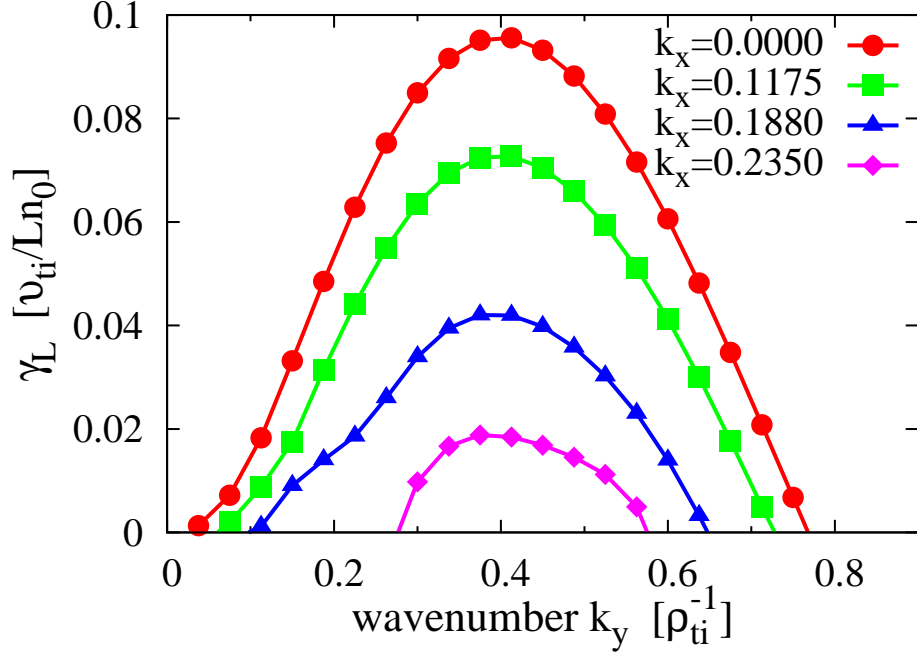
FIG. 5.1: Wavenumber spectrum of the linear growth rate γ_L of the toroidal ITG instability. The spectrum for the toroidal ETG instability is the same as that in the ITG case except for the normalizations with v_{te} and ρ_{te}.

flow components via the transfer term $\mathcal{T}_s^{(zf)}$. When the turbulence reaches a statistically steady state, the balance relations of $\overline{\mathcal{T}}_s^{(zf)} = -\overline{D}_s^{(zf)} \geqslant 0$ and $L_{T_s}^{-1}\overline{Q}_s - \overline{\mathcal{T}}_s^{(zf)} = -\overline{D}_s^{(trb)}$ are realized separately, where the overline denotes the time-average in a steady phase. The entropy balance relations of Eqs. (5.21) and (5.22) provide us with not only the physical insight into the entropy transfer processes among zonal flows and turbulence, but also a good measure for the accuracy of turbulence simulations.

The nonlinear gyrokinetic simulation results, as will be shown below, have been obtained by means of the GKV code, that is a gyrokinetic Vlasov solver with the flux-tube configuration applicable to both the tokamak and helical systems [3]. The physical parameters of $\epsilon = 0.18$, $q_0 = 1.5$, $\hat{s} = 0.4$, $R_0/L_{T_s} = 6.92$, $\eta_s = 2.0$ and $T_i = T_e$ are the same as the Cyclonebase case, except that the smaller values of the magnetic-shear parameter $\hat{s}$ and η_s are used here to make it easier to carry out the ETG turbulence simulation. The weak collisional effect is introduced with $\nu_s L_{n_0}/v_{ts} = 10^{-3}$. The number of Fourier modes in the perpendicular wavenumber space and the number of grids in the z-, $v_\parallel$-, and μ-directions are set to be $(N_{k_x}, N_{k_y}, N_z, N_{v_\parallel}, N_\mu) = (64, 129, 128, 64, 32)$. The corresponding ranges of the phase-space coordinates are given as $0 \leqslant k_x \leqslant k_{x(max)} = 1.5\rho_{ts}^{-1}$, $-k_{y(max)} \leqslant k_y \leqslant k_{y(max)} = 2.4\rho_{ts}^{-1}$, $-\pi \leqslant z \leqslant \pi$, $-5v_{ts} \leqslant$

$v_{\parallel} \leqslant 5v_{\text{ts}}$, and $0 \leqslant \mu \leqslant 12.5(m_{\text{s}}v_{\text{ts}}^2/B_0)$, respectively. The modified periodic boundary condition is imposed in the z-direction [29]. The size of the perpendicular domain is $L_x \times L_y = 266\rho_{\text{ts}} \times 168\rho_{\text{ts}}$, and the non-zero minimum absolute values of the wavenumber are $k_{x(\text{min})} = 0.0235\rho_{\text{ts}}^{-1}$ and $k_{y(\text{min})} = 0.0375\rho_{\text{ts}}^{-1}$. The time integration is carried out with $\Delta t = 0.025(L_{n_0}/v_{\text{ts}})$.

In the followings, physical quantities are normalized as $x = x'/\rho_{\text{ts}}$, $y = y'/\rho_{\text{ts}}$, $v_{\parallel} = v'_{\parallel}/v_{\text{ts}}$, $\mu = \mu'(B_0/m_{\text{s}}v_{\text{ts}}^2)$, $t = t'(v_{\text{ts}}/L_{n_0})$, $v_{\text{s}} = v'_{\text{s}}(L_{n_0}/v_{\text{ts}})$, $F_{\text{Ms}} = F'_{\text{Ms}}(v_{\text{ts}}^3/n_0)$, $\delta f^{(\text{g})}_{s\boldsymbol{k}_{\perp}} = \delta f^{(\text{g})'}_{s\boldsymbol{k}_{\perp}}(v_{\text{ts}}^3/n_0)(L_{n_0}/\rho_{\text{ts}})$ and $\delta\phi_{\boldsymbol{k}_{\perp}} = \delta\phi'_{\boldsymbol{k}_{\perp}}(e/T_{\text{s}})(L_{n_0}/\rho_{\text{ts}})$, where the prime means a dimensional quantity.

The wavenumber spectrum of the linear growth rate γ_{L} for the toroidal ITG instability is shown in Fig. 5.1, where the physical parameters shown above are used. One finds that the maximum growth rate of $\gamma_{\text{L(max)}} = 9.56 \times 10^{-2} v_{\text{ti}}/L_{n_0}$ is observed at $(k_x = 0, k_y = 0.4125\rho_{\text{ti}}^{-1})$. The effect of the finite k_x reduces the growth rate, then the toroidal ITG instability are completely stabilized for $k_x \geqslant 0.3\rho_{\text{ti}}^{-1}$. As will be discussed below, the stabilizing effect in the higher k_x region is important for the regulation of turbulent transport by zonal flows. Also, note that the spectrum of γ_{L} for the toroidal ETG instability is the same as that plotted in Fig. 5.1 except for the normalizations with v_{te} and ρ_{te}.

5.3   Nonlinear simulations

5.3.1   Entropy balance relation

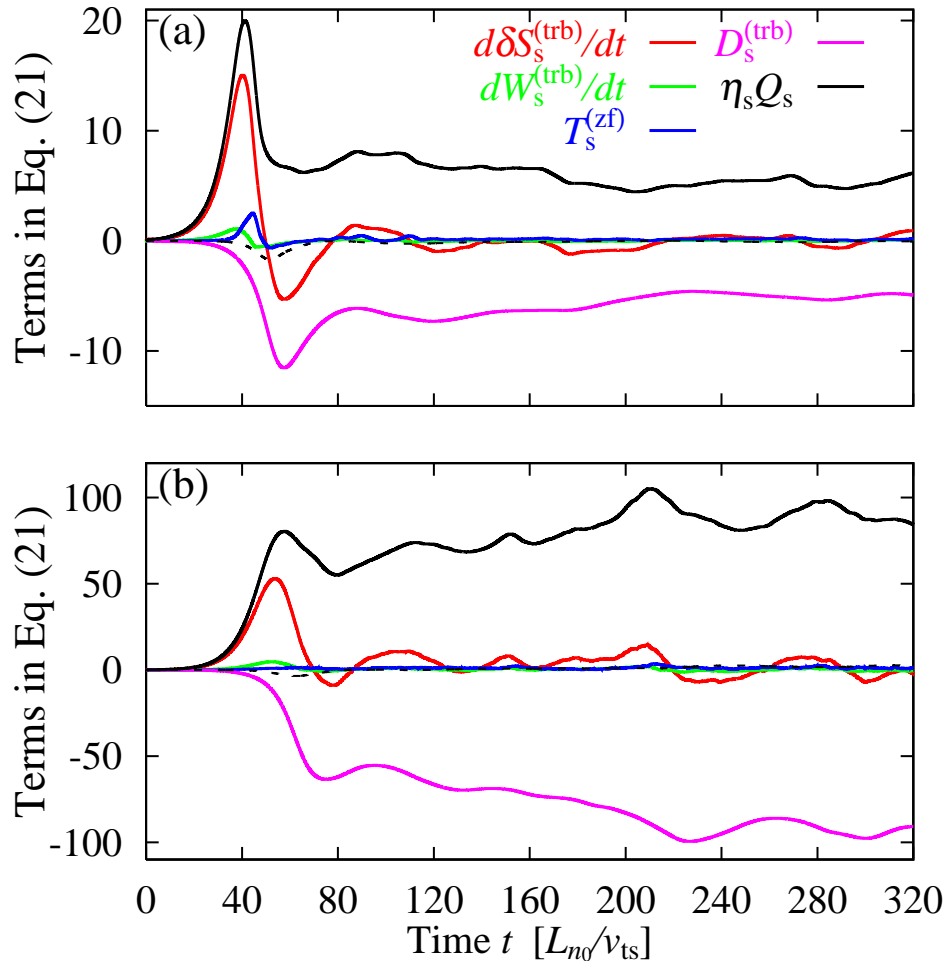The results of nonlinear gyrokinetic simulations for the toroidal ITG and ETG turbulence are shown and discussed in this section. Time evolutions of each term in the entropy balance relation of the turbulence part, Eq. (5.21), for the toroidal ITG and ETG turbulence are plotted in Figs. 5.2(a) and 5.2(b), respectively. Here, the turbulent heat flux $L_{T_{\text{s}}}^{-1}Q_{\text{s}}$ shown in Eqs. (5.9) and (5.11) is rewritten as $\eta_{\text{s}}Q_{\text{s}}$ by the use of the normalization with L_{n_0}. The deviation from the exact balance is also plotted by the dashed line, where one finds that the entropy balance relation is well satisfied for the whole simulation time in both the ITG and ETG cases. As discussed in Sec. 5.2, the turbulence part of the entropy $\delta S_{\text{s}}^{(\text{trb})}$, which characterizes the turbulence intensity, is produced by the ITG (or ETG)-instability-driven heat flux $L_{T_{\text{s}}}^{-1}Q_{\text{s}}$. Then, the saturation of the linear instability growth, which is observed at $t \sim 45(\sim 60)$ for the ITG (ETG) case, occurs due to the nonlinear entropy transfer $\mathcal{T}_{\text{s}}^{(\text{zf})}$ and the collisional dissipation $D_{\text{s}}^{(\text{trb})}$. Thus, the quantity $\mathcal{R}_{\text{s}} \equiv \mathcal{T}_{\text{s}}^{(\text{zf})}/(-D_{\text{s}}^{(\text{trb})})$ provides ones with a good measure for evaluating the effect of the nonlinear entropy transfer to zonal modes on the linear instability saturation. The typical values [evaluated at $t = 45$ (or $t = 60$) for the ITG (or ETG) case] are $\mathcal{R}_{\text{i}} = 5.92 \times 10^{-1}$ and $\mathcal{R}_{\text{e}} = 4.54 \times 10^{-2}$, respectively. The larger value of $\mathcal{R}_{\text{i}}$ indicates that the nonlinear entropy transfer from non-zonal

ITG modes to zonal modes is substantial for the saturation of the ITG instability growth, while the entropy transfer to zonal modes has little contribution to the saturation of the ETG instability growth. Indeed, some earlier works on the gyrokinetic simulations of toroidal ETG turbulence with adiabatic ions have also pointed out that the saturation of the ETG instability is mainly associated with the nonlinear coupling among non-zonal drift-wave fluctuations rather than the zonal-flow generation for the cases with moderate or strong magnetic-shear [25, 33]. It is also found that the statistically steady states are realized for $t \gtrsim 120$ in the ITG case and for $t \gtrsim 220$ in the ETG case, where the balance relation of $\eta_s \overline{Q}_s - \overline{\mathcal{T}}_s^{(zf)} = -\overline{D}_s^{(trb)}$ holds. (The time-average in the steady state is denoted by the overline.) The saturation levels of the turbulent heat flux for the ITG and ETG cases are evaluated as $\eta_i \overline{Q}_i = 5.31$ and $\eta_e \overline{Q}_e = 88.8$ in the unit of $(\rho_{ts}/L_{n_0})^2 (n_0 v_{ts})$,

FIG. 5.2: Time evolutions of each term in the entropy balance relation of the turbulence part, Eq. (5.21), for toroidal (a)ITG (s = i) and (b)ETG (s = e) turbulence. The deviation from the exact balance is also plotted by the dashed line.

respectively, where the time average is taken over $220 \leqslant t \leqslant 320$ for both cases. As will be shown in Sec. 5.3.2, the strong zonal flows are sustained in the steady state of the ITG turbulence, while the radially elongated streamers with high amplitude are formed in the ETG case with the strong electron heat transport [cf. Figs. 5.6].

The similar plots for the entropy balance relation of the zonal-flow part, Eq. (5.22), are shown in Figs. 5.3(a) and 5.3(b). The deviation from the exact balance is quite small in both the ITG and ETG cases so that the linear and nonlinear dynamics of zonal flows are accurately solved. One finds the balance relation of $\overline{\mathcal{T}}_{\mathrm{s}}^{(\mathrm{zf})} = -\overline{D}_{\mathrm{s}}^{(\mathrm{zf})}$ in the statistically steady states. Also, a remarkable difference between the ITG and ETG cases is found in the time evolutions of $\mathcal{T}_{\mathrm{s}}^{(\mathrm{zf})}$. The time evolution of $\mathcal{T}_{\mathrm{i}}^{(\mathrm{zf})}$ shows a higher peak than that of $\mathcal{T}_{\mathrm{e}}^{(\mathrm{zf})}$ in the saturation phase of the linear instability growth ($t \sim 45 - 60$), then it quickly decreases and leads to the steady state with the small value of $\mathcal{T}_{\mathrm{i}}^{(\mathrm{zf})}$. In contrast, no strong peak of $\mathcal{T}_{\mathrm{e}}^{(\mathrm{zf})}$ appears in the saturation phase of the ETG instability growth, while the saturation level of the entropy transfer function is larger than that for the ITG case by a factor of 9.3 in the steady phase. Since the entropy transfer function is proportional to the fluctuation amplitude [see Eqs. (5.16) and (5.17)], the comparisons in terms of the entropy transfer function normalized by the mean heat flux, i.e., $\mathcal{T}_{\mathrm{s}}^{(\mathrm{zf})}/\eta_{\mathrm{s}}\overline{Q}_{\mathrm{s}}$, is more useful for quantifying the role of the entropy transfer in the ITG and ETG turbulence. The time-histories of $\mathcal{T}_{\mathrm{s}}^{(\mathrm{zf})}/\eta_{\mathrm{s}}\overline{Q}_{\mathrm{s}}$ for the ITG and ETG turbulence are shown in Fig. 5.3(c). One again finds that the amplitude of $\mathcal{T}_{\mathrm{i}}^{(\mathrm{zf})}/\eta_{\mathrm{i}}\overline{Q}_{\mathrm{i}}$ is much higher than $\mathcal{T}_{\mathrm{e}}^{(\mathrm{zf})}/\eta_{\mathrm{e}}\overline{Q}_{\mathrm{e}}$ in the saturation phase of $t \sim 45$, where the entropy variable of non-zonal ITG modes is efficiently transferred to zonal modes.

After the saturation of the linear instability, the amplitude of $\mathcal{T}_{\mathrm{i}}^{(\mathrm{zf})}/\eta_{\mathrm{i}}\overline{Q}_{\mathrm{i}}$ decreases quickly to a quit low level which is of the same order of magnitude as (but still 1.8 times larger than) $\mathcal{T}_{\mathrm{e}}^{(\mathrm{zf})}/\eta_{\mathrm{e}}\overline{Q}_{\mathrm{e}}$, where $\overline{\mathcal{T}}_{\mathrm{i}}^{(\mathrm{zf})}/\eta_{\mathrm{i}}\overline{Q}_{\mathrm{i}} = 2.56 \times 10^{-2}$ and $\overline{\mathcal{T}}_{\mathrm{e}}^{(\mathrm{zf})}/\eta_{\mathrm{e}}\overline{Q}_{\mathrm{e}} = 1.42 \times 10^{-2}$ (the time-average is taken over $220 \leqslant t \leqslant 320$). As discussed in the previous section, $\mathcal{T}_{\mathrm{s}}^{(\mathrm{zf})}$ is regarded as a kinetic extension of the zonal-flow production term due to the Reynolds stress, and works as a source for the zonal-flow component of the entropy $\delta S_{\mathrm{s}}^{(\mathrm{zf})}$ and the potential energy $W_{\mathrm{s}}^{(\mathrm{zf})}$ [see. Eq. (5.22)]. From this point of view, one might expect that $\mathcal{T}_{\mathrm{e}}^{(\mathrm{zf})}/\eta_{\mathrm{e}}\overline{Q}_{\mathrm{e}}$ showing the same order of magnitude as $\mathcal{T}_{\mathrm{i}}^{(\mathrm{zf})}/\eta_{\mathrm{i}}\overline{Q}_{\mathrm{i}}$ should cause the strong zonal-flow generation leading to the effective turbulent-transport suppression also in the steady state of the ETG turbulence, and this seems to contradict the results observed in Fig. 5.2(b). However, it should be noted here that the zonal-flow generation is also affected by the coefficients of $|\delta\phi_{k_x, k_y=0}|^2$ found in the right hand side of Eqs. (5.14) and (5.15) (One often refers to the coefficient as the "zonal-flow inertia"), which are quite different between the ITG and ETG cases. In the simple evaluation with the long-wavelength limit of $k_{\perp}^2\rho_{\mathrm{ts}}^2 \ll 1$, the zonal-flow inertia in the ITG and ETG turbulence are given by $1 - \Gamma_{0\mathrm{i}} \simeq k_x^2\rho_{\mathrm{ti}}^2 \equiv \mathcal{M}_{\mathrm{i}}$ and $1 + (T_{\mathrm{e}}/T_{\mathrm{i}}) - \Gamma_{0\mathrm{e}} \simeq (T_{\mathrm{e}}/T_{\mathrm{i}}) + k_x^2\rho_{\mathrm{te}}^2 \equiv \mathcal{M}_{\mathrm{e}}$, respectively. Then, for the typical wavenumber
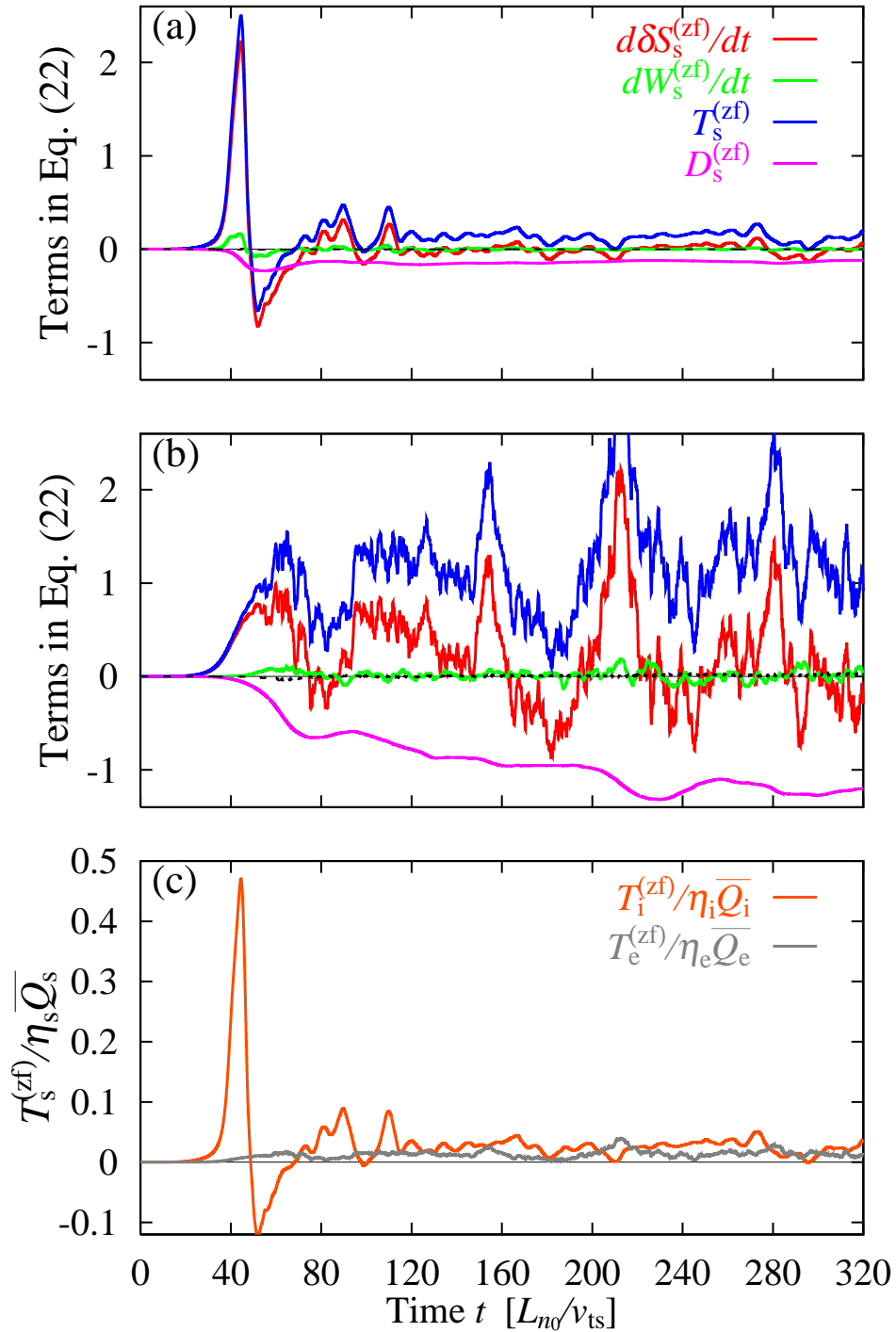
FIG. 5.3: Time evolutions of each term in the entropy balance relation of the zonal-flow part, Eq. (5.22), for toroidal (a)ITG (s = i) and (b)ETG (s = e) turbulence. The deviation from the exact balance is also plotted by the dashed line. (c)The time-histories of the entropy transfer function normalized by the time-averaged heat flux $\mathcal{T}_s^{(zf)}/\eta_s \overline{Q}_s$.

of $k_x \rho_{ts} \sim 0.1$ observed in the turbulence simulations, the zonal-flow inertia for the ETG case is much larger than that for the ITG case: typically, $\mathcal{M}_i / \mathcal{M}_e \sim 10^{-2}$. From the turbulence simulation results, the ratio of the zonal-flow inertia is evaluated as $\tilde{\mathcal{M}}_i / \tilde{\mathcal{M}}_e = 2.41 \times 10^{-2}$, where the effective zonal-flow inertia is defined by $\tilde{\mathcal{M}}_s \equiv (\overline{\delta S}_s^{(zf)} + \overline{W}_s^{(zf)}) / \sum_{k_x} \langle |\delta\phi_{k_x, k_y=0}|^2 \rangle$. The smaller value of $\tilde{\mathcal{M}}_i / \tilde{\mathcal{M}}_e$ indicates that, as well as the case of $\overline{W}_s^{(zf)} / \sum_{k_x} \overline{\langle |\delta\phi_{k_x, k_y=0}|^2 \rangle} \sim \mathcal{M}_s$, the ratio $\overline{\delta S}_s^{(zf)} / \sum_{k_x} \overline{\langle |\delta\phi_{k_x, k_y=0}|^2 \rangle}$ for the ITG case is much smaller than that for the ETG case because the contribution of the zonal density perturbation $\delta n_{s\, k_x, k_y=0}$ to $\delta S_s^{(zf)}$ is significantly reduced for the ITG case. The large zonal-flow inertia in the ETG turbulence, thus, leads to the weaker zonal-flow generation, even though the amplitude of $\mathcal{T}_e^{(zf)} / \eta_i \overline{Q}_e$ shows the similar level as $\mathcal{T}_i^{(zf)} / \eta_i \overline{Q}_i$ in the steady state.

5.3.2 Comparison of vortex structures and zonal flows in toroidal ITG and ETG turbulence

The wavenumber spectra of turbulent vortices and zonal flows in the ITG and ETG turbulence are compared in this section. The time evolutions of k_y-spectra of the fluctuation intensity are shown in Figs. 5.4(a) – (d), where the streamer intensity $\langle |\delta\phi_{k_x=0, k_y}|^2 \rangle$ [(a) and (b)] and the intensity of finite k_x modes $\langle \sum_{k_x \neq 0} |\delta\phi_{k_x, k_y}|^2 \rangle$ [(c) and (d)] for the ITG (upper row) and ETG (lower row) cases are plotted. One finds that the streamer modes with $k_x = 0$ grow linearly until the nonlinear saturation takes place at $t \sim 40 - 60$ both in the ITG and ETG cases. (The linearly most unstable streamer mode with $k_y = 0.4125$ is shown in the figures by the dashed line.) We also find that the strong zonal flow with $k_y = 0$ is nonlinearly generated in the ITG turbulence, and then, the growth of the streamer and the other finite-k_x modes is suppressed significantly [Fig. 5.4(a) and 5.4(c)]. In contrast to the ITG case, the generation of ETG-driven zonal flows is weaker because of the larger zonal-flow inertia. Thus, the ETG turbulence is dominated by the streamer modes with high amplitude [Fig. 5.4(b) and 5.4(d)]. Furthermore, it is clearly shown that, in both the streamer and the finite-k_x modes, the spectrum of the fluctuation intensity is down-shifted to the lower-k_y region through the nonlinear couplings in the saturation phases.

The similar plots for the time evolution of k_x-spectra of the intensity of the zonal-flow potential $\langle |\delta\phi_{k_x, k_y=0}|^2 \rangle$ and the non-zonal modes potential $\langle \sum_{k_y \neq 0} |\delta\phi_{k_x, k_y}|^2 \rangle$ are shown in Figs. 5.5(a) – (d). From Figs. 5.5(a) and 5.5(b), one also finds that the zonal flow generation in the ITG turbulence is much stronger than that in the ETG case. The saturation levels of the zonal-flow intensity integrated over k_x, $\langle \sum_{k_x} |\delta\phi_{k_x, k_y=0}|^2 \rangle$, in the steady states of the ITG and ETG turbulence are $16.4(T_i \rho_{ti} / eL_{n_0})^2$ and $1.79(T_e \rho_{te} / eL_{n_0})^2$, respectively, where the time average is taken over $220 \leqslant t \leqslant 320$. In the saturation phases, the intensity of non-zonal modes, which are linearly
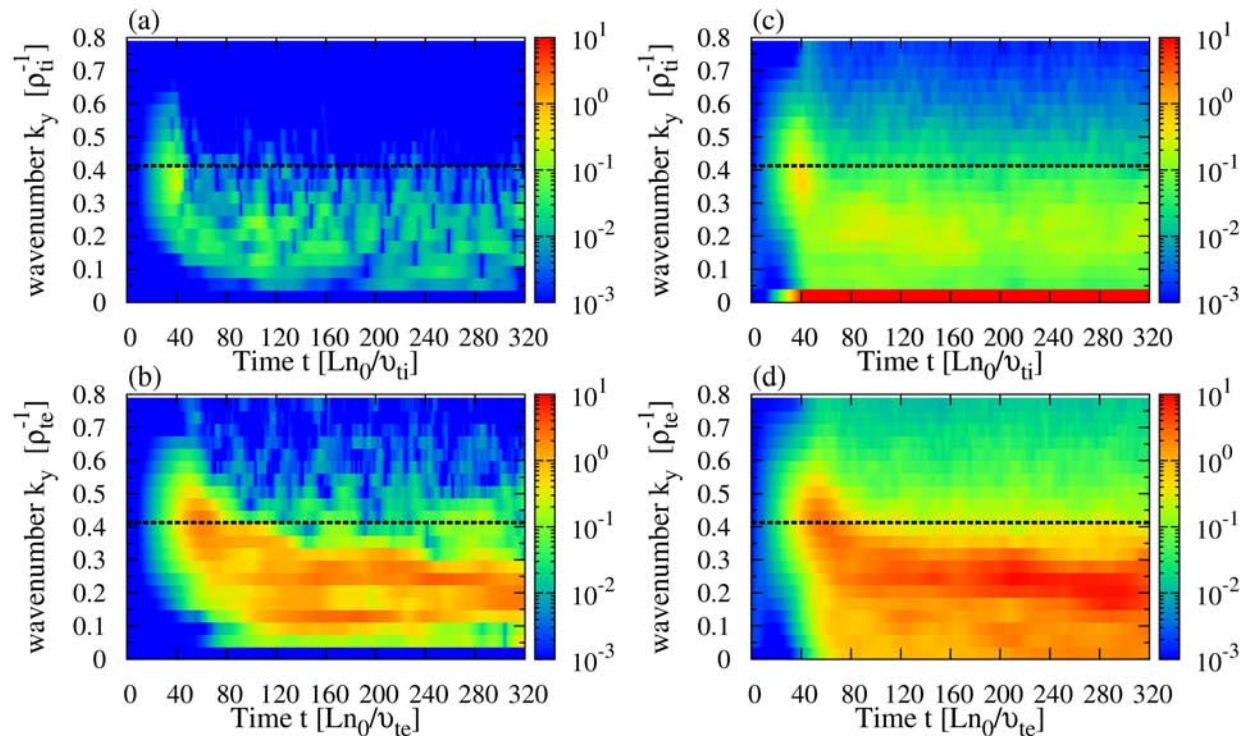
FIG. 5.4: Time evolution of k_y-spectra of the streamer intensity $\langle|\delta\phi_{k_x=0,k_y}|^2\rangle$ [(a) and (b)] and the intensity of finite-k_x modes $\langle\sum_{k_x\neq0}|\delta\phi_{k_x,k_y}|^2\rangle$ [(c) and (d)] for the ITG (upper row) and ETG (lower row) turbulence, where the unit is $(T_s\rho_{ts}/eL_{n_0})^2$ The wavenumber of $k_y = 0.4125$ for the linearly most unstable mode is also shown by the dashed line.

unstable for $t \lesssim 40 - 60$, quickly spreads to the higher-k_x region [(c) and (d)], in contrast to the down-shift to the lower-k_y region as shown in the Figs. 5.4. Then, the non-zonal mode intensity is suppressed by the ITG-driven zonal flows, while the high amplitude streamers with $k_x \simeq 0$ are sustained in the ETG turbulence. The saturation levels of the non-zonal mode intensity $\langle\sum_{k_x,k\neq0}|\delta\phi_{k_x,k_y}|^2\rangle$ in the steady states of the ITG and ETG turbulence are $4.55(T_i\rho_{ti}/eL_{n_0})^2$ and $136(T_e\rho_{te}/eL_{n_0})^2$, respectively.

The vortex and flow structures of the ITG and ETG turbulence in the three-dimensional flux-tube are shown in Figs. 5.6(a) and 5.6(b), respectively, where the potential fluctuations $\delta\phi(x, y, z)$ at $t = 315$ are plotted. As already seen from the spectral analysis, the strong zonal flows, which are translationally symmetric in the y- and z- directions, are observed in the ITG turbulence [Fig. 5.6(a)]. The radially elongated streamers with high amplitudes observed in the ETG turbulence [Fig. 5.6(b)] show the ballooning-type structures, i.e., the amplitude on the perpendicular plane with $z = 0$ (the outboard side of the torus) decreases toward $z = \pi$ (the inboard side of the torus). The different vortex and flow structures between the ITG and ETG turbulence reflect in their
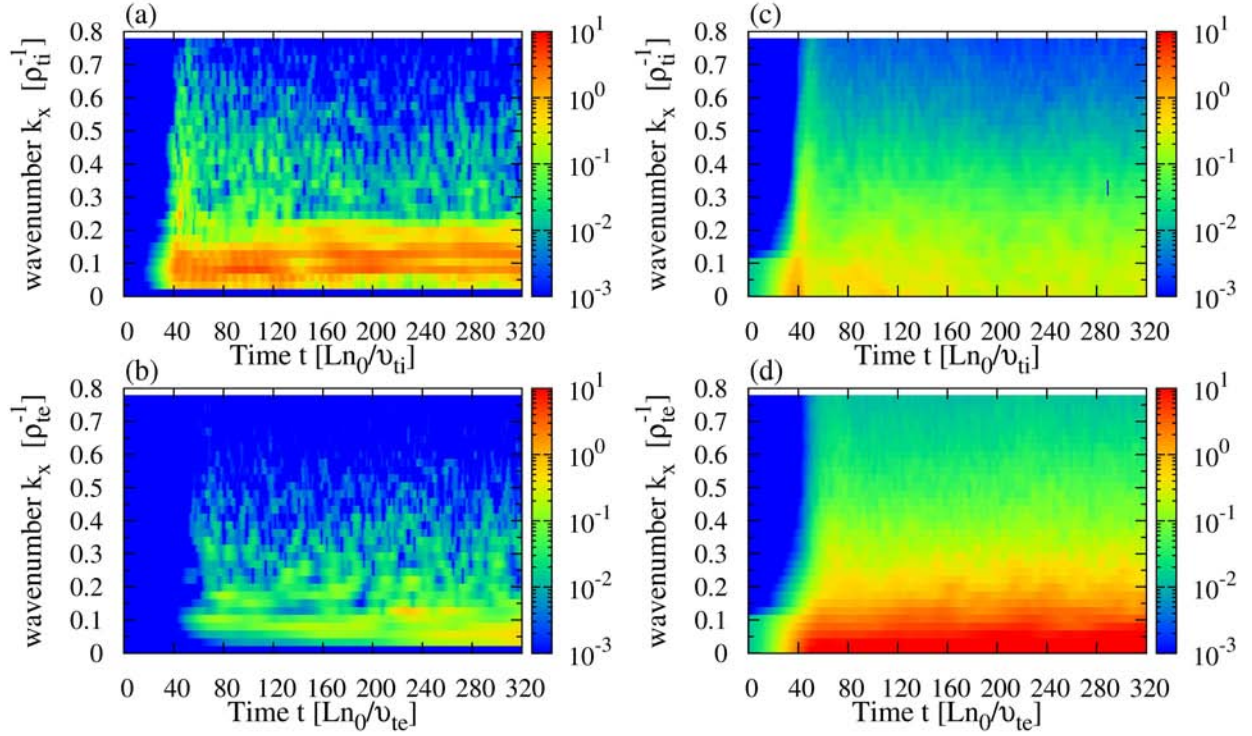
FIG. 5.5: Time evolution of k_x-spectra of the zonal-flow intensity $\langle |\delta\phi_{k_x, k_y=0}|^2 \rangle$ [(a) and (b)] and the intensity of non-zonal modes $\langle \sum_{k_y \neq 0} |\delta\phi_{k_x, k_y}|^2 \rangle$ [(c) and (d)] for the ITG (upper row) and ETG (lower row) turbulence, where the unit is $(T_s \rho_{ts}/eL_{n_0})^2$ The wavenumber giving the linearly most unstable mode is $k_x = 0$.

different nonlinear entropy transfer processes as will be discussed in Sec. 5.4.

Transport properties in the steady states of the ITG and ETG turbulence are compared in terms of the wavenumber spectra of the turbulent heat flux $\eta_s \overline{Q}_{sk_\perp}$ in the two-dimensional $\boldsymbol{k}_\perp$-space which are plotted in Figs. 5.7(a) and 5.7(b). For reference and comparison, the wavenumber spectra of potential fluctuations are also plotted in Figs. 5.7(c) and 5.7(d), where each amplitude is normalized with the maximum value in the non-zonal components ($k_y \neq 0$). While the mode with ($k_x \simeq 0$, $k_y \simeq 0.2\rho_{ts}^{-1}$) makes the largest contribution to the heat transport in both cases, one clearly finds a qualitative difference in the spectra of the turbulent heat flux and potential fluctuations between the ITG and ETG turbulence. The wavenumber spectra for the ITG turbulence significantly expands into the high k_x-region [Figs. 5.7(a) and 5.7(c)] where the modes are stabilized [cf. Fig. 5.1] and make less contribution to the heat transport, while the spectra for the ETG case is confined in the lower-k_x region. The different structures of the wavenumber spectra observed in the ITG and ETG cases will discussed from the view point of the nonlinear entropy transfer in the next section.
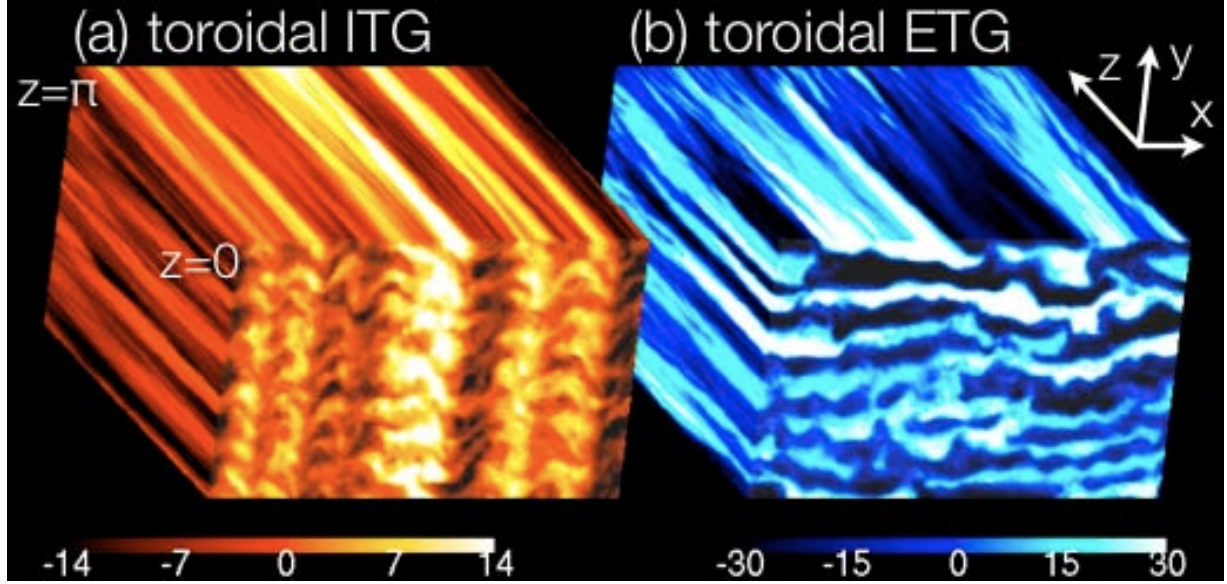
FIG. 5.6: Contours of the potential fluctuations $\delta\phi(x, y, z)$ at $t = 315(L_{n_0}/v_{ts})$ for toroidal (a)ITG and (b)ETG turbulence, where the unit is $(T_s\rho_{ts}/eL_{n_0})$. The box size is $L_x \times L_y \times L_z = 266\rho_{ts} \times 168\rho_{ts} \times \pi$. The (x, y)-cross section shown here is the perpendicular plane in the outboard side of the torus, where $z = 0$.

5.4 Nonlinear entropy transfer via zonal modes

5.4.1 Entropy transfer processes in saturation and steady phases

In this section, nonlinear interactions between zonal flows and the ambient turbulence are addressed based on the spectral analysis of the triad entropy transfer function given in Sec. 5.2. The entropy transfer analysis provides ones with quantitative evaluations for the effects of zonal flows on the transport suppression.

In the previous section, the entropy balance relations for non-zonal and zonal modes in the ITG and ETG turbulence have been discussed (cf. Figs. 5.2 and 5.3). Particularly, the different time-evolution of the normalized entropy transfer function $\mathcal{T}_s^{(zf)}/\eta_s\overline{Q}_s$ has been shown [cf. Fig. 5.3(c)]. The amplitude of $\mathcal{T}_i^{(zf)}/\eta_i\overline{Q}_i$ is much higher than $\mathcal{T}_e^{(zf)}/\eta_e\overline{Q}_e$ in the saturation phase of the linear instability. In the steady state, we observe the lower amplitude of $\mathcal{T}_i^{(zf)}/\eta_i\overline{Q}_i$ with the same order of magnitude as $\mathcal{T}_e^{(zf)}/\eta_e\overline{Q}_e$, which should balance with weak collisional dissipation for zonal modes. Nevertheless, the ITG-driven zonal flows with the high amplitude are sustained in the steady state even with the weak source of $\overline{\mathcal{T}}_i^{(zf)}/\eta_i\overline{Q}_i = 2.56 \times 10^{-2}$ (but still larger than $\overline{\mathcal{T}}_e^{(zf)}/\eta_e\overline{Q}_e = 1.42 \times 10^{-2}$) because of the smallness of the zonal-flow inertia. It should be stressed here that, even in the steady state with little entropy transfer to the zonal modes, the ITG-driven
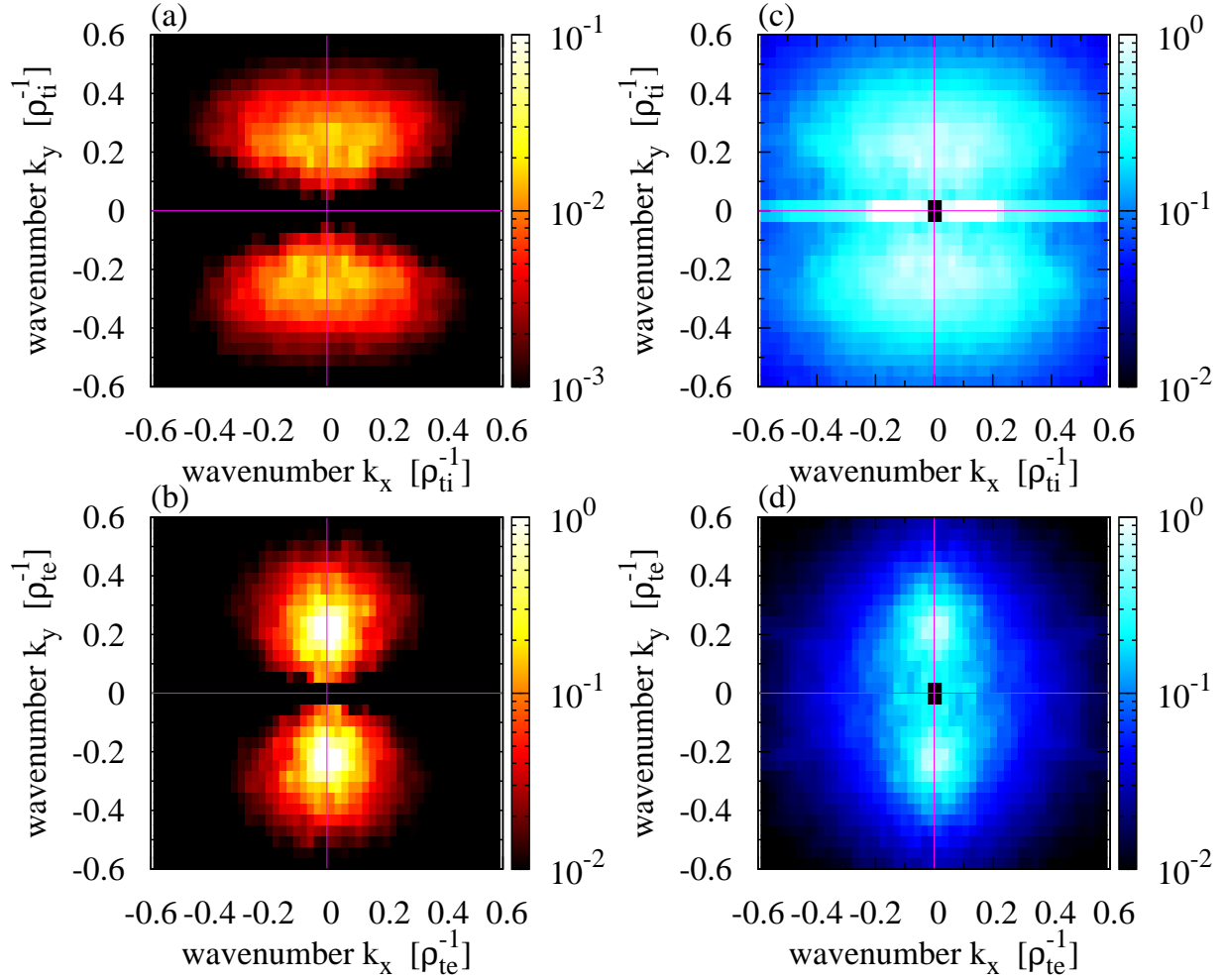
FIG. 5.7: Wavenumber spectra of the turbulent heat flux $\eta_s Q_{sk_\perp}$ [(a) and (b)] and the potential fluctuation $\langle|\delta\phi_{k_\perp}|\rangle$ [(c) and (d)] in the steady states of the ITG (upper row) and ETG (lower row) turbulence, where the amplitudes are averaged over $220 \leqslant t \leqslant 320$. The amplitudes of potential fluctuations are normalized by the maximum value in the non-zonal components.

zonal flows still play an important role in the transport suppression through a different type of the entropy transfer process from that in the saturation phase, as will be shown later. In order to understand more accurately the nonlinear entropy transfer processes in the saturation and steady states, the spectral analysis of the triad entropy transfer function $\mathcal{J}_s[\boldsymbol{k}_\perp|\boldsymbol{p}_\perp, \boldsymbol{q}_\perp]$ (rather than $\mathcal{T}_s^{(\mathrm{zf})}$) with the aid of the detailed balance relation shown in Eq. (5.20) is necessary, because $\mathcal{T}_s^{(\mathrm{zf})}$ (or, equivalently, $\mathcal{T}_{sk_\perp}$) obscures individual entropy transfer processes among the non-zonal modes through the zonal mode, and provides only the net amount of the entropy variable transferred from non-zonal (turbulence) to zonal modes. Indeed, Waltz *et al.* have examined the spectral structures of the entropy transfer function $\mathcal{T}_{ik_\perp}$ for the steady state of ITG-TEM turbulence [25].

However, the relation between the entropy transfer processes and the turbulence regulation by zonal flows has not been shown explicitly. The detailed spectral analysis of the triad transfer function presented in this study can reveal the critical role of zonal flows in the nonlinear entropy transfer processes, which are closely associated with the saturation of instability growth and transport suppression in the steady state.

Hereafter, we consider the entropy transfer processes associated with the nonlinear interactions among two non-zonal modes with $p_\perp$ and $q_\perp$ and a zonal mode with $k_{zf} = k_{zf} \nabla x$, which satisfy the triad-interaction condition $k_{zf} + p_\perp + q_\perp = 0$. (A schematic plot is shown in Fig. 5.8.) First, the non-zonal primary mode with $p_\perp$ is chosen to be the "transport-driving mode" with $(k_x \simeq 0,\ k_y \simeq 0.2\rho_{ts}^{-1})$ which makes the most dominant contribution to the turbulent heat flux, as shown in Figs. 5.7(a) and 5.7(b).

The wavenumber spectrum of the triad entropy transfer function normalized by the time-averaged heat flux, i.e., $\overline{\mathcal{J}}_s[k_{zf}|\, p_\perp, q_\perp]/\eta_s \overline{Q}_s$, in the saturation phases of ITG and ETG instabilities are shown in Figs. 5.9(a) and 5.9(b), respectively, where the time-average is taken over $30 \leqslant t \leqslant 45$. Here, the wavenumbers of the ITG- and ETG-driven zonal flows are, respectively, set to $k_{zf} = 0.1410\rho_{ti}^{-1}$ and $k_{zf} = 0.0705\rho_{te}^{-1}$, which have the largest amplitude in the zonal-flow components. In the ITG turbulence [Fig. 5.9(a)], one clearly finds that the large positive values of $\overline{\mathcal{J}}_i[k_{zf}|\, p_\perp, q_\perp]/\eta_i \overline{Q}_i$ spread over the linearly unstable region around $q_y \simeq 0.4\rho_{ti}^{-1}$ [cf. Fig. 5.1]. This suggests that the saturation process of the ITG instability is closely associated with the high-amplitude zonal-flow generation with the strong flow-shear due to the efficient entropy transfer from the linearly unstable non-zonal modes to zonal modes. On the other hand, the lower amplitude of $\overline{\mathcal{J}}_e[k_{zf}|\, p_\perp, q_\perp]/\eta_e \overline{Q}_e$ is observed in the ETG case [Fig. 5.9(b)] so that the

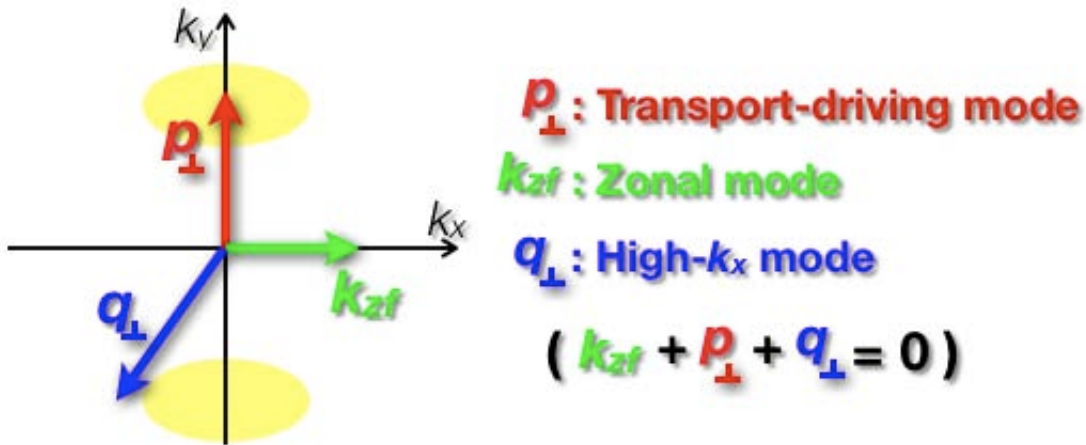FIG. 5.8: Non-zonal and zonal modes which satisfy the triad-interaction condition $k_{zf} + p_\perp + q_\perp = 0$, where $k_{zf} = k_{zf} \nabla x$.
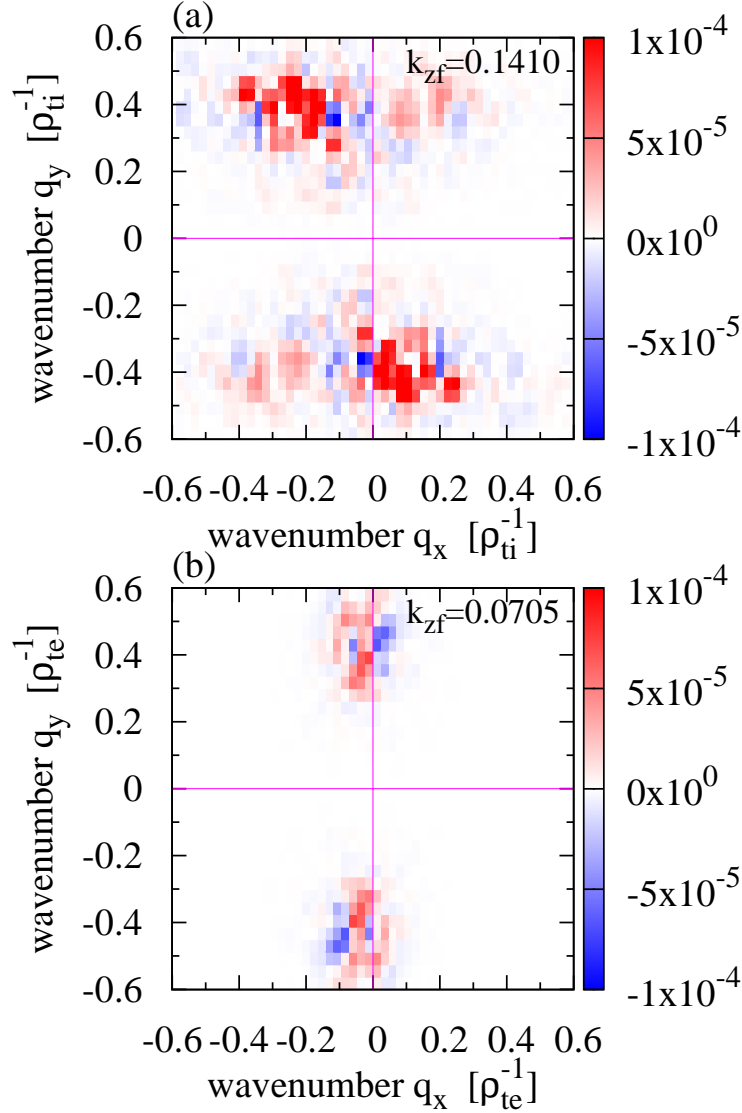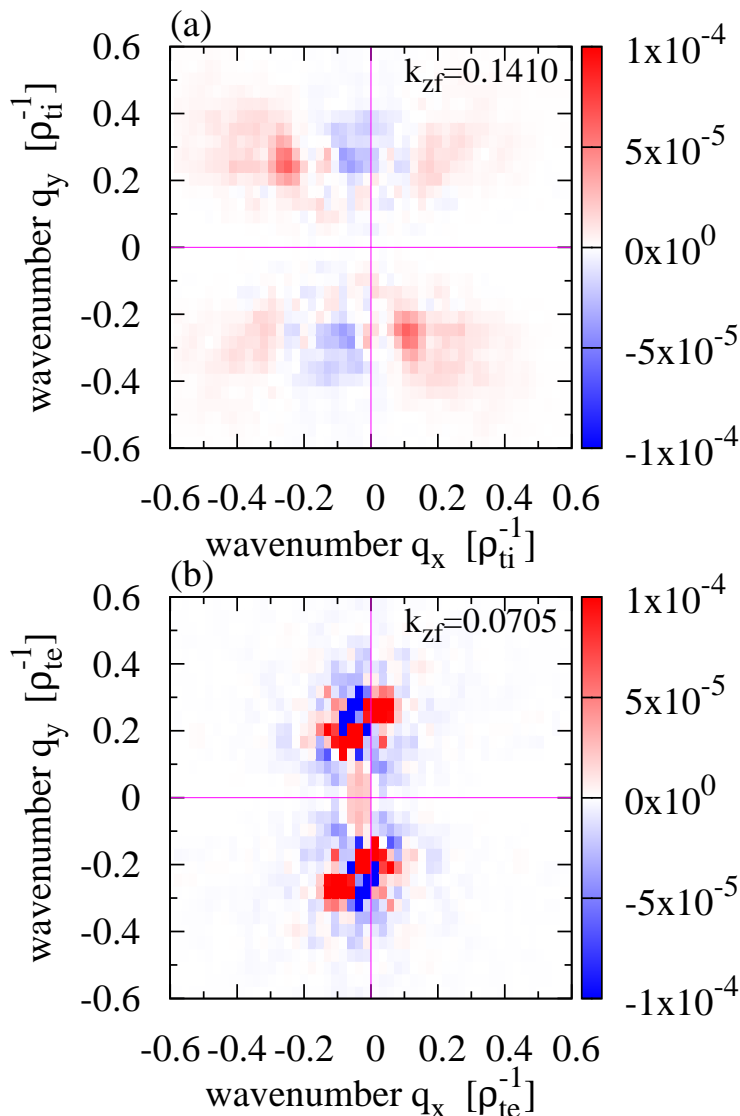
FIG. 5.9: Wavenumber spectrum of the triad transfer function normalized by the mean heat flux, $\overline{\mathcal{J}}_s[\boldsymbol{k}_{zf}|\boldsymbol{p}_\perp,\boldsymbol{q}_\perp]/\eta_s\overline{Q}_s$, for the fixed-$\boldsymbol{k}_{zf}$ in the saturation phase of toroidal (a)ITG (s = i) and (b)ETG (s = e) turbulence, where the time-average is taken over $30 \leqslant t \leqslant 45$.

generation of ETG-driven zonal flows in the saturation process is less effective than that in the ITG case. These results are consistent with the different amplitude of $\mathcal{T}_i^{(zf)}/\eta_i\overline{Q}_i$ and $\mathcal{T}_e^{(zf)}/\eta_e\overline{Q}_e$ observed in the saturation phase, as shown in Fig. 5.3(c).

In the steady state, the entropy transfer processes are qualitatively different from those in the saturation phase. The wavenumber spectra of $\overline{\mathcal{J}}_s[\boldsymbol{k}_{zf}|\boldsymbol{p}_\perp,\boldsymbol{q}_\perp]/\eta_s\overline{Q}_s$ in the steady state are shown in Figs. 5.10. It is observed in Fig. 5.10(a) that the amplitude of $\overline{\mathcal{J}}_i[\boldsymbol{k}_{zf}|\boldsymbol{p}_\perp,\boldsymbol{q}_\perp]/\eta_i\overline{Q}_i$ is quite low in comparison to that in the saturation phase shown above. For the ETG case [Fig. 5.10(b)], the large positive values of $\overline{\mathcal{J}}_e[\boldsymbol{k}_{zf}|\boldsymbol{p}_\perp,\boldsymbol{q}_\perp]/\eta_e\overline{Q}_e$ are found near the region of transport-

FIG. 5.10: Wavenumber spectrum of the triad transfer function normalized by the mean heat flux, $\overline{\mathcal{J}}_s[\boldsymbol{k}_{zf}|\boldsymbol{p}_\perp, \boldsymbol{q}_\perp]/\eta_s \overline{Q}_s$, for the fixed-$\boldsymbol{k}_{zf}$ in the steady state of toroidal (a)ITG (s = i) and (b)ETG (s = e) turbulence, where the time-average is taken over $220 \leqslant t \leqslant 320$.

driving modes [cf. Fig. 5.7(b)], but are partly canceled by the large negative values. Note that, as discussed above, the generation of ETG-driven zonal flows is less effective due to the large zonal-flow inertia, even though the relatively large positive values of $\overline{\mathcal{J}}_e[\boldsymbol{k}_{zf}|\boldsymbol{p}_\perp, \boldsymbol{q}_\perp]/\eta_e \overline{Q}_e$ are observed in comparison to those in the ITG case.

Although the entropy transfer to zonal modes is quite weak in the steady state of the ITG turbulence, i.e., $\overline{\mathcal{J}}_i[\boldsymbol{k}_{zf}|\boldsymbol{p}_\perp, \boldsymbol{q}_\perp] \simeq 0$, the ITG-driven zonal flows still play a "catalytic role" in the entropy transfer from non-zonal transport-driving modes to other non-zonal modes with higher radial-wavenumbers which make less contribution to the turbulent heat flux [cf. Fig. 5.1 and

5.7(a)]. In order to clarify this point, the wavenumber spectra of $\overline{\mathcal{J}}_{\mathrm{i}}[\boldsymbol{p}_\perp|\boldsymbol{q}_\perp, \boldsymbol{k}_{\mathrm{zf}}]/\eta_{\mathrm{i}}\overline{Q}_{\mathrm{i}}$ in the steady state for three different $\boldsymbol{p}_\perp$'s is plotted in Figs. 5.11(a) – (c), where p_y is fixed to $p_y = 0.2250\rho_{\mathrm{ti}}^{-1}$ which is the dominant component driving the heat flux. It is clearly found that all the figures commonly show the two-stripe pattern at $p_y = 0$ and $p_y = -0.2250\rho_{\mathrm{ti}}^{-1}$ which indicates that the $\boldsymbol{p}_\perp$-mode dominantly interacts with other non-zonal modes through the zonal modes. Note that, in general, one can not uniquely determine the direction of the entropy transfer between "two modes" only from the sign of $\overline{\mathcal{J}}_{\mathrm{i}}[\boldsymbol{p}_\perp|\boldsymbol{q}_\perp, \boldsymbol{k}_{\mathrm{zf}}]$ because the "triad" transfer function describes the entropy transfer among "three modes forming a triad interaction". However, the direction of the entropy transfer between two non-zonal modes is identified here as $\boldsymbol{p}_\perp \to \boldsymbol{q}_\perp$ for negative $\overline{\mathcal{J}}_{\mathrm{i}}[\boldsymbol{p}_\perp|\boldsymbol{q}_\perp, \boldsymbol{k}_{\mathrm{zf}}]$, or as $\boldsymbol{q}_\perp \to \boldsymbol{p}_\perp$ for positive one due to the detailed balance relation given in Eq. (5.20) leading to

$$\overline{\mathcal{J}}_{\mathrm{i}}\left[\boldsymbol{p}_\perp|\boldsymbol{q}_\perp, \boldsymbol{k}_{\mathrm{zf}}\right] + \overline{\mathcal{J}}_{\mathrm{i}}\left[\boldsymbol{q}_\perp|\boldsymbol{k}_{\mathrm{zf}}, \boldsymbol{p}_\perp\right] = -\overline{\mathcal{J}}_{\mathrm{i}}\left[\boldsymbol{k}_{\mathrm{zf}}|\boldsymbol{p}_\perp, \boldsymbol{q}_\perp\right] \simeq 0 , \qquad (5.23)$$

where the last equality is confirmed by the small amplitude of $\overline{\mathcal{J}}_{\mathrm{i}}[\boldsymbol{k}_{\mathrm{zf}}|\boldsymbol{p}_\perp, \boldsymbol{q}_\perp]$ in the steady state as shown in Fig. 5.10(a).

The entropy transfer processes shown in Figs. 5.11(a) – (c) are explained more in detail as follows: From Fig. 5.11(a), we observe the large negative values at the zonal mode with $q_x = k_{\mathrm{zf}} = 0.1410\rho_{\mathrm{ti}}^{-1}$ and $q_y = 0$ (represented by solid green arrow) and at the non-zonal mode with $q_x = -k_{zf}$ and $q_y = -p_y = -0.2250\rho_{\mathrm{ti}}^{-1}$ (solid blue arrow), which form a triad with the transport-driving primary mode with $\boldsymbol{p}_\perp$ (solid red arrow). This means that the entropy is transferred from the non-zonal primary mode ($\boldsymbol{p}_\perp$) to the higher radial-wavenumber mode ($\boldsymbol{q}_\perp$) through the catalytic role of the high-amplitude zonal mode ($\boldsymbol{k}_{\mathrm{zf}}$). Besides, the $-\boldsymbol{q}_\perp$-mode, which is equivalent to the $\boldsymbol{q}_\perp$-mode due to the reality of the physical variable, is plotted by the dotted blue arrow in the figure. In Fig. 5.11(b), the previously transferred mode [dotted blue arrow in Fig. 5.11(a)], which consists of a triad with two modes shown by black solid arrows [equivalent to red and green solid arrows in Fig. 5.11(a)], is now considered as the new primary mode with $p_x = 0.1410\rho_{\mathrm{ti}}^{-1}$ and $p_y = 0.2250\rho_{\mathrm{ti}}^{-1}$ shown by red solid arrow. Then, the entropy variable is further transferred to the non-zonal mode with higher radial-wavenumber (solid, or equivalently, dotted blue arrow) via the interaction with the zonal mode with $k_{\mathrm{zf}} \simeq 0.1410\rho_{\mathrm{ti}}^{-1}$. The "successive" entropy transfer to the higher radial-wavenumber mode is also found in Fig. 5.11(c). [One again finds that the entropy of the primary mode (red solid arrow) is coming through the interaction with two modes (black solid arrows), and is going to the higher radial-wavenumber mode (blue arrows) via the interaction with the zonal mode (green solid arrow).]

Furthermore, Figs. 5.12 show the contour of $\overline{\mathcal{J}}_{\mathrm{i}}[\boldsymbol{p}_\perp|\boldsymbol{q}_\perp, \boldsymbol{k}_{\mathrm{zf}}]/\eta_{\mathrm{i}}\overline{Q}_{\mathrm{i}}$ for three different p_x's with $p_y = -0.2250\rho_{\mathrm{ti}}^{-1}$, which indicates a diagonal counterpart of entropy transfer processes
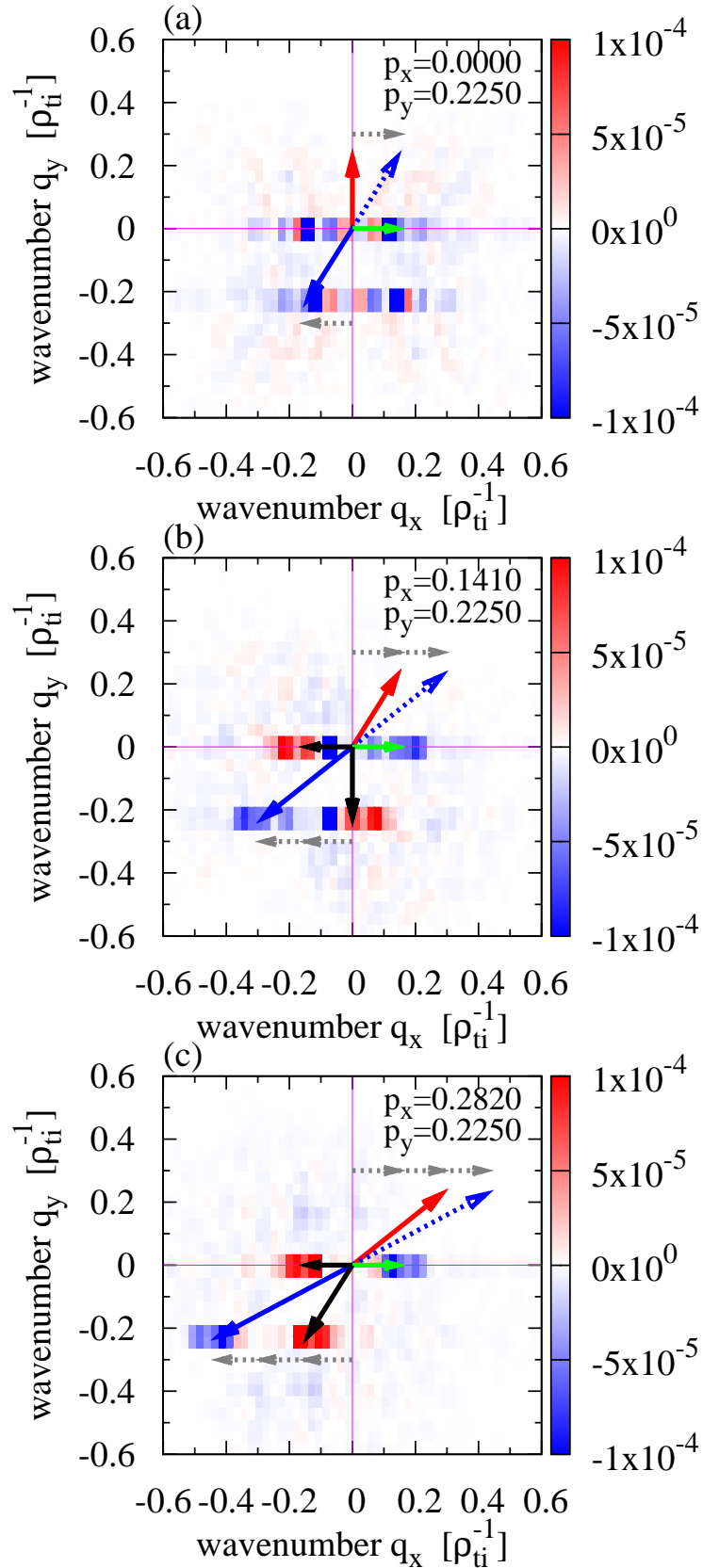
FIG. 5.11: Wavenumber spectra of the triad transfer function normalized by the mean heat flux, $\overline{\mathcal{J}}_i[\boldsymbol{p}_\perp|\boldsymbol{q}_\perp, \boldsymbol{k}_{zf}]/\eta_i\overline{Q}_i$, for three different $\boldsymbol{p}_\perp$'s with $p_y = 0.2250\rho_{ti}^{-1}$(fixed) in the steady state of toroidal ITG turbulence, where the time-average is taken over $220 \leqslant t \leqslant 320$.
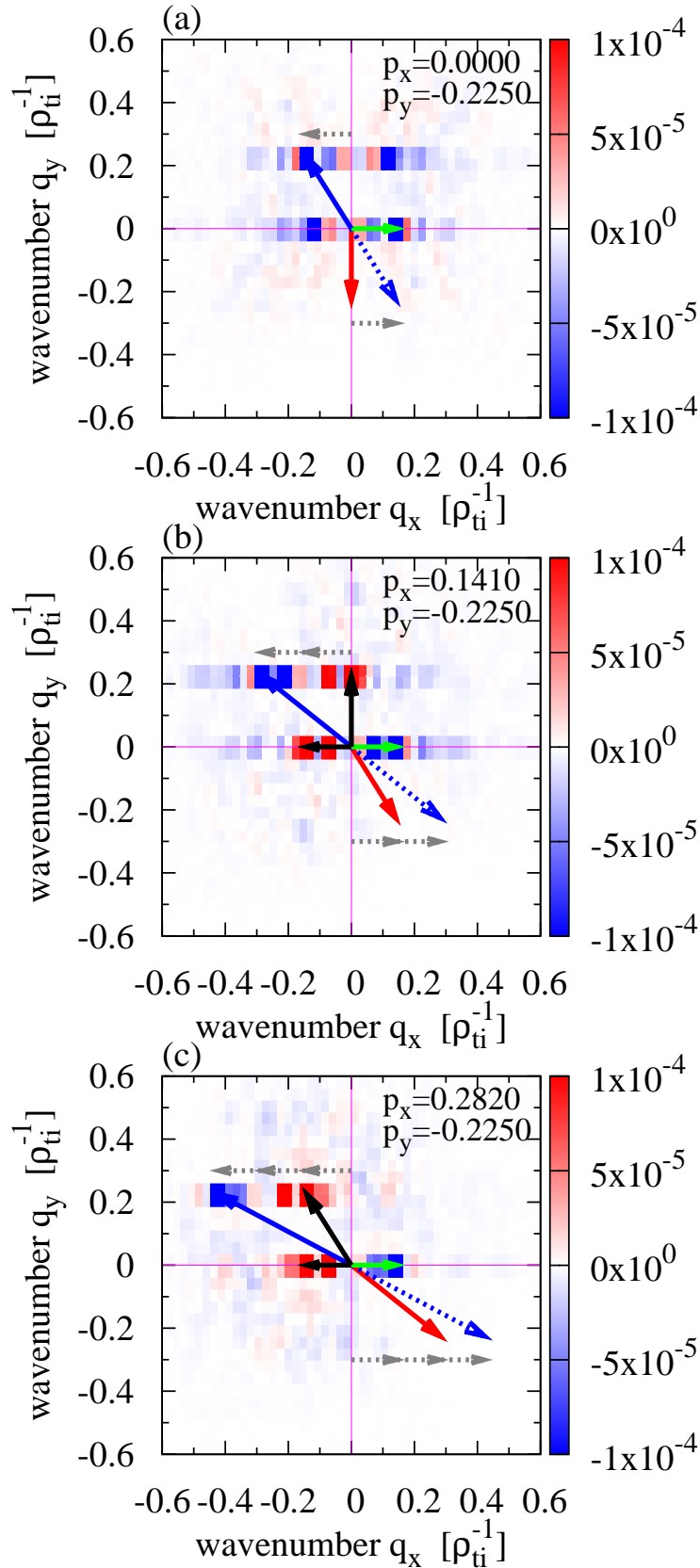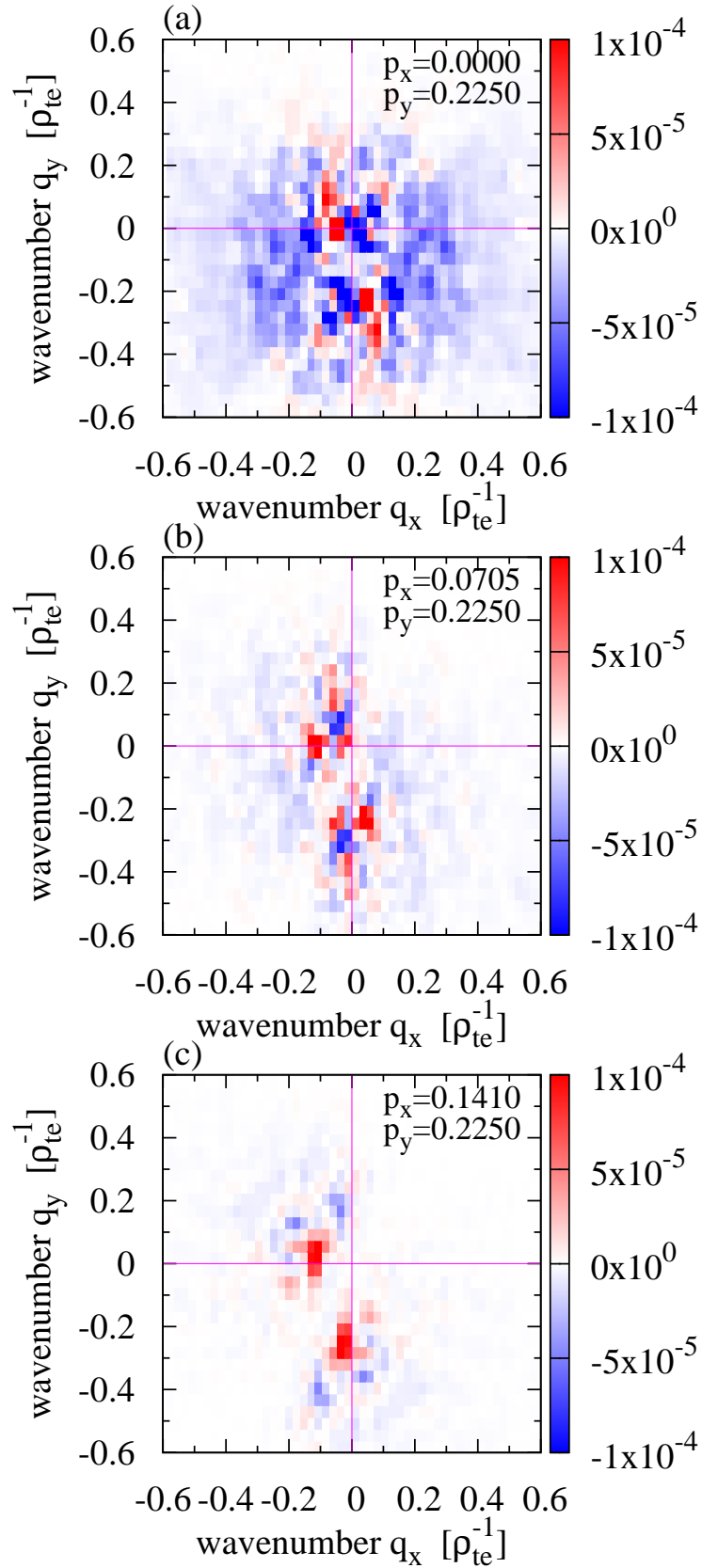
FIG. 5.12: Wavenumber spectra of $\overline{\mathcal{J}}_i[\boldsymbol{p}_\perp | \boldsymbol{q}_\perp, \boldsymbol{k}_{zf}]/\eta_i \overline{Q}_i$ for three different $\boldsymbol{p}_\perp$'s with $p_y = -0.2250\rho_{ti}^{-1}$ (fixed) in the steady state of toroidal ITG turbulence, where the time-average is taken over $220 \leqslant t \leqslant 320$.

FIG. 5.13: Wavenumber spectra of $\overline{\mathcal{J}}_e[\boldsymbol{p}_\perp|\boldsymbol{q}_\perp, \boldsymbol{k}_{zf}]/\eta_e\overline{Q}_e$, for three different $\boldsymbol{p}_\perp$'s with $p_y = 0.2250\rho_{te}^{-1}$(fixed) in the steady state of toroidal ETG turbulence, where the time-average is taken over $220 \leqslant t \leqslant 320$.

shown in Figs. 5.11. The present spectral analysis reveals that, through the non-local interaction with the high-amplitude zonal flows in the wavenumber-space, the entropy of the non-zonal transport-driving modes is successively transferred to the non-zonal modes with higher radial-wavenumbers for which stronger damping due to the finite gyroradius effect occurs. These results provide ones with a novel physical picture of the suppression of the ITG turbulent transport by zonal flows in the steady state, from the view point of the gyrokinetic entropy balance.

Figures 5.13(a) – (c) show the wavenumber spectra of $\overline{\mathcal{J}}_e[\boldsymbol{p}_\perp | \boldsymbol{q}_\perp, \boldsymbol{k}_{zf}]/\eta_e \overline{Q}_e$ in the steady state of toroidal ETG turbulence for three different $\boldsymbol{p}_\perp$'s, respectively. In contrast to the ITG turbulence, no remarkable spectral structures suggesting the successive entropy transfer to the non-zonal modes with higher radial-wavenumbers are observed. Instead, the entropy transfer within a low wavenumber region occurs dominantly through the nonlinear interactions among non-zonal modes. One also finds the net entropy transfer to the primary mode with $\boldsymbol{p}_\perp$ through the coupling of zonal flows and radially elongated streamers with $q_x \simeq 0$ [cf. Fig. 5.13(c)], while the subsequent transfer to non-zonal mode with the higher-radial wavenumber does not occur. Thus, it is concluded that, in both the saturation and steady phases of the ETG turbulence, the role of zonal flows in the successive entropy transfer to the higher wavenumber modes is much weaker than that in the ITG case.

In addition to the individual entropy transfer processes involving the interactions with all components of zonal modes shown above, the wavenumber spectra of $\overline{\mathcal{J}}_s[\boldsymbol{p}_\perp | \boldsymbol{q}_\perp, \boldsymbol{k}_{zf}]/\eta_s \overline{Q}_s$ are plotted in Figs. 5.14 as a function of p_x and q_x, where $p_y = -q_y = 0.2250\rho_{ts}^{-1}$ and k_{zf} giving the largest amplitude in the zonal-flow components are fixed. In the ITG case [Fig. 5.14(a)], one clearly finds the elongated diagonal stripes indicating that the entropy at $p_x = 0$ (transport-driving mode) is transferred to the higher radial-wavenumber non-zonal modes via the successive interactions with zonal modes. The successive transfer processes are represented by the dotted gray arrows in Fig. 5.14(a). In contrast, in the ETG case [Fig. 5.14(b)], the elongated diagonal structures indicating the successive transfer are no longer observed. Recently, for the ITG turbulence, Navarro *et al.* have shown that the entropy transfer (or cascade) from large- to small-scale shells in the $k_\perp$-space occurs locally [33]. There, they have examined the entropy transfer function averaged over isotropic shells in two-dimensional wavenumber-space. However, it should be pointed out that their shell-to-shell transfer analysis obscures the successive entropy transfer via zonal flows (the most important ingredient of the ITG turbulence) revealed in this study.

Finally, in Figs. 5.15, we briefly summarize the nonlinear entropy transfer processes in the saturation and the steady phases of the toroidal ITG and ETG turbulence, which are closely associated with the saturation of the instability growth and the suppression of the turbulent transport in the steady state. In the saturation phase of the toroidal ITG instability growth, the entropy
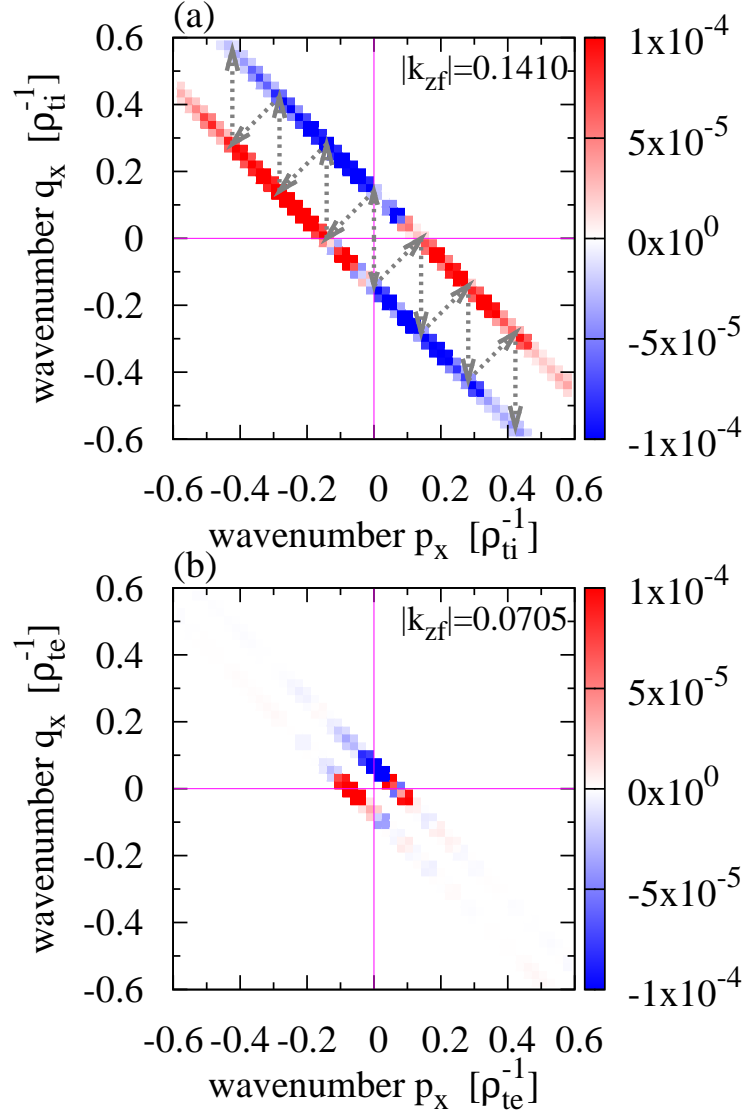
FIG. 5.14: Wavenumber spectrum of $\overline{\mathcal{T}}_s[\boldsymbol{p}_\perp|\boldsymbol{q}_\perp, \boldsymbol{k}_{zf}]/\eta_s\overline{Q}_s$ for fixed-$|k_{zf}|$ with $p_y = -q_y = 0.2250\rho_{ts}^{-1}$ in the steady phases of toroidal (a)ITG (s = i) and (b)ETG (s = e) turbulence, where the time-average is taken over $220 \leqslant t \leqslant 320$. The lower and upper lines in each figure correspond to $k_{zf} + p_x + q_x = 0$ for $k_{zf} > 0$ and $k_{zf} < 0$, respectively.

of non-zonal ITG modes is significantly transferred to zonal modes, then the ITG instability growth is saturated by the high-amplitude zonal flows with strong flow-shear [Fig. 5.15(a)]. In the steady state of the ITG turbulence, the entropy transfer to zonal modes becomes quite weak, i.e., $\mathcal{T}_i^{(zf)}/\eta_i\overline{Q}_i \sim \mathcal{T}_e^{(zf)}/\eta_e\overline{Q}_e \ll 1$. Nevertheless, the ITG-driven zonal flows still play a catalytic role in the entropy transfer process from non-zonal modes strongly driving the heat transport to the higher radial-wavenumber (non-zonal) modes with less contribution to the turbulent heat flux [Fig. 5.15(b)]. The successive entropy transfer to the higher radial-wavenumber modes due to
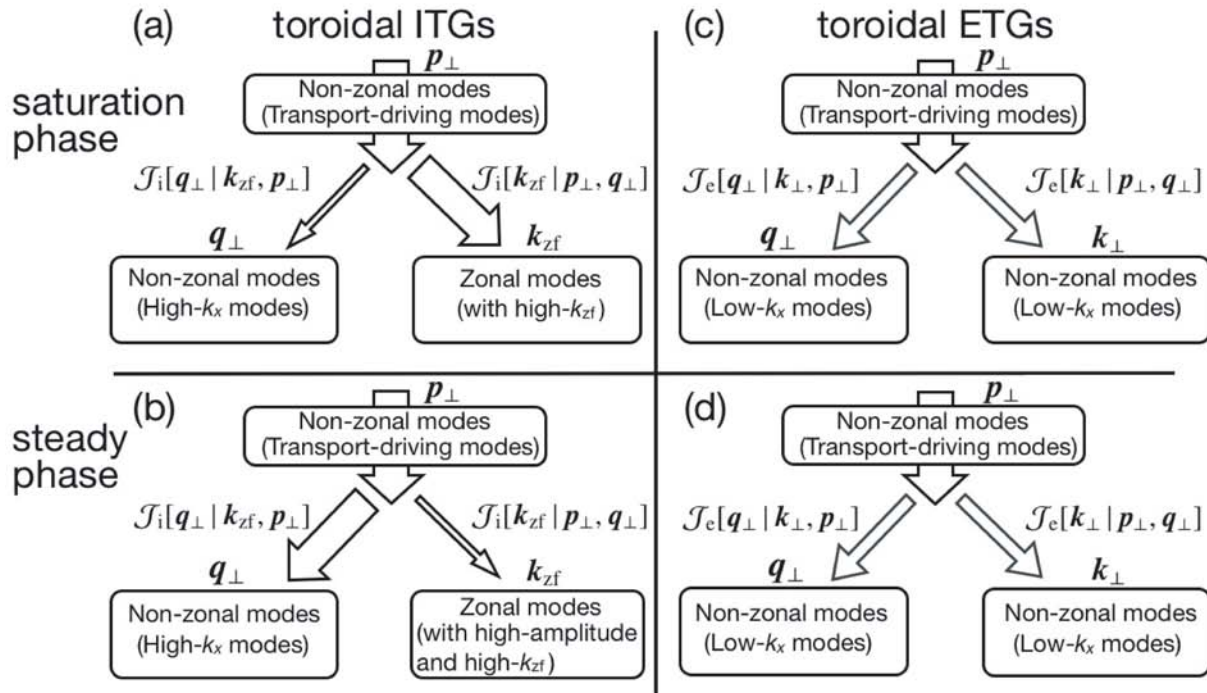
FIG. 5.15: Summary of the entropy transfer processes in the saturation (upper row) and the steady (lower row) phases for the toroidal ITG (left column) and ETG (right column) turbulence, where arrows denote the direction of the entropy transfer.

the non-local interaction with the strong zonal flows in the wavenumber-space is associated with the broadening of the spectra of potential fluctuations and heat flux in the k_x-direction shown in Figs. 5.7(a) and 5.7(c).

In contrast to the ITG case, the nonlinear interactions among the low-wavenumber non-zonal modes including the radially elongated streamers are dominant in the ETG case so that the entropy transfer resulting from the interactions with zonal flows are not effective for both the saturation of the instability growth and the transport regulation in the steady state [Figs. 5.15(c) and 5.15(d)]. As pointed out in some earlier works on the toroidal ETG turbulence [12], the vortex structures and zonal flows strongly depend on the geometrical and plasma parameters. In particular, strong ETG-driven zonal flows are observed in the case with weak (or negative) magnetic shear, where the electron heat transport is significantly reduced. It is not trivial whether the entropy transfer function for the toroidal ETG turbulence with the strong zonal flows shows the similar wavenumber spectrum to that in the ITG case presented here. The entropy transfer analysis for the toroidal ETG turbulence with weak magnetic-shear remains as a future work.

5.4.2　Comparison between slab and toroidal systems

Here, the entropy transfer process in the slab ITG and ETG turbulence are presented and compared to that in the toroidal cases shown above. The entropy transfer analysis is applied to the slab ITG and ETG turbulence simulation results calculated with the physical parameters of Case 1 shown in Chap. 3, where the statistically steady turbulence is observed [see Sec. 3.3.2]. (Note here that the quantities shown below are normalized with L_{n_0}.) In the slab ETG turbulence, the formation of isolated vortices with complicated motion are observed rather than elongated streamers, while the slab ITG turbulence is dominated by strong zonal flows where the turbulent heat flux is quenched [cf. Figs. 3.5(b) and 3.5(c)].
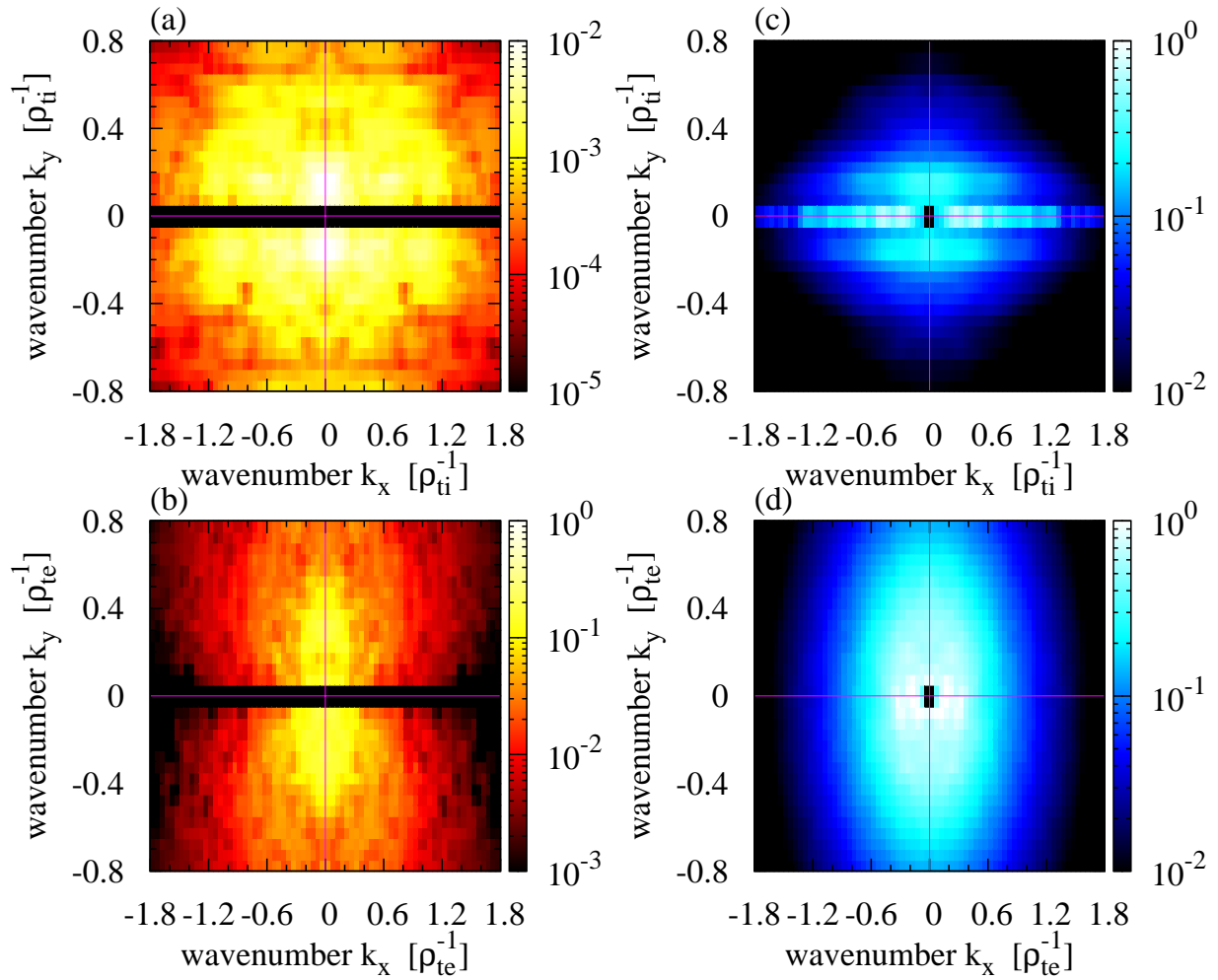

FIG. 5.16: Wavenumber spectra of the turbulent heat flux $\eta_s Q_{s k_\perp}$ [(a) and (b)] and the potential fluctuation $|\delta\phi_{k_\perp}|$ [(c) and (d)] in the steady states of the slab ITG (upper row) and ETG (lower row) turbulence, where the amplitudes are averaged over $400 \leqslant t \leqslant 500$. The amplitudes of potential fluctuations are normalized by the maximum value in the non-zonal components.

Figures 5.16 show the wavenumber spectra of the turbulent heat flux $\eta_s \overline{Q}_{s k_\perp}$ and the potential fluctuation $\langle |\delta \phi_{k_\perp}| \rangle$ for the slab ITG and ETG turbulence, where each amplitude is normalized with the maximum value in the non-zonal components ($k_y \neq 0$). One can see that the mode with $k_x \sim 0$ and $k_y \sim 0.15 \rho_{ti}^{-1}$ makes a dominant contribution to the heat transport in the slab ITG case, while the mode with $k_x \sim 0$ and $k_y \sim 0.05 \rho_{te}^{-1}$ is for the slab ETG case. It is also found that, in the slab ITG case, most fluctuation intensity is accumulated on zonal modes, and the relatively broad k_x-spectrum of the ITG-driven heat flux are observed. It is remarkable that relatively large contribution of zonal flows to the fluctuation intensity in the slab ETG turbulence are found in comparison to that in the toroidal ETG turbulence [cf. Fig. 5.7(d)].

The time-histories of the entropy transfer function $\mathcal{T}_s^{(zf)}$ for the slab ITG and ETG turbulence are shown in Fig. 5.17(a). For reference and comparison, the time-histories for the toroidal
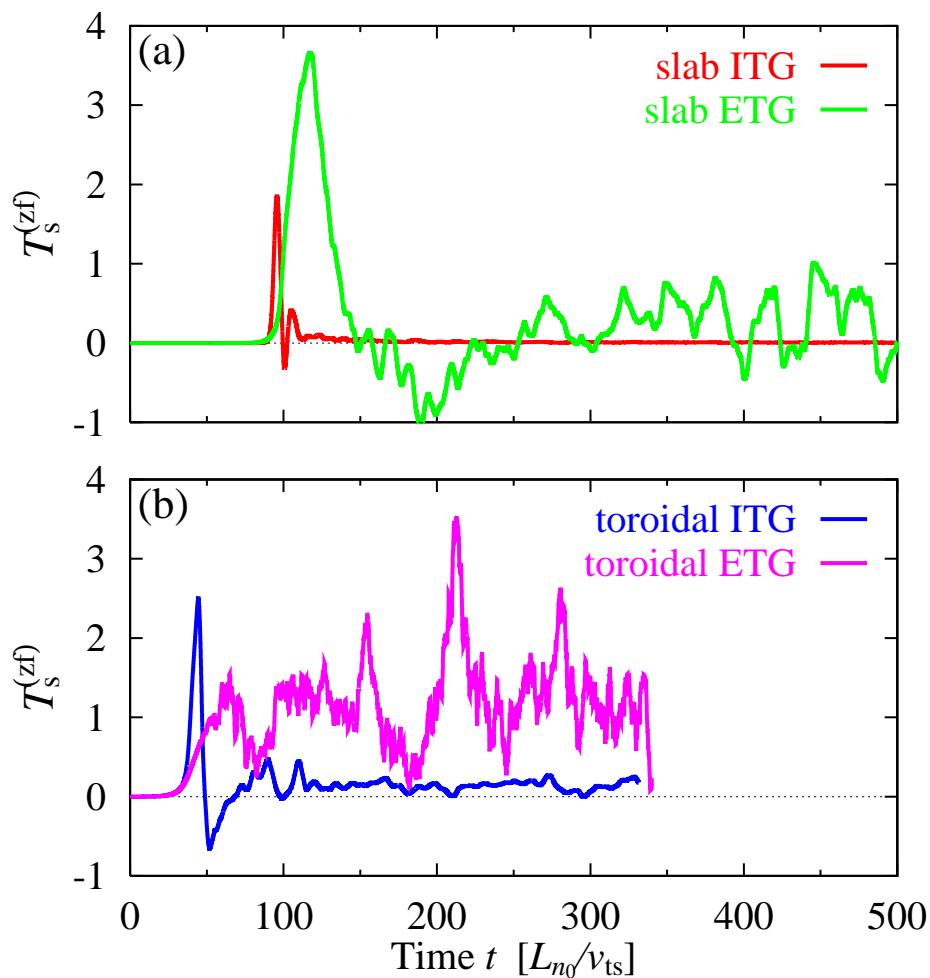

FIG. 5.17: Time evolution of the entropy transfer function $\mathcal{T}_s^{(zf)}$ for (a)slab ITG (s=i) and ETG (s=e) turbulence, and (b)toroidal ITG (s=i) and ETG (s=e) turbulence.

ITG and ETG turbulence are also plotted in Fig. 5.17(b). It is found that the time evolution of $\mathcal{T}_i^{(zf)}$ for the slab ITG case is similar to that for the toroidal ITG case. However, the qualitative difference of $\mathcal{T}_e^{(zf)}$ is observed in the slab and toroidal ETG cases, i.e., the high peak amplitude of $\mathcal{T}_e^{(zf)}$ appears in the saturation phase of the slab ETG instability at $t \sim 120$. This suggests that, in contrast to the toroidal ETG case, the generation of the slab ETG-driven zonal flows somewhat contributes to the saturation of the slab ETG instability growth through the entropy transfer to zonal modes. (Remember that the reduction of the peak amplitude of transport level due to the finite zonal-flow generation is observed in Fig. 3.3.)
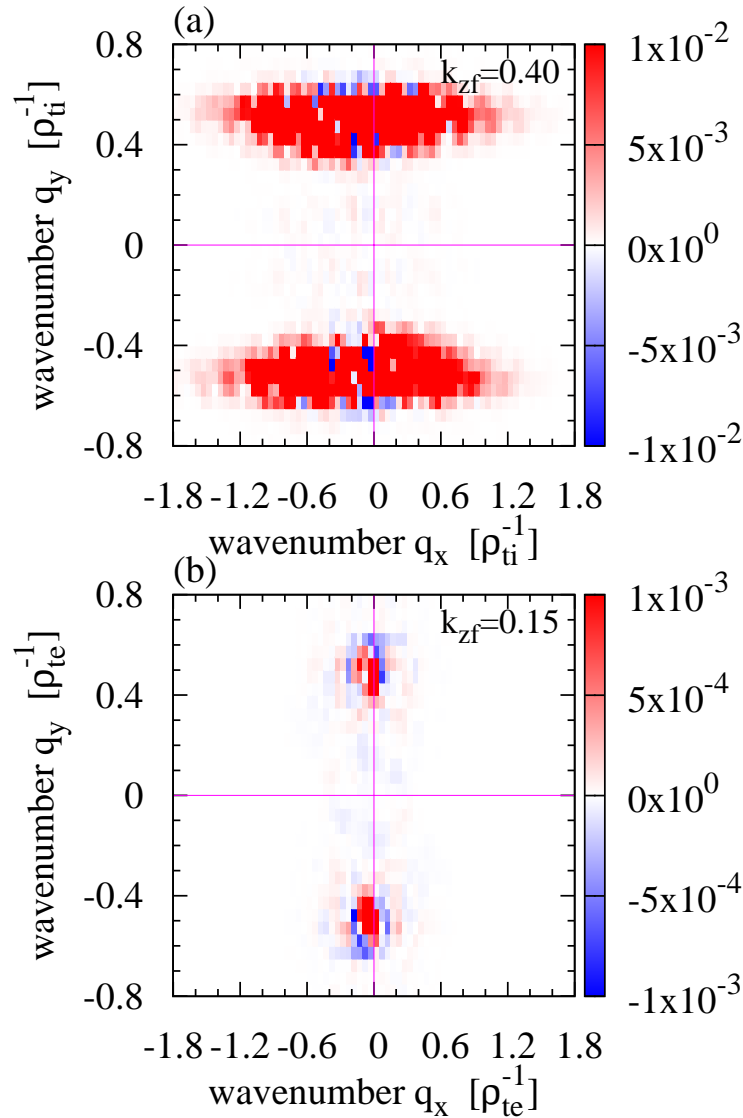

FIG. 5.18: Time-averaged wavenumber spectrum of the triad transfer function normalized by the mean heat flux, $\overline{\mathcal{J}}_s[\boldsymbol{k}_{zf}|\boldsymbol{p}_\perp, \boldsymbol{q}_\perp]/\eta_s \overline{Q}_s$, for the fixed-$\boldsymbol{k}_{zf}$ in the saturation phase of the slab (a)ITG (s=i) and (b)ETG (s=e) turbulence.

Time-averaged wavenumber spectrum of the triad entropy transfer function normalized by the mean heat flux, i.e., $\overline{\mathcal{J}}_s[\boldsymbol{k}_{zf}|\boldsymbol{p}_\perp,\boldsymbol{q}_\perp]/\eta_s\overline{Q}_s$, in the saturation phase of the slab ITG and ETG instability growth are shown in Figs. 5.18(a) and 5.18(b), respectively. The wavenumbers of the slab ITG- and ETG-driven zonal flows are chosen as $k_{zf}=0.40\rho_{ti}^{-1}$ and $k_{zf}=0.15\rho_{te}^{-1}$, respectively. As expected from the high peak amplitude of $\mathcal{T}_i^{(zf)}$ and $\mathcal{T}_e^{(zf)}$ in the saturation phase shown in Fig. 5.17(a), the large positive values of both $\overline{\mathcal{J}}_i[\boldsymbol{k}_{zf}|\boldsymbol{p}_\perp,\boldsymbol{q}_\perp]/\eta_i\overline{Q}_i$ and $\overline{\mathcal{J}}_e[\boldsymbol{k}_{zf}|\boldsymbol{p}_\perp,\boldsymbol{q}_\perp]/\eta_e\overline{Q}_e$ are found in the linearly unstable region with $q_y \sim 0.4$ (cf. Fig. 3.1). Also, one finds the broad spectrum of $\overline{\mathcal{J}}_i[\boldsymbol{k}_{zf}|\boldsymbol{p}_\perp,\boldsymbol{q}_\perp]/\eta_i\overline{Q}_i$ in the q_x-direction, while the spectrum for the ETG case is confined in the
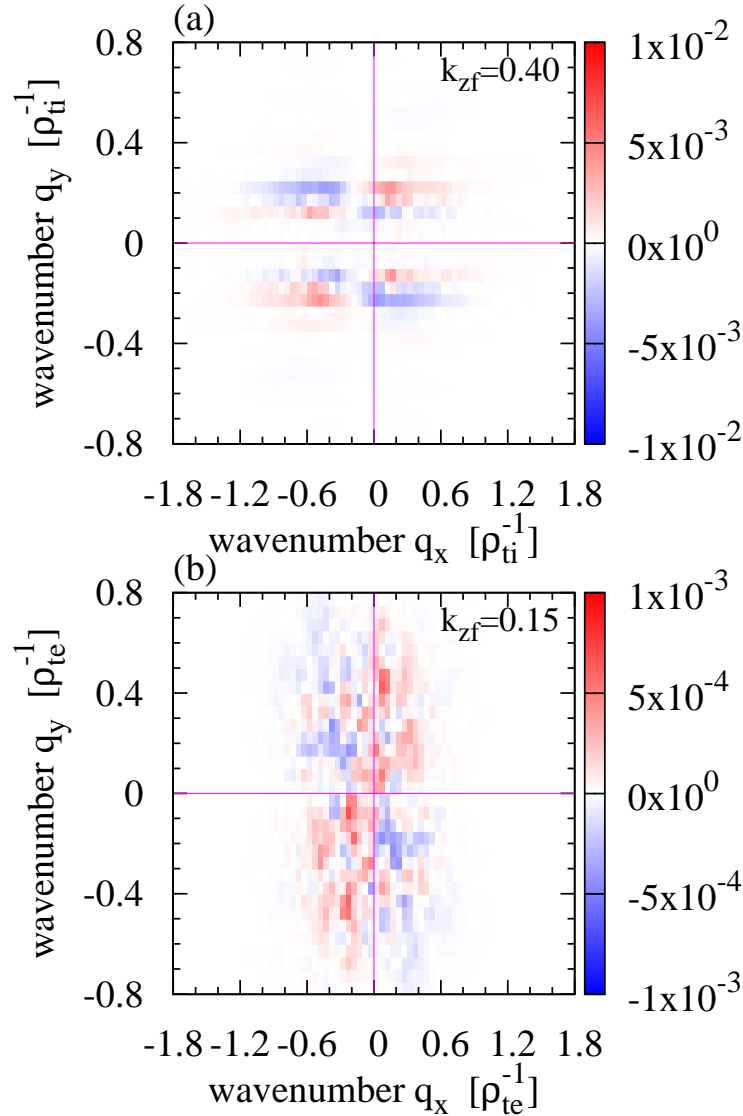

FIG. 5.19: Time-averaged wavenumber spectrum of the triad transfer function normalized by the mean heat flux, $\overline{\mathcal{J}}_s[\boldsymbol{k}_{zf}|\boldsymbol{p}_\perp,\boldsymbol{q}_\perp]/\eta_s\overline{Q}_s$, for the fixed-$\boldsymbol{k}_{zf}$ in the steady state of slab (a)ITG (s = i) and (b)ETG (s = e) turbulence.

lower-q_x region.

The wavenumber spectra of $\overline{\mathcal{J}}_s[\boldsymbol{k}_{zf}|\,\boldsymbol{p}_\perp,\boldsymbol{q}_\perp]/\eta_s\overline{Q}_s$ in the steady state are shown in Figs. 5.19, where the time average is taken over $400 \leqslant t \leqslant 500$. It is found that, in similar to the toroidal ITG case [cf. Fig. 5.9(a) and 5.10(a)], the amplitude of $\overline{\mathcal{J}}_i[\boldsymbol{k}_{zf}|\,\boldsymbol{p}_\perp,\boldsymbol{q}_\perp]/\eta_i\overline{Q}_i$ in the steady state is much lower than that in the saturation phase shown in Fig. 5.18(a). Furthermore, in the slab ETG case [Fig. 5.19(b)], one finds the nearly isotropic spectrum of $\overline{\mathcal{J}}_e[\boldsymbol{k}_{zf}|\,\boldsymbol{p}_\perp,\boldsymbol{q}_\perp]/\eta_e\overline{Q}_e$, where the nonlinear local-interactions among non-zonal modes are dominant.

Figures 5.20 show the wavenumber spectra of $\overline{\mathcal{J}}_i[\boldsymbol{p}_\perp|\,\boldsymbol{q}_\perp,\boldsymbol{k}_{zf}]/\eta_i\overline{Q}_i$ in the steady state of the slab ITG turbulence for three different p_x, where p_y is fixed to $p_y = 0.15$ which is the dominant component driving the heat flux. One clearly finds the two-stripe pattern at $p_y = 0$ and $p_y = -0.15$ with high amplitude, which indicates the strong interaction of the zonal and the other non-zonal modes. Hence, the catalytic role of strong zonal flows in the successive entropy transfer to the higher radial-wavenumber mode causing less turbulent heat flux, which is similar to that observed in the toroidal ITG case, is also demonstrated in the steady state of the slab ITG turbulence.

The wavenumber spectra of $\overline{\mathcal{J}}_e[\boldsymbol{p}_\perp|\,\boldsymbol{q}_\perp,\boldsymbol{k}_{zf}]/\eta_e\overline{Q}_e$ in the steady state of slab ETG turbulence for three different $\boldsymbol{p}_\perp$ are plotted in Figs. 5.21. Similar to the toroidal ETG case shown in Figs. 5.13, one also finds the nearly isotropic entropy transfer in the low wavenumber region through the nonlinear local-interactions among non-zonal modes, rather than zonal flows so that the successive entropy transfer to the higher wavenumber modes due to the interaction with zonal modes is weak in the steady phases of the slab ETG turbulence.

5.5   Concluding remarks

In the present study, the entropy balance relations for non-zonal and zonal modes in toroidal ITG and ETG turbulence have been examined by means of five-dimensional nonlinear gyrokinetic Vlasov simulation code, GKV [3]. Particularly, the nonlinear entropy transfer processes in the saturation and steady phases, which are associated with the instability saturation and the transport regulation, are investigated by the spectral analysis of the triad entropy transfer function. The entropy transfer from non-zonal to zonal modes is regarded as a kinetic extension for zonal-flow energy production due to the Reynolds stress.

The nonlinear simulation results confirm that the entropy balance relations for turbulence (non-zonal) and zonal-flow components, which are coupled with each other through the entropy transfer function $\mathcal{T}_s^{(zf)}$, are accurately satisfied for the whole simulation time both in the ITG and ETG turbulence. It is also found that the statistically steady states of the ITG and ETG
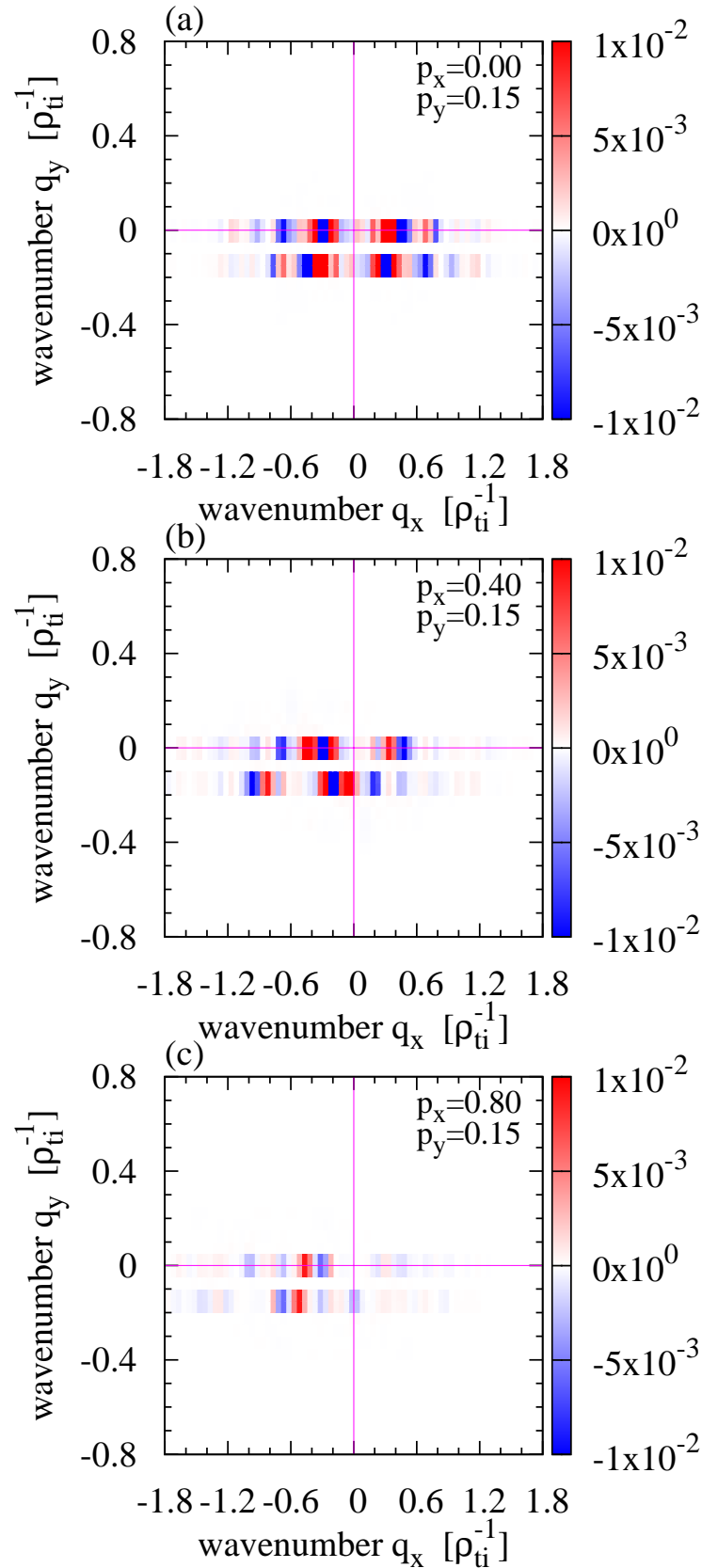
FIG. 5.20: Wavenumber spectra of the triad transfer function normalized by the mean heat flux, $\overline{\mathcal{J}}_i[\boldsymbol{p}_\perp|\boldsymbol{q}_\perp, \boldsymbol{k}_{zf}]/\eta_i \overline{Q}_i$, for three different $\boldsymbol{p}_\perp$ in the steady state of slab ITG turbulence, where the time-average is taken over $400 \leqslant t \leqslant 500$.
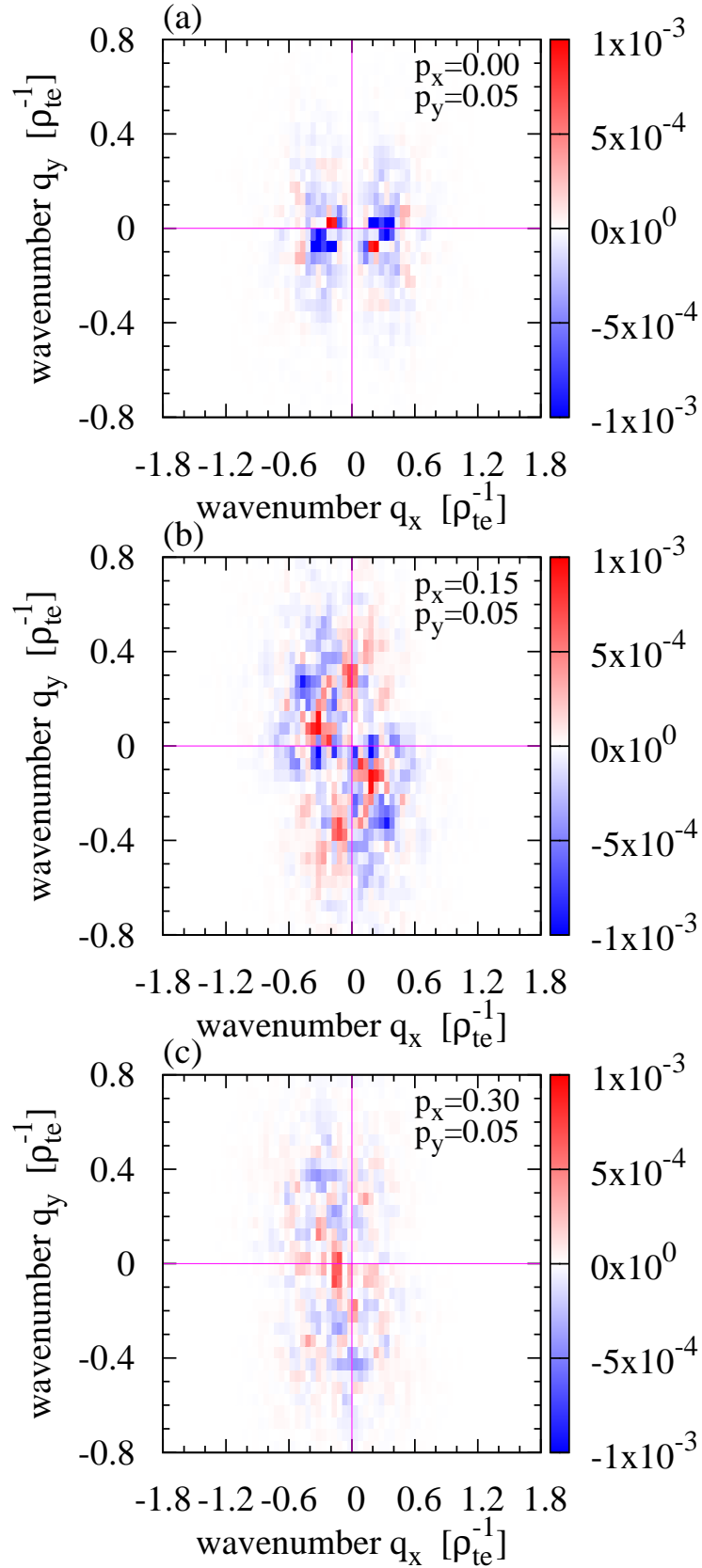
FIG. 5.21: Wavenumber spectra of the triad transfer function normalized by the mean heat flux, $\overline{\mathcal{J}}_e[\boldsymbol{p}_\perp | \boldsymbol{q}_\perp, \boldsymbol{k}_{zf}]/\eta_i \overline{Q}_i$, for three different $\boldsymbol{p}_\perp$ in the steady state of slab ETG turbulence, where the time-average is taken over $400 \leqslant t \leqslant 500$.

turbulence are realized long after the saturation of linear instability, where the balance relations of $\overline{\mathcal{T}}_s^{(zf)} = -\overline{D}_s^{(zf)} \geqslant 0$ and $L_{T_s}^{-1}\overline{Q}_s - \overline{\mathcal{T}}_s^{(zf)} = -\overline{D}_s^{(trb)}$ hold separately for the turbulence and zonal-flow components (the overline denotes the time-average in the steady state). A remarkable difference between the ITG and ETG cases is found in the time evolutions of $\mathcal{T}_s^{(zf)}/\eta_s\overline{Q}_s$. In the saturation phase of the instability growth, the higher peak amplitude of $\mathcal{T}_i^{(zf)}/\eta_i\overline{Q}_i$ in comparison to that of $\mathcal{T}_e^{(zf)}/\eta_e\overline{Q}_e$ is observed, while it decreases significantly in the steady state and becomes same order of magnitude as that for the ETG case, i.e., $\mathcal{T}_i^{(zf)}/\eta_i\overline{Q}_i \sim \mathcal{T}_e^{(zf)}/\eta_e\overline{Q}_e \ll 1$. The nonlinearly generated zonal flows with strong flow-shear play a critical role for the saturation of the ITG instability growth whereas the entropy transfer processes among non-zonal modes are dominant in the ETG case.

The time evolutions of the wavenumber spectra of turbulent fluctuations show that, in the saturation phase, a spectral peak of the fluctuation intensity is down-shifted to a low-k_y region from the linearly most unstable wavenumber. In addition, it is observed that the fluctuation spectrum spreads into the higher-k_x region as well. The strong zonal flows are sustained in the steady state of the toroidal ITG turbulence, while the radially elongated streamers with the high amplitudes, which are associated with the strong electron heat transport, are formed in the ETG turbulence. Although the mode with $k_x \simeq 0$ and $k_y \simeq 0.2\rho_{ts}^{-1}$ makes the most dominant contribution to the heat transport, different spectral shapes of the heat flux and the potential fluctuations are found between the ITG and ETG turbulence, that is, broad k_x-spectra are observed for the ITG case while the spectra for the ETG case are confined within the lower-k_x region.

In order to understand the nonlinear entropy transfer processes in the saturation and steady phases, the wavenumber spectra of the triad transfer functions $\mathcal{J}_s[k_{zf}|p_\perp, q_\perp]$ and $\mathcal{J}_s[p_\perp|q_\perp, k_{zf}]$ for two non-zonal modes with $p_\perp$ and $q_\perp$ and a zonal mode with $k_{zf} = k_{zf}\nabla x$ have been examined. The detailed balance relation, Eq. (5.20) [or Eq. (5.23)], provides us explicitly with the direction of the entropy transfer among the zonal and non-zonal modes. Then, the qualitatively different entropy transfer processes in the saturation and steady phases of the ITG turbulence are clarified. The entropy transfer from non-zonal to zonal modes is substantial in the saturation phase of the ITG turbulence, while, once the high-amplitude zonal flows are generated, the entropy transfer to the zonal modes becomes quite weak in the steady state. Instead, the zonal flows play a catalytic role in the entropy transfer among non-zonal modes, i.e., the entropy of non-zonal modes with low radial-wavenumbers driving the heat transport is successively transferred to the other non-zonal modes with higher radial-wavenumbers with less contribution to the transport. The successive entropy transfer to the high-k_x modes due to the non-local interactions with the strong zonal flows in the wavenumber-space leads to the broadening of the wavenumber spectra in the steady state of the ITG turbulence. In contrast to the ITG case, the nonlinear interactions

among the low-wavenumber non-zonal modes are dominant in the ETG case so that the entropy transfer resulting from the interactions with zonal flows are not effective for the saturation of the instability growth and the transport regulation.

The comparison of the slab and toroidal ITG/ETG turbulence simulation results reveals that the significant entropy transfer from non-zonal modes to zonal modes is commonly observed in the saturation phases of toroidal ITG, slab ITG, and slab ETG turbulence, while the entropy transfer among non-zonal modes is dominant in the toroidal ETG turbulence. Similar to the toroidal ITG case, the entropy transfer to zonal modes are quite weak, and then the successive entropy transfer to the higher radial-wavenumber modes through the catalytic role of the zonal mode is found in the steady state of the slab ITG turbulence. In the steady state of the slab ETG turbulence with isolated vortices and their mergers, the nearly isotropic entropy transfer in the low wavenumber region through the nonlinear local-interactions among non-zonal modes is found, in similar to that of the toroidal ETG case where the radially elongated streamers with high amplitude are formed.

The results obtained in the present study by a novel method of the triad entropy transfer analysis provide ones with not only deeper understandings of the fundamental physics of the nonlinear interaction between turbulence and zonal flows, but also useful suggestions for advanced turbulence diagnostics such as the bi-spectrum analysis. Specifically, the present analysis in terms of the triad entropy transfer function involves the explicit information of the direction of the transfer which has rarely been discussed in the conventional bi-spectrum analysis. Also, the use of entropy variable, which is based on the kinetic equation, enables us to examine systematically both the nonlinear interactions among the zonal and non-zonal modes and their effects on the turbulent transport level.

Bibliography for Chapter 5

[1] Z. Lin, T. S. Hahm, W. W. Lee, W. M. Tang, and R. B. White, Science **18**, 1835 (1998)

[2] A. M. Dimits, G. Bateman, M. A. Beer, B. I. Cohen, W. Dorland, G. W. Hammett, C. Kim, J. E. Kinsey, M. Kotschenreuther, A. H. Kritz, L. L. Lao, J. Mandrekas, W. M. Nevins, S. E. Parker, A. J. Redd, D. E. Shumaker, R. Sydora, and J. Weiland, Phys. Plasmas **7**, 969 (2000)

[3] T.-H. Watanabe and H. Sugama, Nucl. Fusion **46**, 24 (2006)

[4] A. Fujisawa, K. Itoh, H. Iguchi, K. Matsuoka, S. Okamura, A. Shimizu, T. Minami, Y. Yoshimura, K. Nagaoka, C. Takahashi, M. Kojima, H. Nakano, S. Oshima, S. Nishimura, M. Isobe, C. Suzuki, T. Akiyama, K. Ida, K. Toi, S. -I, Itoh, and P. H. Diamond, Phys. Rev. Lett. **93**, 165002 (2004)

[5] P. H. Diamond and S. -I. Itoh, K. Itoh, and T. S. Hahm, Plasma. Phys. Control. Fusion **47**, R35 (2005)

[6] L. Chen, Z. Lin, and R. B. White, Phys. plasmas **7**, 3129 (2000)

[7] P. N. Guzdar, R. G. Kleva, and L. Chen, Phys. plasmas **8**, 459 (2001)

[8] E.-J. Kim and P. H. Diamond, Phys. plasmas **7**, 3551 (2000)

[9] B. N. Rogers, W. Dorland, and M. Kotschenreuther, Phys. Rev. Lett. **18**, 5336 (2000)

[10] F. Jenko, W. Dorland, M. Kotschenreuther, and B. N. Rogers, Phys. Plasmas **7**, 1904 (2000)

[11] Y. Idomura, M. Wakatani, and S. Tokuda, Phys. Plasmas **7**, 3551 (2000)

[12] Y. Idomura, S. Tokuda, and Y. Kishimoto, Nucl. Fusion **45**, 1571 (2005)

[13] M. Nakata, T.-H. Watanabe, H. Sugama, and W. Horton, Phys. Plasmas **17**, 042306 (2010)

[14] M. Nakata, T.-H. Watanabe, H. Sugama, and W. Horton, Phys. Plasmas **18**, 012303 (2011)

[15] J. A. Krommes and G. Hu, Phys. Plasmas **1**, 3211 (1994)

[16] H. Sugama, M. Okamoto, W. Horton, and M. Wakatani, Phys. Plasmas **3**, 2379 (1996)

[17] H. Sugama, T.-H. Watanabe, and M. Nunami, Phys. Plasmas **16**, 112502 (2009)

[18] A. A. Schekochihin, S. C. Cowley, W. Dorland, G. W. Hammet, G. G. Howes, G. G. Plunk, E. Quataert, and T. Tatsuno, Plasma Phys. Control. Fusuon **50**, 124024 (2008)

[19] T.-H. Watanabe and H. Sugama, Phys. plasmas **11**, 1476 (2004)

[20] Ö. D. Gürcan, P. H. Diamond, and T. S. Hahm, Phys. Rev. Lett. **97**, 024502 (2006)

[21] J. Li and Y. Kishimoto, Phys. Plasmas **17**, 072304 (2010)

[22] K. Itoh, Y. Nagashima, S.-I. Itoh, P. H. Diamond, A. Fujisawa, M. Yagi, and A. Fukuyama, Phys. Plasmas **12**, 102301 (2005)

[23] Y. Nagashima, K. Hoshino, A. Ejiri, K. Shinohara, Y. Takase, K. Tsuzuki, K. Uehara, H. Kawashima, H. Ogawa, T. Ido, Y. Kusama, and Y. Miura, Phys. Rev. Lett. **95**, 095002 (2005)

[24] C. Holland and G. R. Tynan *et al*., Phys. Plasmas **14**, 056112 (2007)

[25] R. E. Waltz and C. Holland, Phys. Plasmas **15**, 122503 (2008)

[26] T. Tatsuno, W. Dorland, A. A. Schekochihin, G. G. Plunk, M. Barnes, S. C. Cowley, and G. G. Howes, Phys. Rev. Lett. **103**, 015003 (2009)

[27] A. B. Navarro, P. Morel, M. A. Marc, D. Carati, F. Merz, T. Görler, and F. Jenko, Phys. Rev. Lett. **106**, 055001 (2011)

[28] D. R. Hatch, P. W. Terry, F. Jenko, F. Merz, and W. M. Nevins, Phys. Rev. Lett. **106**, 115003 (2011)

[29] M. A. Beer, S. C. Cowley, and G. W. Hammett, Phys. plasmas **2**, 2687 (1995)

[30] M. Lesieur, "Turbulence in Fluids", Kluwer academic publishers, (1990)

[31] R. H. Kraichnan, J. Fluid Mech. **83**, 497 (1959)

[32] S. Kida and S. Goto J. Fluid Mech. **345**, 307 (1997)

[33] Z. Lin, L. Chen, and F. Zonca, Phys. Plasmas **12**, 056125 (2005)

Chapter 6

Summary

F undamental physics behind the formation of vortex and zonal flow structures and their stability, as well as the related transport properties, in slab/toroidal ITG/ETG turbulence have been extensively explored in this dissertation based on nonlinear gyrokinetic theory and the direct numerical simulations. Then, the highlighted results concerning (i) formation of coherent vortex streets and the resultant transport reduction, (ii) effects of parallel dynamics on the zonal flow generation, and (iii) nonlinear entropy transfer among turbulent vortices, streamers, and zonal flows, are presented.

First, vortex structures in the slab ETG turbulence are investigated, including comparisons with those in the slab ITG case. The evaluation of the entropy balance relation in the slab ETG turbulence shows that the turbulence reaches to the statistically steady state accompanied with weak zonal flow generations, where the turbulent heat flux balances with the collisional dissipation. Through the comparison of the slab ETG (with and without zonal flows) and the slab ITG turbulence simulations, it is found that the zonal flows driven by the slab ETG turbulence play a crucial role in suppressing the $(k_x = 0, k_y = k_{\min})$-mode and in realizing the steady heat transport. Formation of isolated vortices and their mergers with complicated motion are observed in the slab ETG turbulence, while the strong zonal flows dominate and completely suppress the turbulent transport in the slab ITG turbulence. Depending on parameters which determine the growth rate of linear ETG modes, two different flow structures are observed, i.e., statistically steady turbulence with a weak zonal flow and coherent vortex streets along a strong zonal flow. When the coherent vortex streets are formed, phase difference and high wavenumber components of potential and temperature fluctuations are reduced, and the electron heat transport decreases significantly. It is also found that the phase matching with the potential fluctuation is correlated to the reduction of the imaginary part of the perturbed distribution function. In order to describe the coherent vortex streets, a fluid model, which is similar to the conventional Hasegawa-Mima equa-

tion, is derived directly from the gyrokinetic equation for electrons, where the velocity moment of the parallel advection term $\int dv_\parallel \, ik_\parallel v_\parallel \delta f_{k_\perp}$ is ignored. By evaluating the nonlinear simulation results in detail, it is concluded that the coherent vortex streets found in the slab ETG turbulence, which are closely related to the transport reduction, are explained by a traveling wave solution of a Hasegawa-Mima type fluid equation derived here.

Second, effects of parallel dynamics on transition of vortex structures and zonal flows, which are closely associated with transport reduction found in the slab ETG turbulence, are intensively examined by the comprehensive parameter studies. Numerical results show three different types of vortex structures, i.e., coherent vortex streets accompanied with the transport reduction, turbulent vortices with steady transport, and a zonal-flow-dominated state, depending on the relative magnitude of the parallel compression to the diamagnetic drift, which is characterized by the parameter $\Theta = k_\parallel L_T / k_y \rho_{\mathrm{te}}$. In particular, a clear correlation between the formation of coherent vortex streets associated with the strong generation of the zonal flow and transport reduction is found for the cases with weak parallel compression, even though the maximum growth rate of linear ETG modes is relatively large. Power spectra of the entropy variable δS_n and the entropy flux J_n in the $v_\parallel$-space for the different Θ have been examined by means of the Hermite polynomial expansion. Then it is found that the different vortex structures in the real space, which depend on Θ, affect the spectral profiles, especially, the n-spectra of the entropy production region in the lower-n side. A physical mechanism of the secondary growth of zonal flows is discussed based on the modulational instability analysis with a truncated fluid model, where the parallel dynamics with acoustic modes is incorporated, then a linear dispersion relation for the zonal-flow growth rate is derived. The modulational instability driving zonal flows is found to be stabilized by the effect of the finite parallel compression. The theoretical analysis qualitatively agrees with the secondary growth of zonal flows found in the slab ETG turbulence simulations for small-Θ, where the transition of vortex structures and the related transport reduction is observed.

Finally, the investigations of the entropy balance relations, vortex and flow structures are extended to toroidal ITG and ETG turbulence by means of five-dimensional nonlinear gyrokinetic simulations. The nonlinear entropy transfer processes in the saturation and steady phases, which leads to the saturation of the instability growth and with the suppression of turbulent transport, are carefully examined by the spectral analysis of the entropy transfer function. The entropy transfer function describes the nonlinear transfer of the entropy variable from non-zonal to zonal modes, and is regarded as a kinetic extension for zonal-flow energy production due to the hydrodynamic Reynolds stress. It is found that the statistically steady states of the ITG and ETG turbulence are realized long after the saturation of linear instability, where the balance relations of $\overline{\mathcal{T}}_{\mathrm{s}}^{(\mathrm{zf})} = -\overline{D}_{\mathrm{s}}^{(\mathrm{zf})} \geqslant 0$ and $L_{T_{\mathrm{s}}}^{-1}\overline{Q}_{\mathrm{s}} - \overline{\mathcal{T}}_{\mathrm{s}}^{(\mathrm{zf})} = -\overline{D}_{\mathrm{s}}^{(\mathrm{trb})}$ hold separately for the turbulence and

zonal-flow components (the overline denotes the time-average in a saturated phase). Then, the formation of the strong zonal flow is observed in the toroidal ITG turbulence, while the radially elongated streamers, which yield the significant enhancement of heat transport, develop in the toroidal ETG case. The detailed analysis of the triad transfer functions, $\mathcal{J}_s[\boldsymbol{k}_{\mathrm{zf}}|\boldsymbol{p}_\perp, \boldsymbol{q}_\perp]$ and $\mathcal{J}_s[\boldsymbol{p}_\perp|\boldsymbol{q}_\perp, \boldsymbol{k}_{\mathrm{zf}}]$, clarifies the different entropy transfer processes in saturation and steady phases. The entropy transfer from non-zonal to zonal modes is substantial in the saturation phase of the ITG turbulence, while, once the high-amplitude zonal flows are generated, the entropy transfer to the zonal modes becomes quite weak in the steady state. Instead, the zonal flows play a catalytic role in the entropy transfer among non-zonal modes, i.e., the entropy of non-zonal modes with low radial-wavenumbers driving the heat transport is successively transferred to the other non-zonal modes with higher radial-wavenumbers with less contribution to the transport. The successive entropy transfer to the high-k_x modes due to the non-local interactions with the strong zonal flows in the wavenumber-space leads to the broadening of the wavenumber spectra in the steady state of the ITG turbulence. In contrast to the ITG case, the nonlinear interactions among the low-wavenumber non-zonal modes are dominant in the ETG case so that the entropy transfer resulting from the interactions with zonal flows are not effective for the saturation of the instability growth and the transport regulation. The qualitatively similar entropy transfer processes are also revealed in the slab ITG and ETG turbulence by the detailed comparison of the wavenumber spectrum of the entropy transfer function.

In the present study based on the framework of the kinetic theory, the comprehensive analysis of vortex and zonal flow structures and the novel method of the entropy transfer analysis provide ones with not only deeper understandings of the fundamental physics of the nonlinear interaction between turbulence and zonal flows including the turbulent transport processes, but also fruitful suggestions for advanced turbulence diagnostics such as the bi-spectrum analysis.

List of publications

[1] Motoki Nakata, Tomo-Hiko Watanabe, Hideo Sugama, and Wendell Horton, "*Formation of coherent vortex streets and transport reduction in electron temperature gradient driven turbulence*", Physics of plasmas, Volume **17**, 042306 (2010)

[2] Motoki Nakata, Tomo-Hiko Watanabe, Hideo Sugama, and Wendell Horton, "*Effects on parallel dynamics on vortex structures in electron temperature gradient driven turbulence*", Physics of plasmas, Volume **18**, 012303 (2011)

[3] Motoki Nakata, Tomo-Hiko Watanabe, and Hideo Sugama, "*Nonlinear entropy transfer via zonal flows in gyrokinetic plasma turbulence*", submitted to Physics of plasmas (2011)